

FINAL REPORT

Studies of Rain Erosion Mechanisms in a Range of IR Transmitting Ceramics - Including Coated Samples

Contract SPC-92-4032

Dr C.R. Seward, Dr C.S.J. Pickles
E.J. Coad, M. Watt and Dr J.E. Field

Principal Investigator: Dr J.E. Field

January 1994

19970506 081

PCS Fracture Group
Cavendish Laboratory
University of Cambridge
Madingley Road
Cambridge
CB3 0HE

Tel: 0223 - 337 336
0223 - 337 208
Fax: 0223 - 350 266

DISTRIBUTION STATEMENT A

Approved for public release;
Distribution Unlimited

REPORT DOCUMENTATION PAGE

Form Approved OMB No. 0704-0188

Public reporting burden for this collection of information is estimated to average 1 hour per response, including the time for reviewing instructions, searching existing data sources, gathering and maintaining the data needed, and completing and reviewing the collection of information. Send comments regarding this burden estimate or any other aspect of this collection of information, including suggestions for reducing this burden to Washington Headquarters Services, Directorate for Information Operations and Reports, 1215 Jefferson Davis Highway, Suite 1204, Arlington, VA 22202-4302, and to the Office of Management and Budget, Paperwork Reduction Project (0704-0188), Washington, DC 20503.

1. AGENCY USE ONLY (Leave blank)	2. REPORT DATE January 1994	3. REPORT TYPE AND DATES COVERED Final Report
----------------------------------	--------------------------------	--------------------------------------------------

4. TITLE AND SUBTITLE Studies of Rain Erosion Mechanisms in a Range of IR Transmitting Ceramics - Including Coated Samples	5. FUNDING NUMBERS F6170892W0904
-------------------------------------------------------------------------------------------------------------------------------	-------------------------------------

6. AUTHOR(S) Dr. J.E.Field, Dr. C.R.Seward, Dr. C.S.J.Pickles, E.J.Coad, M.Watt	
------------------------------------------------------------------------------------	--

7. PERFORMING ORGANIZATION NAME(S) AND ADDRESS(ES) University of Cambridge Cavendish Laboratory/PCS Fracture Group Mandingley Road Cambridge, UK CB3 0HE	8. PERFORMING ORGANIZATION REPORT NUMBER SPC-92-4032
----------------------------------------------------------------------------------------------------------------------------------------------------------------------	---------------------------------------------------------

9. SPONSORING/MONITORING AGENCY NAME(S) AND ADDRESS(ES) EOARD PSC 802 BOX 14 FPO 09499-0200	10. SPONSORING/MONITORING AGENCY REPORT NUMBER SPC-92-4032
------------------------------------------------------------------------------------------------------	---------------------------------------------------------------

11. SUPPLEMENTARY NOTES

12a. DISTRIBUTION/AVAILABILITY STATEMENT Approved for public release; distribution is unlimited.	12b. DISTRIBUTION CODE A
-----------------------------------------------------------------------------------------------------	-----------------------------

<p>13. ABSTRACT (Maximum 200 words)</p> <p>This report starts by reviewing what is known about the rainfield an aircraft or missile flies through. It then looks at some of the methods available to simulate it. Although not a perfect reproduction of a high velocity raindrop impact, the waterjet techniques, developed in the Cavendish Laboratory, Cambridge, are found to be close enough simulations of the real environment to be useful research tools. A standard method of operation for both SIJA (Single Impact Jet Apparatus) and MIJA (Multiple Impact Jet Apparatus), however is urgently needed. The report therefore reanalyses the theory behind the damage threshold velocity (DTV) and the possible ways of evaluating it. A standard method of data presentation is defined from this analysis and reapplied to the results from MIJA. The last half of the report is therefore a catalogue of the infrared material rain erosion resistance properties evaluated by us over the last two years and presented according to this standard. Data are given on Zns, Ge, sapphire, spinel, CaLa₂S₄, BP, CVD diamond, natural diamond, silicon magnesium fluoride and various coated systems.</p> <p style="text-align: center;">DTIC QUALITY INSPECTED 2</p>

14. SUBJECT TERMS	15. NUMBER OF PAGES 233
	16. PRICE CODE

17. SECURITY CLASSIFICATION OF REPORT UNCLASSIFIED	18. SECURITY CLASSIFICATION OF THIS PAGE UNCLASSIFIED	19. SECURITY CLASSIFICATION OF ABSTRACT UNCLASSIFIED	20. LIMITATION OF ABSTRACT UL
-------------------------------------------------------	----------------------------------------------------------	---------------------------------------------------------	----------------------------------

DISCLAIMER NOTICE



THIS DOCUMENT IS BEST QUALITY AVAILABLE. THE COPY FURNISHED TO DTIC CONTAINED A SIGNIFICANT NUMBER OF PAGES WHICH DO NOT REPRODUCE LEGIBLY.

FINAL REPORT

Studies of Rain Erosion Mechanisms in a Range of IR Transmitting Ceramics - Including Coated Samples

Contract SPC-92-4032

Dr C.R. Seward, Dr C.S.J. Pickles
E.J. Coad, M. Watt and Dr J.E. Field

Principal Investigator: Dr J.E. Field

January 1994

PCS Fracture Group
Cavendish Laboratory
University of Cambridge
Madingley Road
Cambridge
CB3 0HE

Tel: 0223 - 337 336
0223 - 337 208
Fax: 0223 - 350 266

Introduction

The water-jet simulation of high velocity rain impact, pioneered in the Cavendish Labs in Cambridge over 35 years ago, is now being used in over 20 labs around the world. Because the test is reproducible, cheap, quick and easy to carry out it has fast become an attractive simulation technique. Its rapid increase in popularity as a screening method for new materials and manufacturing processes has however recently led to problems. Large amounts of data are now being produced from all these different sources, and analysed and presented in a variety of different formats. In addition there has recently been some criticisms levelled at the effectiveness of the simulation itself.

This report starts by reviewing what is known about the rainfield the aircraft is flying through. It then looks at some of the methods available to simulate it. Although not a perfect reproduction of a high velocity raindrop impact, the water-jet technique is found to be a close enough simulation of the real environment to be a useful research tool. A standard method of operation for both SIJA (Single Impact Jet Apparatus) and MIJA (Multiple Impact Jet Apparatus) however is urgently needed. The report therefore next re-analyses the theory behind the damage threshold velocity (DTV) and the possible ways of evaluating it. A standard method of data presentation is defined from this analysis and reapplied to the results from MIJA. The last half of the report is therefore a catalogue of the infra-red material rain erosion resistance properties evaluated over the last two years and presented according to this standard. To avoid all uncertainty this new standard is repeated on page 1.

ACKNOWLEDGEMENTS

The MIJA work before June 1993 was carried out by Dr C.R. Seward and M.J. Watt, and from June 1993 to January 1994 by Dr C.R. Seward and E.J. Coad. The SIJA and bursting disc work was carried out by C.S.J. Pickles and Jin Ying. Dr J.E. Field has supervised the work on both MIJA and SIJA.

The major sponsors for the Cambridge work on liquid impact have been DRA (Malvern) and DRA (Farnborough). The Science and Engineering Research Council have also provided funds for some of the high-speed camera facilities (Hadland Imacon and IMCO Ultramac cameras). Grants from the USAF through the European office, have also helped significantly in the testing of infra-red "window" materials.

Contents

Chapter 1: The Hazards of Flight

1.1 Environmental Hazards.....	2
1.2 The Rain Environment.....	4
1.3 High Velocity Flight Through Rain.....	4
1.4 The Radome.....	6
1.5 Radome Damage Due to Impact with Rain.....	8
1.6 Conclusion.....	10
References.....	11

Chapter 2: The Problem With Rain

2.1 Creation of Water Drops.....	12
2.1.1 Introduction.....	12
2.1.2 Condensation.....	12
2.1.3 Collision and Coalescence.....	12
2.1.4 Limits to the Size of Water Drops.....	14
2.1.5 Terminal Velocity of Drops.....	16
2.1.6 Size Distribution of Water Drops.....	16
2.2 Drop Shape.....	18
2.2.1 Shape Taken.....	18
2.2.2 Reason for Interest in Drop Shape.....	18
2.2.3 Factors Affecting Drop Shape.....	18
2.2.3.a Surface Tension.....	18
2.2.3.b Internal Hydrostatic Pressure.....	18
2.2.3.c Aerodynamic Pressure.....	20
2.2.3.d Internal Circulation.....	20
2.2.3.e Electric Stress.....	22
2.2.4 Theoretical Calculations of Drop Shape.....	24
2.2.5 Experimental Evaluations of Drop Shape.....	26
2.2.6 Drop Oscillations.....	26
2.2.7 Drop Canting.....	30
2.2.8 Dual Polarisation Technique.....	32
2.3 Breakup of Water Drops.....	34
2.3.1 Introduction.....	34
2.3.2 Forces Acting on the Drop.....	34
2.3.3 Conditions in the Airflow Behind a Shock.....	35
2.3.3.a Velocity of the Airstream Behind the Shock.....	35
2.3.3.b Temperature of the Air Behind the Shock.....	36
2.3.3.c Viscosity of the Air Behind the Shock.....	36
2.3.3.d Reynolds Number for the Flow Around a Water Drop.....	36
2.3.3.e Mach Number of the Airstream Behind the Shock.....	36
2.3.3.f Pressure in the Airstream Behind the Shock.....	36
2.3.4 Modes of Breakup.....	37
2.3.4.a Vibrational ($We \sim <10$).....	37
2.3.4.b Bag Breakup ($We \sim 10 - 20$).....	37
2.3.4.c Umbrella ($We \sim 20 - 70$).....	38

2.3.4.d Stripping ($We \sim 1000$)	39
2.3.4.e Catastrophic ($We \sim 50,000$)	40
2.3.5 Breakup in the Shock Layer of a High Speed Vehicle	40
2.3.5.a Air Flow Round a Moving Body.....	40
2.3.5.b Nondimensional-Parameters for Drop Behaviour.....	41
2.3.5.c Drop Deceleration and Trajectory	41
2.3.5.d Drop Breakup Time	41
2.3.5.e Drop Deformation and Mass Loss	42
2.3.5.f Heating Effects	44
2.3.5.g A Sample Problem	44
2.3.6 Protection for a Radome by Drop Breakup	44
2.3.7 Drop Deformation in Subsonic Flight	44
2.4 Summary	46
References	47

Chapter 3: Simulation Of Liquid Impact

3.1 Introduction	55
3.2 Wheel and Jet	55
3.3 Whirling Arm Rigs.....	56
3.3.1 Power Consumption.....	56
3.3.2 High Centrifugal Forces	58
3.3.3 Drop Distortion Before Impact	58
3.3.4 Sample Temperature	60
3.3.5 Presence of a Water Film on the Specimens	60
3.3.6 The Specimen Holder	62
3.3.7 Comparison of Whirling Arm Rig Results	62
3.4 Rocket Sleds.....	62
3.5 In-Flight Evaluation	64
3.6 Sabot Fired At A Suspended Drop.....	64
3.7 Interrupted Jet	66
3.8 Single Impact Jet Apparatus	66
3.9 Wind Tunnel	68
3.10 Repeating Jet	68
3.11 Ballistic Range	70
3.12 Sounding Rockets	71
3.13 Comparison With Solid Impact.....	71
3.14 Single Wave Impact Facility	71
3.15 Laser Simulation	72
3.16 Multiple Impact Jet Apparatus (MIJA)	72
3.17 Multiple Particle Launch Facility	74
3.18 Conclusion	76
References	78

Chapter 4: Threshold Evaluation For A Brittle Material

4.1 The Impact Of A Liquid.....	84
4.2 The Threshold Velocity For Damage.....	86
4.2.1 Definition of Damage Threshold	86
4.2.2 Correlation with Material Properties	86
4.2.3 SIJA Threshold Evaluation	88

4.3 MIJA Threshold Evaluations	88
4.3.1 The 'Petal' Test.....	90
4.3.2 Statistical Threshold Evaluation	90
4.3.3 Threshold Evaluation For Large Samples	90
4.3.4 Threshold Evaluation For Small Samples	92
4.4 Conclusion	92
References	94

Chapter 5: Liquid Impact of IR Materials

Introduction	95
5.1 Sapphire (Aluminium Oxide).....	96
5.1.1 Material Characteristics	96
5.1.2 Material Description	96
5.1.3 Published Rain Erosion Work	96
5.1.4 MIJA Results	97
5.1.4.a Batch 1.....	98
5.1.4.b Batch 2	98
5.1.4.c Batch 3.....	98
5.1.4.d Batch 4	99
5.1.5 Discussion	99
5.1.7 Conclusion	100
5.2 Spinel (Magnesium Aluminate)	108
5.2.1 Material Characteristics	108
5.2.2 Material Description	108
5.2.3 Published Rain Erosion Work	108
5.2.4 MIJA Results	109
5.2.5 Conclusion	110
5.3 Magnesium Fluoride	114
5.3.1 Material Characteristics	114
5.3.2 Material Description	114
5.3.3 Published Rain Erosion Work	114
5.3.4 MIJA Results	115
5.3.5 Conclusion	116
5.4 Silicon	120
5.4.1 Material Characteristics	120
5.4.2 Material Description	120
5.4.3 Published Rain Erosion Work	120
5.4.4 MIJA Results	121
5.4.5 Conclusion	121
5.5 Zinc Sulphide	124
5.5.1 Material Characteristics	124
5.5.2 Material Description	124
5.5.3 Published Rain Erosion Work	124
5.5.4 MIJA Results	126
5.5.5 Conclusion	126
5.6 Diamond II A	132
5.6.1 Material Characteristics	132
5.6.2 Material Description	132
5.6.3 Published Rain Erosion Work	132
5.6.4 MIJA Results	132
5.6.5 Conclusion	134

5.7 Germanium	136
5.7.1 Material Characteristics	136
5.7.2 Material Description	136
5.7.3 Published Rain Erosion Work	136
5.7.4 MIJA Results	137
5.7.5 Conclusion	137
5.8 Calcium Lanthanum Sulphide	140
5.8.1 Material Characteristics	140
5.8.2 Material Description	140
5.8.3 Published Rain Erosion Work	140
5.8.4 MIJA Results	141
5.8.4.a Batch 1 - Sample VX239	141
5.8.4.b Batch 2 - Samples VX262 and VX263	141
5.8.4.c Batch 3 - Sample VX273	141
5.8.4.d Damage patterns.....	141
5.8.5 Conclusion	142
5.9 CVD Diamond	148
5.9.1 Material Characteristics	148
5.9.2 Material Description	148
5.9.3 Published Rain Erosion Work	148
5.9.4 MIJA Results	148
5.9.4.a CVD Diamond on Silicon	149
5.9.4.b Free standing CVD Diamond.....	151
5.9.5 Conclusion	155
5.9.6 Future Research	156
5.10 Amorphous Diamond Coating On Zinc Sulphide	158
5.10.1 Material Characteristics	158
5.10.2 Material Description	158
5.10.3 Published Rain Erosion Work	159
5.10.4 MIJA Results	159
5.10.5 Conclusions.....	160
5.11 Particulate Composites Of Diamond In Zinc Sulphide	162
5.11.1 Material Characteristics	162
5.11.2 Material Description	162
5.11.3 Published Rain Erosion Work	163
5.11.4 MIJA Results	163
5.11.5 Conclusion	164
5.12 Silicon Nitride Coating On BK7 Glass	168
5.12.1 Material Characteristics	168
5.12.2 Material Description	168
5.12.3 Published Rain Erosion Work	168
5.12.4 MIJA Results	168
5.12.4 Conclusions.....	168
5.13 Germanium Carbide Coating On Zinc Sulphide	168
5.13.1 Material Characteristics	170
5.13.2 Material Description	170
5.13.3 Published Rain Erosion Work	170
5.13.4 MIJA Results	171
5.13.5 Conclusions.....	171
5.14 Boron Phosphide Coatings	174
5.14.1 Material Characteristics	174
5.14.2 Material Description	174
5.14.3 Published Rain Erosion Work	174

5.14.4 MIJA Results	175
5.14.4.a Fused Silica Substrate (Feb 1989).....	175
5.14.4.b Zinc Sulphide Substrate (Feb 1990, Dec 1992)	175
5.14.4.c Germanium (May 1993).....	176
5.14.4.d Sapphire (June 1993).....	177
5.14.5 Conclusions.....	177
5.14.5.a Fused Silica Substrate.....	178
5.14.5.b Zinc Sulphide Substrate	178
5.14.5.c Germanium Substrate	178
5.14.5.d Sapphire Substrate.....	179
5.15 Parameters Investigated In This Study.....	190
References	192

Chapter 6: **Summary**

6.1 Rain Erosion.....	198
6.2 The Rain Environment	198
6.3 Simulation Of The Rain Environment	199
6.4 The Damage Threshold Velocity (DTV)	200
6.5 Material Response	202
6.5.1 Substrates	202
6.5.2 Coatings	204
6.5.3 Composites.....	204
6.6 Future Research.....	206
6.7 Conclusion.....	206

Water-Jet Impact Standard

All Damage Threshold Velocities (DTV) produced by SIJA and MIJA should be quoted as the velocity of the 0.8 mm jet at the point of impact on the specimen. Results converted to equivalent 2 mm diameter drops using the correlation data published by the Cavendish (Hand, 1987) should not be quoted on their own. Data should be prefixed in the following way to avoid any doubt as to the technique used to evaluate the DTV, the method of damage assessment, number of impacts used, and to ensure it is realised that the values are jet velocities and not equivalent 2 mm drops.

"0.8 mm jet DTV (mechanical) = " this is the damage threshold velocity found by assessing a materials *strength* after 10 impacts with a 0.8 mm water jet. The DTV is the velocity at which the strength suddenly drops.

"0.8 mm jet DTV (X impacts) = " this is the threshold velocity for the first appearance of any visible *circumferential cracking* after X impacts with a 0.8 mm jet, as viewed at x200 magnification on a microscope.

It is recognised that additional modes of damage are now being recorded (e.g. central damage in CVD diamond) and that these sometimes occur at velocities below the visual damage threshold velocity as defined above. It is not however known for sure whether these new modes of damage have a threshold velocity of their own, although it is probable. Therefore for the moment all other types of damage recorded should be quoted as: "0.8 mm jet DTV (central damage - 10 impacts) = "

When X is large the value of 0.8 mm jet DTV (X impacts) \approx 0.8 mm jet DTV (mechanical). With MIJA it is therefore possible to get near this mechanical threshold value by doing \sim 300 impacts on one site (assuming only circumferential cracking is present). With SIJA it is clearly impractical to fire this many impacts, and it is therefore suggested that DTV data published from SIJA quote the values for the first appearance of any visible circumferential cracking at x200 magnification after 1, 3 and 10 impacts. This will allow initial ranking of material performance to guide research efforts and allow easy comparison before more extensive evaluations can be carried out.

Finally to enable proper comparison of data the accuracy with which the DTV was evaluated should be indicated. For example, for spinel the 0.8 mm jet DTV (1 impact) = $490 \pm 10 \text{ m s}^{-1}$. This means that circumferential cracking occurred on the site impacted once at 500 m s^{-1} , but not on the site impacted once at 480 m s^{-1} .

Examples of this notation used for the MIJA and SIJA results from spinel:

0.8 mm jet DTV (mechanical) = $325 \pm 25 \text{ m s}^{-1}$
0.8 mm jet DTV (300 impacts) = $355 \pm 5 \text{ m s}^{-1}$
0.8 mm jet DTV (10 impacts) = $375 \pm 5 \text{ m s}^{-1}$
0.8 mm jet DTV (3 impacts) = $415 \pm 5 \text{ m s}^{-1}$
0.8 mm jet DTV (1 impact) = $490 \pm 10 \text{ m s}^{-1}$
0.8 mm jet DTV (central damage - 300 impacts) = $280 \pm 30 \text{ m s}^{-1}$
or 0.8 mm jet DTV (1, 3, 10 impacts) = $490 \pm 10, 415 \pm 5, 375 \pm 5 \text{ m s}^{-1}$
or 0.8 mm jet DTV (300 impacts) = $355 \pm 5 \text{ m s}^{-1}$ ($\sim 430 \pm 10 \text{ m s}^{-1}$ for a 2mm drop)

This is a first attempt at creating a usable standard for the water-jet technique. We would therefore appreciate comments from all those who use either the data or the apparatus into future improvements.

Chapter 1

The Hazards of Flight

The aim of this chapter is to show that rain is an important problem during high speed flight, and that it is in particular a problem for the radome since this is now often made of brittle infrared transmitting ceramics, and damage to the radome may affect the guidance of the aircraft or missile.

1.1 ENVIRONMENTAL HAZARDS

The field of aircraft and missile design yields a vast number of complex engineering problems. One important set of difficulties encountered are those arising from the environmental conditions in which high speed vehicles must function. The economics of airline operation, and the requirements of a round-the-clock vigil defensive system, dictate the need for all-weather operational capabilities for civil aircraft and missile alike. There are many environmental hazards facing the designer; atmospheric radiation of all kinds, wind gusts and wind shear, lightning strikes, and an assortment of impact phenomena ranging from snow, raindrops and hailstones to large birds. In these impact phenomena the speed of the hazard is generally unimportant as it is slow compared to the vehicle speed, however with the advent of space flight the encounter of very high speed meteoric particles has been added as an additional threat.

NASA (1991) laid down practices for design and testing of components for civil space programs and suggested that to ensure a reliability-orientated design a Life-Cycle Environment Profile should be evaluated that forecasts events and associated environmental conditions that an item experiences from manufacture to retirement. The code of practice also considers combined environments as these may potentially be more detrimental to reliability than a single environment (see figure 1.1). Although some of these environments are not so relevant to the problem of aircraft and missiles, they are nevertheless instructive as a guide to the careful considerations that need to be taken.

The problem of rain encountered during flight has been around since the beginning of aviation history. With the advent of high speed flying the problem went beyond the prevention of ingress of water, and of its removal for the purpose of vision, and into the erosion damage of forward-facing surfaces. The NASA guidelines break the problem of rain down into four main parts:

1. *physical stress* - leading to structural collapse
2. *water absorption and immersion* - leading to increase in weight, electrical failure and structural weakening
3. *erosion* - leading to removal of protective coatings, structural weakening and surface deterioration
4. *corrosion* - causing enhancement of chemical reactions

This thesis tackles the problem of erosion due to impact with rain, and is therefore only looking at a very small part of the environmental hazards faced by the aircraft. Although this is only a small area, the damage generated may be so severe as to affect the performance, and eventually the airworthiness of the aircraft or missile, and therefore the problem is a very real one and constitutes a threat to the safe advance of high speed aviation.

1.2 THE RAIN ENVIRONMENT

The most common parameters of rainfall quoted by workers on natural precipitation are intensity, drop shape, size and size distribution, horizontal and vertical extent of occurrence, terminal velocity of fall, and probability of occurrence. These parameters are of course latitude and season related and the physical properties of events may vary. The aircraft designer who is concerned with fairly long flight times is interested in the average rain data. In contrast a missile designer whose vehicle may have a flight time of < 30 s after carriage is interested in both the average and the instantaneous value.

The drop shape, sizes, terminal velocity and breakup are considered in detail in chapter two, here we shall instead briefly mention some cloud characteristics.

There are two main cases to be considered for clouds, precipitating, and non-precipitating. The main characteristics of these are shown in tables 1.1 and 1.2. The horizontal and vertical limits for rain occurrence within the flight plan, in conjunction with the intensity, will determine the total number of impact stress cycles to be sustained. The extent of rain has been evaluated for four typical rain conditions:

1. *drizzle or light rain* ($0 - 2.5 \text{ mm hr}^{-1}$) - belts 500 - 1500 km long and 300 km wide
 2. *moderate to heavy rain* ($2.5 - 10 \text{ mm hr}^{-1}$) - 250 km long and wide
 3. *tropical rain* ($10 - 25 \text{ mm hr}^{-1}$) - 150 - 500 km long and 15 km wide
 4. *thunderstorms or cloudbursts* (*over* 25 mm hr^{-1}) - cells 15 - 30 km across
- In comparison the vertical extent of rain is typically 5,000 - 6,500 m with cloud tops often extending up to 16,000 m.

A great deal of rain statistics data is available in the "Handbook of Geophysics" (Camden, 1960), and an excellent study of the variables relating to flight through rain is given by Denis and Balageas (1979). Once all the controlling factors have been identified the probability of rain occurrence for various flights can be evaluated. For example the British Meteorological Office have shown that there is a 0.01% probability of encountering rain which will necessitate simulation of 25 mm hr^{-1} intensity over 500 km of any 1,500 km flight from London.

1.3 HIGH VELOCITY FLIGHT THROUGH RAIN

The effects of high-speed rain impact are observed by airline operators and by military groups alike. The latter usually employ faster aircraft at lower altitudes, and in more severe weather situations than the former and it is from service conditions that most evidence of liquid impact damage is available. Schulz (1974) did a complete review of positions of rain erosion damage on a Starfighter F.104. He observed damage in the pitot tubes (used for velocity determination), radomes, infrared windows, centre windshields, angle-of-attack transducers, leading edges of the air-intake ducts, antenna, leading edges of the wings, infrared seekers of the sidewinders, supports of the missiles, tips of the external tanks, navigation lights on the wing tips, fin leading edges and engine compressor blades. Further tests were conducted by Roys (1961) using a Convair Delta Dart F-106A, and paint peeling and shearing of rivet heads was also noted on Boeing 707's by the civil air authorities.

In order to best assess the rain erosion hazard during high velocity flight, a study should be conducted of a typical flight plan for a supersonic transport aircraft, in which the history of one flight in terms of the speeds and times at various altitudes is defined (figure 1.2). In practice, this would be further elaborated by inclusion of variations of aircraft attitude to the line of flight. The dimensions and geometric configuration of the radome, its materials, and type of construction are also required as is the estimated influence of the aerodynamics of the vehicle on drop

Table 1.1 Main characteristics of non-precipitating clouds (*Denis and Balageas, 1979*)

Altitude	General types of clouds	Mean diameter of particles (μm)	Mean concentration (g m^{-3})	Lowest cloud temp. ($^{\circ}\text{C}$)	Type of particle
Lower cloud	Stratus (St)	5	0.1	-5	water vapour
	Strato cumulus (Sc)	20	0.2	-10	(ice particles seldom)
Medium clouds	Alto stratus (As)	25	0.15	-25	water vapour
	Nimbus stratus (Ns)	20	0.2	-8	supercooled water
	Cumulus (Cu)	10	0.01	-20	ice particles
	Alto cumulus (Ac)	15	0.05	-15	
High clouds	Cirrus uncinus (Ci)	500 to 800	0.1 to 0.5	-50	ice particles
	Cirrus stratus (Cs)	200 to 500	0.03	-35	

Table 1.2 Rainfall characteristics at ground and in precipitation-generating clouds. (*Denis and Balageas, 1979*)

	Type of clouds	St	St As	As Ns	Thick Cu	Cu Cong.	Cb
In the clouds	Ice water concentration (g m^{-3})	0.045	0.2	0.3 to 1.3	1.3 to 2.2	2.2 to 8	8
Under the clouds	Mean precipitation duration	10 hr	2 hr	1 hr	30 min	30 min	10 min
	Liquid water concentration (g m^{-3})	0.005	3×10^{-2}	5×10^{-2} to 0.25	0.25 to 0.5	0.5 to 2	2
	Mean drop diameter (mm)	0.2	0.7	0.7 to 1.3	1.3 to 1.6	1.6 to 2.1	2.1
	Rain fall rate (mm hr^{-1})	0.1	0.1 to 1	1 to 5	5 to 10	10 to 40	40
Precipitation characteristics	Drizzle	Slight rain	Ordinary rain	Slight shower	Shower	Thunder storm shower	
Type of rainfall							

break-up. From meteorological data pertinent to the operating altitudes and geographical location of the mission, and by use of empirical relationships which have been derived from simulation tests, the erosion behaviour of the radome should then be predicted and compared to acceptable levels. Sellers (1970) attempted this analysis for wind gusts, hail and rain, but he only had sufficient data to complete the study for the first two. Current aircraft and missiles attain even greater speeds, manned aircraft Mach 2 - 3 and missiles Mach 2 - 5, but little further published data can be found in the literature on attempts to evaluate exposure during a typical flight.

In all the assessments conducted there is an assumption that the aircraft or missile is still capable of operating under the defined rain environment. Although it is unlikely that the rain conditions will be so severe as to effect the airworthiness of the aircraft, the radar effectiveness may be dramatically reduced. An attempt to theoretically calculate the expected reduction in IR-visibility due to different rain intensities and target distances was carried out by Hingst (1993). In this work he compared the visibility reduction factor obtained in two different ways. First by a 'no hidden drop' method based on work by van de Vries (1976), and then by his own 'hidden drop' method which allows for drop overlap in a rainfield masking the drops behind it. The effect this visibility reduction has on the acquisition range for a target can be seen in figures 1.3 and 1.4. In cases where accurate guidance is therefore important, it may be necessary to adjust the erosion resistance requirement in accordance with the capability of the radar system in rain.

1.4 THE RADOME

Essentially all forward facing areas of a missile or aircraft are susceptible to damage during high-speed flight through rain. The radome however, because it is often the foremost portion of the vehicle is particularly vulnerable to raindrop impact, and Tatnall (1970) noted the large number of composite radomes needing replacement by service personnel.

The radome on a missile is designed to cause minimum distortion of the electrical characteristics of the antenna so that boresight errors as well as absorption and transmission losses are kept small (Fyall, 1970). The boresight error is the apparent change in the angular position of a radar source or target. The boresight error is reduced as the antenna size increases, therefore it is desirable to use as large a radome as the vehicle will permit. The missile shape meanwhile is controlled by electrical and aerodynamic considerations. The electrical design is simplified and performance improved by a smooth shape with a large radius of curvature, such as a hemisphere. The hemisphere however is not so good aerodynamically, and instead for supersonic applications ogival shapes are preferred. An ogive is a figure of rotation defined by a line segment which is part of an arc of a circle having a radius larger than the base radius of the radome. Whatever the shape, the material selected must be infrared transparent. For modern all-aspect tracking systems it must be transparent in both the 3 - 5 μm and 8 - 12 μm wavelengths. The 3 - 5 μm admits the black body radiation from a jet exhaust while the 8 - 12 μm admits radiation from objects at body temperature such as the aircraft skin. Unfortunately the materials available for an infrared window are brittle ceramics such as ZnS, ZnSe, CaLa_2S_4 and germanium (Savage, 1985, Pickles, 1991). These ceramics get damaged if they impact a raindrop with a velocity component perpendicular to the surface above a certain threshold velocity for a given drop diameter. For uncoated ZnS the threshold velocity for initiation of damage is 175 m s^{-1} for a 2 mm diameter drop, a value small enough to be exceeded after the launching of a missile from an aircraft, or even during its carriage prior to firing.

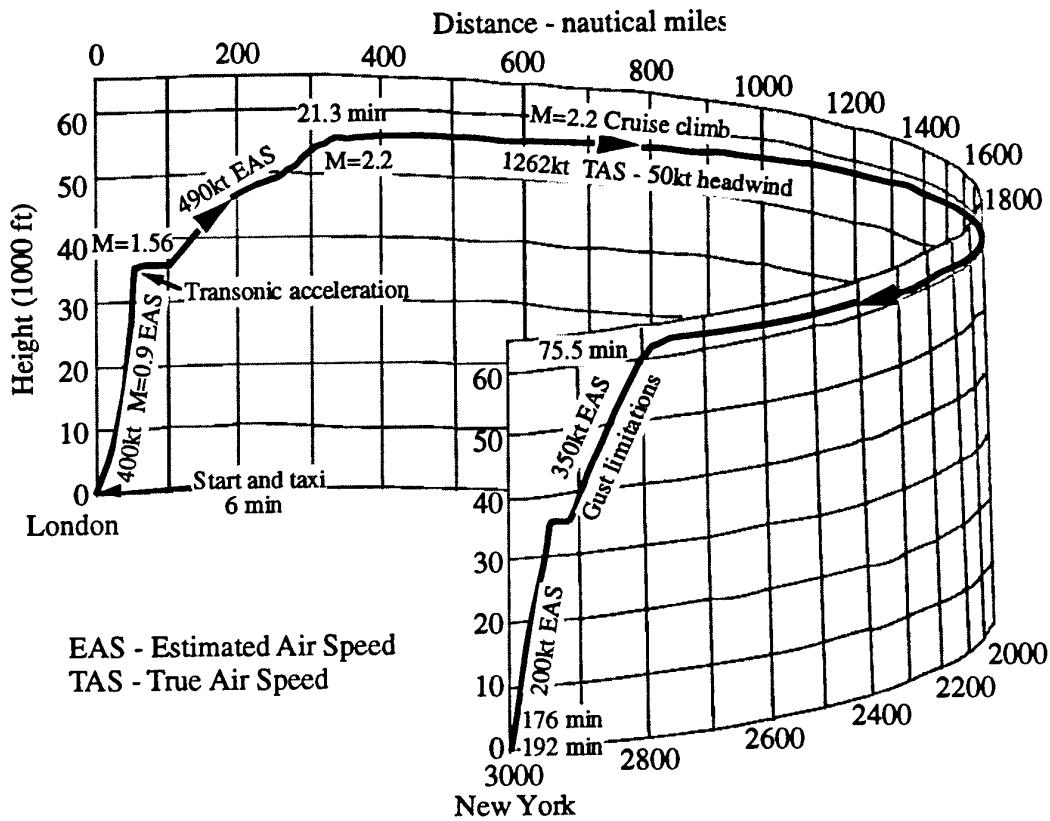


Figure 1.2 Typical flight plan for a Mach 2.2 supersonic aircraft. (Fyall, 1970)

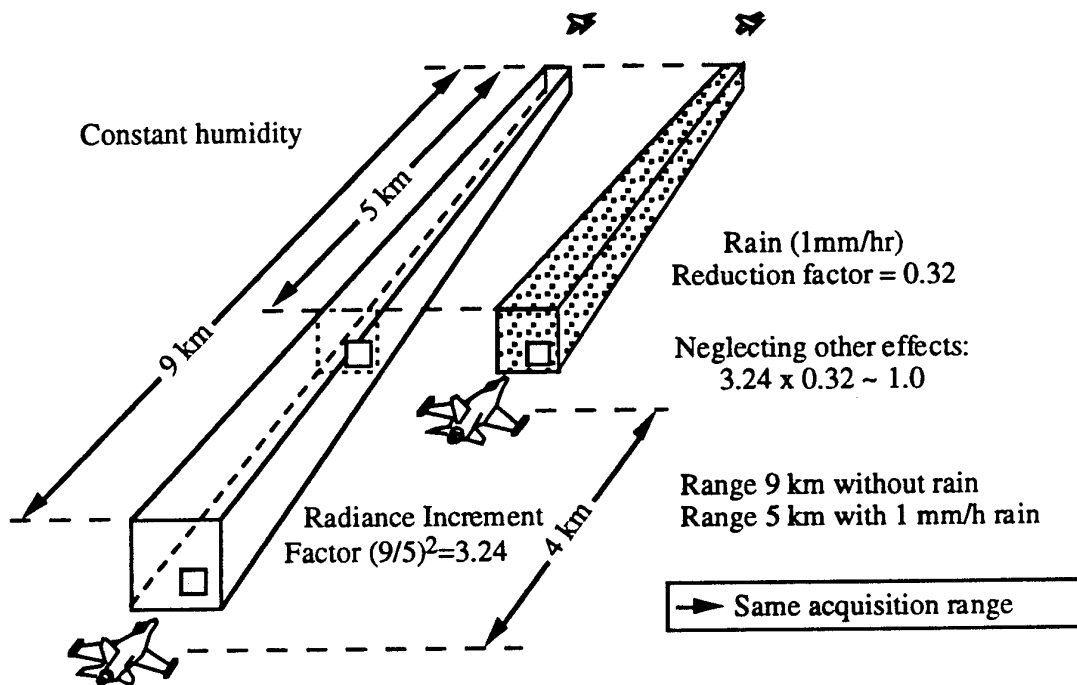


Figure 1.3 Effect of rain visibility reduction factor on acquisition range

In an attempt to eliminate the damage produced by the impact with a raindrop, the missile designer may try positioning a flat infrared window on the side of the missile at an angle to the direction of travel, thus reducing the normal component of the impact (Graham and Freeland, 1990). Alternatively he may try to break the drop up by an aerodynamic shock generated by a spike on the front of the missile (Adams and Smith, 1967), or simply to hide the window by placing a cover over it during carriage, or mounting the missile in the aircraft fuselage. The material scientists meanwhile try and develop new substrates and coatings that are more rain erosion resistant, while maintaining their infrared transparency.

1.5 RADOME DAMAGE DUE TO IMPACT WITH RAIN

The character of the damage produced by multiple water drop impacts is dependent on the magnitude of the impact velocity compared with the damage threshold for a particular material. Adler (1987) cross-sectioned and analysed the crack patterns produced from single impacts on zinc sulphide and identified two regions of cracks. The inner ring of type I cracks started at 65° to the surface while the outer ring of type II started at 45° (figure 1.5). McClintock (1978) suggested that the transmission coefficient for these areas be set to zero, so the transmittance difference was simply the ratio of the total area minus the fracture surface, to the undamaged area. Adler (1987) used theoretical and experimental data to show that the type I cracks actually had smaller transmission coefficients than the type II because they were denser and therefore overlapped more, but that the coefficients were in any case very dependent on the wavelength of interest. These coefficients can be seen in table 1.3 where L is the crack opening distance and is here taken as $0.05 \mu\text{m}$. The transmission loss model developed by Adler was only applicable as long as the water drop impact damage remained noninteracting, because no quantitative evaluation of multiple impact damage was available. Adler's aim was to link drop size and velocity with the crack damage and transmission loss produced, and to eventually add on the effect of crack enlargement by multiple impact on the losses, to allow prediction of transmission loss for a proposed flight plan such as figure 1.2.

Springer and Yang (1975) developed an analytical model for the degradation of the optical transmittance of transparent and translucent materials subjected to repeated impact with liquid droplets. Cassaing et al. (1989) compared this model with results from the SAAB whirling arm rig for nine IR materials and found that despite the formulas complexity and the number of parameters considered the agreement was poor. They looked for a simpler relation based on their results, but were unable to justify their new correlation parameter theoretically.

An investigation of the effects of environmental damage on the optical performance of real germanium radome windows was carried out by Lewis and Jennings (1982). The most common form of damage was found to be a roughening of the external surface of the window, due to rain impact on aircraft mounted imagers, or due to the use of windscreen wipers on land and sea based systems. They found that for rain eroded samples reductions in transmittance at $10 \mu\text{m}$ ranged from a few percent to $\sim 35\%$. They then examined the effect this damage had on the spatial resolution, as measured by the modulation transfer function (MTF) in the $8 - 12 \mu\text{m}$ range. The results showed that although reduced range performance was seen from damaged imagers there was no corresponding reduction in optical resolution as measured by the MTF. They therefore concluded that for tasks where range performance was not critical, but where resolution performance is essential (i.e. recognition) severe damage to the outside surface of the optical component could be tolerated.

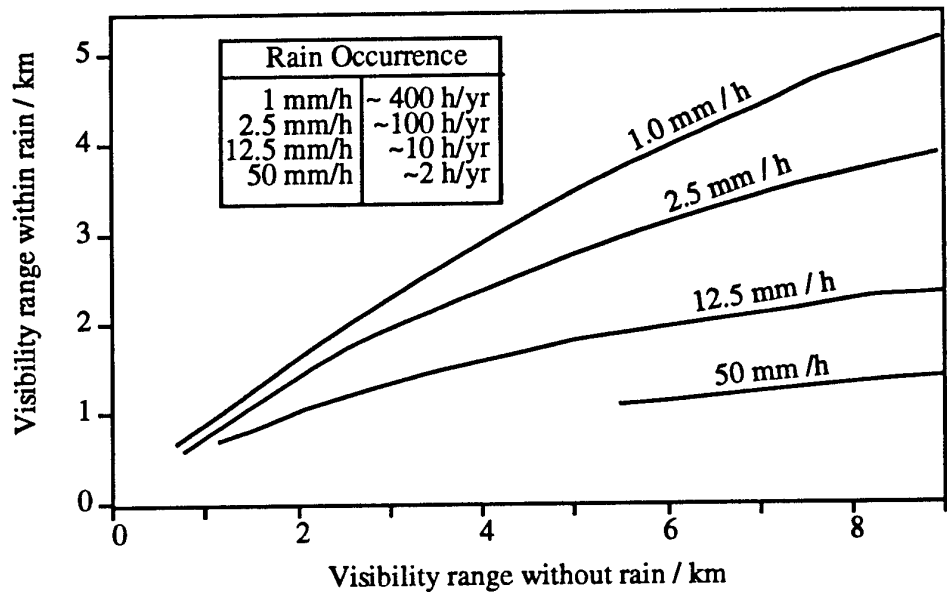


Figure 1.3 Approximation for IR-acquisition range

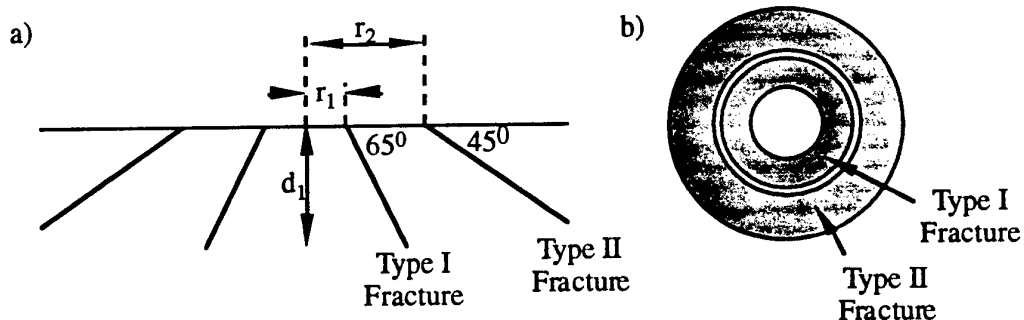


Figure 1.4 Idealised fracture surfaces for water drop impact on zinc sulphide a) cross section b) top view. (Adler, 1987)

Table 1.3 Transmission coefficients for type I and type II fractures. (Adler, 1987)

$\lambda / \mu\text{m}$	L / λ	Transmission coefficient	
		Type I Fractures	Type II fractures
0.5	0.1	0	0.38
2.5	.02	0.18	.94
10.0	.005	.88	1.00

A more complete evaluation of the effects of scattered light on optical resolution was carried out by Bennet and Ricks (1986) and Ricks (1987). In their studies they considered the effects of both surface and bulk defects and looked at different resolution criterion such as Rayleigh, Abbe, Sparrow and Mie. Their findings suggested that the scatter was not a significant problem for resolving two equally intense point sources, but that the integrated scatter from a broad source may significantly wash out a dim source or a nearby dark object point.

A more recent paper by Stover (1990) suggested that a more important quantity than the transmission loss was the bidirectional transmittance distribution function (BTDF). This is the scatter density normalised by the incident power and given in units of inverse steradians. Their rationale behind this was that as the window degrades, either through contamination or impact damage, the signal to noise ratio is affected in two ways. First the transmission loss to the sensor, which they claim is usually less than 1%. Second the bright sources of radiation outside the field of view (such as the sun), that illuminate the window section inside the field of view, and now scatter within the sensor field of view. Because the sun is brighter than the target signal, the potential exists for a dramatic drop in signal to noise as window scatter increases. Stover (1990) then demonstrated experimentally that the reflective scatter measurement (BRDF) produced comparable results to the BTDF, this was then used in the development of an in-situ flight-line test technique to evaluate radome damage.

1.6 CONCLUSION

The damage caused by rain on aircraft transparencies during high velocity flight can be both expensive and hazardous. At the very least the damage may cause deterioration of the optical transmission properties (Springer and Yang, 1975, Lewis and Jennings, 1982, Bennett and Ricks, 1986, and Ricks, 1987), while in more severe cases it may necessitate the replacement of the component. In one instance reported by Daniel (1988) a replacement military aircraft canopy cost £22,000 and took 26 months to deliver. In the worst cases the eventual catastrophic failure of the radome has led to breakup of the window and to parts being sucked into the jet engines. This has on occasions been known to cause engine failure, and can even lead to the loss of the aircraft. The consideration of rain impact at the early stages of design is thus now accepted as being of great importance and testing must be evaluated according to specified standards for each country. In the U.S. this is covered by sections 3.4.2.1 and 3.4.2.2 of Military Specification MIL-R-77058 for radomes printed in February 1988. This specification states that for supersonic vehicles the sample shall withstand a rainfield with the size distribution and intensity of a natural one inch / hour rainfall at its maximum flying speed for at least one minute without delamination or fracture. While for subsonic vehicles the sample shall withstand the test for five minutes without delamination or fracture. In the U.K. the test standards for rain impact and erosion are currently being revised, and these will soon be published as Def Stan 08 - 5 Chapter 5-308 and Leaflets 5-308 / 1 and 5-202 / 3.

REFERENCES

- Adams R.H. and Smith M.R. "Design and development of RECAP, an aerodynamic device for rain erosion protection of optical domes on missiles", Proc. 2nd Meersburg Conf. on Rain Erosion and Allied Phenomena., (ed. Fyall and King, Royal Aircraft Establishment, England), pp.935-968, (1967)
- Adler W.F. "Development of design data for rain impact damage in infrared-transmitting windows and radomes", Opt. Eng., Vol.26, No.2, pp.143-151, (1987)
- Bennett H.E. and Ricks D.W. "Effects of surface and bulk defects in transmitting materials on optical resolution and scattered light", SPIE Vol.683, Infrared and Optical Transmitting Materials, pp.153-159, (1986)
- Camden C. "Handbook of Geophysics", MacMillan Co., New York, (1960)
- Daniel P. "Not difficult to see", Ind. Diamond Review, Vol.4, pp.152-155. (1988)
- Denis J. and Balageas D. "Probabilistic evaluation of hydro-erosion hazards for missile radomes", Proc. 5th Int. Conf. on Erosion by Solid and Liquid Impact, (ed. J.E. Field), Paper 19, (1979)
- Fyall A.A. "Radome Engineering Handbook", (ed. JD Walton Jr) Dekker, New York ISBN 0-8247-1757-0, (1970)
- Graham P.M. and Freeland C.M. "Dual waveband IR and millimetric sandwich windows", Third Workshop on passive IR optical materials and coatings (1990)
- Harris D.C. "Infrared window and dome materials", ISBN 0-8194-0998-7, Vol. TT10 SPIE Optical Engineering Press, (1992)
- Hingst U.G. "Occurrence of critical raindrop impacts on infra-red domes", Fourth Workshop on passive IR optical materials and coatings, (1993)
- Lewis C. and Jennings J.P. "Effect of surface damage on the IR optical performance of Ge", Applied Optics, Vol.21, No.14, pp.2468-2470, (1982)
- McClintock F.A. "Mechanical properties of infrared transmitting materials", Natl. Materials Advisory Board Report NMAB-336, (1978)
- NASA Reliability and Maintainability Steering Committee "NASA reliability preferred practices for design and test", NASA Technical Memorandum 4322, NASA Office of Safety and Mission Quality, Washington DC, Sept. (1991)
- Pickles C.S.J. "Infrared transmitting materials in the high velocity environment", PhD University of Cambridge, August (1991)
- Ricks D.W. "Scattered light from eroded domes", AEDC-TR-87-21, (1987)
- Roys G.P. "Operations of an F-106A in thunderstorms at supersonic and subsonic speeds", Tech. Note Aeronautical System Div., No. 61 - 97, (1961)
- Savages J.A. "Infrared optical materials and their antireflection coatings", Adam Hilger Ltd., (1985)
- Schulz M. "Erosion damage on high speed aircraft and missiles", Proc. 4th Meersburg Conf. on Rain Erosion and Ass. Phenomena., (ed. Fyall and King, Royal Aircraft Establishment, England), pp.29-62, (1974)
- Sellers G.D. "Rain erosion - design data for rain encounters", Proc. 3rd Meersburg Conf. on Rain Erosion and Ass. Phenomena., (ed. Fyall and King, Royal Aircraft Establishment, England), pp.977-992, (1970)
- Springer G.S. and Yang C.I. "Optical transmission losses in materials due to repeated impacts of liquid droplets", AIAA, Vol.13, No.11, pp.1483-1487, (1975)
- Stover J.C. "Practical measurement of rain erosion and scatter from IR windows", SPIE Vol.1326 Window and Dome Technologies and Materials II (ed. P. Klocek, Texas Instruments Inc), pp.321-330, (1990)
- Tatnall G. "Military service experience and design philosophy in flight vehicle rain erosion", Proc. 3rd Meersburg Conf. on Rain Erosion and Ass. Phenomena. (ed. Fyall and King, Royal Aircraft Establishment, England), pp.969-976, (1970)
- van de Vries Jr. J.B. "Theory and measurements of the effect of rainfall on infrared transmission", TNO Research Group 2, Report No. PHL 1976-07, March (1976)

Chapter 2

The Problem With Rain

In order to understand rain erosion damage we must know the size and shape of the raindrops we impact. This chapter looks at the creation of rain in order to determine the drop size distribution, and then finds the shape raindrops take on as they fall under gravity. The problem is then extended by looking at the effects of the shock-wave ahead of a moving vehicle on the drop shape. Finally the overlap of impact damage sites is mentioned.

2.1 CREATION OF WATER DROPS

2.1.1 Introduction

A cloud is a collection of minute water or ice particles sufficiently dense to be seen. Most cloud droplets are spheres with diameters ranging from a few to $\sim 100 \mu\text{m}$. As the drop gets larger its speed of fall increases and the time for it to evaporate gets longer. When a drop is sufficiently large for it to reach the ground before evaporation, it is called a raindrop (see table 2.1.1). Meteorologists have decided that drops $< 200 \mu\text{m}$ diameter are termed cloud droplets, those between 200 and $500 \mu\text{m}$ are drizzle drops, and those above $500 \mu\text{m}$ are raindrops.

The spectrum of cloud droplet size varies from one cloud type to the next, and among clouds of the same species depending on the time and place. The distribution of drop sizes is dependent on the processes of condensation, collision coalescence, and drop breakup. Each of these processes will now be examined briefly.

2.1.2 Condensation

A rising body of air expands and is cooled adiabatically, this promotes a rise in the relative humidity and an increase in the likelihood of condensation. Within this body of air there is usually a large population of particles, $0.01 - 0.1 \mu\text{m}$ in diameter, that can serve as condensation nuclei (see table 2.1.2). A substantial fraction of these particles are soluble substances that are hygroscopic and become aqueous solutions at relative humidities less than 100% (e.g. sodium chloride 75%), these allow condensation to take place in air at a supersaturation of less than 1% (supersaturation in the atmosphere seldom exceeds 1%). The process of condensation on hygroscopic particles was shown experimentally by Aitken (1923), and the criterion for it set down by Koehler (1926), further theoretical studies have shown that insoluble particles play no part in the process, but that particles that are a mix of the soluble and insoluble substances do (see table 2.1.3 Junge and McLaren, 1971). The importance of these hygroscopic particles is realised when it is pointed out that pure water vapour requires a supersaturation of several hundred percent before condensation can take place! (see figure 2.1.1).

2.1.3 Collision and Coalescence

Once water drops are nucleated in the vapour, they will continue to grow by

Table 2.1.1 Fall velocity of water drops in still air at sea level. (*List, 1958*)

Type of drop	Diameter (μm)	Fall velocity (cm s^{-1})	Fall distance for complete evaporation (m)
Cloud droplet	20	1.0	less than 1
Drizzle	200	72	150
Raindrop	2000	649	4200

Table 2.1.2 Size distribution of particles in the atmosphere. (*Battan, 1979*)

Nucleii	Diameter (μm)	Concentration (particles / cm^3)
Aitken	< 0.2	$10^4 - 10^5$
Large	0.2 - 2.0	10^2
Giant	> 2.0	1

Table 2.1.3 Activation supersaturations of mixed nuclei consisting of salt and an insoluble wettable part. (*Houghton, 1985*)

Volume fraction of salt	1.0	0.4	0.1	0.01	0.0001	0.0
Activation supersaturation %						
a. dry radius 10^{-6} cm	1.4	2.3	3.7	6.1	8.4	13.0
b. dry radius 10^{-5} cm	0.04	0.06	0.13	0.34	0.65	1.2

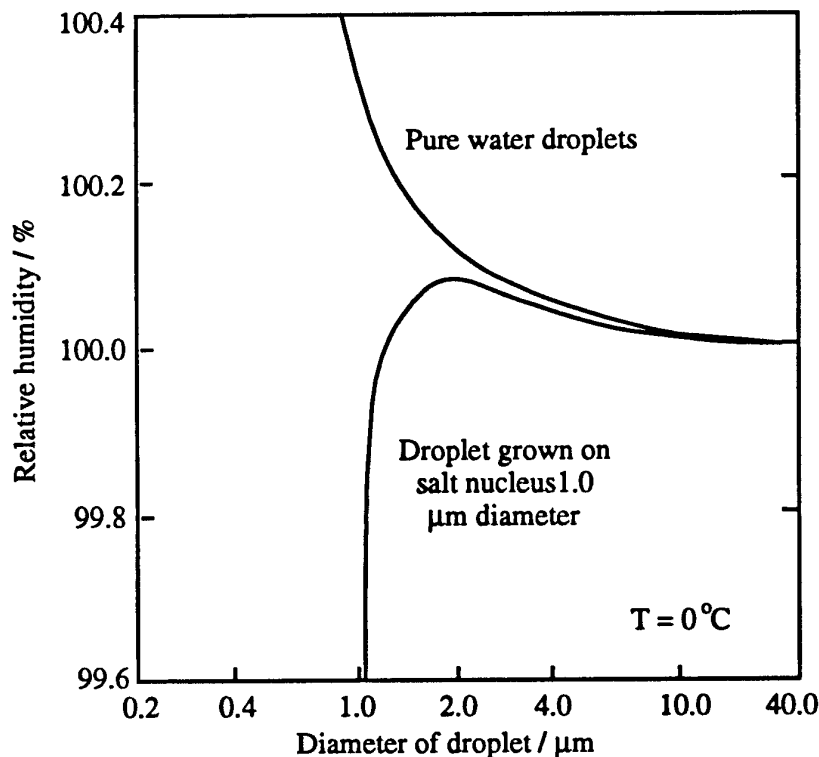


Figure 2.1.1 The relative humidity needed for a raindrop to grow by condensation with and without a hygroscopic nucleus. (*Battan, 1979*)

condensation, and eventually the larger drops will fall at a speed of several centimetres per second or more and begin to collide with the smaller drops. Langmuir (1948) and Bowen (1950) were among the first to compute the growth of raindrops by collisions and coalescence using a "continuous" growth equation. This considers the growth of a big drop, in a cloud of smaller drops of one size, where the drops are considered to be uniformly and continuously distributed in space.

Improvements on this were made by Telford (1955) and Twomey (1966), with the stochastic coalescence equation that considered a non-continuous space distribution of drops, this enhanced the growth rate of some drops while retarding that of others. The stochastic theory has since been improved by Long (1971), Drake (1972) and Gillespie (1972), and more recently been solved numerically by Valdez and Young (1985), List et al. (1987) and Brown (1987, 1990).

A number of experimenters have shown that some drops on collision trajectories do not coalesce, but instead bounce off, as a result of a cushion of air acting as a barrier between the two drops as shown in figure 2.1.2 (Whelpdale and List, 1971 and Levin and Machnes, 1977). This process was modelled numerically by Arbel and Levin (1977), but Low and List (1982) failed to observe this in the 761 collisions they analysed. Low and List looked at three main geometric shapes formed by the drops after initial contact, (filaments, sheets and discs), and the fragment size distribution after breakup. They found coalescence occurred only when drops < 0.6 mm in diameter were struck by larger ones and the energy of impact was adequately dissipated. Ochs and Czys (1987, 1988) showed that the chances of coalescence could be improved by placing a charge on the colliding drops. Figure 2.1.3 shows their results from 915 collisions between a 380 μm and 680 μm diameter drop. Above the 43° impact angle threshold for coalescence the outcome of the impact is determined by the charge on the drops colliding.

2.1.4 Limits to the Size of Water Drops

Blanchard (1950) was able to suspend drops of 9 mm diameter in a low-turbulence wind tunnel. A mechanism for the breakup of drops bigger than this was proposed by Komabayasi et al. (1964), and assumed Lamb's (1932) theory of infinite, plane-parallel surface waves. These waves were applied to the top and bottom surface of the drop, and Komabayasi suggested that drop breakup was related to the condition for their instability. In the free atmosphere the largest raindrops observed are about 5 - 7 mm in diameter, and are typically found in thunderstorms. The largest drops observed in warm rain showers however are only 2.5 - 3.0 mm in diameter. Blanchard (1950) therefore conjectured that drop breakup in the free atmosphere was instead due to turbulence and collisions, and aerodynamic breakup was unimportant except perhaps in thunderstorms.

Drop disintegration on collision has recently been studied experimentally by McTaggart-Cowan and List (1975) and Low and List (1982). For high-energy collisions, filaments usually occurred as the small drop hit the larger one near the outer edge, while sheets and discs were formed as the impact point progressed towards the large drops centre line of fall. As the energy decreased and the size-ratio became larger, the filament mode of separation into two or more fragments remained the only mode of breakup, regardless of the initial point of contact. List (1977) concluded that rupture due to collision was an important process in the evolution of drop size spectra, and that this was responsible for the upper size limit of warm raindrops. List also suggested that the larger drops in thunderstorms, were due to the melting of hailstones too close to the ground for collisional processes to destroy them.

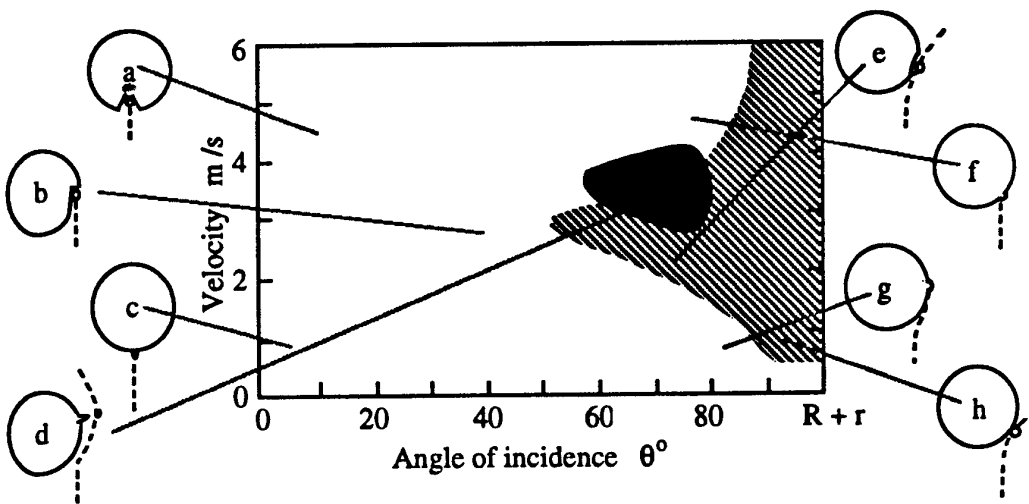


Figure 2.1.2 Various stages of collisions and conditions under which they occur. Unshaded area represents coalescence; hatched area represents bouncing; solid shaded area represents partial coalescence. a) High velocity coalescence carrying air bubbles into the drop b) Coalescence with droplet ploughing water ahead c) Low velocity coalescence without appreciable deformation d) Partial coalescence e) Bouncing droplet after deformation f) High velocity coalescence g) Low velocity coalescence after deflection h) Low velocity bounce. (*Whelpdale and List, 1971*)

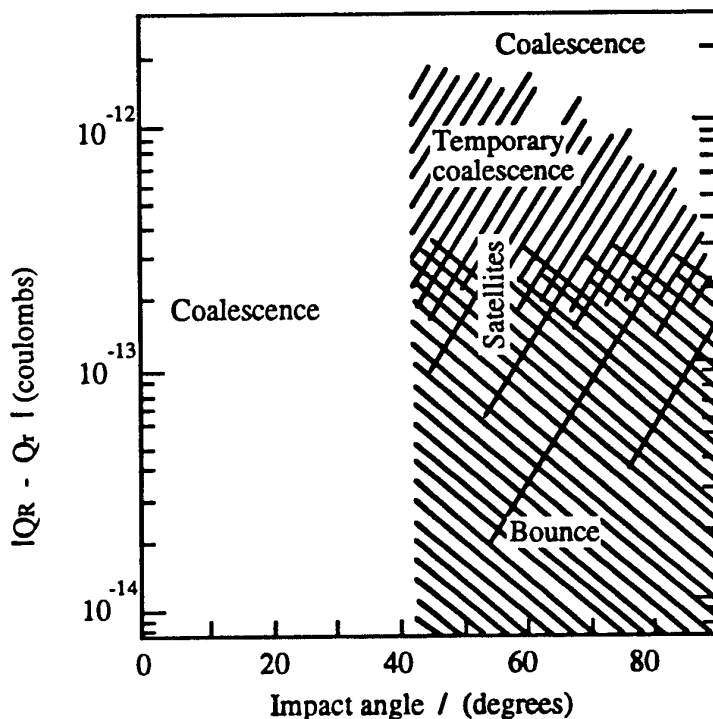


Figure 2.1.3 Collision outcome as a function of impact angle and relative charge. Clear area = coalescence. Hatched area sloping down left to right = bouncing. Hatches sloping down right to left = temporary coalescence. Stippled area = satellite formation. Concentration of hatches gives relative occurrence of events. (*Ochs and Czyns, 1987*)

2.1.5 Terminal Velocity of Drops

It has been customary to compute the fall speeds of cloud drops from Stoke's Law, which assumes viscous flow and no slip:

$$v = \frac{2g}{9\eta}(\rho_L - \rho_A)r^2 \quad (2.1.1)$$

where v is the terminal fall speed in cm s^{-1} , η is the dynamic viscosity of air, g is the gravitational constant, and ρ_L and ρ_A are the densities of the liquid and of air respectively. Beard (1976) showed that this equation underestimates the fall speeds of drops smaller than about $8 \mu\text{m}$ in diameter, and overestimates for drops larger than about $60 \mu\text{m}$ in diameter. Thus its useful range just about covers cloud drops formed by condensation.

Small raindrops fall at the same terminal velocity as solid spheres of the same size and density. Their fall speeds may thus be calculated from the well-known drag coefficients of spheres. This approach is valid for diameters up to 0.9 mm at sea level. As the diameter increases further, the drop becomes progressively more oblate and the fall speed must be obtained by direct measurement.

Terminal velocities of fall for five different atmospheric conditions are shown in figure 2.1.4 from data by Gunn and Kinzer (1949), and an extrapolation technique of Foote and de Toit (1969). From their results it can be seen that the fall speed of raindrops increases with elevation.

2.1.6 Size Distribution of Water Drops

Raindrop size spectra near the ground have been measured by a number of workers, starting with Laws and Parsons (1943). Marshall and Palmer (1948) showed that observed raindrop size spectra may, on average, be represented by:

$$N(D) = N_0 \exp(-\Lambda D) \quad (2.1.2)$$

where $\Lambda = 41 R^{-0.21} \text{ cm}^{-1}$, $N_0 = 0.08 \text{ cm}^{-4}$ and $N(D)\Delta D$ is the concentration of raindrops in the diameter range D to $D + \Delta D$, and R is the Rainfall rate in mm hr^{-1} (figure 2.1.5). Raindrop size spectra aloft have been deduced from radar measurements, and the spectra are found to be exponential but steeper than the Marshall-Palmer distribution. Srivastava (1974) in a review of drop size distributions concluded that by and large the available observational data seems to indicate that raindrop size distributions may be represented by an exponential distribution, but not necessarily having the slope and intercept given by (2.1.2)

Best (1950) developed a more complex exponential expression, which seems to fit the observed data better than the Marshall-Palmer equation, but it has not been so extensively used. Data from his observations are shown in table 2.1.4.

There are other functions containing two parameters that might better fit the $N(D)$ observed (Cataneo and Stout, 1968 and Austin and Geotis, 1979), and hence would be better for estimating $N(D)$ parameters from radar measurements. Although functions containing three or more parameters can better fit a wider variety of observed $N(D)$, more independent measurements may be required to specify these parameters.

Many theoretical models have been proposed to calculate the drop size distribution, Kovetz and Olund (1969), Bartlett (1966), Srivastava (1967), Ogura and Takahashi (1973) and Clark (1973), and more work still remains to be done.

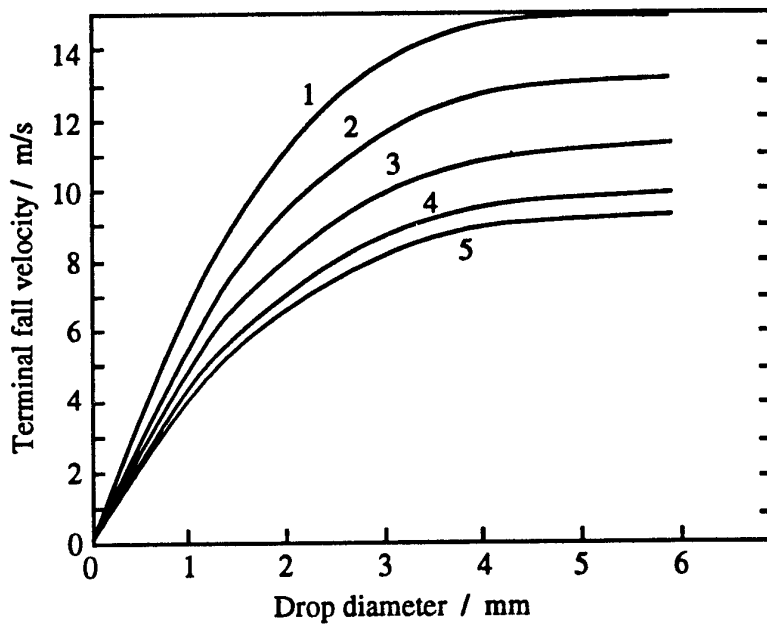


Figure 2.1.4 Terminal velocities of fall of raindrops in five atmospheres 1) 250 mbar -20°C ~10 km above sea level; 2) 380 mbar -10°C ~8 km; 3) 575 mbar 0°C ~5 km; 4) 850 mbar 10°C ~2 km; 5) 1013 mbar 20°C ~sea level . (Houghton, 1985)

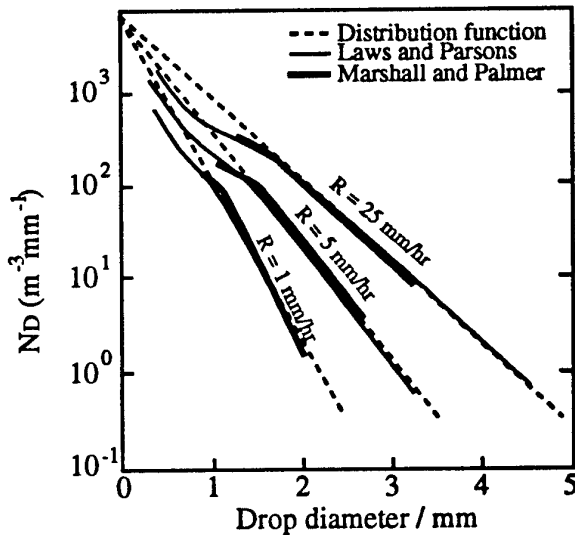


Figure 2.1.5 Exponential distribution function for drop diameters compared with the experimental results of Marshall and Palmer (1948) in Ottawa, summer 1946, and Laws and Parsons (1943). (Marshall and Palmer, 1948)

Table 2.1.4 (right) Drop Distribution data from Best (1950).

I mm / hr	1.0	5.0	25.0
Drop diameter / mm	Number drops per m ³		
0.00 - 0.25	1585	2685	4538
0.25 - 0.50	208	364	625
0.50 - 0.75	74	140	248
0.75 - 1.00	33	71	132
1.00 - 1.25	16	40	80
1.25 - 1.50	7	23	52
1.50 - 1.75	3.27	14	35
1.75 - 2.00	1.37	8	25
2.00 - 2.25	0.53	4.87	17
2.25 - 2.50	0.19	2.76	12
2.50 - 2.75	0.06	1.52	8
2.75 - 3.00	0.02	0.81	6
3.00 - 3.25	0.004	0.41	4.03
3.25 - 3.50		0.20	2.74
3.50 - 3.75		0.10	1.83
3.75 - 4.00		0.04	1.2
4.00 - 4.25		0.02	0.77
4.25 - 4.50		0.01	0.49
4.50 - 4.75		0.003	0.31
4.75 - 5.00		0.001	0.19
5.00 - 5.25			0.11
5.25 - 5.50			0.06
5.50 - 5.75			0.04
5.75 - 6.00			0.02
6.00 - 6.25			0.011
6.25 - 6.50			0.006
6.50 - 6.75			0.003
6.75 - 7.00			0.001

2.2 DROP SHAPE

2.2.1 Shape Taken

Water drops falling in air may depart markedly from the spherical shape. While drops smaller than 0.3 mm diameter may be considered as spherical, those between 0.3 mm and 1 mm are oblate spheroids, and those over 1 mm become progressively more deformed like asymmetric spheroids (see figure 2.2.1).

2.2.2 Reason for Interest in Drop Shape

Part of the current motivation for the research on raindrop shape is the need to understand depolarisation of electromagnetic waves in rain. Depolarisation degrades communication signals by cross-polar interference, but can also be a source of information about rainfall characteristics. As a result there have been numerous studies on the effects of raindrop shape on the propagation of microwaves in communication links, and on backscattering of microwaves as detected by weather radars (see review articles by Oguchi, 1981, Olsen, 1981 Rogers, 1984 and Doviak and Zrnich, 1984)

2.2.3 Factors Affecting Drop Shape

There are five factors affecting the shape of a drop in freefall: surface tension, internal hydrostatic pressure, aerodynamic pressure, internal circulation and electric stress.

2.2.3.a Surface Tension

As a consequence of the net inward attraction exerted on the surface molecules by those lying deeper within the drop, the surface tension of the water in a raindrop produces an increase of pressure within the drop, above that prevailing in the air outside. This increment in pressure Δp_s , at a given point on the drop surface is given by:

$$\Delta p_s = \gamma \left(\frac{1}{R_1} + \frac{1}{R_2} \right) \quad (2.2.1)$$

where γ is the surface tension, and R_1 and R_2 are the principle radii of the surface curvature at the point in question (Adam, 1949).

When the forces of surface tension act alone, or nearly so, as in the case of cloud drops, drizzle and even small raindrops, it succeeds in moulding a drop into a shape characterised by minimum surface-to-volume ratio i.e. a sphere.

2.2.3.b Internal Hydrostatic Pressure

In a co-ordinate system moving with a drop which is falling at terminal velocity, an observer would regard the drop as being just supported against gravity by the vertical components of aerodynamic pressure forces and the surface shear stresses due to the apparently upward-rushing air. Consequently, there must exist within the drop a vertical pressure gradient of exactly the sort found in any mass of fluid at rest in a gravitational field. This hydrostatic pressure between top and bottom becomes important for larger drops, but is insignificant compared to the surface tension effects for drops < 1 mm diameter (see table 2.2.5). For a sphere

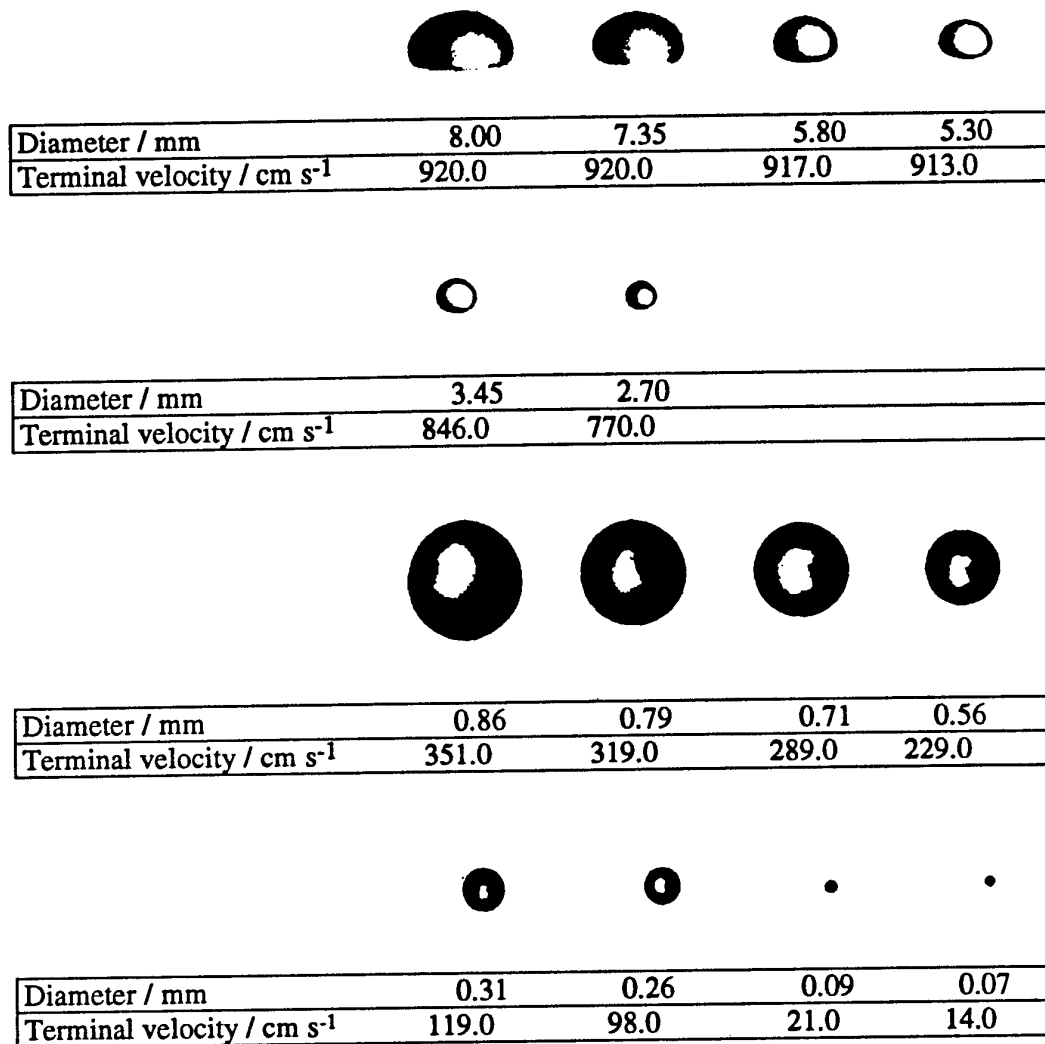


Figure 2.2.1 Typical shape of drops falling at terminal velocity through air with their respective drop size. (Pruppacher and Beard, 1970)

Table 2.2.5 Values of surface tension and internal hydrostatic pressure for various spheroid drops falling at terminal velocity. (McDonald, 1954)

Diameter / cm	$\Delta p_s = 2\gamma / r$ N m ⁻²	$2\rho_w g r$ N m ⁻²
0.002	15,000	0.2
0.02	1,500	1.96
0.10	300	9.9
0.20	150	19.6
0.40	75	39.2
0.60	50	58.8
0.80	37	78.4
1.00	30	98.0

the contribution is given by $2\rho_Lgr$, (where ρ_L is the density of the liquid, r the drop radius and g the gravitational constant) while the case for a sessile drop (a drop resting on a flat plate) is considered in Bashforth and Adams (1883).

2.2.3.c Aerodynamic Pressure

The aerodynamic pressure distribution over the surface of a drop falling through the air, is itself determined by the very shape one wishes to deduce. Two common techniques for determining the distribution are found in the literature. Firstly analysis of photographs of actual drops of known size and speed, by first calculating the stagnation pressure at the lower pole of the drop (McDonald, 1954, figure 2.2.2). Secondly by taking an empirical pressure distribution around a sphere (Savic, 1953, figure 2.2.3), and refining it by including variation in the pressure distribution with Reynolds number and drop distortion (Beard and Chuang, 1987).

2.2.3.d Internal Circulation

Lenard (1904) suggested that the tangential shear stresses at the surface of a falling raindrop would induce an internal circulation within the drop. Unfortunately both Lenard (1904) and Flowers (1928) got the sign wrong, so they thought that internal circulation would cause a bulge at the waist, in fact it should decrease the curvature in this region, and thus the deformation. Foote (1969) showed that the values calculated by McDonald (1954) for the pressure induced near the equator of a drop with internal circulation were too low. Contrary to the conclusions of McDonald he demonstrated that internal circulation, if of the order of 10 cm s^{-1} near the equator of the drop, would significantly affect the shape of a water drop.

Several attempts have been made to measure the circulation current using small tracer particles injected into the water drop, the results of these measurements are shown in figure 2.2.4.

Drop Size / mm	Current velocity	Paper
	none seen (tracers too big?)	Blanchard (1949)
	$< 1 \text{ cm s}^{-1}$	Kinzer (unpublished)
$d = 4 - 6$	$7 - 18 \text{ cm s}^{-1}$	Garner and Lane (1959)
$d = 0.71$	3 cm s^{-1}	Pruppacher and Beard (1970)
$d = 0.62 - 3.36$	$0 - 20 \text{ cm s}^{-1}$	LeClair et al. (1972)

LeClair et al. (1972) did experiments on 111 drops and tried 4 different theoretical techniques to evaluate the size of the internal circulation:

- 1) creeping flow inside and outside a water sphere.
- 2) potential flow outside and inviscid motion inside a water sphere.
- 3) boundary layer theory.
- 4) numerical method to solve Navier-Stokes equation of motion inside and outside a water sphere.

As can be seen in figure 2.2.5, (1) strongly underestimates the motion because the Stokes drag is lower than the actual drag; (2) is not included, as it strongly overestimates the circulation speed because it is physically untenable to disregard the viscous nature of the flow inside and outside the drop; (3) has good agreement for drops $< 500 \mu\text{m}$; (4) provides the best fit for drops $< 500 \mu\text{m}$, and fits the trend of the higher drop sizes if the terminal velocity is adjusted for a deformed drop.

The discrepancies between theory and experiment could result from a number of causes: the drop becoming less spherical as the size increases; oscillations disrupting the circulation leading to a periodic breakup and reformation of the currents; or the external flow pattern becoming increasingly important with eddy shedding being clearly seen from the rear of the drop. What however is apparent

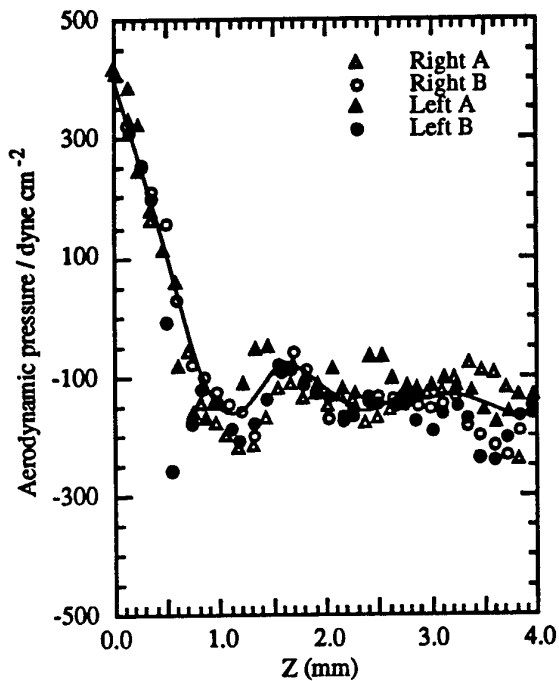


Figure 2.2.2 The computed aerodynamic pressure against height above stagnation point for four measurements on a drop. (McDonald, 1954)

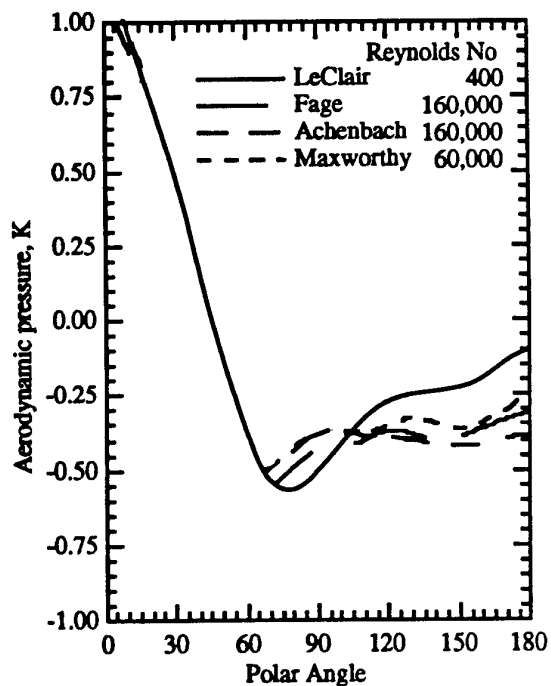


Figure 2.2.3 Aerodynamic pressure distributions for a sphere. Solid curve has an attached wake, dashed curves all have detached wakes. (Beard and Chuang, 1987)

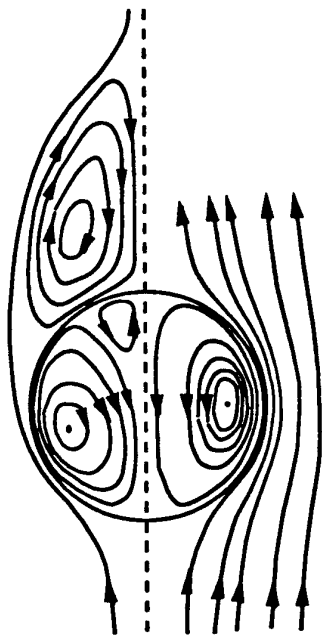


Figure 2.2.4 Streamline pattern of flow inside and outside a sphere falling at terminal velocity. Left side: observed flow outside drop, Taneda, (1956) and inside Pruppacher and Beard (1970). Right side: theoretical pattern for Stokes flow.

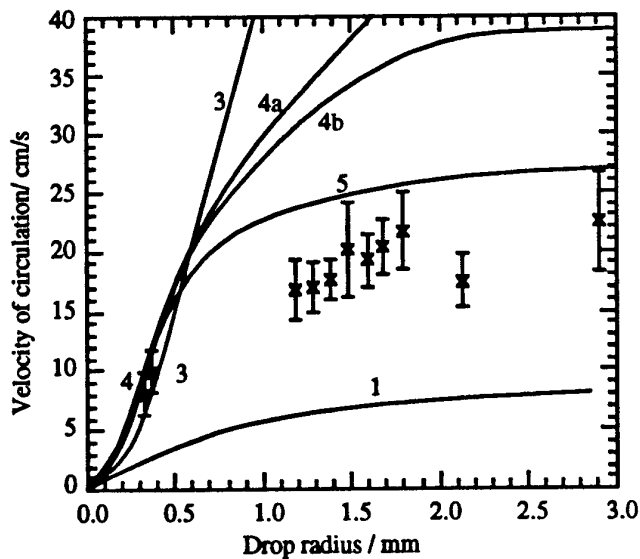


Figure 2.2.5 Comparison between experimentally and theoretically determined velocity at the surface of a circulating water drop in air. 1. Creeping flow 3. Boundary layer 4a Numerical for spheres 4b Numerical for spheroids 5. Upper bound of experimental error. Lowest two experimental data points are Garner and Lane (1959) others are LeClair et al. (1972).

from theoretical calculations neglecting internal circulation, is that there is a good agreement between drop deformations in experiments and theoretical results, so internal circulation effects on the shape of a falling drop are likely to be negligible.

2.2.3.e Electric Stress

The drops in many clouds are electrically charged at an early stage of the cloud life cycle, and are then exposed to the external electric fields present in the electrically charged clouds. By electrostatic standards, water in a natural raindrop is a good conductor. It can be shown that a conductor carrying a local surface charge-density σ experiences an outward directed tension (negative pressure) whose magnitude per unit area is given by:

$$T = 2\pi\sigma^2 \quad (2.2.2)$$

This electrostatic tension opposes the surface tension.

The effect of a uniform vertical electric field on a drop shape was calculated theoretically by Brazier-Smith (1971a, b) for a stationary drop, and showed a tendency for the drop to become prolate (figure 2.2.8c). In experiments performed by Richards and Dawson (1971), and Rasmussen et al. (1985), the falling drop was similarly found to elongate due to a field, hence increasing its terminal velocity (figure 2.2.6 and figure 2.2.8e). This causes a higher stagnation pressure which maintains the flatness of the base. Since the drop is a deformable conductor for a given external field, the electric stress at any point on the drop surface, and hence its curvature, is determined by the shape of the remainder of the drop. If the curvature of the lower surface of the drop is decreased by forces other than electrical (e.g. aerodynamic in this case), then the electric stress at the upper surface will also be reduced. The result of flattening the drop base, is thus to require a higher external field to produce instability at the upper surface.

These feedback mechanisms were omitted from the theoretical calculation of Zrníc et al. (1984), who used the hydrostatic model of Green (1975) to calculate the axis ratio dependence on drop charge and electric field. The coupling was however included in the theoretical calculations of Beard et al. (1989a), who used a perturbation model for drop shape including effects of electric distortion by a reduction in surface tension forces, and Chuang (1989) who used a numerical model. All three theoretical studies predicted that the axis ratio decreases with increasing drop size for larger drops, even for a high electric field of 10 kV cm^{-1} as seen in figure 2.2.7. The small disagreement between the theories is a consequence of the different models used, for example strictly speaking the perturbation model used by Beard et al. (1989a) should only be applied to small distortions, and for larger drops it therefore produces a flattened bottom to the drop, where experiment shows it to be rounded. More significant however is the discrepancy between the theoretical and experimental results. The results of Richards and Dawson show a reasonable fit to the theory, while those of Rasmussen produce higher axis ratios as the drop size increases. This is most likely due to a marked increase in drop oscillations at diameters of $\sim 4 \text{ mm}$ in the Rasmussen experiment which weren't allowed for in the measurements.

The effect of a horizontal electric field is of less interest for clouds, but was investigated experimentally by Ausman and Brook (1967) and Mathews (1967). Of more relevance is the effect of a charge held on a drop. The theoretical calculation shown in Chuang and Beard (1990), indicates that the charge concentrates just below the waist of the drop, therefore extending it horizontally. This increases the drag that slows the drop down, and makes it more symmetric in

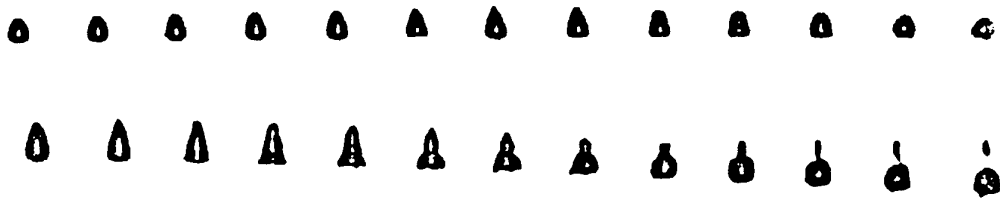


Figure 2.2.6 In both sequences time increases left to right and frames are 2.5 ms apart. (Top): Typical instability of a medium-sized uncharged water drop of radius 2.0 mm in a slowly increasing vertical field. (Bottom): Drop radius 2.4 mm, in a rapidly increasing negative field of 10.3 kV cm^{-1} . (Richards and Dawson, 1971)

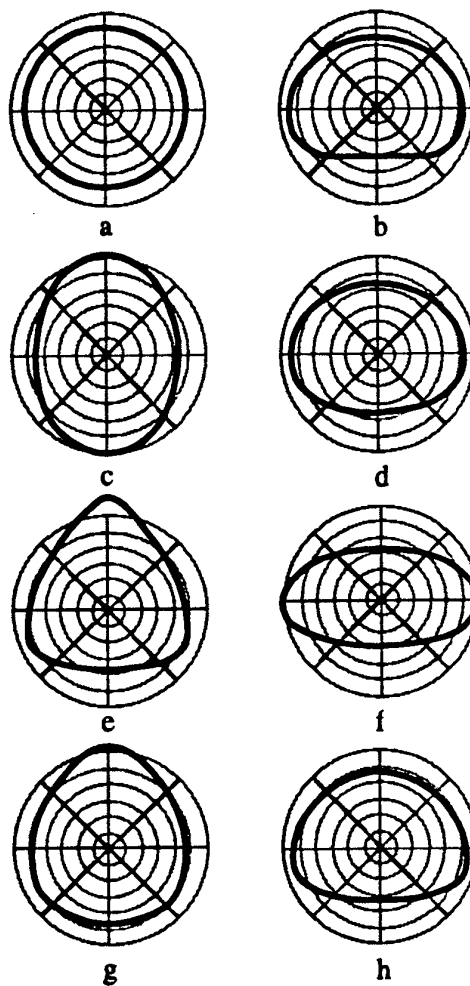
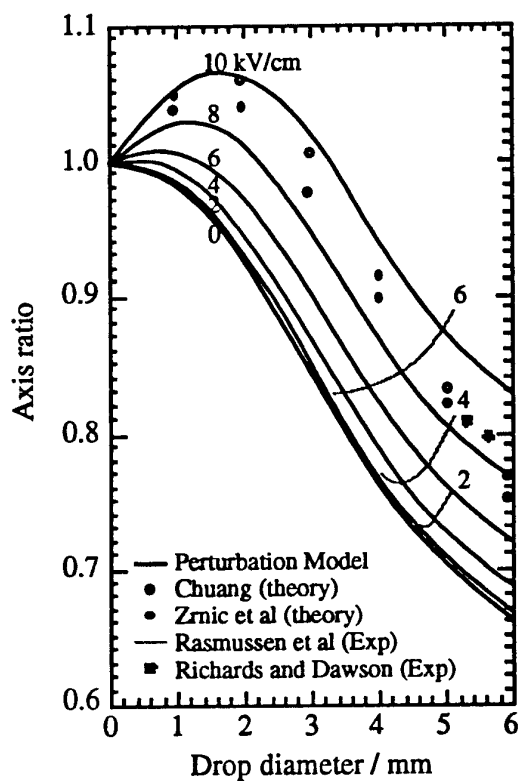


Figure 2.2.7 Perturbation axis ratios for electrostatic-aerodynamic shapes as a function of drop diameter for vertical electric fields in comparison to other theories and to wind tunnel experiments. (Beard et al., 1989a)

Figure 2.2.8 (above right) Drop shapes for various distortions: a) stationary drop b) sessile drop c) stationary drop in vertical electric field d) falling raindrop e) raindrop with $E_0 = 12 \text{ kV cm}^{-1}$ f) charged raindrop $Q = Q_R$ g) raindrop with max field-charge combination, with upward electric force h) same as g) but downward force. (Chuang and Beard, 1990)

shape (figure 2.2.8f). The comparison of theory with the experimental data of Ryan (1976) for drops of varying surface tension, falling in electric field appears good.

The combination of the effects of a charged drop and of an electric field was looked at by Chuang and Beard (1990). If a downward force is produced the electrostatic stress at the top is weakened, this increases the fall speed producing more aerodynamic distortion, and the drop thus becomes similar in shape to an uncharged drop (figure 2.2.8h). Alternatively, if an upward force is produced it enhances the electric stretching, and thus reduces the aerodynamic flattening of the base. This leads to pronounced stretching along the direction of the electric field, and higher axis ratios (figure 2.2.8g).

Taylor (1964) studied the deformation of drops in electric stresses, and showed that they would eventually become unstable if the electric field was raised high enough. Fields in thunderstorms are 1 kV cm^{-1} with a maximum of $2 - 4 \text{ kV cm}^{-1}$ and 10 kVcm^{-1} on lightning initiation. The results show that observed electric fields in clouds have a modest effect on drop shape and axis ratio, whereas stronger fields for highly charged drops lead to instability. Other effects are likely to be due to shape change on evaporation as a drop reaches its charge limit, or to pairs of drops colliding producing elongated drops, which by virtue of geometrical intensification are able to emit corona streamers at lower external fields.

2.2.4 Theoretical Calculations of Drop Shape

Spilhaus (1948) produced a simple equation for drop shape by suggesting the vertical flattening of large drops is due to the combined action of surface tension and aerodynamic pressures. The model was inadequate as it assumed the drop to be symmetrical about its horizontal plane over the whole range of drop sizes. This was done so he could use experimental data on drag coefficients for oblate ellipsoids. The model also ignored internal hydrostatic pressures, and incorrectly assumed a variation in surface tension that was only applicable to a sphere.

Imai (1950) calculated the axis ratio of raindrops in a potential flow using Laplace's equation $\sigma(1/R_1 + 1/R_2) = \Delta p$. He disregarded the internal hydrostatic pressure, and the external viscous effects to produce drops with the shape of an oblate spheroid for small deformations. The theory produced a very good correlation with the experimental results of Pruppacher and Beard (1970) for drop diameters $280 \mu\text{m} - 1 \text{ mm}$, however Beard et al. (1989b) consider the distortion to be exaggerated because the aft pressure is much too large for separated flow.

Savic (1953) expressed Laplace's equation, $\sigma(1/R_1 + 1/R_2) = \Delta p$ as a series of $\cos(n\theta)$ (Landau and Lifshitz, 1987), and used a measured aerodynamic pressure distribution for a sphere (Flachsbart, 1927). By solving a system of linear equations, he obtained the shape coefficients for falling drops. Savic found that the distortion depended on the aerodynamic pressure but was independent of the internal hydrostatic pressure. Pruppacher and Pitter (1971) criticised Savic's analysis saying that the pressure balance was in error by a constant term; the hydrostatic pressure gradient was only approximately taken into account; better distributions than Flachsbar's were available for a sphere; and that Savic neglected effects of internal circulation.

McDonald (1954) found the aerodynamic surface pressure from photos of Magono (1954) and roughly estimated the magnitude of internal circulation at the waist. He concluded that the hydrostatic pressure due to gravity was an important component of drop shape, and that the separation in the airflow around the drop was primarily responsible for the asymmetry of large raindrops. A measurable drop deformation was only found for drops with a diameter $> 280 \mu\text{m}$, corresponding to

the onset of a circulating wake at the rear of a sphere, (Taneda, 1956). While the onset of a linear relationship between the drop deformation and the drop size at diameters greater than 1 mm, coincided with the onset of shedding of vortices at the rear of a sphere, (Möller, 1938).

Taylor and Acrivos (1964) considered creeping flow with results that are inapplicable to separated flow for drops falling in gases, and thus only true for very small Reynolds numbers. When compared with the experimental results of Pruppacher and Beard (1970) for drop diameters 280 μm - 1 mm, Taylor and Acrivos theory appeared to overestimate the drop deformation.

Pruppacher and Pitter (1971) made adjustments to Savic's model, using measurements of Fage (1937) for the aerodynamic pressure distribution around a rigid sphere for $\text{Re } 10^3 - 10^5$, and of LeClair et al. (1970) for $\text{Re } 0.01 - 400$. The results showed that: 1) drops with $d \leq 340 \mu\text{m}$ can with negligible error be considered spherical, 2) drops with $d = 0.34 - 1.0 \text{ mm}$ can be approximated to an oblate spheroid, 3) drops with $d \geq 1.0 \text{ mm}$ become progressively deformed into asymmetric spheroids until at $d = 4 \text{ mm}$ a flat base is produced, 4) drops with $d \geq 4 \text{ mm}$ develop concave depressions in the base of the drop which rapidly deepen as d increases. This concave depression has not been seen experimentally except by Köenig (1965), and is likely to be a consequence of a large perturbation in the model as a response to the maximum external pressure in the region of the upstream stagnation point, rather than a natural phenomena.

Green (1975) wanted to use a simple approach that would produce reasonable results, and could be applied to models in which temperature or surfactant distributions have significant effects on the processes. The model constructed assumed that the drops had oblate spheroidal figures. It then assumed that the aerodynamic pressure is insignificant compared to the hydrostatic and surface curvature pressures at the equator of the spheroid (based on the observations of McDonald, 1954). This allowed the principle radii to be evaluated around the equator and hence the flattening of the spheroid to be calculated. The axis ratios produced agree very well with those found experimentally by Pruppacher and Beard (1970), Jones (1959) and Magono (1954).

Beard (1982,1984) showed that axis ratios could be obtained from a potential energy balance using only gravity and surface tension.

Beard and Chuang (1987) refined Savic's technique of taking an empirical pressure distribution around a sphere, to include variations in the pressure distribution with Reynolds number and drop distortion. The model produces better agreement with the experimental results of other studies, and produces a rounded base with a positive curvature up to drop diameters of 8 mm. The remaining theoretical uncertainties in the model, are dependent on the approximate nature of the dynamic pressure distribution. Firstly, the hydrodynamic pressure from the internal circulation is ignored. Secondly, the aerodynamic pressure has been approximated by the measured distribution around a sphere at high Reynolds number, after first using a potential flow adjustment for the symmetric oblate distortion in the unseparated flow region, and then a pressure drag adjustment in the wake.

Beard, Feng and Chuang (1989) developed a first-order perturbation model for the shape of falling drops in the presence of electric fields and charges by extension of Savic's method for including aerodynamic effects in the pressure balance equation of Laplace. The perturbation equation of Savic was preferred over Pruppacher and Beard, because it contained only first-order terms and could be readily solved algebraically. Pruppacher and Beard's equation contained a second-order hydrostatic term that had a negligible effect. The effect of charge on the sphere was incorporated by treating it as a uniform reduction in surface tension.

2.2.5 Experimental Evaluations of Drop Shape

Although Thomson (1885) made some observations on the shape of liquid drops moving through various fluids, the first serious attempt to examine the meteorological problem of the shape of large raindrops appears to have been made by Lenard (1904). Using a vertical airstream with water drops suspended freely inside, Lenard carried out a number of experiments on terminal velocities, deformation, and breakup. Further qualitative observations of drop shape were conducted by Flower (1928), Edgerton and Killian (1939) and Laws (1941). These were followed by quantitative measurements in the laboratory using drops falling in a long column of quiet air by Best (1947), Blanchard (1950) and Magono (1954). A column length of 12 m was typically used which according to Laws (1941) would be long enough for the drop to attain terminal velocity. The first observations in natural rain were conducted by Kumai and Itagaki (1954), but because they only photographed the drops in two dimensions, they assumed all the drops were oblate ellipsoids. A subsequent examination of 1783 drops between 2 and 6.4 mm in diameter by Jones (1959) used two cameras to obtain a three dimensional drop profile and to distinguish between spherical, oblate and prolate drops. More recent work with a refined wind tunnel (Pruppacher and Beard, 1970 and Pruppacher and Pitter, 1971) has provided more detailed information on axis ratio as a function of raindrop size (figure 2.2.9). The wind tunnel used is described in detail in Pruppacher and Neiburger (1968). It was constructed at UCLA for cloud physics research and consisted of a horizontal air conditioning unit with a vertical flow control system. This system allowed air speeds between 1 cm s^{-1} and 10 cm s^{-1} to be obtained with a flat velocity profile across the tube. Drops of 0.02 - 9.0 mm diameter could then be suspended under all temperature and humidity conditions for long enough to reach equilibrium. The drops were simply injected into the air stream at the bottom and the velocity adjusted until the air stream was travelling at the terminal velocity for that drop.

The experimental results of Pruppacher and Beard can be seen in figure 2.2.1 and are compared to the theory of Beard and Chuang in figure 2.2.9. It was found that for drops smaller than $280 \mu\text{m}$ diameter there was no detectable deformation from a spherical shape. While for drop diameters $280 \mu\text{m} - 1 \text{ mm}$ there was a slight deformation into an oblate spheroid and for $1 - 9 \text{ mm}$ the deformation was found to be linearly related to the drop size.

2.2.6 Drop Oscillations

Best (1947) said that the natural state of a raindrop was "one of oscillation about a mean shape". In the literature five main causes of oscillation are described: intrinsic aerodynamic forces for smaller drops, and collisions, coalescence, turbulence and shear for larger drops.

Drop oscillation occurs in modes composed of spherical harmonic perturbations with the surface defined by:

$$r_{n,m}[t, \theta, \phi] = r_0 + A \sin \omega t P_{n,m} \cos m\phi \quad (2.2.3)$$

where r_0 is the undistorted radius, A is an arbitrary amplitude, and $P_{n,m}$ are the associated Legendre functions. Rayleigh (1879) determined that the oscillation frequencies depend on the order n , drop size r_0 interfacial tension σ , and drop density ρ :

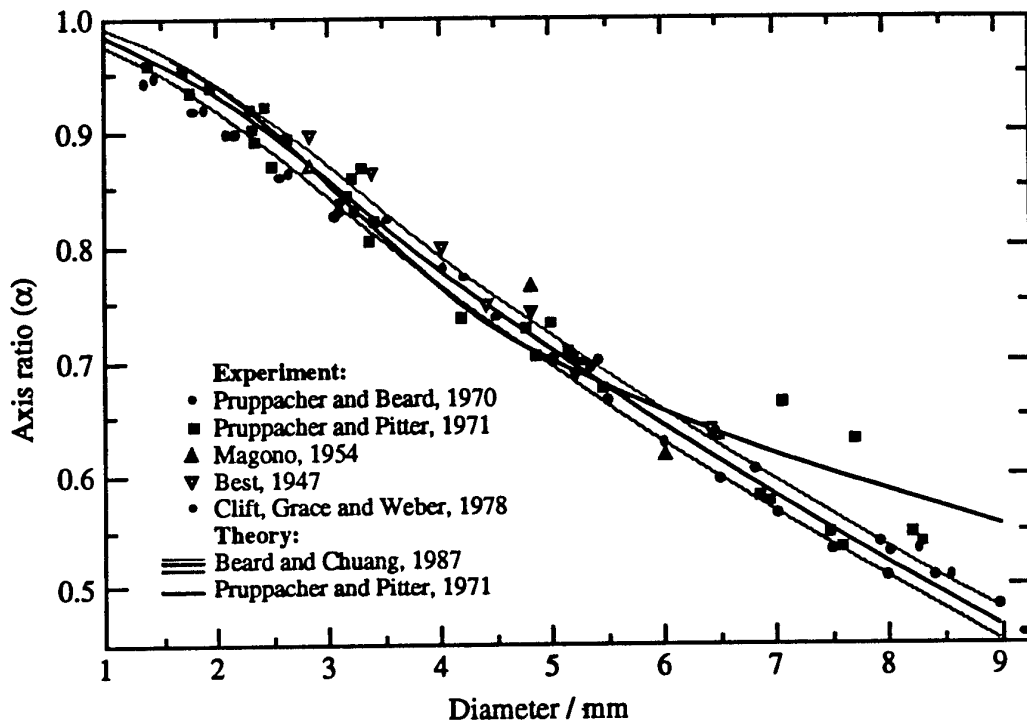


Figure 2.2.9 Experimental and model results for axis ratio (α) as a function of drop diameter. The grey lines show the Beard and Chuang (1987) theoretical model upper and lower bounds. (*Beard and Chuang, 1987*)

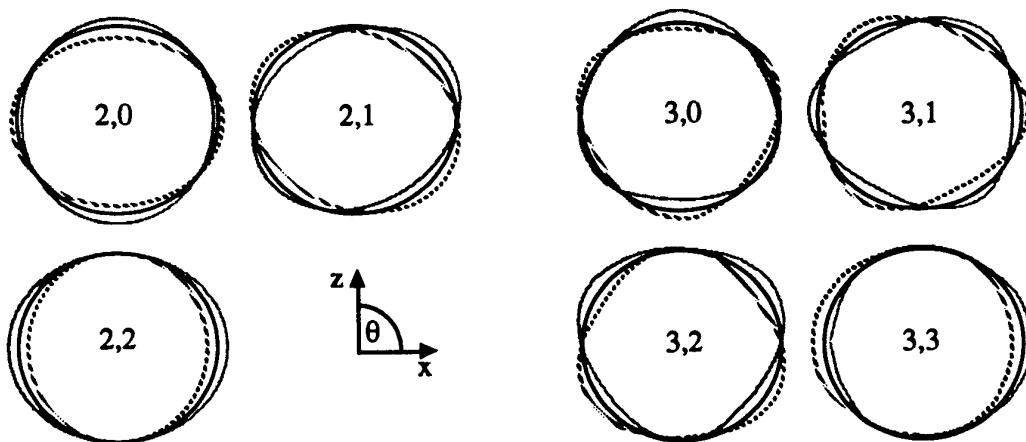


Figure 2.2.10 Spherical harmonics for $n = 2$ and 3 with perturbation maxima normalised to 10% of the undistorted radius viewed along the y axis (in the plane of the maximum amplitude for the asymmetric modes where $\cos m\phi = \pm 1$). The curves in grey are for positive amplitude ($\sin\alpha x > 0$) and those with stripes are for negative amplitude. The solid shows the undistorted sphere. (*Beard and Kubesh, 1991*)

$$f_n = [n(n-1)(n+2)\sigma]^{1/2} [4\pi\rho r_0^3]^{-1/2} \quad (2.2.4)$$

Each frequency allows $m = n+1$ "degenerate" modes having unique spatial orientations. These can be written as (n, m) to designate a mode e.g. (2, 1)

The most commonly mentioned modes can be seen in figure 2.2.10, this shows the two lowest frequencies, the fundamental ($n = 2$) and the first harmonic ($n = 3$). The fundamental oscillations are:

(2, 0) - Vertical mode; vibration along the vertical axis giving an axisymmetric prolate - oblate oscillation, this gives a two-sided axis ratio variation about unity for a sphere.

(2, 1) - Transverse mode; the maximum vertical extent increases more than the maximum horizontal extent for some views so that it gives a one-sided axis-ratio variation above unity for a sphere.

(2, 2) - Horizontal mode; vibration along the horizontal axis with major and minor axis 90° apart, this gives a two-sided axis-ratio variation about unity for a sphere.

Other rigorous theoretical studies on drop oscillations using the spherical equilibrium shape have been published by Lamb (1932), Foote (1973), Tsamopoulos and Brown (1983) and Naterajan and Brown (1987), while more recently a study has been published by Feng and Beard (1991) using an asymptotic analysis with the method of multiple-parameter perturbations.

Several experimental studies of drop oscillation have been conducted and observations have been made for a range of drop diameters (d). These mostly deal only with the fundamental harmonic $n = 2$.

<u>Drop Size / mm:</u>	<u>Oscillation observed:</u>	<u>Paper:</u>
$d \leq 1$	quiescent drop shape	Beard, Ochs and Kubesh (1989)
$d \approx 1.0$	(2, 1)	Gunn (1949)
$d \approx 1.0 - 1.3$	(2, 1)	Beard, Ochs and Kubesh (1989)
$d \approx 1.0 - 1.3$	(2, 1), (3, 1)	Beard and Kubesh (1991)
$d \approx 1.4 - 1.5$	(2, 0)	Beard, Ochs and Kubesh (1989)
$d \approx 1.4 - 1.5$	(2, 0), (3, 1)	Beard and Kubesh (1991)
$d \approx 1.0 - 3.0$	(2, 0)	Nelson and Gokhale (1972)
$d \approx 3.7 - 5.6$	approximately (2, 0)	Brook and Latham (1968),
$d \approx 3 - 6$	(2, 0), (2, 1)	Beard (1984)
$d \approx 4.5$	(2, 0), (2, 1)	Musgrove and Brook (1975)
$d \approx 4 - 7$	undefined	Nelson and Gokhale (1972); Beard (1984) said Nelson and Gokhale data showed (2, 0) and (2, 1)
$d \approx 4 - 7$	(2, 0), (2, 1), (2, 2)	Goodall (1976)
$d \approx 6 - 10$	(2, 2)	Blanchard (1948, 1950)

The onset of raindrop oscillations at $d \approx 1.0$ mm coincides closely with the onset of the shedding of vortices at the rear of a sphere, and was proposed as a resonance response by Gunn (1949) (figure 2.2.12). The results from Beard et al. (1989b) in figure 2.2.11 of axis ratio variation with drop diameter show the quiescent value measured for $d \leq 1.0$ mm. For larger drop diameters $d = 1.0 - 1.3$ mm there is a moderate one-sided scatter above the theoretical curve which fits with modes (2, 1) and (3, 1), while for $d = 1.4 - 1.54$ there is a shift in the average axis ratio consistent with a transverse mode (3, 1) as well as a two-sided scatter consistent with an axisymmetric mode (2, 0). Beard and Kubesh (1991) reported

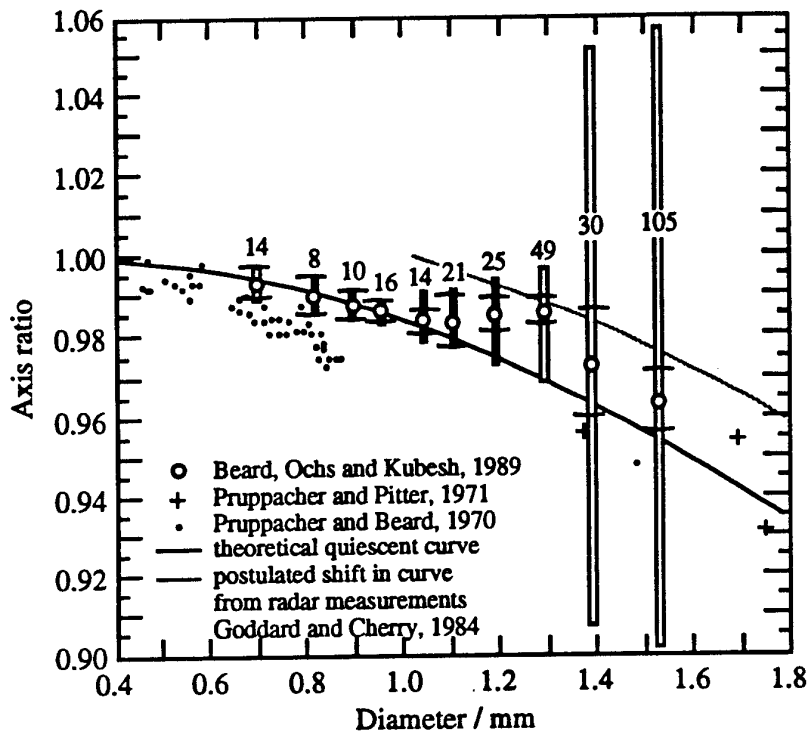


Figure 2.2.11 Measured axis ratios as a function of drop diameter. The vertical bars show the range of measured values, including scatter and estimated experimental uncertainty. Also displayed are mean axis ratios (circles), 95% confidence intervals (arcs) and number of measurements. (*Beard et al., 1989b*)

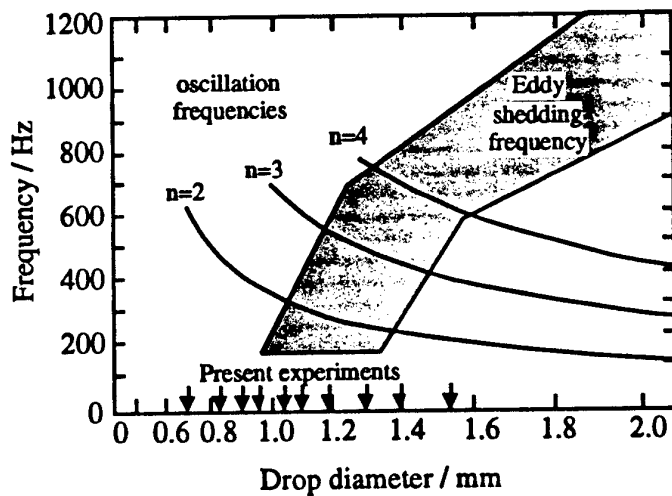


Figure 2.2.12 Oscillation and eddy shedding frequency as a function of diameter for water drops falling in air. Curves are the oscillation frequency for water drops in air ($n = 2, 3$ and 4). Eddy shedding frequencies are shown by the shaded region. The arrows at the bottom show the drops looked at by Beard et al (1989b). The onset of eddy shedding is at $1.0 - 1.1$ mm for $n = 2$. For diameters $1.2 - 1.3$ the eddy shedding frequencies overlap both $n = 2$ and 3 . (*Beard et al., 1989b*)

that the primary resonance seems responsible for the production of the transverse modes (2, 1) and (3, 1) because of a good match between the forcing and response frequencies, and because the spatial pattern of eddy shedding has a good match between its forcing pattern (pressure perturbations off to the side of the upper pole) and the response pattern of modes (2, 1) and (3, 1) as seen in figure 2.2.4. The occurrence of (2, 0) may be a secondary resonance, a subharmonic response at $n = 2$, to forcing near $n = 4$, and there is therefore no requirement for the forcing pattern to match the response. The results of Beard and Kubesh (1991) indicate that there is a possibility that both modes can occur on the drop together for $d \approx 1.1 - 1.2$ mm but this appears to be rare.

Since secondary resonance, which does not require a good frequency match, has been detected by Beard and Kubesh (1991), it is conceivable that eddy shedding could promote raindrop oscillations for much larger raindrop sizes. The more common sources of oscillations for the larger raindrops however are collisions and air turbulence. Warner (1977) indicates that in heavy rainfall each raindrop experiences collisions with other raindrops every few seconds. This means that there should be between 1 - 10 collisions per second in a cubic meter of air during moderate-to-heavy rainfall.

Beard et al. (1983) used a potential energy model to calculate oscillation energies and the corresponding axis ratios for fundamental mode oscillations due to collisions. The calculated axis ratios are shown in figure 2.2.13 and compare favourably with the wind tunnel findings of Brook and Latham (1968) and the raindrop observations of Jones (1959). After collision the degree to which a drop stays in an agitated state depends on both the energy input from the collision and the rate at which the oscillations are damped. It must also be remembered that breakup may follow a collision, so collisional energy is not always available for oscillations (Low and List, 1982). Chandrasekar et al. (1988) used an airborne two-dimensional precipitation probe to determine the axis ratios of raindrops ($d = 2 - 6$ mm) more than 1 km above the surface (figure 2.2.14). At light rain rates the mean axis ratios agreed with Green (1975) and Pruppacher and Pitter (1971) for $d > 3$ mm, but were higher for $d < 3$ mm i.e. drops were more spherical than theory predicted. At higher rain rates the mean axis ratios are higher than Pruppacher and Pitter (1971) and Green (1975) for $d < 4$ mm, but compare well to Beard (1984) who adjusted for collisions determining the amplitude of oscillation. The axis ratios for $d > 4$ mm however are closer to the equilibrium value, possibly because of suppression by ice cores in partially melted raindrops, or suppression in a melted drop due to an ice core being present earlier.

2.2.7 Drop Canting

The polarisation properties of precipitation are determined by the particle shapes and the degree of common orientation among the scatterers (Atlas et al., 1953, and McCormick and Hendry, 1974)

In the presence of wind shears, raindrops which normally fall with a flat bottom parallel to the surface of the earth, have been observed to tilt from the horizontal with canting angles that are symmetrically distributed about a mean of zero with standard deviations of $\sim 30^\circ$ (Saunders, 1971). This set of results is not however applicable above the surface layer because they were collected near the ground where canting is the result of wind shear and gusts produced by boundary friction (Brussard, 1976 and Maher et al., 1977).

Other estimates of the canting angle from microwave studies based on assumed size distributions and shapes range from $0 - 15^\circ$ Watson and Arbabi

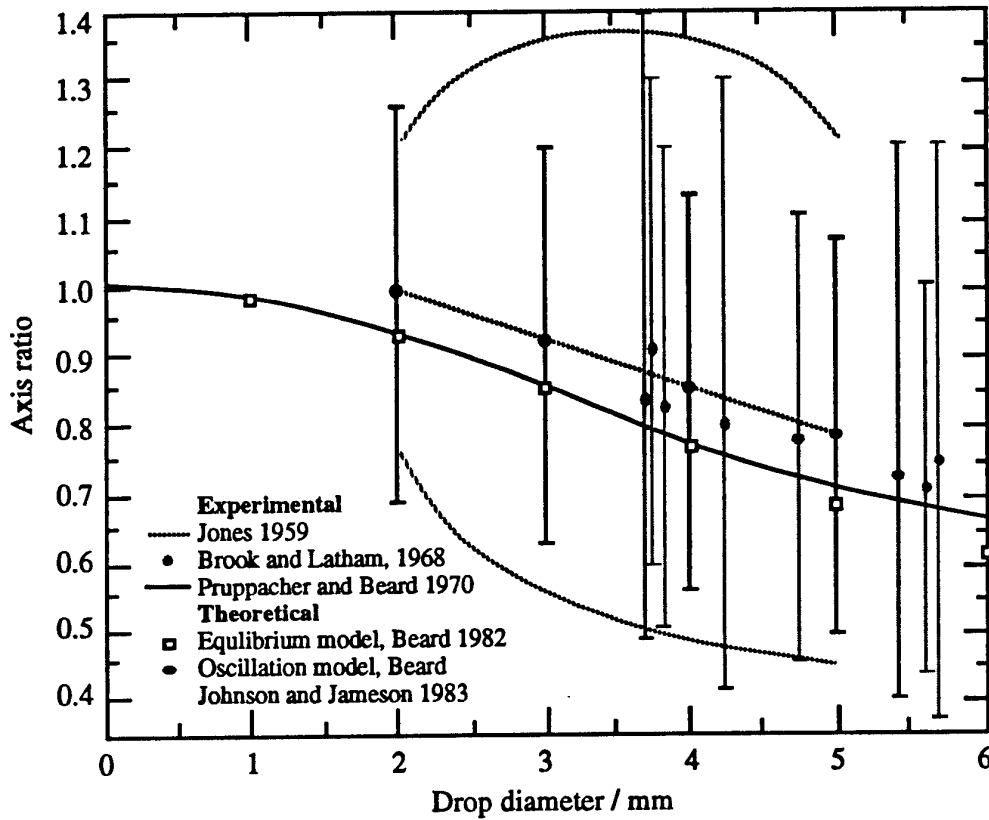


Figure 2.2.13 Observed and experimental axis ratio variation as a function of drop diameter. The solid curve of Pruppacher and Pitter (1971) is the equilibrium value. The results of Jones show mean and extremes for actual raindrops. Brook and Latham results show mean and extremes for water drops in a wind tunnel. (*Beard et al., 1983*)

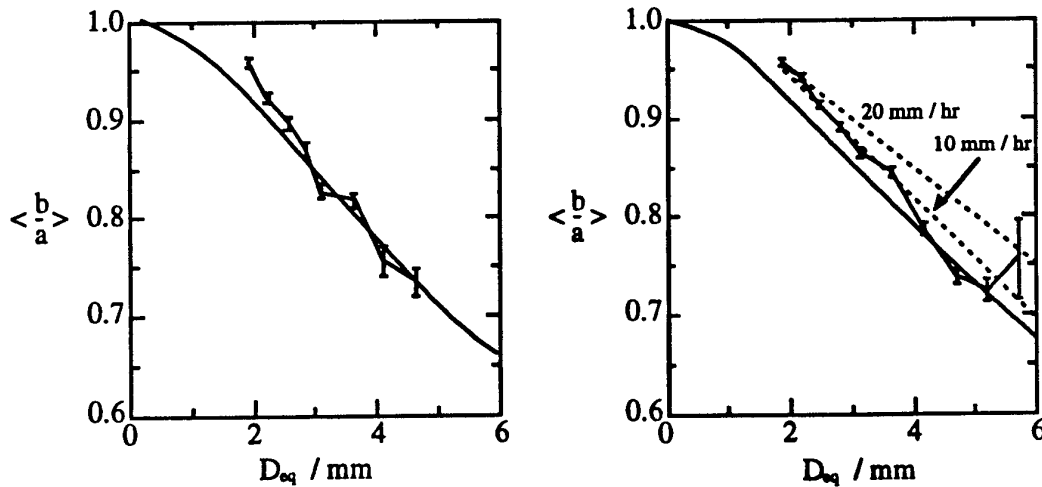


Figure 2.2.14 Mean axis ratio $\langle b/a \rangle$ as a function of the volume-equivalent diameter D_{eq} . Above left light rain rate, above right higher rain rate. (*Chandrasekar et al., 1988*)

(1973) up to 25° Chu (1974).

The most sensitive measurements of canting angle are provided by the polarisation radar investigations of McCormick and Hendry (1974). Using the backscatter returns from circularly polarised transmissions they obtained a mean canting angle of 0.48° with a standard deviation of 1.77°. This compares well with the theoretical calculations of Beard and Jameson (1983), who found for a turbulent intensity $\leq 0.2 \text{ m}^2\text{s}^{-3}$ the mean canting angle was 0° with a standard deviation $\leq 4^\circ$. Therefore raindrop canting angles are small and narrowly distributed about a mean close to zero, these magnitudes should have a negligible effect on the measurements of differential reflectivity (Seliga and Bringi, 1976).

2.2.8 Dual Polarisation Technique

This technique relies on the fact that large falling raindrops distort to become approximately oblate spheroids, each with its axis of symmetry near vertical, and that the degree of oblateness increases with drop size. Consequently, the effective radar reflectivity factor measured using horizontal polarisation is greater than that measured with vertical polarisation.

The reflectivity per unit volume of space filled with precipitation is given by:

$$Z_{H,V} = \int_0^{\infty} N(D)\xi_{H,V}(D)dD \quad (2.2.5)$$

where $N(D)dD$ is the number of precipitation particles per unit volume with diameters in the interval dD , and $\xi(D)$ is the radar cross section of a particle of diameter D .

A theoretical relationship was worked out by Seliga and Bringi (1976) to try and work out the drop size distribution from the effective reflectivity factors $Z_{H,V}$ for horizontal and vertical polarisation, and the differential reflectivity factor Z_{DR} defined as:

$$Z_{DR} = 10 \log_{10}(Z_H/Z_V) \text{ dB} \quad (2.2.6)$$

The technique has three assumptions: raindrops have approximately oblate spheroidal shapes; the drops fall with the major axis horizontal; the drop size distribution is of a general exponential form:

$$N(D) = N_0 \exp(-3.67D/D_0) \quad (2.2.7)$$

where N_0 and D_0 are free parameters. Results produced using this technique by Hall et al. (1980) are illustrated in Fig 2.2.15. The local rainfall rate and precipitation type have been evaluated, however the results of drop oscillation as set out by Beard (1984), or shape change due to electric stress shown in Chuang and Beard (1990) have not been allowed for. Because the backscattering properties of spheroids depend in a non-linear way on the axis ratios, neither the average shape nor the equilibrium shape may be appropriate for interpreting the radar. Further research in this area is therefore still necessary, but the potential to be able to determine drop size distribution in a cloud in this manner is an extremely attractive one.

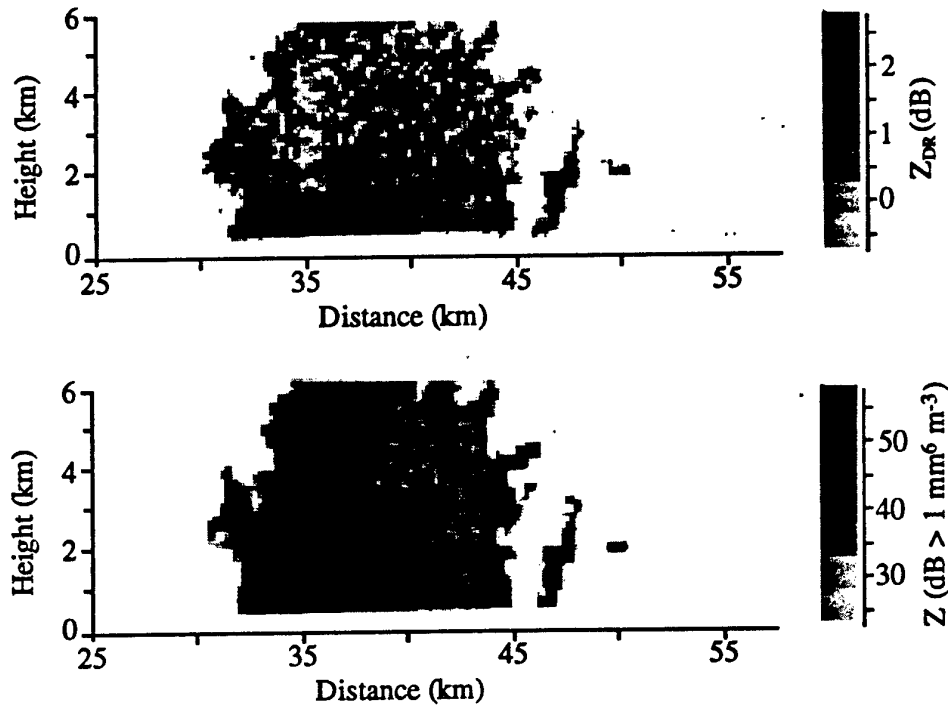


Figure 2.2.15 A vertical scan through raincells at 13.17 UT on 15th August 1978. (Top) Differential reflectivity Z_{DR} ; (Bottom) Absolute reflectivity factor, Z . If both values are high then the cells represent rain, sleet or wet snow; if both values are low then drizzle, cloud or fog; if Z is high and Z_{DR} is variable then it is wet hail; if Z is medium and Z_{DR} is low then ice. A change can be seen from rain to ice at the 0°C isotherm at 2 km. (Hall et al., 1980).

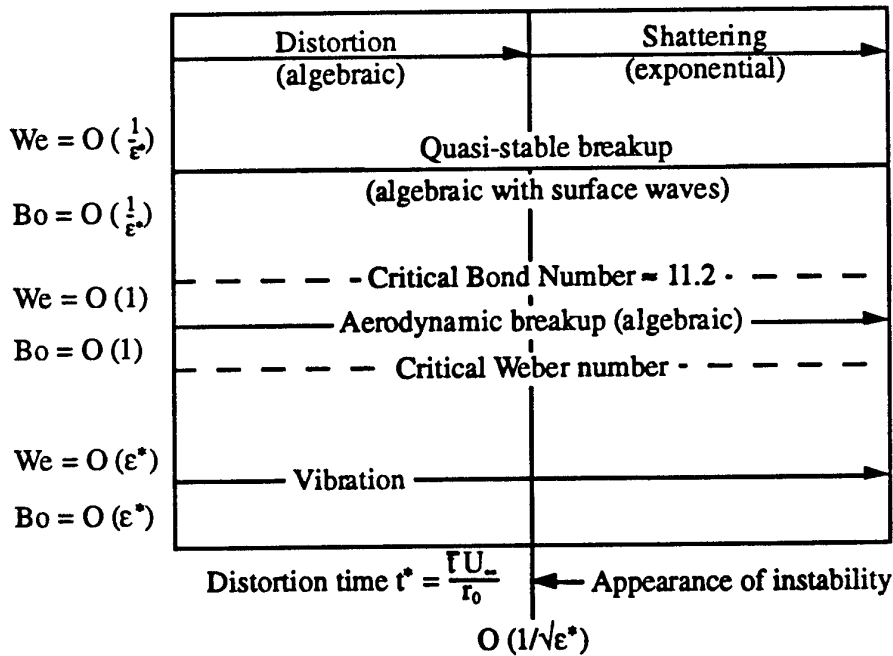


Figure 2.3.1 Regimes of the dynamic response. (Harper et al., 1972)

2.3 BREAKUP OF WATER DROPS

2.3.1 Introduction

The fragmentation of liquid drops resulting from their sudden exposure to a high-velocity gas stream, has important applications in the fields of propulsion, aerodynamics, agricultural and insecticidal spraying and the production of aerosols for therapeutic and other purposes. For example, the rate of mixing and combustion of liquid fuel droplets in propulsion studies, can be greatly enhanced by virtue of the fragmentation process when compared to that obtained under conditions of low velocity and forced convection, where no disintegration occurs (Ragland et al., 1968, Ranger and Nicholls, 1969, Kauffman and Nicholls, 1971). With regard to aerodynamics, a reduction in the damage sustained by an aircraft or missile flying in rain, can be achieved by designing a body whose detached shock is sufficiently far removed, to allow for drop shattering in the region separating the shock from the body surface (Engel, 1958, Jenkins, 1966, Reinecke and Waldman, 1970).

In order to evaluate the effectiveness of drop Breakup, the time required, distance travelled, and sizes of secondary droplets or residue formed need to be evaluated.

2.3.2 Forces Acting on the Drop

The forces acting on the surface of a droplet, that has a translatory motion relative to an ambient fluid, have a tangential component caused by effects of viscosity of the ambient fluid, and a non-uniform surface pressure distribution caused by the velocity pressures of the ambient fluid. For large Reynolds' numbers ($Re > 1000$), the effect of the tangential component of the forces on the deformation is small compared with that caused by the normal component and may be neglected (Hinze, 1949). The droplet is however, subject not only to deformation due to the forces on the surface, but also to the possible simultaneous effects of instability due to acceleration.

Two numbers are often used to characterise the stability of the drop:

1. The Bond number:

$$B_0 = \frac{\rho_L a r_0^2}{\sigma} \quad (2.3.1)$$

where ρ_L is the density of the liquid drop with initial radius r_0 , σ is the surface tension and a the acceleration. This parameter represents the ratio of inertial to surface tension forces.

2. The Weber number:

$$We = \frac{\rho_A U^2 r_0}{\sigma} \quad (2.3.2)$$

where ρ_A is the density of the air flow of velocity U , r_0 is the drop's initial radius and σ is its surface tension. This parameter represents the ratio of the aerodynamic force to the surface tension restoring force.

The state of the drop for varying Weber and Bond numbers has been investigated theoretically by Harper et al. (1972) and is summarised in figure 2.3.1 (on the

previous page). For a drop with Weber and Bond numbers below certain critical values the drop vibrates for all time. Once the Weber number is above its critical value the response is not vibratory, instead the drop breaks up by deforming due to the aerodynamic forces. The value of the Bond number associated with this critical Weber number is below its critical value of 11.2, and the drop is said to be stable to small disturbances (stability only refers to the absence of exponentially growing surface waves). Above the lowest critical value of the Bond number, 11.2, the drop is unstable to small disturbances of arbitrary form. However, until the Bond number reaches a rather large value, say 10^5 , the rate of growth of the unstable modes is rather small compared with the aerodynamic deformation. This regime is therefore defined as 'quasi-stable', the deformation is aerodynamically induced (algebraic in time), and the effects of acceleration are manifest as waves on the windward surface. At large values of Bond number ($> 10^5$) the effects of acceleration dominate the breakup by shattering the drop from the windward surface.

There are two forms of time related breakups commonly considered. The first is when the droplet is exposed to an air flow uniformly increasing in speed from zero to a constant value, as with drops falling under gravity ('steady' airflow). While the second is when the droplet is suddenly exposed to a change in air velocity, for example in the passage through the shock wave of a supersonic moving vehicle ('transient' airflow). The behaviour of falling drops has been dealt with in section 2.2 so we shall next briefly examine the conditions a drop is exposed to in the airflow behind a moving shock.

2.3.3 Conditions in the Airflow Behind a Shock

A blunt object moving through air at supersonic velocity is preceded by a detached shock wave that is separated from the leading surface of the object by a zone in which air is moving forward at high velocity in front of the object. The conditions that exist in the air through which the shock has moved constitute the environment in which the water drop finds itself after the air-shock-water drop collision.

2.3.3.a Velocity of the Airstream Behind the Shock

For a stationary shock formed in a shock tube, the continuity equation is:

$$\rho_1 u_1 = \rho_2 u_2 \quad (2.3.3)$$

where u_1 is the velocity of the airstream entering the shock, and ρ_1 is the density of this air, u_2 is the velocity of the airstream after passing through the shock, and ρ_2 is the density of this air. For the case of a moving shock, the airstream velocities on either side of the shock are those seen by an observer who is moving toward the shock at the velocity u_1 . For this observer the velocity of air approaching the shock is U_1 and $U_1=0$. The shock appears to be approaching this observer at a velocity U_s , where $U_s=-u_1$. The velocity of air on the opposite side of the shock as seen by this observer is U_2 and $U_2=u_2 - u_1$. For this moving shock Ames (1953) gives the continuity equation as:

$$U_2 = U_1 \left[1 - \frac{(\gamma-1)M_s^2 + 2}{(\gamma+1)M_s^2} \right] \quad (2.3.4)$$

where M_s is the Mach number of the shock, and γ is the ratio of the heat capacity at constant pressure to the heat capacity at constant volume, which for air is 1.4. The calculated values of the velocity and other parameters of the airflow behind shocks that have Mach numbers of 1.3, 1.5 and 1.7 are given in table 2.3.1.

2.3.3.b Temperature of the Air Behind the Shock

The ratio of the temperature of the airstream behind the moving shock, T_2 , to the temperature of the undisturbed air into which the shock is advancing, T_1 , is given by Ames (1953) as:

$$\frac{T_2}{T_1} = \frac{[2\gamma M_1^2 - (\gamma - 1)][(\gamma - 1)M_1^2 + 2]}{(\gamma + 1)^2 M_1^2} \quad (2.3.5)$$

2.3.3.c Viscosity of the Air Behind the Shock

The viscosity of the air behind the shock affects the Reynolds number of the airflow around the water drop. This can be approximated by an expression from Ames (1953):

$$\frac{\eta_2}{\eta_1} = \left(\frac{T_2}{T_1}\right)^{0.76} \quad (2.3.6)$$

2.3.3.d Reynolds Number for the Flow Around a Water Drop

Knowing the velocity, U_2 , the viscosity coefficient, η_2 , and the density, ρ_2 , of the airstream flowing behind the shock, the Reynolds number of the flow around a 2 mm water drop can be calculated. The results for Mach 1.3, 1.5 and 1.7 are given in table 2.3.1.

2.3.3.e Mach Number of the Airstream Behind the Shock

To determine the Mach number of the airflow behind the moving shock, M_2 , it is necessary to know the speed of sound in this air, c_2 . This can be calculated from an expression given by Burgers (1943):

$$c_2^2 = c_1^2 + \frac{2(\gamma - 1)}{(\gamma + 1)^2} \left[\gamma U_1^2 - (\gamma - 1)c_1^2 - \frac{c_1^4}{U_1^2} \right] \quad (2.3.7)$$

where c_1 is the speed of sound in the undisturbed air.

2.3.3.f Pressure in the Airstream Behind the Shock

A knowledge of the free-stream pressure in the airflow behind the shock is required to evaluate the pressure on the windward and leeward faces of the water drop. This can be calculated from Burgers (1943):

$$p_2 = p_1 \left[\frac{c_1^2}{\gamma} + U_1 U_2 \right] \quad (2.3.8)$$

Table 2.3.1 Conditions in the air-stream flowing behind an air shock assuming that $\rho_1 = 0.0011766 \text{ g cm}^{-3}$; $T_1 = 300^\circ\text{K}$ (Engel, 1958)

Shock Mach no. M_s	Velocity U_2 m s^{-1}	Sound speed, c_2 m s^{-1}	Mach no. M_2	Density ρ_2 g / cm^3	Temp. T_2 $^\circ\text{C}$	Pressure p_2 N m^{-2}	Stagnation Pressure, p_t N m^{-2}	Reynolds number for a 2 mm drop
1.3	152	375	0.40	0.00178	84	1.79×10^5	1.99×10^5	26,000
1.5	237	396	0.60	0.00218	123	3.10×10^5	3.10×10^5	45,000
1.7	316	416	0.76	0.00256	165	4.65×10^5	4.65×10^5	66,000

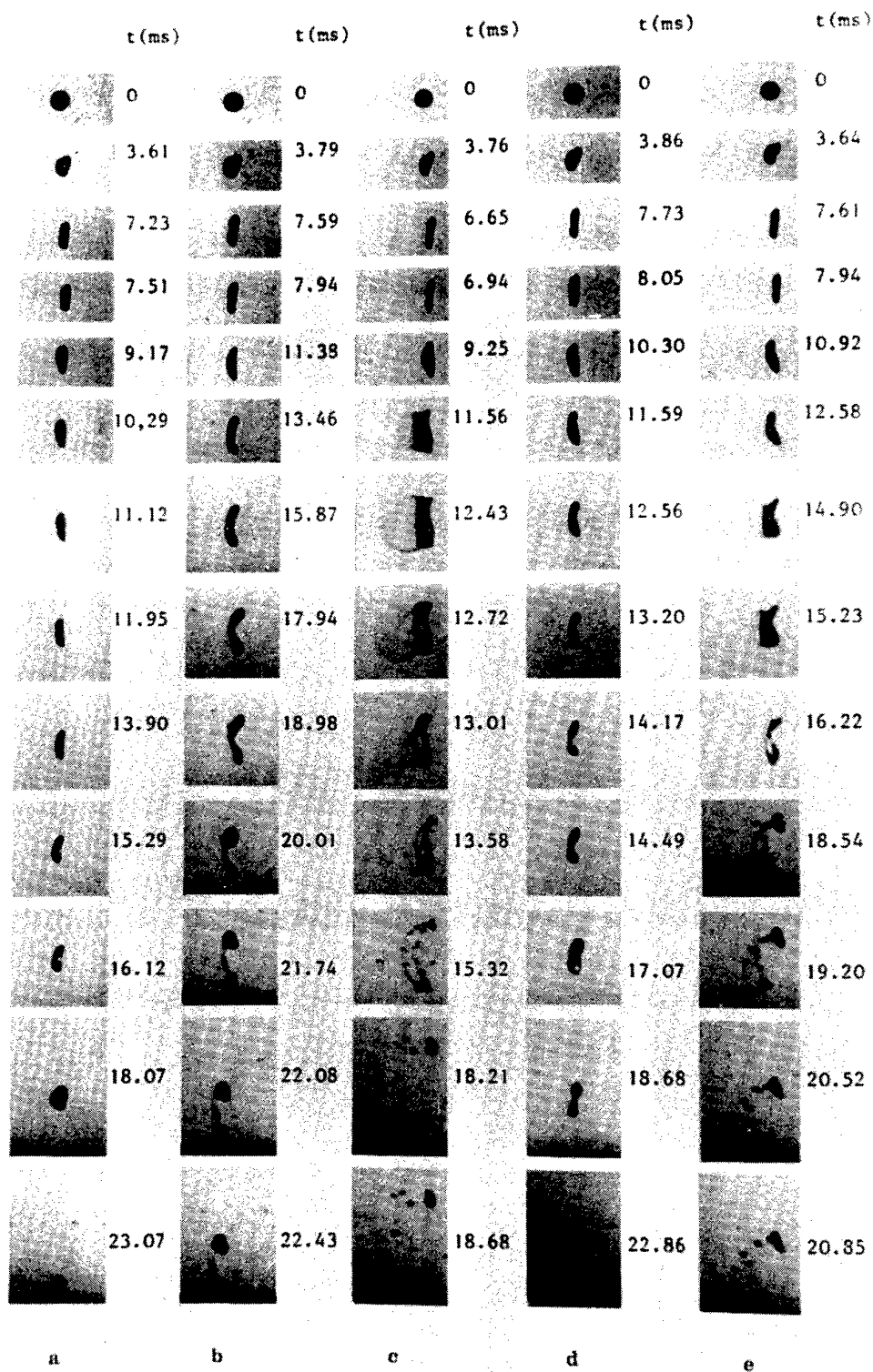


Figure 2.3.2 Different types of droplet deformation and breakup at nearly critical Weber numbers $d_0 = 2,600 \mu\text{m}$, $We = 12.51$. (Taken from Wierzba, 1990)

2.3.4 Modes of Breakup

There are five common modes of breakup for a water drop, and the type observed can be broadly identified by the Weber number. These modes will be classified below as follows: vibrational, bag breakup, umbrella, stripping, and catastrophic. The Weber number on its own is in fact inadequate as a breakup criterion as the behaviour also depends on the liquid viscosity, the droplet diameter, and the time for which the gas flow acts upon the droplet. Hinze (1949) for example, using the results of Merrington and Richardson (1947) estimated the $We_{crit} = 10$ for "low" viscosity drops, and $We_{crit} = 20$ for "high" viscosity drops, while Hanson et al. (1963) discussed the effects of drop diameter, and Taylor (1949) put forward an explanation for the air velocity for breakup in transient blasts being lower than in the steady stream, and for the increase in the discrepancy for smaller drops. Hinze (1955) tried to clarify the criterion by incorporating the effect of viscosity into his critical Weber number, while Borisov et al. (1981) used a combination of We number range and $WeRe^{-0.5}$ range to specify the likely mode of disintegration.

2.3.4.a Vibrational ($We \sim <10$)

The original work on the vibratory response of drops is discussed in Lamb (1932), and numerous experiments have demonstrated that the fundamental frequency ω_0 agreed well with Rayleigh's (1879) result:

$$\omega_0 = (2\sigma / \pi^2 \rho_L r_0^3)^{\frac{1}{2}} \quad (2.3.9)$$

The vibration of drops subjected to an airflow that is uniformly increasing in speed has already been dealt with in section 2.2.6 for drops falling under gravity. An early survey of research in this low Weber number range has been given in Lane and Green (1956). Once the drop reaches a critical value of the Weber number it ceases to vibrate and undertakes a monotonic deformation, this limits raindrops to a maximum diameter of 8-9 mm according to Hinze (1949). Wierzba (1990) defined the critical Weber number such that it was sufficient to complete the bag type breakup of 100% of the tested droplets. He observed that for near critical Weber numbers the process of droplet deformation was very sensitive to small fluctuations in the experimental conditions such as relative velocity, drop diameter, drop vibrations, flow fluctuation etc. Wierzba showed that if the interaction between a drop and the gas stream was such that the vibration of the drop was amplified and if the duration of this interaction was sufficiently long, then a narrow 'neck' appeared after some time, and then the drop broke into two parts. Very often a small droplet would be formed as a result of the evolution of the neck. This kind of breakup can be seen in figure 2.3.2b. Two further developments of a vibration breakup type mode were observed by Wierzba. In the first the neck appears and then the vibration ceases and the droplet doesn't breakup, figure 2.3.2d. In the second the vibrational breakup type mode turns into a bag-breakup in the second phase, figure 2.3.2e.

2.3.4.b Bag Breakup ($We \sim 10 - 20$)

($8 \leq We \leq 40$ and $0.2 \leq WeRe^{-0.5} \leq 1.6$ according to Borisov et al., 1981)

This form of breakup appears to have been first observed by Hochschwender (1919), who was measuring the electric charge generated in the breaking of water drops. Hochschwender allowed water drops to fall into a free upward-flowing current of air and saw that some of them were blown inside out. The phenomenon was later rediscovered and examined in detail by Lane and Edwards (1948), Lane (1951) and Magarvey and Taylor (1956). These papers analysed the various stages of bag breakup seen for a drop falling under gravity in a vertical wind tunnel or in stagnant

air, but failed to observe the bag breakup mode for transient airflows. In contrast Hanson et al. (1963) showed that bag breakup always occurs in the transient case except when the air velocity is greatly in excess of the critical value.

The basic features of bag breakup can be seen in figure 2.3.2c. After the lateral deformation of the drop reaches a maximum, instead of the appearance of a narrow 'neck', as seen with the vibrational breakup, the central part of the drop becomes concave to the flow direction, and is then blown off in the downstream direction into a hollow bag attached to a toroidal rim. Hanson et al (1963) observed small dark spots surrounded by concentric rings on the surface of the bags (figure 2.3.3). He conjectured that they were the beginnings of points of rupture based on similar observations on spray films by York (1963). After an appropriate time the bag in figure 2.3.2c bursts into a large number of small droplets. This breakup was shown by Wierzba (1990) to occur more quickly than the breakup for the vibrational mode, and it was estimated that the bag only contained 25% of the drops total water content. The rim then breaks into twenty small droplets and two comparatively large ones. The droplets produced by the ring are not uniform in size due to irregularities in the rim thickness. These irregularities are a consequence of the formation of lobes on the rim. As a result of the initial vibration of the droplets, there are most frequently 2, 3 or 4 lobes formed on the rim during bag type breakup. Each lobe forms one large droplet after breakup.

Several attempts have been made to model bag breakup theoretically. Gordon (1959) estimated the magnitude of the pressures caused by the aerodynamic forces, the surface tension, and the viscosity and combined these with the inertial effects to get a differential equation that would give the breakup time. Dodd (1960) developed expressions to predict the distortion and disintegration so that he could look at the survival probability for water drops situated in the path of a solid sphere moving through the air. He found that for a given solid sphere diameter and velocity a larger drop might collide while a smaller drop would burst. This is in spite of the fact that a higher critical relative speed is required for the smaller drop. The explanation for this is that the smaller drop is more easily blown up once the critical point is past due to the smaller thickness of the bag. Ho and Hoglund (1969) used a special linearization of the Navier-Stokes equation, as did Harper et al (1970), but this was found to give a faster distortion rate than that actually measured, because it overestimated the lateral distortion of the drop, because the surface pressure distribution is modified by the deformation (Simpkins, 1971). The most recent attempt at simulating bag breakup has been a numerical model developed by Liang et al (1988) which has produced some promising initial results.

The critical Weber number has been used generally in the literature to define the conditions for the onset of the bag type breakup. This has resulted in a wide range of critical Weber numbers ranging from 2.2 to 99.6 (listed in Wierzba, 1990) depending on the experimental technique used, the effects of viscosity and drop diameter and the precise definition of the breakup conditions taken for that experiment. Wierzba (1990) evaluated the percentage of droplets that undertook regular bag type breakups for varying Weber number, and defined the critical Weber number as when 100% of the tested droplets undertook the bag type breakup. This was found to be between We 13.7 - 14.07 for droplets between 2.22 and 3.90 mm (figure 2.3.4).

2.3.4.c Umbrella ($We \sim 20 - 70$)

This mode has been allotted a number of names in the literature, amongst them are umbrella, bag and stem, bag and stamen, and clavicle. At first the liquid disk forms under the action of the aerodynamic and surface tension forces, but rather than blowing through to form a hollow bag, the liquid then contracts into a stem and simultaneously develops a canopy. The development of this phenomenon is shown in



Figure 2.3.3 Breakup of water drop in the bag mode showing dark spots and concentric circles on the bag. Initial drop diameters from left to right, 603, 651 and 705 μm . Air velocity is 33.5 m s^{-1} and moves from left to right. (Hanson *et al*, 1963)

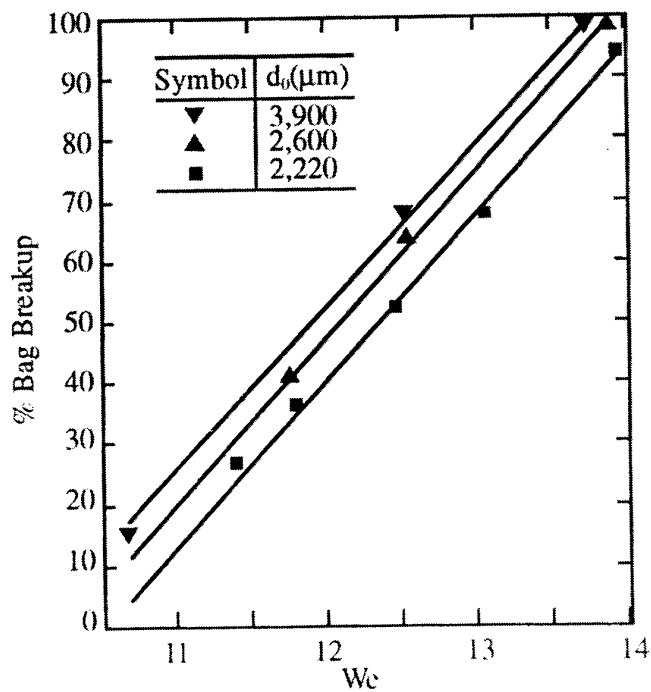


Figure 2.3.4 Percentage of bag type breakup vs Weber number. (Wierzba, 1990)

Hanson et al. (1963) and Simpkins (1971) (figure 2.3.5). A notable difference between the bag and umbrella response, is that the annular rim which supports the canopy forfeits mass to the stem in the latter of these cases.

Hanson et al. (1963) looked at more viscous silicone oils in addition to water and showed that the increase in viscosity caused the rim and stamen to breakup with the formation of more numerous and persistent ligaments (figure 2.3.5).

2.3.4.d Stripping ($We \sim 1000$)

($20 \leq We \leq 2 \times 10^4$ and $1 \leq WeRe^{-0.5} \leq 20$ according to Borisov et al., 1981)

The stripping type breakup of liquid drops was first observed by Lane et al. (1949) and reported in Lane (1951) and in Lane and Green (1956). Lane attempted to evaluate the degree of drop atomisation produced by different shock velocities, and proposed that the process of disintegration was either a layer of liquid being stripped off the drop by the air blast, or the production of unstable waves on the surface of the drop.

The first model for the action of wind in stripping the surface layer off a fluid was proposed by Taylor (1949), based on the formation of boundary layers in the gas and liquid. This analysis was applied to drops in high speed flow by Ranger (1968), and Ranger and Nicholls (1969). However Borisov et al (1970), and Reinecke and Waldman (1970), found that for drops of ~ 1 mm diameter boundary layer stripping could not account for destruction within the experimentally determined times. The second model for stripping presented by Taylor (1949) was for waves generated by the air flow over the drop having certain unstable wavelengths which increase rapidly, these result in a droplet being formed during disintegration that has a diameter equal to this wavelength. This proposed mechanism was shown by Lane (1951) to produce droplet diameters smaller than those measured .

Hinze (1955) emphasised the importance of the formation of surface waves on the windward surface of the drop due to its acceleration. Engel (1958) proposed several other possible causes of breakup such as vaporisation due to shock heating, sound wave resonance, surface waves, and turbulence. However one of her set of drop breakup photos showed up the surface waves of Hinze very well. The roll of these capillary waves was discussed by several authors. Engel (1958), Buzukov (1963) and Rojec (1963) all attributed the removal of microdrops to capillary surface wave erosion from the broken crests of capillary waves on the drop surface. Reinecke and Waldman (1970), and Harper et al (1972) meanwhile considered the unstable rapid growth of the surface waves lead to shattering, and Collins and Charwat (1971) suggested that the capillary waves grew in amplitude as they moved radially outward and resulted in intermittent disintegration. This last model fitted the data of Reinecke and Waldman (1970) well and was subsequently improved by Fishburn (1974) with a better estimate of the boundary thickness.

Recent improvement in experimental observation of the breakup of the drops by using double exposure holography, has revealed the internal structure of the 'fireball' (Yoshida and Takayama, 1990). This structure had previously been hidden because most of the early photos were just shadowgraphs. The actual observed stripping process has been broken down into four stages by Wierzba and Takayama (1988).

i) Following interaction of the shock with the drop, the shock wave induced flow field is established around the drop and disruption of the liquid drop surface is initiated. During this stage the drop remains spherical, except for a small lip formed on the leeward surface of the drop at the separation point (figure 2.3.6a).

ii) In this stage the drop deformation takes place with the leeward surface has started to be flattened between the separation points. Stripping is initiated at the separation point on the leeward surface and by boundary-layer separation on the windward surface (figure 2.3.6b and m).

iii) Continuous deformation of the drop and stripping of microdrops now takes place. The microdrops are entrained in the wake as the drop becomes plano-convex (figure 2.3.6c) and then crescent shaped (figure 2.3.6d). The drop surface is significantly corrugated and stripping of microdrops takes place over a substantial area of the windward and leeward surfaces. The stripping is very intense at the trailing edge of the drop, and the lateral deformation reaches a maximum, resulting in the remaining part of the drop becoming unstable and breaking up into comparatively large fragments (figure 2.3.6f, g and h).

iv) The final stage has a more chaotic process where stripping of microdrops takes place from fragments produced by the breakup of the remaining drop in what might be called a 'secondary stripping' process (figure 2.3.6f - k). At the end of this stage the last portion of the unstripped liquid phase loses its opaqueness on the hologram, and everything is converted to micromist (figure 2.3.6l).

2.3.4.e Catastrophic ($We \sim 50,000$)

$(2 \times 10^3 \leq We \leq 2 \times 10^5 \text{ and } 20 \leq WeRe^{-0.5} \leq 2 \times 10^2, \text{ Borisov et al., 1981})$

No distinct boundary exists between the catastrophic and stripping modes since both processes exist simultaneously. The catastrophic mode may cause the drop to shatter before all the material is removed by stripping if $45 We^{-1/4} < 3.5$ (Reinecke and Waldman, 1970). The dominant effect in the catastrophic mode is the rapid growth of surface waves on the windward face of the drop. Taylor (1950) pointed out that when the direction of acceleration of a fluid interface is from the less dense fluid to the more dense, waves on the interface will be unstable and grow exponentially. In the catastrophic mode these surface waves grow rapidly until their amplitude is comparable to the dimensions of the drop, at which point the drop is torn apart. Observations of drops broken in this way have been made by Reinecke and McKay (1969) and Reinecke and Waldman (1970).

2.3.5 Breakup in the Shock Layer of a High Speed Vehicle

There are five stages in the evaluation of drop breakup due to an approaching high speed vehicle. First the values of the air velocity components in the region between the shock-wave and the vehicle need to be evaluated. Then an experimental and theoretical study of drop deceleration and trajectory in this region needs to produce an estimate of the non-dimensional time to impact as a function of drop diameter. Thirdly, the drop breakup criteria are used to ascertain the appropriate non-dimensional breakup time as a function of drop diameter. Next these two times are compared in order to determine the fraction of drops entering the shock layer that will actually strike the vehicle surface as a function of drop diameter. Finally, for the drops impinging an evaluation of the drop deformation and mass loss due to aerodynamic breakup and vaporisation yields the effective drop size impacting the vehicle surface. This function can then be integrated over the rainstorm drop distribution function to find the full effect of the passage of the vehicle through rain.

2.3.5.a Air Flow Round a Moving Body

A large number of dedicated computer codes exist for calculating the air flow round a moving body, and in addition flow fields for some of the more common geometries can be found in standard aerodynamic textbooks or in tabulated form (e.g. M.I.T. 1947). Analysis of the passage through rain of a variety of different aerodynamic shapes has been attempted over the years. Engel (1958), Dodd (1960), Waldman and Reinecke (1971, 1972), Reinecke and Waldman (1975) and Adler (1989) have investigated spherical surfaces, Jenkins (1955), Reinecke and Waldman (1975) and Adler and Mihora (1989) different cone angles, Tribus and Guibert

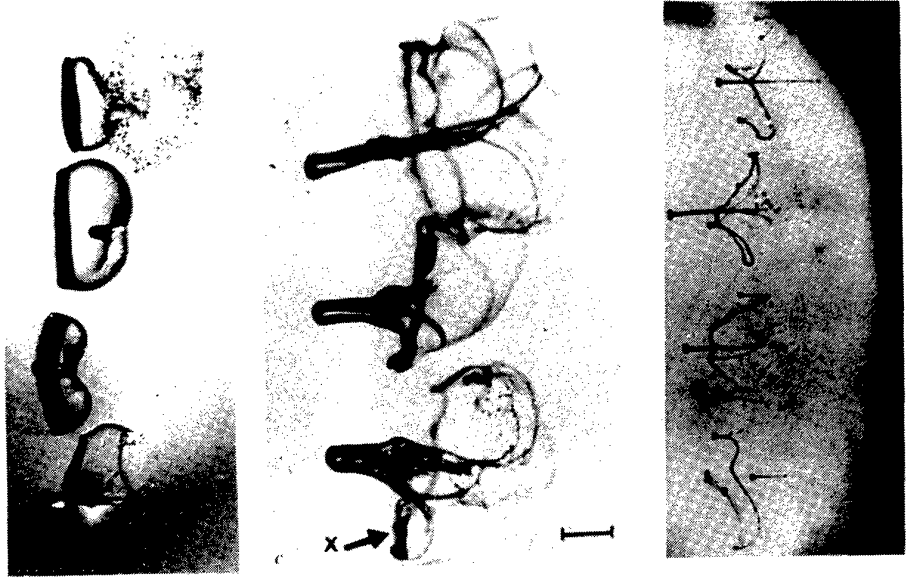


Figure 2.3.5 (Left) Breakup of water drops showing a reentrant portion during bag breakup. (Hanson et al, 1963) (Middle) Umbrella response. (Simpkins, 1971). (Right) Breakup with silicon oil showing an increase in viscosity causes the formation of more numerous and persistent ligaments. (Hanson et al, 1963)

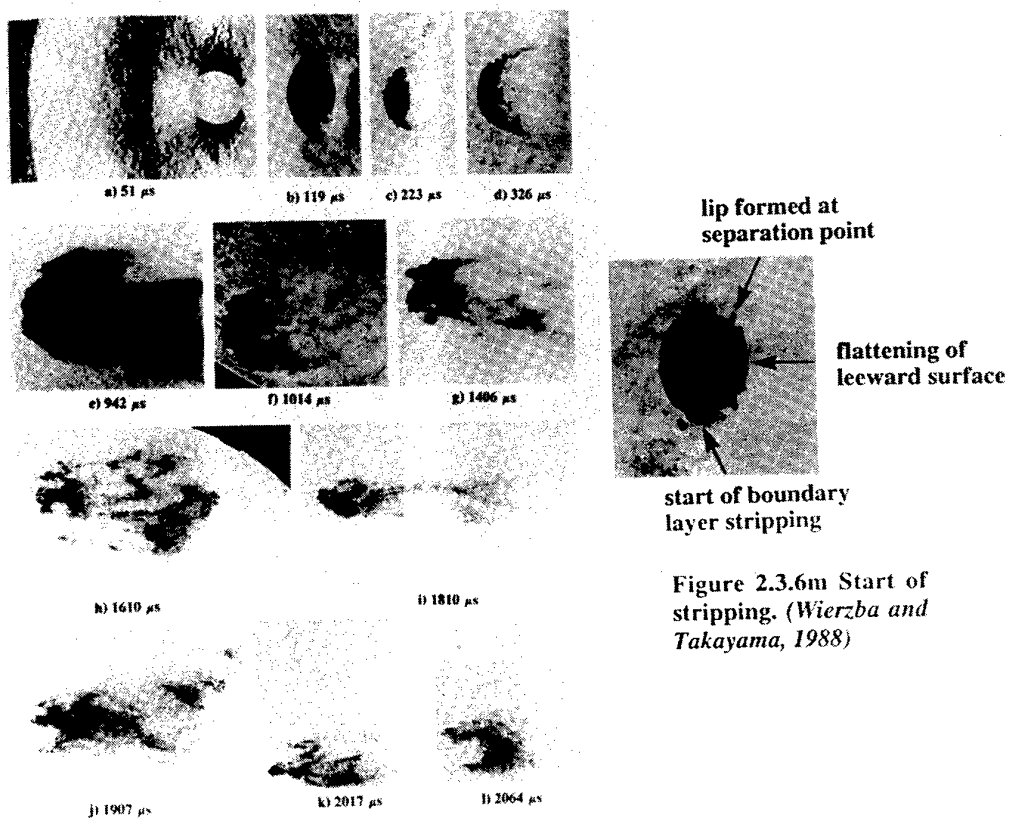


Figure 2.3.6 History of a water drop after its interaction with a shock wave, $M_s = 1.35$, $d_0 = 4,300 \mu\text{m}$, $We = 3,590$, $Re = 67,700$. (Wierzbna and Takayama, 1988)

(1952), Serafini (1954) and Forney (1990) have looked at wedges, and Adler and Mihora (1989) has looked at aircraft pods.

2.3.5.b Nondimensional-Parameters for Drop Behaviour

Many of the experimentally observed drop parameters after shock passage are expressed as non-dimensional numbers in the literature. Therefore:

- a) lateral dilatation of the drop, d , becomes, d / d_0 , where d_0 is initial drop diameter.
- b) drop mass, m , becomes, m / m_0 , where m_0 is initial drop mass.
- c) axial displacement, x , becomes, $X = x / d_0$,
- d) drop breakup time, t , becomes, $T = t \left(\frac{v}{d_0} \right) \sqrt{\left(\frac{\rho_A}{\rho_L} \right)}$ where v is the relative velocity of the air with respect to the drop, and ρ_A and ρ_L are gas and liquid density respectively.

2.3.5.c Drop Deceleration and Trajectory

Although attempts have been made to analyse the trajectory of a drop in a uniform flow field (Krausse, 1970 and Bernard and Saric, 1971), the coupling with the mass loss, the lateral deformations effect on the drag coefficient, and the changing dynamic pressure environment of the drop, prevent a simple result. Correlations with experimental data can however be made with little compromise in accuracy. These results indicate that the trajectory of an initially motionless drop following shock passage can be evaluated by:

$$X = AT^2 \quad (2.3.10)$$

where A can be used to relate the Bond number and the Weber number by:

$$Bo = \frac{A}{2} We \quad (2.3.11)$$

The value of A is dependent on the Weber number as seen in figure 2.3.7. Using the data of Reinecke and Waldman (1970), Reinecke and McKay (1969), Engel (1958), Nicholson (1967) and Hässler (1970) gives the following correlations for A :

$$\begin{aligned} A &= 0.252 \ln We & 12 \leq We \leq 300 \\ A &= 2.966 - 0.268 \ln We & 300 \leq We \leq 8000 \\ A &= 0.062 \ln We & 8000 \leq We \end{aligned} \quad (2.3.12)$$

Using this equation of motion together with the distance from the shock wave to the body found in section 2.3.5.a the time of flight of the drop can be evaluated.

Jenkins (1966) used this simple approach for a cone assuming that the drop continues in a straight line once past the shock, however a better solution was evaluated by Forney (1990), who's trajectory calculations took into account the deflection of the drop away from the cone body. It should be noted that this deflection also has the effect of reducing the final contact angle the drop makes with the cone and thus reducing the extent of the damage.

2.3.5.d Drop Breakup Time

The drop breakup time for the catastrophic mode was shown experimentally to be dependent on the Weber number such that $T \sim We^{-1/4}$ (Reinecke and Waldman, 1970) This was in agreement with the theory for unstable waves, growing exponentially and

tearing the drop apart when their amplitude reaches the order of the drop diameter. Doubt as to whether this was in fact the case was raised by Bernard and Saric (1971) and a full discussion of this dilemma can be read in Reinecke and Waldman (1975). For the purpose of evaluating the lifetime of the drop Reinecke and Waldman (1975) plotted all the available data on We number versus breakup time and found the best fit curves assuming the relationship had a $We^{-1/4}$ dependence. This data is seen in figure 2.3.8, and the form of the correlation applied to the data is:

$$T\sqrt{Q_m} = f(We) \quad (2.3.13)$$

The factor Q_m is the maximum value of the ratio of the dynamic pressure of the air at the drop surface to the dynamic pressure of the air flow ahead of the drop. This value is dependent on the Mach number as seen in figure 2.3.9.

Reinecke and Waldman (1975) chose to fit the data in figure 2.3.8 with three curves rather than one as Engel's and Nicholson's data both corroborated that the region between $We = 1,000$ and $We = 5,000$ actually shows an abrupt rise in the breakup time with increasing Weber number. They dubbed this region the "Devil's angle", and the curves fitted were:

$$\begin{aligned} TQ_m^{\dagger} &= 23(We - 8)^{-\dagger} & We \leq 1,700 \\ TQ_m^{\dagger} &= 0.013(We - 8)^{\dagger} & 1,700 < We \leq 2,700 \\ TQ_m^{\dagger} &= 35(We - 8)^{-\dagger} & We > 2,700 \end{aligned} \quad (2.3.14)$$

As the Weber number reaches its critical value (approximately 8) the value of the time to breakup grows without limit. Using these curves the breakup time for the drop can be evaluated and compared to the flight time found in section 2.3.5.c.

2.3.5.e Drop Deformation and Mass Loss

Several theoretical evaluations of the drop deformation have been made, most notably by Burgers (1958), Ho (1969) and Reinecke and Waldman (1970). The variation of the lateral deformation as a function of dimensionless time has also been determined experimentally by Engel (1958), Ranger and Nicholls (1969), Krausse and Leadon (1971), Aeschliman (1971), Reinecke and Waldman (1975), Wierzba and Takayama (1988) and Yoshida and Takayama (1990). The data from some of these experiments can be seen in figure 2.3.10. The most accurate values are those by Wierzba and Takayama as these are made with holographic interferometry and not with shadowgraphs so the detail is not obscured by a mist of stripped drops. The difference between the values that can be obtained by these two different techniques can be readily seen in figure 2.3.11a and 2.3.11b from Yoshida and Takayama (1990).

A set of empirical relations were taken from the data in figure 2.3.10 by Adler and Mihora (1989) to determine the lateral deformation. These gave:

$$\begin{aligned} d / d_0 &= 1.0 + 1.8 T & \text{for } T < 1.25 \\ d / d_0 &= 2.25 (1 + \cos(\pi T / T_s)) & \text{for } T \geq 1.25 \end{aligned} \quad (2.3.15)$$

A similar expression was given for the mass loss with time by Reinecke and Waldman (1970):

$$m / m_0 = 0.5 (1 + \cos(\pi T / T_s)) \quad (2.3.16)$$

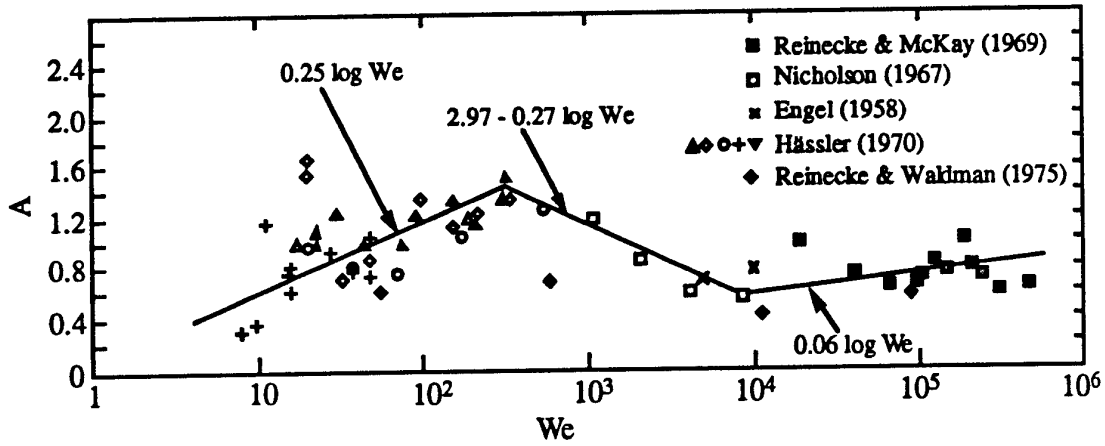


Figure 2.3.7 Drop trajectory data: Variation of A with Weber number (Reinecke and Waldman, 1975)

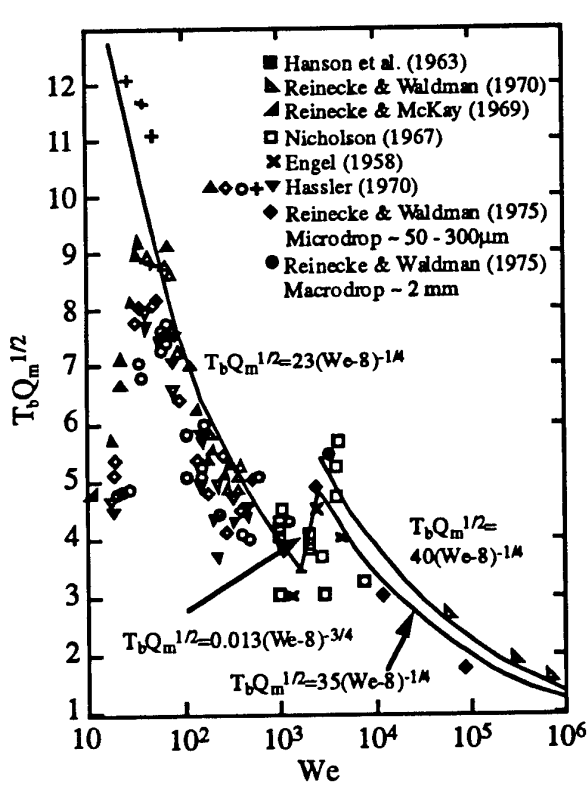


Figure 2.3.8 Drop breakup time. (Reinecke and Waldman, 1975)

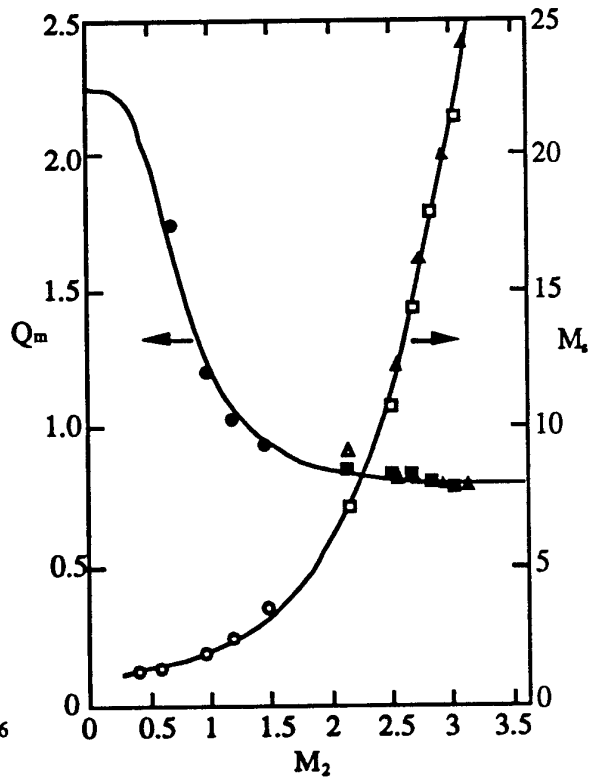


Figure 2.3.9 Max. dynamic pressure factor Q_m , and Shock Mach number M_1 , versus Flow Mach number M_2 , behind the shock. (Reinecke and Waldman, 1975)

2.3.5.f Heating Effects

Reinecke and Waldman (1975) evaluated the aerodynamic heating effect of the drop, but considered it unimportant because it was only a surface effect, and the surface mass stripping would probably keep the drop sufficiently cool for the heating not to cause vaporisation.

2.3.5.g A Sample Problem

Assessments of the raindrop size surviving passage through the shock wave of a moving body, and the degree of distortion created were carried out using a computer code called DROPS by Adler and Mihora (1989). He considered three different cases, hemispherical and conical missile domes, and aircraft pods. Figure 2.3.12 summarise his results for a conical missile with a half cone angle of 12° for velocities of 1,220, 1,830 and 2,440 m s^{-1} and an altitude of 6 km. The minimum water drop diameters striking the aft most location are 371, 567 and 537 μm respectively. Also shown are the non-dimensional times $T = 0.5$ and 1.0 which bound the most severe impact conditions because of the large increase in lateral areas and the minimal mass loss.

2.3.6 Protection for a Radome by Drop Breakup

There are several ways of extending the protection afforded to a radome from liquid impact, such as placing it at an angle to the flight trajectory or concealing it in the wings. The use of shock waves to break up the drops has also been attempted in two main ways. The first is by placing a spike on the nose tip (Tatnall, 1967, Nicholson, 1967). This spike generates a secondary shock wave from its tip, however because the air speed behind this is comparable with that in front the effect on drop breakup is small. The success of the technique is instead reliant on the establishment of a region of separated flow, that is a portion of 'dead-air' carried along by the moving object. Drops entering the dead-air have their erosive effects reduced both because of drop breakup, and due to deceleration and deflection.

The second technique of protection is known as RECAP (Rain Erosion Captive Air Protection) and is described in Dynner and Hill (1970) and Adams and Smith (1970). The device basically consists of a conical shell cut off to provide an opening at its front that provides a restricted field of view. The air is trapped inside the cone and moves with the missile, the length of the trapped air thus determines the size of drop that can be shattered. The original RECAP design had to be jettisoned before the missile was used, however King (1974) attempted to develop one that could be kept permanently in place.

2.3.7 Drop Deformation In Subsonic Flight

In this case the aerodynamic forces on the raindrops are applied gradually. It is therefore necessary to calculate the cumulative effects of a variable dynamic pressure on the drop deformation as shown in Dynner and Hill (1970).

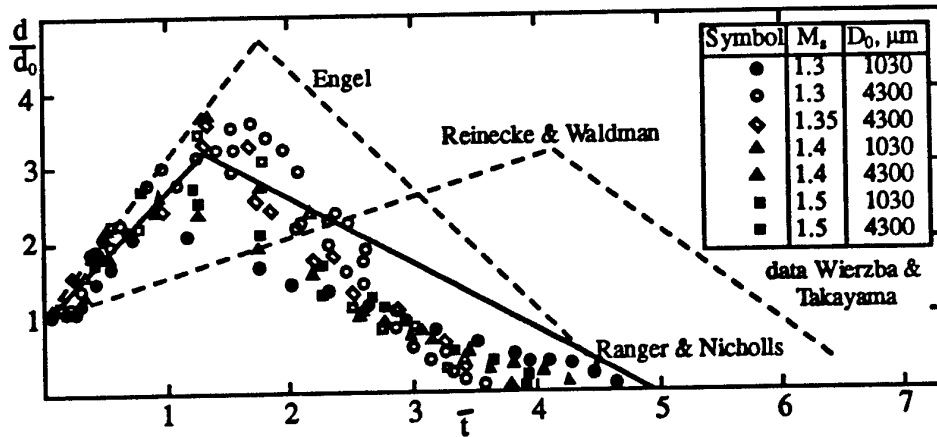


Figure 2.3.10 Lateral drop distortion as a function of non-dimensional time. (Wierzba and Takayama, 1988)

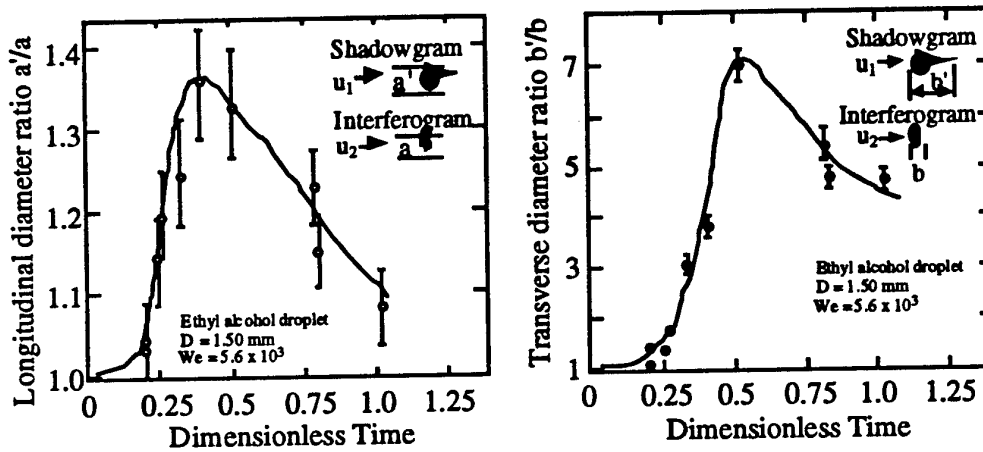


Figure 2.3.11a. (above left) time variation of longitudinal diameter ratio b . (above right) time variation of transverse diameter ratio. (Yoshida and Takayama, 1990)

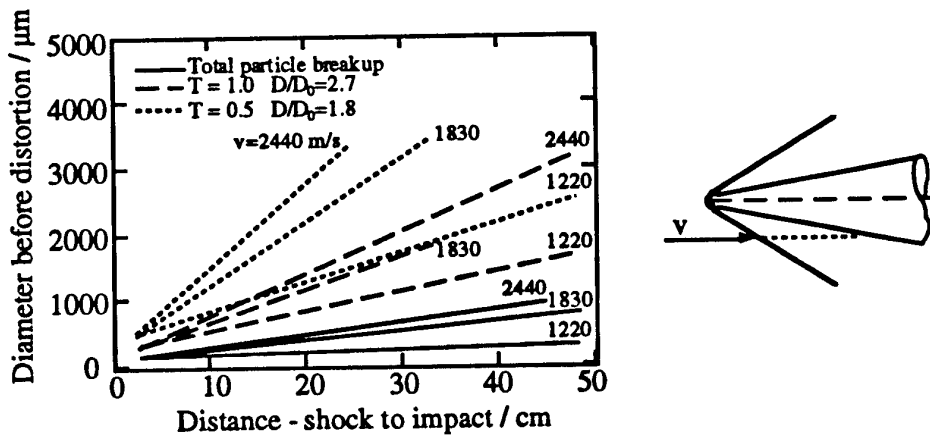


Figure 2.3.12 Distortion of raindrops impacting aft region of a supersonic radome for various velocities at an altitude of 6 km. (Adler and Mihora, 1989)

2.4 SUMMARY

In order to evaluate the chances of damage occurring on the radome of an aircraft or missile due to impact with raindrops, the shape and number of drops likely to be encountered needs to be estimated. In order to do this the first problem is to define the drop size distribution of interest, since this will vary depending on the season, intensity, location and type of cloud. Next the deformation due to surface tension, internal hydrostatic pressure, aerodynamic pressure, internal circulation and electric stress needs to be estimated for each different drop diameter. This can already be done fairly well from existing models, however the raindrops shapes' are not static and collision and coalescence causes the drops to oscillate. Already the problem is becoming a difficult one to model, but add to this the problem of further drop distortion and drop deflection due to the approach of the aircraft or missile; the angle of impact of the drop on the dome or window; and heating and stress effects on the window due to its flight, and the necessity for experimental simulation techniques is clear. Because of the extent of the drop deformations and distortions described in this chapter, the requirement for spherical raindrops in these simulations is only preferable to enable comparisons with theory. From the point of view of comparing different materials ability to withstand impacts with raindrops during flight, the main requirement is that the impacts simulated are reproducible so that a ranking of materials is possible.

For the simpler cases of spherical drops entering shocks ahead of moving vehicles computer modelling can provide some interesting results (Adler and Mihora, 1989, 1992), and the drop diameters likely to survive the passage through the shock can be evaluated. The largest effective drop diameter likely to be encountered has an important significance for the radome since this determines whether it is impacted above or below its threshold velocity for damage. If the threshold velocity is exceeded then smaller drops also have an importance and crack propagation and impact site overlap has to be investigated. Field and Davies (1988) estimated the exposure time needed to obtain overlap by finding the time required to reach a tessellation on the surface, however this study only investigated drop overlaps between drops of the same size. In actual fact the more likely situation is for an impact site from a large drop to be impacted by a smaller one, and here once again computer simulation can be of benefit.

Although this chapter has not presented a way of evaluating the exact drop profiles impacted by a missile in flight, it has described the many factors affecting the profiles, and allows an assessment of different simulation techniques to be made in chapter 3 with a better insight into the environment that is being simulated.

REFERENCES

- Achenbach E. "Experiments on the flow past spheres at very high Reynolds numbers", J. Fluid Mech., Vol. 54 pp.565-575 (1972)
- Adam N.K. "The physics and chemistry of surfaces", London, Oxford Press, 436 pp. (1949)
- Adams R.H. and Smith M.R. "Design and development of RECAP, an aerodynamic device for rain erosion protection of optical domes on missiles", Proc. of the Third Int. Conf. on Rain Erosion and Ass. Phen., pp.935-968, (1970)
- Adler W.F. and Mihora D.J. "Aerodynamic effects on raindrop impact parameters", Proc. of the Fifth European Electromagnetic Windows Conf., Sept. (1989)
- Adler W.F. and Mihora D.J. "Infrared-transmitting window survivability in hydrometeor environments", SPIE Vol.1760, Window and Dome Technologies and Materials III, pp.291-302, (1992)
- Aeschliman D.P. "An experimental study of the response of water droplets to flows behind plane shock waves", Sandia Labs, Albuquerque, NM, Research Rept. SC-RR-71 0540, (1971)
- Aitken J. Collected Scientific Papers, Cambridge: Cambridge University Press (1923)
- Ames Research Staff NACA Report 1135 (1953)
- Arbel N. and Levin Z. Pure Appl. Geophys., Vol.115 pp.864-893, 895-914 (1977)
- Atlas D., Kerker M. and Hitschfeld W. "Scattering and attenuation by non-spherical atmospheric particles", J. Atmos. Terr. Phys., Vol.3 pp.108-119 (1953)
- Ausman E.L. and Brook M. "The distortion and disintegration of water drops in strong electric fields", J. Geophys. Res., Vol.72 pp.6131-6135 (1967)
- Austin P.M. and Geotis S.G. "Raindrop sizes and related parameters for GATE", J. Appl. Meteorol., Vol.18 pp.569-575 (1979)
- Bartlett J.T. "The growth of cloud droplets by coalescence. Computations of droplet growth for various initial distributions assuming Hocking's values of collection efficiency", Quart. J. Roy. Meteorol. Soc., Vol.92 pp.93-104 (1966)
- Bashforth F. and Adams J.C. "An attempt to test the theories of capillary action by comparing the theoretical and measured forms of drops of fluid", Cambridge University Press, London, 94pp. (1883).
- Battan L.J. "Fundamentals of Meteorology", Prentice-Hall, Inc., Englewood Cliffs New Jersey, 07632, ISBN 0-13-341131-1 (1979)
- Beard K.V. J. Atmos. Sci., Vol.33 pp.851-864 (1976)
- Beard K.V. "Raindrop oscillation", Preprints Conf. on Cloud Physics, Chicago, Amer. Meteor. Soc. pp.244-246 (1982)
- Beard K.V., Johnson D.B. and Jameson A.R. "Collisional forcing of raindrop oscillations", J. Atmos. Sci., Vol.40 pp.455-462 Feb. (1983)
- Beard K.V. and Jameson A.R. "Raindrop canting", J. Atmos. Sci., Vol.40 pp.448-454 Feb. (1983)
- Beard K.V. "Raindrop oscillations: evaluation of a potential flow model with gravity", J. Atmos. Sci., Vol.41 pp.1765-1774 (1984)
- Beard K.V. and Chuang C. "A new model for the equilibrium shape of raindrops", J. Atmos. Sci., Vol.44 No.11 pp.1509-1524 (1987)
- Beard K.V., Feng J.Q. and Chuang C. "A simple perturbation model for the electrostatic shape of falling drops", Vol.46 No.15 pp.2404-2418 (1989)
- Beard K.V., Ochs H.T. and Kubesh R.J. "Natural oscillations of small raindrops", Nature, Vol.342 pp.408-410 Nov. (1989)

- Beard K.V. and Kubesh R.J.** "Laboratory measurements of small raindrop distortion. Part 2: Oscillation Frequencies and Modes", J. Atmos. Sci., Vol.48 No.20 pp.2245-2264 October (1991)
- Bernard R.S. and Saric W.S.** "The Rayleigh-Taylor instability applied to liquid drops", Sandia Corp., SC-TM-70-725, (1971)
- Best A.C.** "The shape of raindrops and mode of disintegration of large drops", Air Ministry, Great Britain, Meteor. Res. Comm., M.R.P.330 (1947)
- Best A.C.** "The size distribution of raindrops", Quart. J. Roy. Meteor. Soc., Vol. 76 pp.16-36 (1950)
- Blanchard D.C.** "Observations on the behaviour of water drops at terminal velocity in air", Occas. Rep. 7, Gen. Elec. Res. Lab., Schenectady, New York (1948)
- Blanchard D.C.** "Experiments with water drops and the interaction between them at terminal velocity in air", General Electric Research Laboratory, Schenectady, New York (Project Cirrus, Occasional Report No 17), 29pp. (1949)
- Blanchard D.C.** "The behaviour of water drops at terminal velocity in air", Trans. Amer. Geophys. Union., Vol.31 pp.836-842 (1950)
- Borisov A.A., Gel'fand B.E., Gubin S.A., Kogarko S.M. and Podgrebenkov A.L.**, "The reaction zone of two-phase detonations", Astronautica Acta, Vol.15, pp.411-417 (1970)
- Borisov A.A., Gel'fand B.E., Natanzon M.S. and Kossov O.M.** "Droplet breakup regimes and criteria for their existence", J. of Eng. Phys., Vol.40, No.1, pp.64-70 (1981)
- Bowen E.G.** "The formation of rain by coalescence", Australian J. Res., A3, pp.193-213 (1950)
- Brazier-Smith P.R.** "The stability of a water drop oscillating with finite amplitude in an electric field", J. Fluid Mech., Vol.50 pp.417-430 (1971)
- Brazier-Smith P.R.** "Stability and shape of isolated and pairs of water drops in an electric field", Phys. of Fluids, Vol.14 pp 1-6 (1971)
- Brook M. and Latham D.J.** "Fluctuating radar echo: Modulation by vibrating drops", J. Geophys. Res., Vol.73 pp.7137-7144 (1968)
- Brown P.S.** "Parameterization of drop-spectrum evolution due to coalescence and breakup", J. Atmos. Sci., Vol.44 pp.242-249 (1987)
- Brown P.S.** "Reversals in evolving raindrop size distributions due to the effects of coalescence and breakup", J. Atmos. Sci., Vol.47 pp.746-754 (1990)
- Brussard G.** "Rain-induced cross polarization and raindrop canting", Electron. Lett., Vol.10 pp.411-412 (1976)
- Burgers J.M.** Ned. Akad. v. Wetensch. Afd. Natuurkunde, LII, No.8 en 9 (1943)
- Burgers J.M.** Private communication referenced in Engel (1958)
- Buzukov A.A.** "Shock wave shattering of liquid droplets and jets", Zhurnal Prikladnoi Mekhaniki i Tiekhnicheskio Fiziki, No.2, pp.154-158 (1963)
- Cateneo R. and Stout G.E.** "Raindrop-size distributions in humid continental climates, and associated rainfall rate-radar reflectivity relationships", J. App. Meteorol., Vol.7 pp.901-907 (1968)
- Chandrasekar V., Cooper W.A. and Bringi V.N.** "Axis ratios and oscillations of raindrops", J. Atmos. Sci., Vol.45 No.8 pp.1323-1333 April (1988)
- Chu T.S.** "Rain-induced cross-polarisation at centimeter and millimeter wavelengths", Bell Sys. Tech. J., Vol.53 pp.1557-1559 (1974)
- Chuang C.** "A numerical model of the electrostatic-aerodynamic shape of raindrops", PhD thesis, University of Illinois, Urbana-Champaign, 121pp. (1989)

- Chuang C. and Beard K.V. "A numerical model for the equilibrium shape of electrified raindrops", *J. Atmos. Sci.*, Vol.47 No.11 pp.1374-1389 (1990)
- Clark T.L. "Numerical modelling of the dynamics and microphysics of warm cumulus convection", *J. Atmos. Sci.*, Vol.30 pp.857-878 (1973)
- Clift R., Grace J.R. and Weber M.E. "Bubbles, Drops and Particles", Academic Press, New York, 380 pp (1978)
- Collins R. and Charwat A.F. "The deformation and mass loss of liquid drops in a high-speed flow of gas", *Israel Journal of Technology*, Vol.19, No.5, pp.453-465 (1971)
- Dodd K.N. "On the disintegration of water drops in an air stream", *J. Fluid Mech.*, Vol.9, pp.175-182 (1960)
- Doviak R.J. and Zrnic D.S. "Doppler radar and weather observations", Academic Press Inc., ISBN 0-12-221420-X (1984)
- Drake R.L. "A general mathematical survey of the coagulation equation", *Topics in Current Aerosol Research (Part 2)*, ed. G.M. Hidy and J.R. Brock, Pergamon pp.201-384 (1972)
- Dyner H.B. and Hill J.A.F. "Drop break-up in accelerating and decelerating streams", *Proc. of the Third Int. Conf. on Rain Erosion and Ass. Phen.*, (ed. A.A. Fyall and R.B. King), pp.669-690, (1970)
- Edgerton H.E. and Killian J.R. "Flash! Seeing the unseen by ultra-high speed photography", Boston: Hale, Cushman and Flint, 203 pp. (1939)
- Engel O.G. "Fragmentation of waterdrops in the zone behind an air shock", *Int. Res. of the Nat. Bureau of Standards*, Vol.60, No.3 March (1958)
- Fage A. "Experiments on a sphere at critical Reynolds Numbers", *Aero. Res. Comm.*, England, Rep. and Memo. No. 1766, 20pp. (1937)
- Feng J.Q. and Beard K.V. "A perturbation model of raindrop oscillation characteristics with aerodynamic effects", *J. Atmos. Sci.*, Vol.48 No.16 pp.1856-1868 August (1991)
- Field J.E. and Davies P.N.H. "Statistics of raindrop impact", Report, Jan. (1988)
- Fishburn B.D. "Boundary layer stripping of liquid drops fragmented by Taylor instability", *Acta Astronautica*, Vol.1, pp.1267-1284, (1974)
- Flachsbart O. "Neuere Untersuchungen uber den Luftwiderstand von Kugeln", *Phys. Z.*, Vol.28 pp.461-469 (1927)
- Flowers W.D. "The terminal velocity of drops", *Proc. phys. Soc. London*, Vol.40 pp.167-176 (1928)
- Foote G.B. "On the internal circulation and shape of large raindrops", *J. Atmos. Sci.*, Vol.26 pp.179-180 Jan. (1969)
- Foote G.B. and de Toit P.S. *J. Appl. Meteor.* Vol.8 pp.249-253 (1969)
- Foote G.B. "A numerical method for studying liquid drop behaviour: Simple oscillation", *J. Comput. Phys.*, Vol.11 pp.507-530 (1973)
- Forney L.J. "Droplet impaction on a supersonic wedge: Consideration of similitude", *AIAA Jnl.*, Vol.28, No.4, pp.650-654, (1990)
- Garner F.H. and Lane J.J. "Mass transfer to drops of liquid suspended in a gas stream", *Trans. Instn. Chem. Eng.*, Vol.37 pp.167-172 (1959)
- Gillespie D.T. "The stochastic coalescence model for cloud droplet growth", *J. Atmos. Sci.* Vol.29 pp.1496-1510 (1972)
- Goddard J.W.F. and Cherry S.M. "The ability of dual-polarization radar (copolar linear) to predict rainfall rate and microwave attenuation", *Radio Sci.*, Vol.19 pp.201-208 (1984)
- Goodall F. "Propagation through distorted water drops at 11 GHz", PhD dissertation, Post Graduate School of Electronic and Electrical Engineering, University of Bradford, U.K. 205pp. (1976)

- Gordon G.D.** "Mechanism and speed of breakup of drops", J. of Applied Physics, Vol.30, No.11, pp.1759-1761 Nov.(1959)
- Green A.W.** "An approximation for the shapes of large raindrops", J. Appl. Meteor., Vol.14 pp.1578-1583 (1975)
- Gunn R.** "Mechanical resonance in freely falling drops", J. Geophys. Res., Vol.54 pp.383-385 (1949)
- Gunn R and Kinzer G.D.** J. Meteor. Vol.6 pp.243-248 (1949)
- Hall M.P.M., Cherry S.M., Goddard J.W.F. and Kennedy G.R.** "Rain drop sizes and rainfall rate measured by dual-polarization radar", Nature, Vol.285 pp.195-198 May (1980)
- Hanson A.R., Domich E.G. and Adams H.S.** "Shock tube investigation of the breakup of drops by air blasts", The Physics of Fluids, Vol.6, No.8, Aug., pp.1070-1080, (1963)
- Harper E.Y., Grube G.W. and Simpkins P.G.** "On the transient response of a droplet to a suddenly applied pressure distribution", 6th U.S. Congress of Applied Mechanics, Cambridge, (1970)
- Harper E.Y., Grube G.W. and Chang I.Deer** "On the breakup of accelerating liquid drops", J. Fluid Mech., Vol.52, No.3 pp.565-591 (1972)
- Hässler G.** "Break-up of large water drops under the influence of aerodynamic forces in a steady stream of steam at subsonic velocities", Proc. of the Third Int. Conf. on Rain Erosion and Ass. Phen., pp.707-727, (1970)
- Hinze J.O.** "Forced deformations of viscous liquid globules", Appl. Sci. Res. A1 pp. 263-272 (1948)
- Hinze J.O.** "Critical speeds and sizes of liquid globules", Appl. Sci. Res., Vol A1, pp.273-288 (1949)
- Hinze J.O.** "Fundamentals of the hydrodynamic mechanism of splitting in dispersion process", A.I.Ch.E. Journal, Vol.1, No.3, pp.289-295 (1955)
- Ho P.Y.** "Dynamics of bag-type breakup of droplets in various flow fields", PhD Thesis, Purdue University (Jan. 1969)
- Ho P.Y. and Høglund R.F.** "Dynamics of bag-type breakup of droplets in various flow fields", AIAA paper 69-669, San Fransisco, (1969)
- Hochschwender E.** PhD Heidelberg, Germany (1919)
- Houghton H.G.** "Physical Meteorology", MIT Press, Cambridge, Massachusetts, ISBN 0-262-08146-6 (1985)
- Imai I.** "On the velocity of falling raindrops", Geophys. Mag., Tokyo, Vol.21 pp.244-249 (1950)
- Jenkins D.C. and Booker J.D.** "The time required for high speed airstreams to disintegrate waterdrops", Tech. Notes Royal Aircraft Establishment, (Mech. Engng), no. 401, (1964)
- Jenkins D.C.** "Disintegration of raindrops by shock waves ahead of conical bodies", Phil. Trans. of the Roy. Soc. of Lond., Series A No.1110 Vol.260 pp153-160 July (1966)
- Jones D.M.A.** "The shape of raindrops", J. Meteorol., Vol.16 pp.504-510 October (1959)
- Junge Chr. and McLaren E. J.** Atmos. Sci Vol 28 pp.382-390 (1971)
- Kauffman C.W. and Nicholls J.A.** "Shock wave ignition of liquid fuel drops", AIAA Journal, Vol.9, No.5, pp.880-885 May (1971)
- King R.B.** "Protection of missile domes from rain erosion damage by means of aerodynamic break-up of drops", Proc. of the Fourth Int. Conf. on Rain Erosion and Ass. Phen., (ed. A.A. Fyall and R.B. King), pp.63-95, (1974)
- Kinzer** (unpublished)
- Koehler H.** Meddel. Meteor. - Hydrografiske Anstalt, Stockholm, 3, No.8 (1926)

- Koenig L.R. "Drop freezing through drop breakup", J. Atmos. Sci., Vol.22 pp.448-451 July (1965)
- Komabayasi M., Gonda T. and Isono K. "Lifetime of water drops before breaking and size distribution of fragment drops", J. Meteor. Soc. Japan, Series 2, Vol. 42 pp.330-340 (1964)
- Kovetz A. and Olund B. "The effect of coalescence and condensation on rain formation in a cloud of finite vertical extent", J. Atmos. Sci., Vol.26 pp.1060-1065 (1969)
- Krausse W.E. "Water drop deformation and fragmentation due to shock wave impact", PhD Thesis, University of Florida, (1970)
- Krausse W.E. and Leadon B.M. "Deformation fragmentation of water drops due to shock wave impact", AIAA Paper 71-392, (1971)
- Kumai M. and Itagaki K. "Shape and fall velocity of raindrops", J. Meteor. Soc. Jap., Ser. 2, Vol.32 pp.11-18 (1954)
- Lamb H. "Hydrodynamics", 6th ed., New York, Dover, 738pp (1932)
- Landau L.D. and Lifshitz E.M. "Fluid Mechanics", (2nd ed.), Vol.6 of a Course of Theoretical Physics, Pergamon Press, (1987)
- Lane W.R. and Edwards J. Unpublished Ministry of Supply Report (1948)
- Lane W.R., Prewett W.C. and Edwards J. Unpublished Ministry of Supply Report (1949)
- Lane W.R. "Shatter of drops in streams of air", Industrial and Engineering Chemistry, Vol.43, No.6, pp.1312-1317 June (1951)
- Lane W.R. and Green H.L. "The mechanics of drops and bubbles", from Surveys in Mechanics (ed. G.K. Batchelor and R.M. Davies), Cambridge University Press pp.162-215 (1956)
- Langmuir I. "The production of rain by chain reaction in cumulus clouds at temperatures above freezing", J. Meteorol., Vol.5 pp.175-192 (1948)
- Laws J.O. "Measurement of the fall-velocities of water drops and rain drops", Trans. Amer. Geophys. Union, Vol.22 pp.709-721 (1941)
- Laws J.O. and Parsons D.A. "The relation of raindrop size to intensity", Trans. Amer. Geophys. Union, Vol.24 part II pp.452-460 (1943)
- LeClair B.P., Hamielec A.E. and Pruppacher H.R. "A numerical study of the drag on a sphere at low and intermediate Reynolds numbers", J. Atmos. Sci., Vol. 27 pp.308-315 (1970)
- LeClair B.P., Hamielec A.E., Pruppacher H.R. and Hall W.D. "A theoretical and experimental study of the internal circulation in water drops falling at terminal velocity in air", J. Atmos. Sci., Vol.29 pp.728-740 (1972)
- Lenard P. "Über Regen", Meteor. Z., Vol.21 pp.248-262 (1904)
- Levin Z. and Machnes B. "Experimental evaluation of the coalescence efficiencies of colliding drops", Pure Appl. Geophys., Vol.115 pp.845-867 (1977)
- Liang P.Y., Eastes T.W. and Gharakhari A. "Computer simulations of drop deformation and drop breakup", AIAA-88-3142, Paper A88-48041, AIAA/ASME/SAE/ASEE 24th Joint Propulsion Conference, Boston, Massachusetts, July 11 - 13, (1988)
- List R.J. "Smithsonian Meteorological Tables", 6th ed.(1958)
- List R. Trans. Roy. Soc. Canada, Series 4, Vol. 15 pp.333-347 (1977)
- List R., Donaldson N.R. and Stewart R.E. "Temporal evolution of drop spectra to collisional equilibrium in steady and pulsating rain", J. Atmos. Sci., Vol.44 pp.362-372 (1987)
- Long A.B. "Validity of the finite-difference droplet collection equation", J. Atmos. Sci., Vol.28 pp.210-218 (1971)

- Low T.B. and List R.** "Collision, coalescence and breakup of raindrops. Part I: Experimentally established coalescence efficiencies and fragment size distributions in breakup", *J. Atmos. Sci.*, Vol.39 pp.1591-1604, July (1982)
- M.I.T.** "Tables of supersonic flow round cones", M.I.T. Tech. Report no. 1, (1947)
- Magarvey R.H. and Taylor B.W.** "Free fall breakup of large drops", *J. Applied Phys.*, Vol.27, No.10, pp.1129-1135 Oct.(1956)
- Magono C.** "On the shape of water drops falling in stagnant air", *J. Meteorol.* Vol.11 pp.77-79 Feb.(1954)
- Maher B.O., Murphy P.J. and Sexton M.C.** "A theoretical model of the effect of wind gusting on rain-induced cross polarisation", *Ann. Telecommun.*, Vol.32 pp.404-408 (1977)
- Marshall J.S. and Palmer W.McK.** "The distribution of raindrops with size", *J. of Meteorology*, Vol.5 pp.165-166 August (1948)
- Mathews J.B.** "Mass loss and distortion of freely falling water drops in an electric field", *J. Geophys. Res.*, Vol.72 pp.3007 (1967)
- Maxworthy T.** "Experiments on the flow around a sphere at high Reynolds numbers", *J. Appl. Mech.*, *Trans A.S.M.E.*, Vol.36 pp.598-607 (1969)
- McCormick G.C. and Hendry A.** "Polarization properties of transmission through precipitation over a communication link", *J. Rech. Atmos.*, Vol.8 pp.175-187 (1974)
- McDonald J.E.** "The shape and aerodynamics of large raindrops", *J. of Meteorol.* Vol. 11 pp.478-494 (1954)
- McTaggart-Cowan J.D. and List R.** "Collision and breakup of water drops at terminal velocity", *J. Atmos. Sci.*, Vol.32 pp.1401-1411 (1975)
- Merrington A.C. and Richardson E.G.** "The breakup of liquid jets", *Proc. Phys. Soc.*, Vol. 59, pp.1, (1947)
- Möller W.** "Experimentelle Untersuchungen zur Hydrodynamik der Kugel", *Phys. Z.*, Vol.39 pp.57-80 (1938)
- Musgrove C. and Brook M.** "Microwave echo fluctuations produced by vibrating water drops", *J. Atmos. Sci.*, Vol.32 pp.2001-2007 October (1975)
- Naterajan R. and Brown M.** "Third-order resonance effects and the nonlinear stability of drop oscillations", *J. Fluid Mech.*, Vol.183 pp.95-121 (1987)
- Nelson A.R. and Gokhale N.R.** "Oscillation frequencies of freely suspended water drops", *J. Geophys. Res.*, Vol.77 No.15 pp.2724-2727 May (1972)
- Nicholson J.E.** "Drop breakup by airstream impact", *Proc. of the Second Meersburg Conf. on Rain Erosion and Allied Phen.*, (ed. A.A. Fyall and R.B. King), pp.263-298, (1967)
- Ochs H.T. and Czys R.R.** "Physics in action - Charging up raindrops", *Phys. Bull.* Vol. 38 pp.373-374 (1987)
- Ochs H.T. and Czys R.R.** "When charged raindrops collide", *Endeavour*, New Series, Vol. 12 No.4 (1988)
- Oguchi T.** "Scattering from hydrometeors: A survey", *Radio Sci.*, Vol.16 pp.691-730 (1981)
- Ogura Y. and Takahashi T.** "The development of warm rain in a cumulus model", *J. Atmos. Sci.*, Vol.30 pp.262-277 (1973)
- Olsen R.L.** "Cross polarization during precipitation on terrestrial links: A review", *Radio Sci.*, Vol.16 pp.761-770 (1981)
- Pruppacher H.R. and Neiburger M.** "The UCLA Cloud tunnel", *Proc. Int. Conf on Cloud Physics*, Toronto, pp.389-392 (1968)
- Pruppacher H.R. and Beard K.V.** "A wind tunnel investigation of the internal circulation and shape of water drops falling at terminal velocity in air", *Quart. J. Roy. Met. Soc.* Vol.96 pp.247-256 (1970)

- Pruppacher H.R. and Pitter R.L.** "A semi-empirical determination of the shape of cloud and rain drops", *J. Atmos. Sci.*, Vol.28 pp.86-94 (1971)
- Ragland K.W., Dabora E.K. and Nicholls J.A.** "Observed structure of spray detonations", *The Physics of Fluids*, Vol.11, No.11, pp.2377-2388 Nov.(1968)
- Ranger A.A.**, "The aerodynamic shattering of liquid drops", PhD Dissertation, Univ. of Michigan, Ann Arbor, MI, (1968)
- Ranger A.A. and Nicholls J.A.** "Aerodynamic shattering of liquid drops", *AIAA Journal*, Vol.7, No.2, pp.285-290 Feb.(1969)
- Rasmussen R., Walcek C., Pruppacher H.R., Mitra S.K., Lew J., Levizzani V., Wang P.K. and Barth U.** "A wind tunnel investigation of the effect of an external, vertical electric field on the shape of electrically uncharged rain drops", *J. Atmos. Sci.*, Vol.42 No.15 pp.1647-1652 (1985)
- Rayleigh, Lord** "On the capillary phenomena of jets", *Proc. Roy. Soc. London* Vol.29 pp.71-97 (1879)
- Reinecke W.G. and McKay W.L.** "Experiments on waterdrop breakup behind Mach 3 to 12 shocks", Sandia Corp., Report SC-CR-70-6063, (1969)
- Reinecke W.G. and Waldman G.D.** "An investigation of water-drop disintegration airstreams behind strong shock waves", *Proc. of the Third Int. Conf. on Rain Erosion and Ass. Phen.*, (ed. Fyall and King, RAE England), Aug. (1970)
- Reinecke W.G. and Waldman G.D.** "Shock layer shattering of cloud drops in reentry flight", *AIAA Paper 75-152, A75-20283*, AIAA 13th Aerospace Sciences Meeting, Pasadena, Calif., Jan 20-22, (1975)
- Richards C.N. and Dawson G.A.** "The hydrodynamic instability of water drops falling at terminal velocity in vertical electric fields", *J. Geophys. Res.*, Vol.76 No.15 pp.3445-3455 May (1971)
- Rojec E.A.**, "Photographic investigation of shear type droplet breakup", Rocketdyne Research Rept. 63-69 (1963)
- Rogers R.R.** "A review of multiparameter radar observations of precipitation", *Radio Science*, Vol. 19, No.1 pp.23-36 Jan-Feb (1984)
- Ryan R.T.** "The behaviour of large, low-surface-tension water drops falling at terminal velocity in air", *J. Appl. Meteor.*, Vol.15 pp.157-165 (1976)
- Saunders M.J.** "Cross polarization at 18 and 30 GHz due to rain", *IEEE Trans. Antennas Propag.*, Vol.AP19 pp.273-277 (1971)
- Savic P.** "Circulation and distortion of liquid drops falling through a viscous medium", *Natl. Res. Council, Canada, Rep. NRC-MT-22*, 50 pp. (1953)
- Seliga T.A. and Bringi V.N.** "Potential use of radar differential reflectivity measurements at orthogonal polarization for measuring precipitation", *J. Appl. Meteor.*, Vol.15 pp.69-76 (1976)
- Serafini J.S.** "Impingement of water droplets on wedges and double-wedge airfoils at supersonic speeds", *NACA TN 1159*, (1954)
- Simpkins P.G.** "Non-linear response of deforming drops", *Nature Physical Science*, Vol.233, pp.31-33, Sept.(1971)
- Spilhaus A.F.** "Raindrop size, shape, and falling speed", *J. Meteorol.*, Vol.5 pp.108-110 June (1948)
- Srivastava R.C.** "On the role of coalescence between raindrops in shaping their size distribution", *J. Atmos. Sci.*, Vol.24 pp.287-292 (1967)
- Srivastava R.C.** "The cloud physics of particle size distributions: A review", *J. de Recherches Atmosphériques*, pp.23-39 (1974)
- Taneda S.** "Experimental investigation of the wake behind a sphere at low Reynolds numbers", *Rept. Res. Inst. Appl. Mech.*, Kyushu University, Vol.4(16) pp.99-105 (1956)

- Tatnall G.J.** "The aerodynamic spike for drag reduction and rain drop disintegration at low supersonic velocities", Proc. of the Second Meersburg Conf. on Rain Erosion and Allied Phen., (ed. A.A. Fyall and R.B. King), pp.239-262, (1967)
- Taylor T.D. and Acrivos A.** "On the deformation and drag of a falling viscous drop at low Reynolds number", J. Fluid Mech., Vol.18, pp.466-476 (1964)
- Taylor G.I.** Unpublished Ministry of Supply Report AC 10647 / Phys C69 (1949)
- Taylor G.I.** "The instability of liquid surfaces when accelerated in a direction perpendicular to their planes", Proc. Roy. Soc. A, Vol. CCI, pp.192-196, (1950)
- Taylor G.** "The disintegration of water drops in an electric field", Proc. Roy. Soc. London, A Vol.280 pp.383 (1964)
- Telford J.W.** "A new aspect of coalescence theory", J. Meteorol., Vol 12, pp436-444 (1955)
- Tribus M. and Guibert A.** "Impingement of spherical water droplets on a wedge at supersonic speeds in air", Jnl. Aeronautical Sciences, Vol.19, No.6, pp.391-394, June (1952)
- Tsamopoulos J.A. and Brown R.A.** "Nonlinear oscillations of inviscid drops and bubbles", J. Fluid Mech., Vol.127 pp.519-537 (1983)
- Twomey S. J.** Atmos. Sci. Vol. 23 pp.405-411 (1966)
- Valdez M.P. and Young K.C.** "Number fluxes in equilibrium raindrop populations: a Markov chain analysis", J. Atmos. Sci., Vol.42 pp.1024-1036 (1985)
- Waldman G.D. and Reinecke W.G.** "Particle trajectories, heating, and breakup in hypersonic shock layers", AIAA Jnl, Vol.9, No.6, pp.1040-1048, June (1971)
- Waldman G.D., Reinecke W.G. and Glenn D.C.** "Raindrop breakup in the shock layer of a high-speed vehicle", AIAA Jnl, Vol.10, No.9, pp.1200-1204, Sept. (1972)
- Warner C.** "Collision frequencies of raindrops", IEEE Trans. Antennas Propag. Vol.25 pp.583-585 (1977)
- Watson P.A. and Arbabi M.** "Rainfall cross polarisation at microwave frequencies", Proc. IEEE., Vol.120 pp.413-418 (1973)
- Whelpdale D.M. and List R.** "The coalescence process in raindrop growth", J. Geophysical Research, Vol.76 No.12 pp.2836-2856, April (1971)
- Whitham G.B.** "Linear and Nonlinear Waves", ISBN 0-471-94090-9, Wiley, (1974)
- Wierzba A. and Takayama K.** "Experimental investigation of the aerodynamic breakup of liquid drops", AIAA Journal, Vol.26, No.11, pp.1329-1335, Nov. (1988)
- Wierzba A.** "Deformation and breakup of liquid drops in a gas stream at nearly critical Weber numbers", Experiments in Fluids, Vol.9, pp.59-64 (1990)
- York J.L.** private communication to Hanson et al (1963)
- Yoshida T. and Takayama K.** "Interaction of liquid droplets with planar shock waves", J. Fluids Eng., Trans of the ASME, Vol.112, pp.481-486, Dec (1990)
- Zrnic D.S., Doviak R.J. and Mahapatra P.R.** "The effect of charge and electric field on the shape of rain drops", Radio Sci., Vol.19 pp.75-80 (1984)

Chapter 3

Simulation Of Liquid Impact

This chapter looks at different simulation techniques which have been used over the years to study liquid impact. The chapter indicates some of the relative merits of the different techniques, and gives the reader a guide to a few of the papers published using each technique.

3.1 INTRODUCTION

The first two chapters have presented a general view of the encounter of rain during a missile flight. They have indicated how to determine the probability of hitting a raindrop, and also how the shape of the raindrop just before impact can be evaluated. The problem of simulating this phenomenon in a controlled experiment is an intriguing one and many solutions have been proposed. The important fact to remember is that there are several stages of development for a new radar dome for a missile and one testing technique is probably not sufficient to cover all of them. This chapter will first present the different techniques available and then look at the testing requirements and how they can best be achieved.

3.2 WHEEL AND JET

The first experimental investigation of erosion by repeated liquid impact was conducted by Honegger (1924, 1927) using a 'wheel and jet' apparatus. The apparatus consisted of a metal disc 1 ft in diameter with cylindrical or prismatic specimens screwed into the rim. The disc was rotated at high speed by an electric motor on an axis parallel to a continuous jet of liquid. The jet was positioned such that the specimen cut through the jet on each revolution and in this way impact velocities up to 225 m s^{-1} could be obtained. This is the velocity of the specimen relative to the jet, the jet velocity (a few metres per second) was not taken into account.

The second recorded use of such a rig was given by Cook (1928), who used a ring of turbine blades with two sprayers projecting a fine spray across the moving blades.

Further improvements were made on these initial designs by Hengstenberg (1932) with a turbine driven disc that could reach velocities of 366 m s^{-1} , and by Gardner (1932), who with a similar set-up reached 335 m s^{-1} whilst also being able to vary the ambient pressure. De Haller (1933, 1940) used specimens of various shapes; circular, flat and concave, while Mousson (1937) varied the temperature of the liquid used for erosion. Von Schwarz and Mantel (1936) produced a rotating arm rather than a wheel, as did Vater (1937, 1938, 1944) who arranged the specimens along the side of the rotor arm so that they all simultaneously cut through a corresponding water jet. In this way Vater was able to test a material over a whole range of velocities in one experiment.

Studies with a wheel and jet at the Cavendish Labs were started by Brunton (1959) who used an electric motor to drive an 8" diameter duralumin disc that could obtain peripheral velocities of 138 m s^{-1} . The apparatus had two specimens mounted on the rim of the disc and two nozzles producing jets of diameters between 0.3 and 2.5 mm. The same rig was then used by Hancox (1962) who showed that the jet velocity had no effect providing that it was sufficient for the jet to reform between

impacts, and Thomas (1966) who upgraded the motor so he could obtain a top speed of 250 m s^{-1} .

Subsequent users of the wheel and jet technique have increased the impact speeds attainable still further. Marriott and Rowden (1966) could obtain 600 m s^{-1} with a 0.4 mm jet, while Smith (1966) achieved 600 m s^{-1} with a set-up using a contrarotating disc and sprayer.

A comparison of erosion results from 4 'wheel and jet rigs' with 6 'whirling arm rigs' (see section 3.3) was conducted by Heyman (1979). He suggested that the velocity dependence of the erosion rate, as well as the incubation period, should differ for drops and jets. This is because for a jet the number of impacts actually equals the number of impacts for the specific target area, whereas for drops they are evenly distributed over the entire area. The actual forces involved in the impact of a jet compared to a drop were evaluated by Hancox (1962), and the critical nature of the specimen alignment in obtaining reproducible results was shown by Lesser and Field (1983). Although the wheel and jet proved useful for studying erosion mechanisms in early investigations and provided a ranking of material for erosion resistance, a test that simulated reality more closely was needed in order to produce meaningful design data for radome engineers. The obvious development was to use drops instead of jets.

3.3 WHIRLING ARM RIGS

The first whirling arm rig was built in 1745 by Benjamin Robins and was used to establish the foundations of aerodynamic drag. Despite having been largely superseded by the wind tunnel by 1900, the use of a whirling arm continued, and Robertson et al. (1946) gave the first account of its use in studying rain erosion at the Radiation Laboratory of the Massachusetts Institute of Technology. The rig used by Robertson consisted of a streamlined arm 28 inches long, rotated at 3400 r.p.m. by a 7.5 Kilowatt motor. Two samples were mounted on the arm, one at either end, each with an exposed area of one square inch. A water spray was directed downward into the path of the samples giving an impact velocity with the drops of water of 116 m s^{-1} . This technique was soon adopted at other laboratories, Wahl (1948) reported its use at Cornell Aeronautical Laboratory where they reached a top speed of 313 m s^{-1} , while Phillips (1951) describes how a "Bulldog" propeller with samples attached to its leading edge was rotated in a simulated rain field at the Royal Aircraft Establishment in England.

One of the initial benefits of the whirling arm rig was that it allowed the experimenter the opportunity to study multiple impact at speeds where individual impacts were unable to cause surface breakdown but where fatigue sometimes could.

The whirling arm rigs however suffered from several drawbacks, some of which they share with the wheel and jet described in section 3.2. The more important of these drawbacks are: high power consumption, high centrifugal force on the specimen, control of the drop shape on impact, control of the temperature and pressure on the sample, the size of the sample, and the limitation in speeds attainable.

3.3.1 Power Consumption

The whirling arms size results in a large surface area moving at high speed through the atmosphere. The power required for a blade of constant cross section and drag coefficient increases directly with the blade length and the cube of the tip velocity. Wahl (1967) did calculations for the Bell Aerospace rig that showed that to operate the proposed 5.48 m diameter blade in air at one atmosphere and a speed of

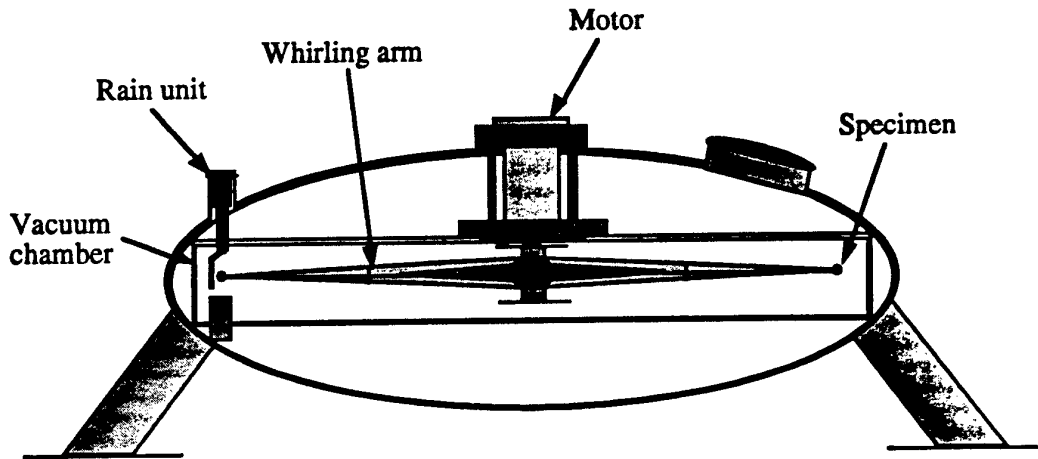


Figure 3.3.1 Dornier Mach 3 rain erosion testing device at Friedrichshafen, Germany. (Schaefer, Koidl and Sah, 1990)

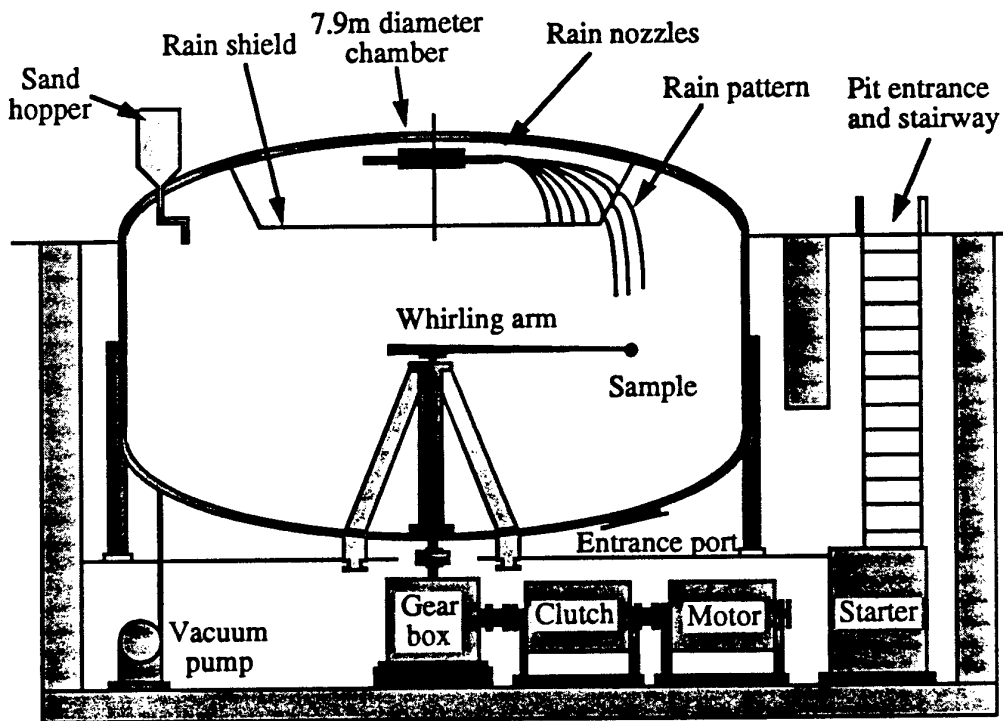


Figure 3.3.2 Bell Aerospace Company whirling arm rig. (Wahl, 1970)

1,020 m s⁻¹ would require roughly 4 Megawatts. This power would largely be converted into heat which would accentuate temperature and heat dissipation problems. In the Bell Aerospace rig the operating pressure was reduced to 1/3 atmospheric pressure so that the power required dropped to 1.3 Megawatt and then a 3 Megawatt substation was built to operate the rig. In contrast for the Dornier rig with a proposed maximum speed of 1,000 m s⁻¹ they reduced the pressure right down to 1/100th atmospheric so only 80 Kilowatt was needed.

3.3.2 High Centrifugal Forces

Fyall (1966) considered one of the major disadvantages of whirling arm rigs to be the imposition of high centrifugal forces on the specimen which would not be present in actual use, the magnitude of some of these forces can be seen in table 3.2. Despite Fyall's criticism there does not appear to have been a study to analyse the effects of these forces, and there is little evidence to indicate the extent they influence the results. Rieger (1970) noted their effects on ductile substances above 400 m s⁻¹ on the Dornier rig, where they resulted in an increase in the rate of erosion with increasing velocity. Vogel (1991) also observed the effects of these forces in the catastrophic failure of some brittle specimens above 600 m s⁻¹ due to contact stresses from point loads on manufactured samples. Similar problems with such brittle failures on the Wright Patterson rig in the 80's at lower velocities were eradicated by the addition of a thin neoprene sheet under the specimen similar to that used at RAE.

3.3.3 Drop Distortion Before Impact

The influence of shock waves generated by the rotating blade and specimen on the flow and break up of the rain drops was examined by Taulbee (1965). In his analysis the flow field was broken into two parts; the wake induced by the shock wave in front of the specimen, and the wake induced by the viscous drag which imparts a swirl or rotation to the surrounding air and water vapour. These two mechanisms tend to accelerate the water drop and can cause its disintegration. Taulbee's analysis showed that breakup of a 2 mm drop in the Bell rig with its reduced pressure was unlikely even at top velocity, and his observations, and those of Wahl (1969) using a TV monitor system, seemed to confirm this. Rieger (1970) used the equations for drop breakup of Nicholson (1967) to show that as the drop diameter decreased the acceleration it underwent in the region ahead of the specimen increased. This meant the relative velocity decreased, but there was a better chance for drop disintegration.

A more comprehensive study of drop distortion in whirling arm rigs was conducted by Adler (1989a) who used polymethylmethacrylate (PMMA) witness plates to record the drop imprints for a short exposure in the rig being studied. His survey investigated the drop impacts for three different whirling arms, those at NADC (Naval Air Development Centre), UDRI (University of Dayton Research Institute) and RAE (Royal Aircraft Establishment). Adler measured the damage sites on the witness plates from each rig to find the drop size distribution for the rig, and counted the number of damage marks that were circular, elliptical, highly distorted, contained voids etc. (table 3.1 and figure 3.3). He found that despite the NADC and UDRI rigs both producing spherical 2 mm drops they actually showed damage marks that would indicate the presence of drop diameters over a much wider range (0.5 - 6.0 mm) (figure 3.4). This result is a consequence of the flow fields in the rotating arm facility sending the drops into oscillation as soon as they are produced, and because these flow fields are dependent on the geometry of the containment the final drop distortions and effective drop diameter distributions are rig dependent.

Table 3.1 Distribution of water drop imprint types: C - Circular; CV - Circular with voids; E - Elliptical; EV - Elliptical with voids; P - Partial; HD - Highly distorted.

Specimen identification	Exposure time (Seconds)	Water drop imprint type (Percent)						Total impacts counted	Total impacts calculated
		C	CV	E	EV	P	HD		
RAE Rotating Arm Facility									
R3	11	23	70	2	1	4	~0	350	-
R4	11	54	44	-2	0	-0	0	345	-
R7	10	56	38	3	0	2	1	474	-
R8	10	27	28	4	0	21	20	488	-
NADC Rotating Arm Facility									
N1	15	46	19	14	5	5	11	108	117
N5	20	64	23	6	3	2	2	190	156
N6	20	75	2	19	-0	2	2	168	156
N7	20	66	9	16	4	2	3	149	156
N8	30	69	19	6	2	4	0	276	233
UDRI Rotating Arm Facility									
U6	20	17	68	2	8	4	1	292	298
U7	30	29	44	5	9	6	7	457	446
U8	30	24	54	2	9	6	5	411	446

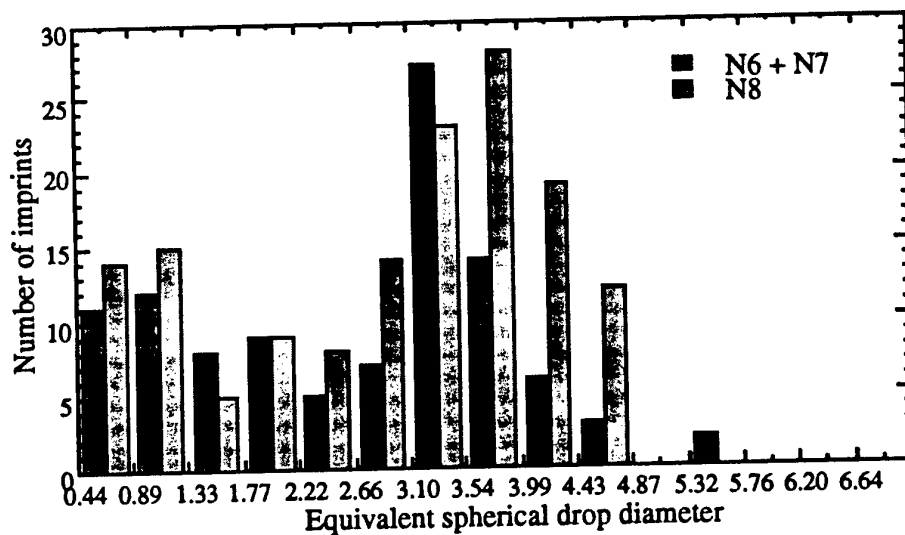


Figure 3.3 Distribution of equivalent drop diameters for the NADC rotating arm facility. (Adler, 1989a)

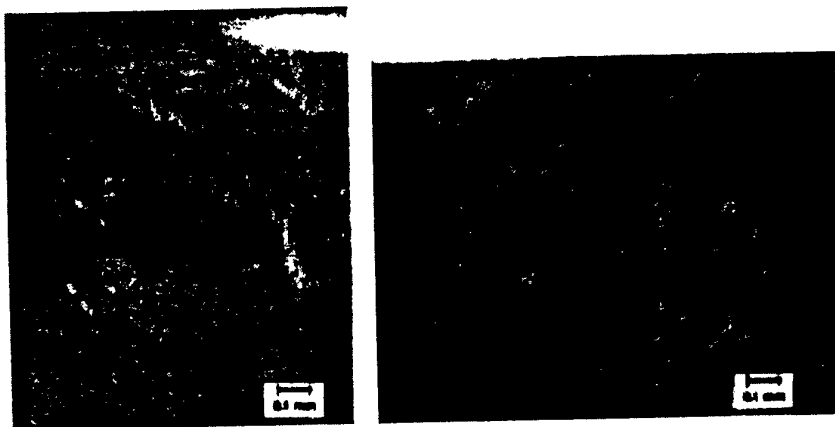


Figure 3.4
 (left): CV on NADC rig
 (right) P on RAE rig
 (Adler, 1989a)

3.3.4 Sample Temperature

According to Wahl (1967) the temperature of the atmosphere within the test chamber can increase both from the frictional heating due to the blade rotation, and from inadequate dissipation of the power consumed in driving the blade. This makes the rise in temperature in the rig a problem even if it is operating at a low pressure. To combat this problem refrigeration units are sometimes added to help cool the air, and together with the mixing currents from the blade rotation transferring heat to the container walls, this is normally sufficient to limit the temperature rise to a small value.

The rise in temperature of the specimen due to frictional heating was also evaluated by Wahl (1967) and was found to be a function of the square of the speed. Since the speed varies linearly with radius, the ends of the arm (i.e. the specimens) are subject to the highest temperature rise. Typical sample temperatures have been measured by Morris et al. (1970) using temperature-sensitive paints. They found at 341 m s^{-1} the temperature was 38°C , while at 512 m s^{-1} it was 150°C , at 683 m s^{-1} it was 260°C , and at 1000 m s^{-1} it was 500°C . This increase in temperature is important as it will often lead to a decrease in material strength.

Using the original Dornier rig Hoff et al. (1967) found that in addition to the aerodynamic heating there was a specimen cooling due to the water drop impacts. They measured the specimen temperature for a velocity of 410 m s^{-1} as 85°C as expected, but found this dropped to 35°C on exposure to rain. This result conflicts with the statement in Rieger (1970) that the temperature will rise as a result of energy absorbed from the drop impacts, and that the more deformable the material the greater the resultant temperature rise.

One final complication with heating effects was discussed by Behrendt (1974) in a comparison between the old Dornier Mach 1.4 and the new Dornier Mach 4 whirling arm rigs. This looked at the effect of the reduced pressure (6 - 18 torr, $\sim 1/100$ th atm) in the Mach 4 rig on the stagnation temperature compared to atmospheric on the older Mach 1.4 rig. He found that the specimen temperature dropped from 100°C to 80°C as the pressure was decreased, and that this introduced only a slight discrepancy between the two rigs results for the erosion performance of Aluminium, but quite a large one for the plastics tested. The operating pressure of the rig must therefore be taken into account when comparing results between rigs.

3.3.5 Presence of a Water Film on the Specimens

The problem presented by residual surface water was mentioned by Rieger (1970), who said that an increase in the density of drops causes an amplification of the water-film's protective effect i.e.. an increase in impact frequency decreases the extent of the rain erosion. Behrendt (1974) observed this effect on pure aluminium where the erosion rate for 1.2 mm drops did actually decrease for an increase in impact frequency.

Drops not actually involved in a collision with the specimen may be broken up by the arm rotation and air disturbance in the rig and form a mist in the chamber. Surface water on the specimen may therefore also result purely from rotation through this mist. The formation of the 'voids' noted on the surface of PMMA by Adler (1989a) may actually be a result of a drop impact on an area where there is residual water on the specimen, and not due to gas in the water as suggested by Adler.

Facility	Year built	Max. Mach No.	Arm Diameter (m)	Drop Sizes Possible (mm)	Rainfall Rate (mm/hr)	Drop Production	Specimen Size (mm)	Centrifugal Force g	Pressure (atm)	Velocity spread over sample / %
RAE Farnborough, England	1956	0.67	3.4	simulated rain	25.4	spinning disc	25.4 sq	3,000	1	1.8
The arm diameter was originally 2.89 m, it was increased to 3.4 m in 1985 to reduce the noise and power consumption. A water drop distribution close to that of 25 mm/hr rain is produced by pumping water onto a 28" metal disc spinning at 185 rpm and allowing the water to be flung off the periphery. Fyall and Strain (1956), Fyall (1970), Corney and Minter (1987), Tattershall and Minter (1991)										
Dornier System GmbH Friedrichshafen FRG	1959	1.4	2.4	1.2 or 2.1	23 - 183	8 spray nozzles, using needles to get drop	16.8 ø	19,000	1	1.4
First supersonic rig, specimen tip 40°C, water degassed. Hoff et al (1967), King (1967), Fyall (1970)										
SAAB (Svenska Aeroplan Aktiebolag), Linköping, Sweden	1965	0.76	3.2	1.2 - 2.0	1.4 - 25	originally spinning disc, now vibrating needles	16.8, 50 ø	4,000	1	0.8
1.03	4.38							5,500		
2 speeds depending on arm length. Control of specimen temp and stress added by Déom. Eskilsson (1967), Fyall (1970), Déom (1990)										
Wright-Patterson AFB Dayton, Ohio	1968	1.2	2.44	1.5 - 2.0	25.4	96 No.27 hypodermic needles drops form from jet breakup	61.9 x 25.4	6,500	1	2.1
First supersonic capability in U.S. Fyall (1970), Hurley and Schmitt (1970)										
Bell Aerosystem Co. Buffalo, New York	1968	3.0	5.5	0.7 - 2.5	10 - 25	nozzles		37,500	1/3	
No drop breakup seen because of reduced pressure. Despite reduced pressure the rig needed its own 3 Mw substation. The rig went out of service when it was flooded because the water was accidentally left on! Wahl (1967), Fyall (1970), Wahl (1970), Hackworth (1979)										
Rolls-Royce Ltd Notts., England	1970	1.54	2.44	3 Ranges 0.45 - 0.55 0.75 - 1.30 1.80 - 2.60	3 Ranges 25.0 4.0 0.15	vibrating nozzle	25.0 sq	21,000	1	2.0
Alderson (1970)										
Dornier System GmbH Friedrichshafen FRG	1972	3.0	2.4	0.5 0.6 1.2 1.7	1.8, 3.6, 5.4 3.1, 6.2, 9.3 25, 50, 75 81	oscillating capillary tubes - up to 4 rain producing systems available	16.8 ø	80,000	0.005 - 0.05	1.4
Speed constant to 0.1 %. Experiment cost ~10,000 DM per day. Kunz (1974), Behrendt (1974), Vogel (1991)										
NADC Warminster PA	1978	2.0	2.44	2.0	12.2	30 hypodermic needles	25.4 ø	36,000	1	2.1
Single specimen on a counterbalanced arm. Last reported top velocity not exceeded 0.65 M. Adler (1991)										
Bell Helicopter Fort Worth, TX		0.75	2.44	Natural rain	76.2		airfoil	5,000	1	
Adler (1991)										

Table 3.2 Comparison of some of the more important whirling arm rigs.

3.3.6 The Specimen Holder

Déom et al. (1987b) discovered that for a given material, tested with the same erosion parameters, with a specific specimen holder, on a given rotating arm, the results were reproducible. However they found it was possible to obtain different results (within a factor of two) by merely changing the design of the specimen holder, particularly with experiments on angled impact. This result was also observed by Tattershall (1992) at the RAE rig in Farnborough.

3.3.7 Comparison of Whirling Arm Rig Results

Several comparisons have been made between different whirling arm rigs. King (1967) compared erosion rate results for a wide range of materials between the Dornier and RAE rigs. Heyman (1979) compared six rigs, Wright Patterson, Bell, Dornier, Goodrich, RAE and SAAB using four different materials. Déom et al. (1987) looked at the differences between Dornier and SAAB and most recently Adler (1989a) investigated the rainfields in several different rigs. From the results it is clear that further data is still required in order to produce an effective method of cross-correlation, this is currently being attempted by Déom amongst others.

3.4 ROCKET SLEDS

Utilisation of sled track facilities for rain erosion evaluation was pioneered by the Convair (San Diego) research team under Dittman (1953.b). The technique allows testing to be conducted of the component of interest with as much structure of the surrounding vehicle as is aerodynamically appropriate. It allows higher velocities to be reached than available on whirling arm rigs, with no centrifugal forces or size limitation, but with the major limitation of the impracticality of building up long flight times.

The full story behind the Convair sled track is told in Barr and Steeger (1957) and Steeger et al (1957). Soon after this development the Materials Department of the Royal Aircraft Establishment, converted the rocket sled track at Pendine in South Wales to allow rain erosion testing (Fyall and King, 1962). This track was 915 m long with a constant velocity region between 280 and 430 m from launch. Although wind effects were a problem, a top velocity of 536 m s^{-1} was obtained with a drop size distribution that was a good approximation to a 25 mm hr^{-1} rainfall, but with an actual intensity of $125 - 175 \text{ mm hr}^{-1}$.

Meanwhile back in the States the rocket sled test program that was underway at the Naval Ordnance Test Station in 1965 was moved to the Holloman Air Force Base in New Mexico as a result of a joint program in summer 1966 between the U.S. Air Force Materials Lab and the U.S. Naval Air Development Centre. It was hoped that the longer track of the Holloman Base would enable higher velocities to be reached and a longer rainfield to be simulated. These developments are documented in Tatnall et al (1967) and Fyall (1970).

Requirements for rain erosion testing for 1 to 6 km s^{-1} were discussed by Mortenson (1970). In addition to a well controlled rainfield, the facility needs, a controlled and known velocity at entry into the rainfield, a near constant velocity through the rainfield, and a slowdown and recovery sequence which does not put more damage into the specimen. The current state of the Holloman sled track is described in their brochure "The High Speed Test Track : Facilities and Capabilities" written in 1989. The track was last extended in 1972 so it is now $15,480 \text{ m}$ long (figure 3.5), it has a top velocity of 2.7 km s^{-1} if the load doesn't need to be recovered.

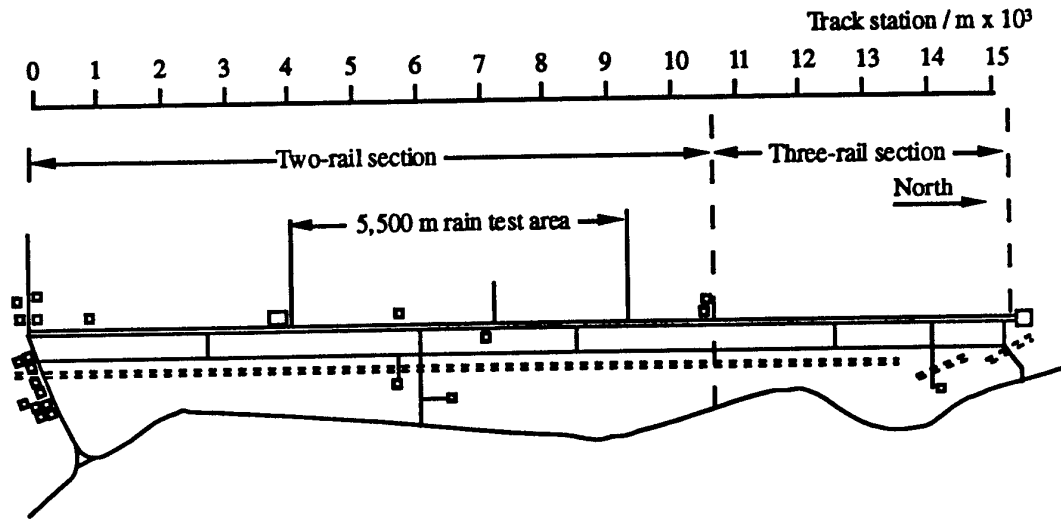


Figure 3.5 Test track facility at Holloman Air Force Base, New Mexico.

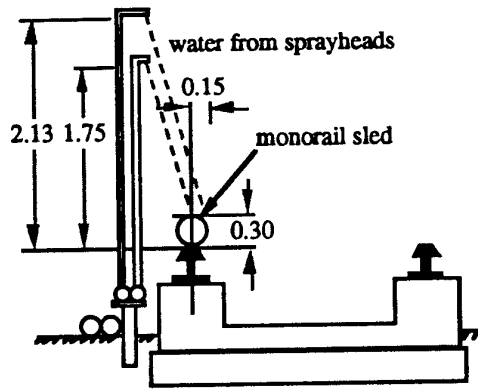


Figure 3.6 Layout of track rainfield, showing sprayheads aligned for use

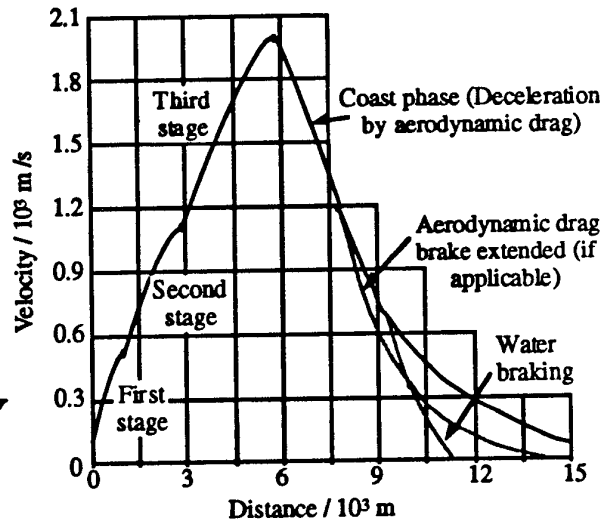


Figure 3.7 Typical sled run trajectory for the Holloman Air Force Base test track.

Table 3.3 Rain rate capabilities for the rocket sled test track at the Holloman Air Force Base, New Mexico.

Volumetric rain rate / mm hr ⁻¹	12.7	66	140	300	710
TRACK					
VRR Range/ mm hr ⁻¹	0-25	53-79	-	-	635-787
Mass median diameter	-	1.33	-	-	2.65
Existing or planned	E	E	P	P	E
Full or partial development	P	F	-	-	F
Wind Limitation	0.5	3	-	-	3
BALLISTIC					
VRR Range	-	-	102 - 178	254 - 356	635 - 787
Mass Median Diameter	-	-	-	-	-
Existing or planned	-	P	E	E	E
Full or partial development	-	-	P	P	P
Wind Limitation (Ktg)	-	-	1	-	2

and 2.3 km s^{-1} if it does. There are over 300 sled designs in existence, propulsion is provided by a variety of solid propellant rocket engines, while braking is achieved by a combination of aerodynamic drag, water brakes and arresting straps. The rainfield is about 1,800 m long and the velocity during the traversal of the field typically varies by about 100 m s^{-1} with the peak in the middle of the field (figure 3.7). The rainfield is produced by sets of spray heads on the trackside (figure 3.6). A variety of spray heads and water pressures are available that enable different drop size distributions and rain intensities to be simulated (table 3.3). Alternatively a drop generator can be used to provide impact with predefined drops at specified locations.

The advantage of a facility such as this is that it can safely imitate flight through rain and allow examination of the specimen afterwards. The exact impact history of the specimen may remain unknown for some flights, but the drops do undergo the sort of aerodynamic distortion they would be subjected to under real flight (bearing in mind the effects of low altitude on air pressure and drop distortion). Other weaknesses of the rocket sled are the failure of brittle samples due to lateral and axial acceleration (Krupovage, 1991); the difficulty of decoupling effects of aerothermal ablation and rain erosion on mass loss (Letson, 1979); the turn around time for testing; and the cost of an experiment \$25,000 - \$75,000 !

3.5 IN-FLIGHT EVALUATION

Flight testing cannot be avoided because at some stage the results obtained on ground facilities must be verified. Lapp et al. (1955) made a comparison of material erosion performance from flight tests with those from whirling arm tests. Although the same ordering for performance was obtained, they found the results did not exactly reproduce the amount of erosion experienced in an equal time interval under actual service conditions. Comparison of results was actually made more difficult because the flight test time had been the result of small increments of flight through rain of varying intensities and drop diameters. Bigg et al. (1956) also comment on the difficulty of characterising the rain encountered and the hazardous and costly nature of test flying. Despite these early sceptical comments Schmitt (1967, 1970) produced several comparisons of materials tested by flight on a F-100F with the Wright Patterson whirling arm rig and obtained not only the same ranking but the same modes of failure in each case. Flight testing thus continues to be a useful final test of survival for a component, but in early stages of material optimisation the rainfield is too ill-defined to be of use in producing comparative results between sample batches.

3.6 SABOT FIRED AT A SUSPENDED DROP

The first reported use of this technique appears to be by Jenkins (1955). He suspended a drop of known diameter on a fine web composed of a solution of 'Perspex' in aniline (a method suggested by Lane (1951)). A sabot with a specimen mounted on the front was then fired from a compressed air-gun at speeds up to 250 m s^{-1} so that after striking the drop it entered an energy absorbing tube that decelerated the specimen without further damaging the surface. High speed photographic evidence was required to show the drop profile before impact and to calculate its velocity. Jenkins in this way found that the web appeared to be blown away by the air proceeding the sabot leaving the spherical drop to be struck by the projectile. This same set-up at RAE was later used by Fyall (1967, 1970) who was able to achieve 450 m s^{-1} by using hydrogen as the propellant rather than compressed

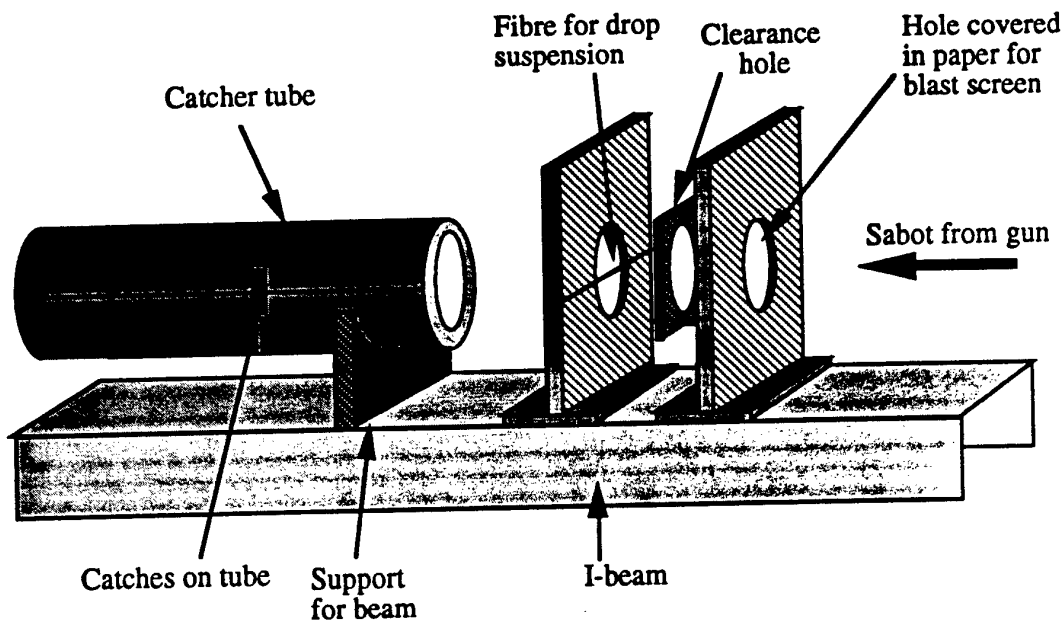


Figure 3.8 Drop suspension and blast screen set-up for Cavendish Labs. large gas gun.

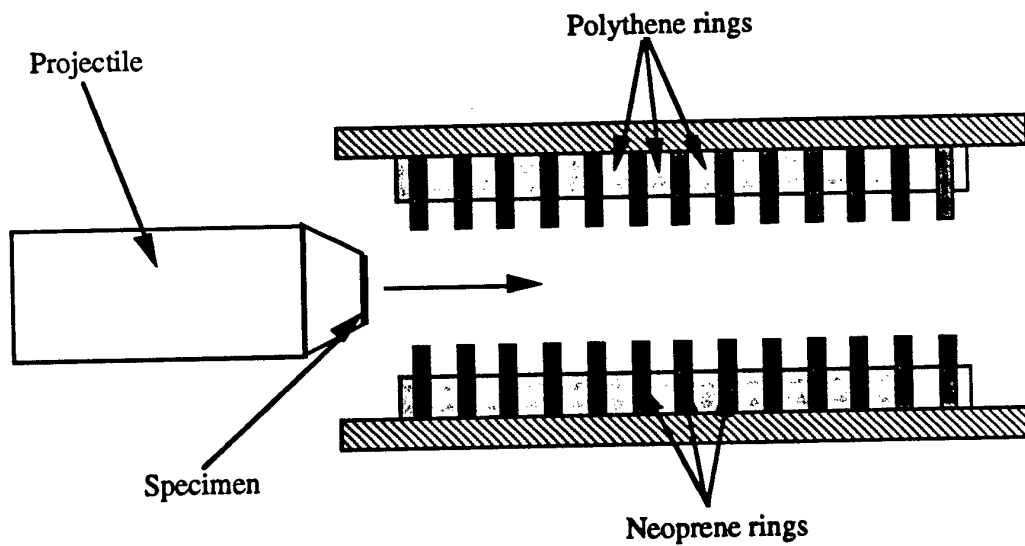


Figure 3.9 Catcher system for large gas gun used at the Cavendish Labs., showing the alternate polythene and neoprene rings used for slowing the sabot down without causing further damage to the specimen.

air or nitrogen. Because of the high deceleration forces the technique was not suitable for many brittle materials, particularly those with a thin cross-section (Fyall, 1970).

A similar technique was also adopted by Rickerby (1976) in the Cavendish Laboratory. Rickerby constructed a gun barrel length of 1.98 m and 25 mm diameter, and a catcher tube system that used alternating discs of neoprene and polythene (figs. 3.8 & 3.9). The holes in the polythene were cut to be larger than the sabot, whereas the neoprene holes were cut slightly smaller so they would rub on the sides of the sabot and slowly decelerate it. Rickerby criticised the results of Fyall (1967) because he claimed the drops were distorted, firstly by their suspension on the web, and secondly by the air shock ahead of the sabot. The technique used by Rickerby (1976) and later Blair (1981) and Hand (1987) therefore introduced two blast screens of paper in front of the suspended drop, and a series of Imacon shots of the impact event.

Adler and James (1979) and Adler (1979, 1989b) also describe the development of such a facility. Their system however has a single drop falling in a chamber at .0001 atm whose fall is timed so the sabot collides with it. The drop is thus not subjected to an air shock before impact, however because it is below the vapour pressure of water it is actually not pure water but an 80 % water 20 % ethylene glycol mix. Their maximum velocity is dependent on the material survivability, so brittle materials may only be tested at 610 m s^{-1} , while the top velocity for tougher materials is 1370 m s^{-1} . Drop diameters from 1.5 to 5.0 mm are possible on this rig, however the time taken for each shot makes it a very costly experiment (~ \$1,000 per shot). As with the Cavendish apparatus a photo is taken of the drop just before impact, and the velocity is measured from the length of time the sabot obscures a laser beam.

3.7 INTERRUPTED JET

Early development by North American Aviation Inc. of an interrupted jet apparatus is described by Engel (1957). The machine consisted of a continuous flow high pressure pump that forced a continuous jet of water at high velocity through a nozzle. A slotted rotating disc chopped the jet into discrete slugs of water. With this apparatus the water-drop was actually a water cylinder struck from the end. Further development of this machine as a device for testing the rain erosion resistance of materials was discontinued because the results obtained were too inaccurate. As a consequence although there have been many subsequent attempts to produce interrupted jets these have been aimed at jet-cutting applications rather than drop impact simulation.

3.8 SINGLE IMPACT JET APPARATUS

This apparatus was developed by Bowden and Brunton (1958, 1961). Its use allows the specimen to be kept stationary while short, coherent jets of water are fired at it out of a nozzle. The nozzle design and loading is critical to the success of the technique and has been developed by a succession of researchers at the Cavendish Laboratory (figure 3.13). The nozzle is initially filled with the liquid to be fired and sealed with a neoprene diaphragm. This diaphragm is adjusted until an outward curving meniscus is formed at the front of the nozzle, and then a 0.22" lead slug is fired into the rear of the nozzle from a converted air-rifle (figure 3.10). The air-rifle in current models is powered by a small gas reservoir (figure 3.11) and enables jet velocities up to $1,000 \text{ m s}^{-1}$ to be obtained. A modified filling technique using a boroscope to check the position of the meniscus in the nozzle has been used at the Naval Air Warfare Center in the U.S. to produce a tighter spread in jet velocities.

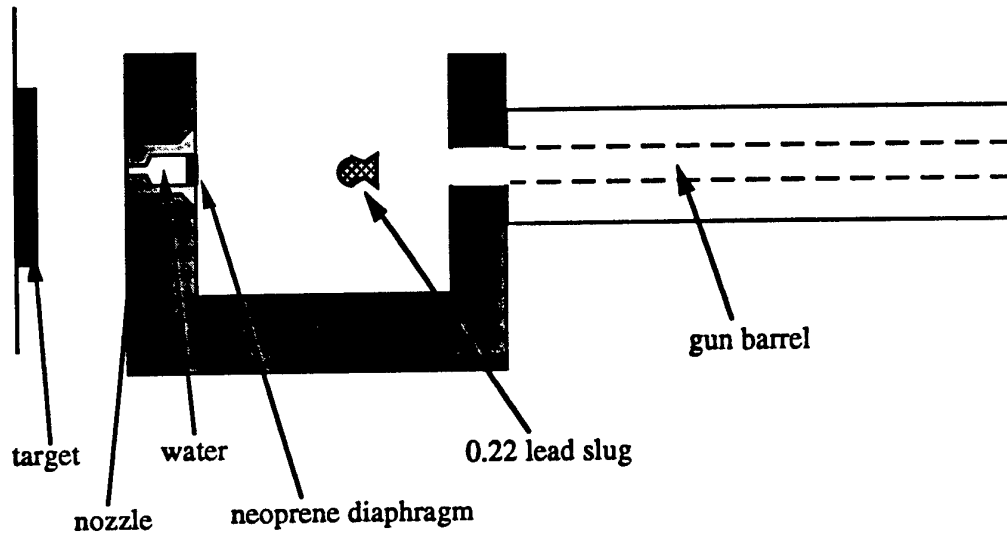


Figure 3.10 Nozzle arrangement at the head of the Single Impact Jet Apparatus.

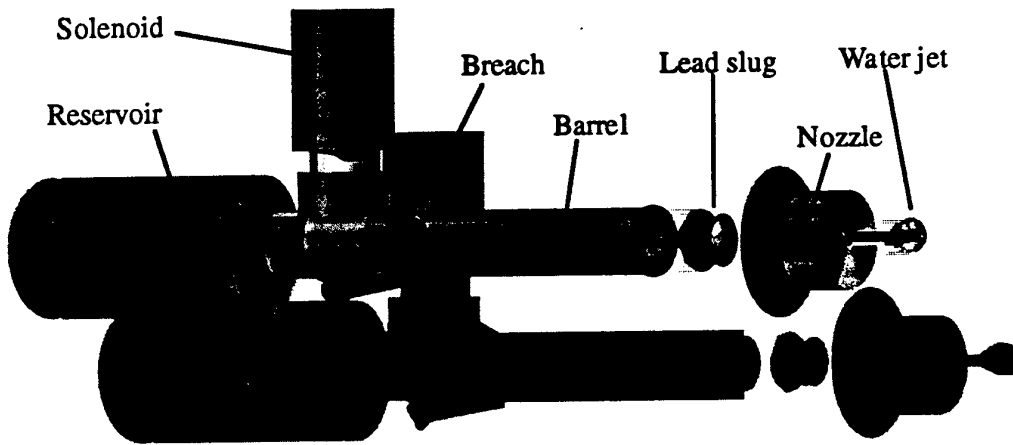


Figure 3.11 The full SIJA apparatus showing the gun barrel, air reservoir and nozzle.

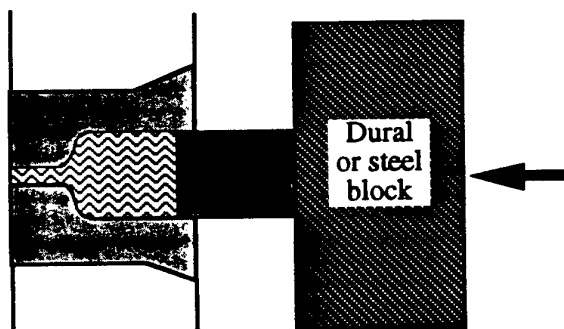


Figure 3.12 To obtain low velocities a 'momentum exchanger' is required. This consists of a block of dural or steel introduced into the path of the lead slug.



Figure 3.13 The internal profile of the nozzle has been the subject of considerable research, and is critical for the techniques success

The jets produced tend to be slightly flattened towards the front by their passage through the air, however they have a highly reproducible front radius of curvature and results can therefore be compared easily between experiments. The apparatus came under criticism by Adler (1991) who claimed that whilst the damage produced by a jet is qualitatively similar to a comparable water-drop impact it is quantitatively quite different because it is not a sphere. A large amount of research has been conducted at the Cavendish Laboratory to evaluate such differences between jets and spherical drops, and correlation curves have been attempted. However the use of such correlations must also be assessed. Chapter 2 shows that real raindrops are not spherical and therefore a simulation with a non-spherical jet is no less arbitrary than a simulation with a spherical drop. The advantages of a small, inexpensive quick test far outweighs the possible drawbacks. As a result SIJA is now in use in over 20 laboratories around the world and allows new materials to be tested instantly and reproducibly, and allows results to be compared between labs.

3.9 WIND TUNNEL

At the request of the French governmental technical department of aviation in 1965, O.N.E.R.A. attempted to build an artificial rainfield into their S3 Wind Tunnel at the Modane Test Center (Fasso, 1966, Fasso et al., 1967, Fyall, 1970). They considered the advantages of such a technique were that they could observe continuously the erosion processes of a real component of an airplane or missile, and could use a well-defined type of rain at high subsonic and even transonic speeds.

The principle idea was to use an injector positioned 3.5 m upstream from the specimen, with 0.3 litres per second of water being projected out of it under pressure. The water-jet pressure was adapted to the air speed in the tunnel so that the jet broke into drops whose mean diameter was known. When the injector was left fixed there was an excessive local water content in the airstream, and a thick water film was observed on the specimen, so instead the injector was set into oscillations in the vertical and horizontal plane. By the time the beam of drops reached the specimen they had an amplitude of oscillation of 30 cm with a frequency of 2 cps. The rain produced in this way supposedly represented realistic drop size spectra and median volumes, but with concentrations of liquid water 50 to 100 times greater than in real atmospheric conditions. The effective altitude of the results was deduced from the test section static pressure and was found to be approximately 300 m i.e. equivalent to low-level flight.

The wind tunnel actually suffered from several limitations which were never really adequately solved and remained in later reports of results (Armand and Fugain, 1979). The velocity range was restricted to 200 - 275 m s⁻¹; the maximum useful run time was only 100 s due to the amount of water that could be injected; the temperature was difficult to control because of the air expansion; it was not clear whether the surface was always dry between impacts; the drop size could not be accurately controlled; the higher concentration of drops resulted in greater drop distortions, collisions and oscillations; the size of the specimen was restricted to 260 mm diameter; and the results were difficult to compare with other techniques.

3.10 REPEATING JET

The first recorded attempt to produce a repeating jet apparatus was by Kenyon and Scoles (1967) for the Associated Electrical Industries. Their machine consisted of a nozzle pointing vertically upwards behind which was a conical chamber filled with

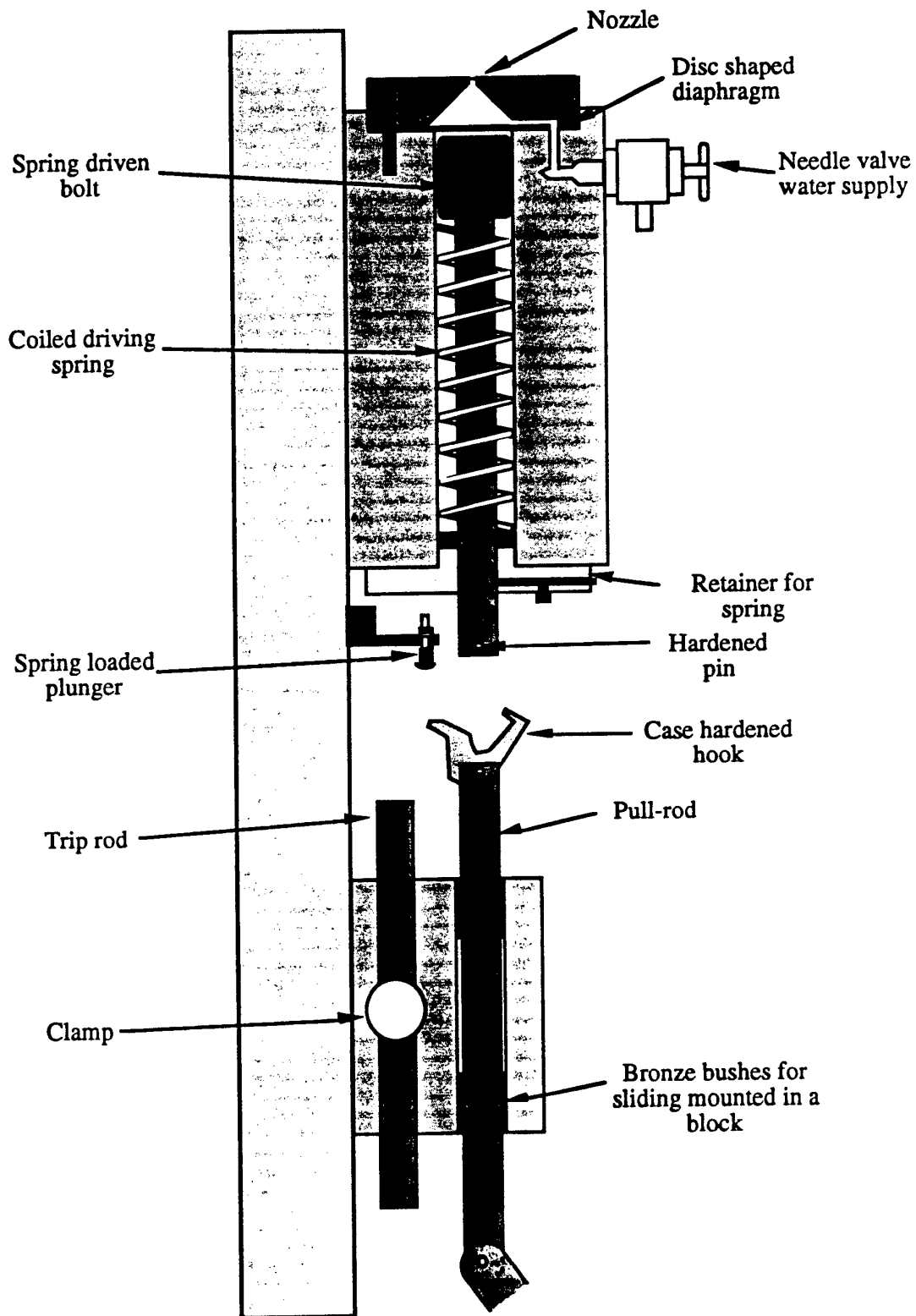


Figure 3.14 The repeating jet apparatus designed by Kenyon and Scoles.

water (figure 3.14). This chamber was fairly large with a base diameter of 32 mm and it was filled through a fine hole in the diaphragm. A jet was extruded by striking the diaphragm with a spring-driven bolt, the head of which was slightly domed. During repetitive operation the chamber was refilled between cycles and the meniscus was formed by overflowing the nozzle and sucking off the excess. The bolt worked by means of a pull-rod, driven by a crank and sliding in bronze bushes in a block. At the top of the stroke, a case-hardened pawl, was brought into contact with a spring loaded plunger, whereby it was tilted so as to engage a hardened pin on the shank of the bolt. On the down stroke of the pull-rod, the bolt was pulled down and the driving spring compressed until the nose of the pawl met the top of a trip rod. This tilted back the pawl and released the bolt, which, driven by the spring, flew up and struck the diaphragm. The trip rod could be fixed at any desired height to give control of the strength of the blow and hence the jet velocity.

The specimen was typically held 15.9 mm from the nozzle. The orifice was 1.64 mm, and jets could be produced up to 220 m s^{-1} at the rate of 30 per minute and roughly with a velocity spread of 5 %. The machine had several weaknesses however. The driving spring was prone to fracture; the diaphragms had a short lifetime before they became domed; the shape and velocity of jet was often poor; the meniscus prior to firing was unsymmetrical; the results were inconsistent.

This apparatus was developed further by Hammitt et al (1974) who increased the maximum repetition rate to 110 per minute, with a velocity range of 300 - 600 m s^{-1} . Unfortunately in tests the jets appeared badly formed particularly as the velocity increased, and the damage rate of materials actually decreased with increasing velocity above 480 m s^{-1} !

3.11 BALLISTIC RANGE

The main advantage of ballistic techniques is the speed that can be attained in what is often a controlled temperature, pressure and rain environment. The disadvantages however are the complexity of data gathering; the time and expense per shot; the difficulty of recovering the sample and the restriction in the sample size.

An early program at Edgewood Arsenal sponsored by the U.S. Air Force fired shells vertically in natural rain at velocities of Mach 2 - 2.75 (Anon., 1956). The projectiles rose to 7,000 m in 80 - 95 s and then returned to earth tail first (achieved by weighting the base) and buried into the ground without further damaging the nose section. Rainfall was recorded during the test and the height of the cloud found from radar.

Artificial rain tests have been conducted at a number of other establishments and have allowed higher velocities to be reached with a more rigorously defined rainfield. The Convair Division of General Dynamics (San Diego) used a shell holding a 15 mm diameter specimen, modified so that a fuse was ignited after firing it from a weapon. This fuse burned for a set time interval, and then ignited a separation charge that expelled the nose, and allowed it to float to the ground on a small parachute (Dittman et al., 1953a). The initial range was only 150 m with a 50 mm hr^{-1} rainfall intensity and a 1.6 mm average drop diameter, but this was increased to 460 m with 300 mm hr^{-1} rain and samples of 50 mm diameter. The shell typically reached velocities of Mach 2, but the extreme axial accelerations involved made the test more useful for plastics than ceramics.

A linear ballistic gun operated by SAAB in Linköping, Sweden (Eskillsson, 1965), used a 3 m long gun, a 3 m rain section, and a 9 m braking section operated by a compressed air blast (timed with the gun firing), to reach Mach 2 - 4 with 800 x 2 mm drops in the flight path. In the U.S., at the United States Naval Ordnance

Laboratory (N.O.L.), in White Oak, Maryland, a 300 m long range that could reach 6 km s^{-1} was constructed with 20 screens of 1 - 1.5 mm drops from hypodermic needles, produced in two 9.3 m long banks (Lankford, 1968, Mortenson, 1970). The specimens in this rig were unrecoverable, instead erosion was followed by in-flight photography. Preheating was made possible by a laser and a new system of drop production allowed screens of 0.6 mm drops on 200 nm thick Parylene to be prepared (Mortenson, 1974).

A guided rail ballistic range was also constructed at the N.O.L. which grew from an initial 2 m track with 24 m recovery tube (Mortenson, 1974), to a 300 m rail enabling model recovery at speeds up to 6 km s^{-1} (Mortenson, 1979). This facility also allowed the flight trajectory through the rain to be accurately known so that instrumentation was focused in for better accuracy, and specimens weren't lost with collisions with the chamber walls.

3.12 SOUNDING ROCKETS

The first sounding rocket was a two-stage vehicle developed in 1970 (Mortenson, 1974). Known as the Terrier/Recruit vehicle, it was able to carry a 27 kg payload and telemetry system at up to 2.6 km s^{-1} and return to the ground by parachute. The system was later upgraded to three stages, TATER, and achieved 3.2 km s^{-1} with a delayed ignition sequence allowing greater trajectory control.

3.13 COMPARISON WITH SOLID IMPACT

The use of nylon spheres in a modified 'grit-blasting' machine was promoted by Campbell (1983) who attempted to calibrate the apparatus by comparison of results with the RAE whirling arm rig. Edwards (1987) and Field et al (1991) have subsequently made a comparison of the impact forces and damage mechanisms for nylon spheres and water drops. They both concluded that whilst the use of nylon balls was superficially attractive, great care needs to be taken in interpreting the results as despite qualitative similarities, particularly at higher velocities, there were still several quantitative differences. Further extensive studies have also been made at the Applied Physics Laboratory of John Hopkins University (Jenkins et al, 1961) using polyethylene spheres.

Adler (1987) and Adler and Flavin (1987) used a capacitor discharge technique that could propel nylon beads at velocities from Mach 2 - 8, and more recently they have used nylon beads in a Multiple Particle Launch Facility (section 3.17)

Walton and Gorton (1970) tried using lead shot but considered that it produced a longer flatter pressure pulse which gave different failure patterns in brittle materials. A further discussion of liquid impact simulations attempted with solid particles can be found in Fyall (1970).

3.14 SINGLE WAVE IMPACT FACILITY

This facility was operated by Science Applications Inc., Irvine, California. It used a 4 segment sabot with a cavity in it that was filled with a mixture of 97 % water and 3 % gelatine. The sabot was accelerated to speeds of $1,000 - 4,500 \text{ m s}^{-1}$ by an electrical discharge from a capacitor bank into a gun chamber charged with hydrogen or helium. The rapid increase in temperature and pressure accelerated the sabot and the segments were then stripped off during flight through the vacuum chamber to

allow the water/gelatine drop to continue to the sample. Few results appear to have been obtained (Sullivan and Hockridge, 1974).

3.15 LASER SIMULATION

Pirri (1977) proposed to simulate erosion by particles using a pulsed laser beam focused on a target in a vacuum. The key assumption was that the important parameter in a particle impact was the rapid energy transfer, resulting in high impact pressures and thus creating a shock wave in the target that would be responsible for the cratering. Work on using this technique to study liquid impact on graphite and slip-cast fused silica was carried out by Deom et al. (1983, 1987a), and assumed that the droplet characteristics of size, mass and velocity could be related to the laser irradiation parameters of energy and pulse duration. The results presented are unconvincing and the work has received little further attention.

3.16 MULTIPLE IMPACT JET APPARATUS (MIJA)

Following the great success of the Single Impact Jet Apparatus (SIJA) described in section 3.8, an automated version was sought that would allow greater reproducibility of the jet velocity and front profile. Work was started on such a machine in 1982 by Davies (1988) and led to the completion of a fully computer controlled apparatus by Seward in 1991. A diagram of the Mk IV apparatus developed from 1989 to 1992 is shown in figure 3.15. The apparatus consists of a horizontal main pressure vessel with various solenoids and pressure sensors attached. At the top of the main pressure vessel is a firing solenoid, and beneath it a trigger piston blocking a discharge tube leading to the main body. Once the desired firing pressure is achieved in the main pressure vessel the firing solenoid is triggered, and the compressed air allowed to pass down into the vertical main body of the apparatus. This main body houses a piston that can move freely up and down its length. The piston is initially at the top of the main body and on firing it is accelerated down the bore until it comes into contact with the titanium shaft held in the endpiece at the lower extent of its travel. Inside this endpiece is a bearing that is used to accurately guide the shaft into a nozzle full of water. The specimen is placed below this nozzle on an X-Y stage, and the jet velocity is measured by a series of fibre-optics and ultra-fast electronics as it traverses the distance from the nozzle orifice to the specimen. The cycle is finished by clearing the residual water off the specimen surface and then returning the shaft and piston to their initial positions.

The whole of the operation is controlled by an IBM computer that allows impacts to be positioned accurately on a sample in a random pattern, rectangular grid, or a user-defined array. The major development efforts have been placed into establishing a tight control of the velocities produced (0.5 - 1.5 %) whilst also ensuring that jet profiles are reproducible, and also enabling a velocity measurement system capable of accurately measuring jet velocities of 600 m s^{-1} to be fitted into the 10 mm gap between the nozzle orifice and the specimen.

MIJA allows rain erosion studies to be conducted with known and reproducible velocities, equivalent drop sizes, and damage patterns, thus offering a better control over the rain erosion than that currently available on whirling arm rigs. In addition MIJA's experiments are reproducible not just between different specimens on the same machine, but also between different machines world-wide. This means that erosion experiments over a defined area with measurements of mass loss, transmission loss, roughness etc. are all possible, and because of the stationary specimen different operating temperatures and stresses can be easily imposed.

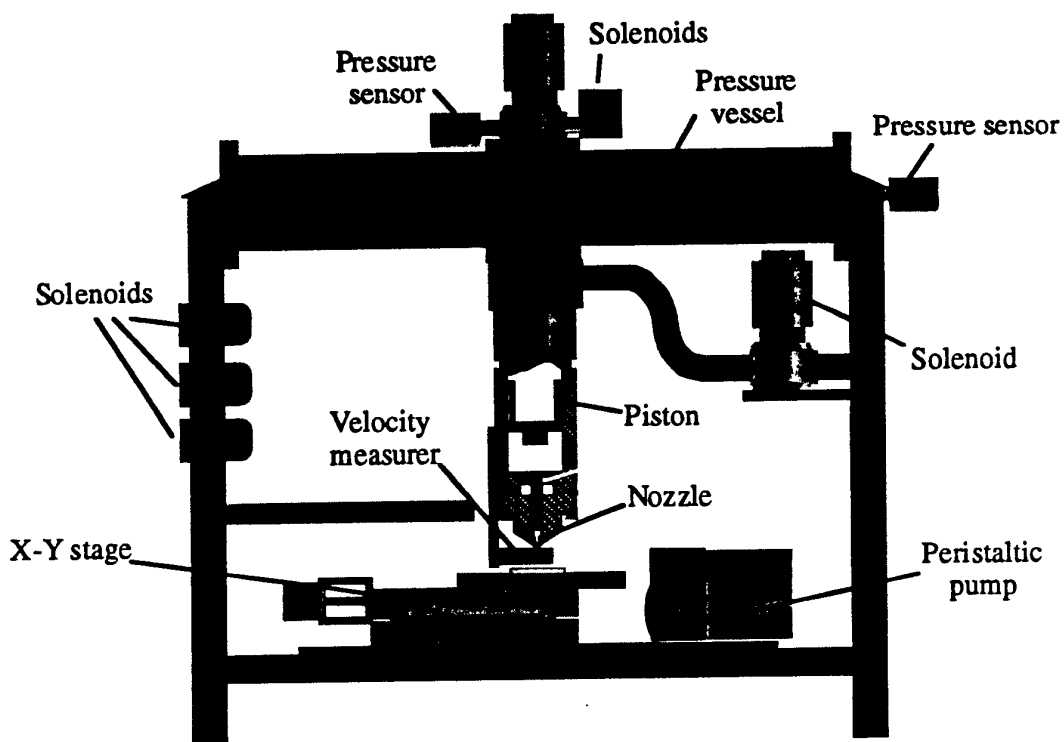


Figure 3.15 Schematic diagram of MIIA Mk IV showing some of the internal moving parts in the main body.

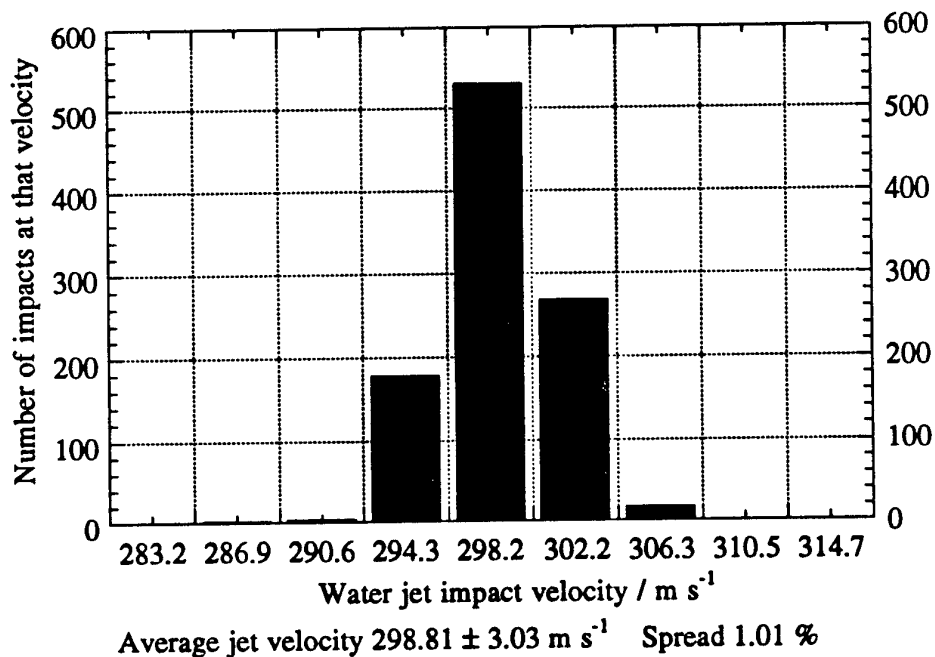


Figure 3.16 Typical velocity distribution for 1,000 shots fired on MIIA Mk

In addition to erosion studies threshold evaluations can be carried out for brittle materials using multiple impacts on one site as described in section 4.3.3. The testing technique this offers allows a reproducible threshold curve to be obtained from a single 25 mm disc. Thus making testing of exotic and expensive materials possible.

SPECIFICATION OF MIJA MK IV

- Compact laboratory apparatus
- Samples can be of almost any size, shape or material
- Computer provides experiment automation, sample database, and results analyser
- Reproducible drop sizes and velocities (30 - 600 m s⁻¹, with a spread of 0.5 - 1.5 %)
- In-situ velocity measurement
- High repetition rate (~ 20 impacts per minute)
- Accurate positioning of impact sites on a computer controlled X-Y specimen stage

A new MIJA Mk V is now in final testing and has been made to a specification suitable for industrial use, with improved accuracy in velocity measurement, X, Y, Z and θ computer controlled movement, easier operation, higher safety standards, and a greater durability. This new design can be seen in plate 7.1.1

The main disadvantage with the water jet technique on either SIJA or MIJA is that the jets are not spherical. However as the previous chapter showed raindrops aren't spherical themselves, and therefore a flattened jet is no less arbitrary a shape to choose for rain simulation. The more important qualities for a simulation are its cost, flexibility, ease of use, availability, test duration, reproducibility, and that the damage produced is typical of that which may occur during an actual flight through rain. On all of these points the water jet technique scores very highly.

3.17 MULTIPLE PARTICLE LAUNCH FACILITY

This facility developed at the General Research Corporation in Santa Barbara is designed to propel a collection of particles onto the test article at supersonic speeds Adler (1990). The apparatus can be seen in figure 3.15, the whole gun is operated at 100 mtorr to prevent distortion of the beads used for impact during their free-flight. A powder gun launcher tube 1.2 - 7.6 m long accelerates a 200 g sabot with a particle array on the front to velocities of 200 - 1,700 m s⁻¹ (velocity control to ~5%). This launcher tube leads into a specially designed venting section, for use at low pressures, to remove the propellant gases. The sabot with the array then enters a sabot deceleration section to gently dislodge the particles from the sabot and allow them to continue down the range to the target. The sabot is stopped in the sabot deflection chamber by means of a ramp which redirects its flight so that it collides with a secondary target. The particles continue downstream to the target and a photo is taken to capture their moment of impact. The particles are typically made of nylon or silicone and range from 1 - 6 mm in size. The same specimen can be subjected to several sets of impacts, the sabot being able to supply 1 - 30 particles at a time, and at a range of impact angles.

Initial results from this rig using nylon bead impact on ZnS have been published in Adler et al. (1992) with a top velocity of ~825 m s⁻¹. The results supposedly show a good correlation with water impact although the paper adds that further quantification of the differences between nylon and water impact damage need to be made.

The main disadvantages are the expense per shot, time to build up a large number of impacts, and use of polymer beads to simulate liquid impact and therefore the need for correlation experiments. The main advantage is that the bead is spherical, however since raindrops aren't spherical this is only of real importance in theoretical studies.

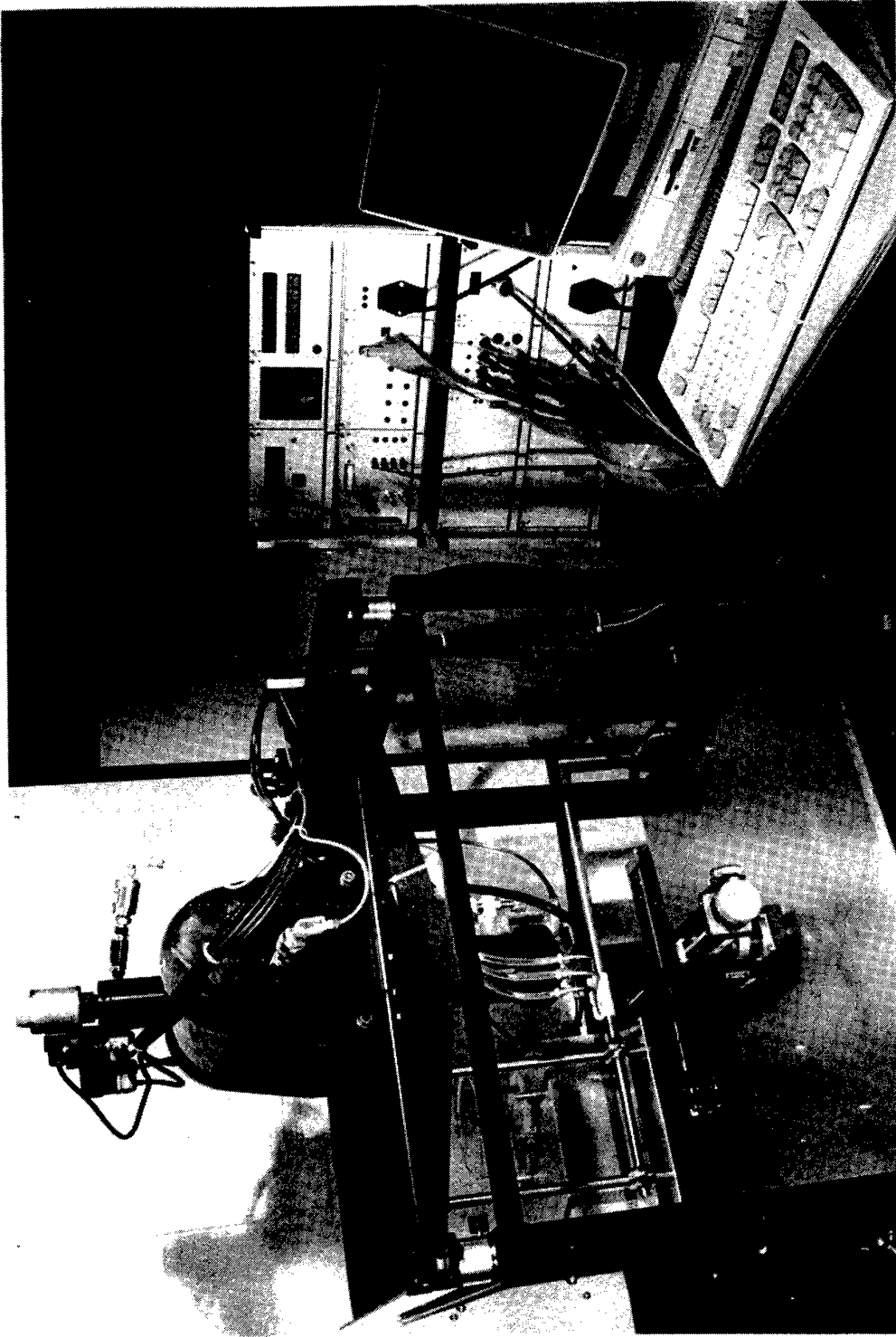


Plate 7.1.1 Photo of MLJA Mk V showing the new frame, electronics interface boxes, and IBM computer

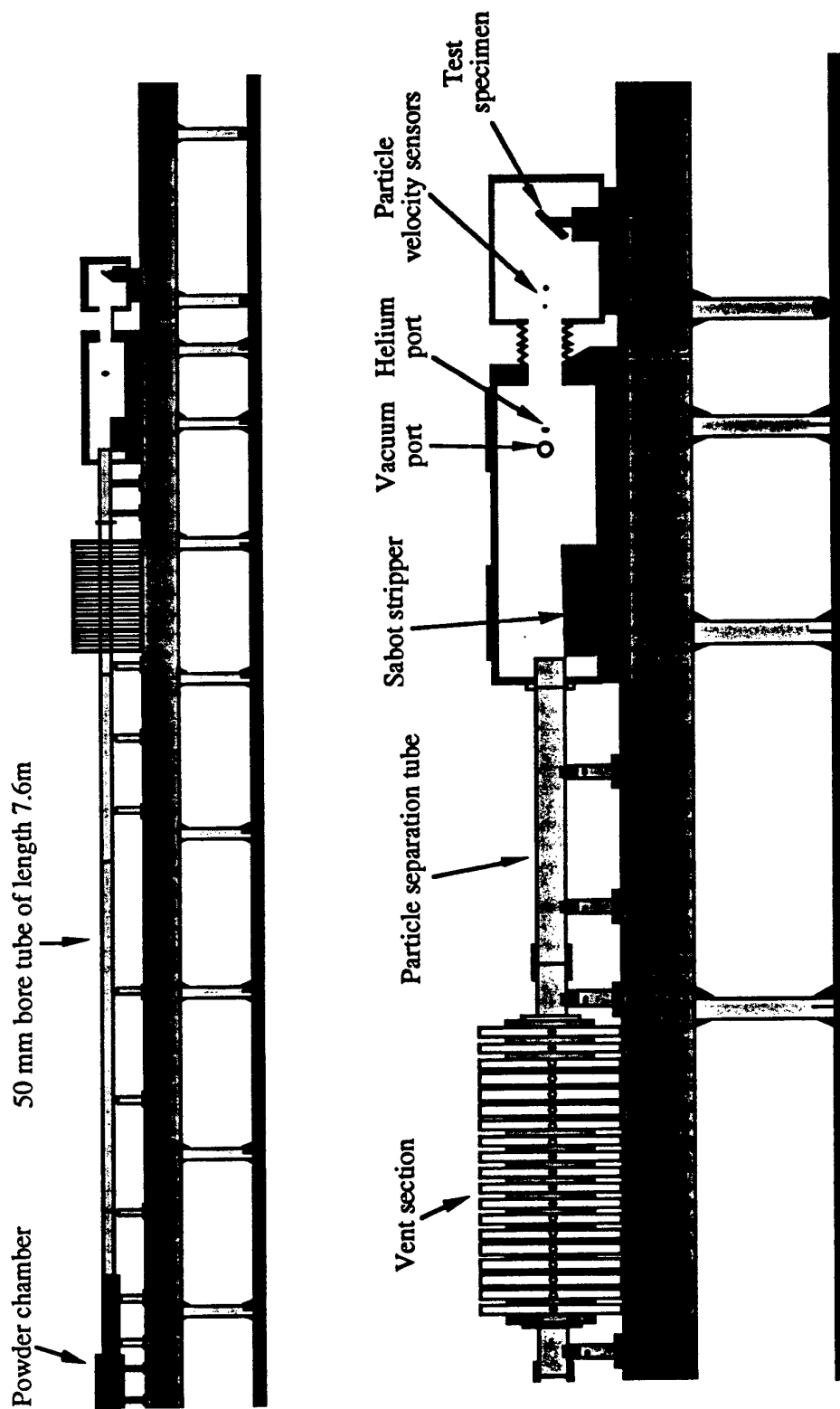


Figure 3.15 Schematic diagrams of the Multiparticle Supersonic Impact Apparatus at General Research Corporation, Santa Barbara, USA

3.18 CONCLUSION

The ability to create a controlled impact with a spherical drop on a material is of a great importance in attempting to uncover the fundamental relationships between the impacting object and the impacted media. However until the predictive properties of these relationships can be established, there remain three main stages in the evaluation of the rain erosion performance of a new aircraft or missile radome:

Stage one: A study of the materials available

OBJECTIVE:

Comparison of different substrates, coatings and surface finishes. The two main parameters to identify are:

- a) the threshold velocity
- b) the rate of degradation of the optical and mechanical properties of the material in use above the threshold velocity.

TEST REQUIREMENTS:

a) A simple, fast, cheap test that could ideally be conducted on the site where material development takes place for immediate feedback into optimisation of material processing techniques.

b) In order to allow easy comparison between materials produced and tested in different laboratories, the same type of rig should produce the same results anywhere in the world, and the test should ideally only use one drop size.

c) The drop front profile should be reproducible and rounded, but need not be spherical since as seen in chapter 2 raindrops are not necessarily spherical when impacted, so to simulate a raindrop with a sphere would be just as arbitrary as a simulation with a jet where the front profile is a little flatter. Impact with water should however ideally be preserved to avoid doubts about the similarity of impacts with solids such as nylon over the full velocity range.

BEST SIMULATION TECHNIQUE TO USE:

The best solution appears to be MJA which can evaluate both parameters set out in the objective with one 25 mm disc.

For threshold evaluation SIJA can be used with a strength test such as bursting disc or ring on ring, this however requires ~ 20 discs of the material.

The whirling arm used to be favoured for these early material studies but the cost of running such a unit and difficulty of comparing results no longer merits its use at this stage.

Stage two: Extended evaluation of the chosen material

OBJECTIVE:

Once a candidate material has been selected a more extended study of suitability for the application is required before committing the material to production.

TEST REQUIREMENTS:

- a) A rain field that can be controlled to study different drop sizes.
- b) A test velocity that is comparable to the one of most interest in use (this may be low velocities during the carriage of the missile, or high velocities during its firing).
- c) The facility for long exposure times .

BEST SIMULATION TECHNIQUE TO USE:

For low velocities - the whirling arm.

For intermediate velocities - the rocket sled.

For high velocities - the ballistic range.

Table 3.4 The following table indicates the survival requirements set out by Schmitt for the U.S. Air Force in 1966. (*Schmitt, 1966*)

REQUIREMENTS	TIME AT SPEED IN RAIN	MAX TEMP °C
Present tactical support aircraft	30 min at Mach 0.7	90
Improved tactical support aircraft	30 min up to Mach 2 (low level)	230
Mach 3.0 military	120 min at Mach 0.9 60 min at Mach 1.5	340
Mach 2.2 SST	300 min at Mach 0.9	260
Mach 3.0 SST	60 min at Mach 1.0	340
High performance missile (to Mach 5)	up to 30 sec; up to Mach 5	1,090

Stage three: Evaluation of the complete radome

OBJECTIVE:

This stage should allow testing of the full structural unit in completed form. This introduces the effects of the mounting; the missile aerodynamics and its effect on heating and drop distortion; and the effects of the finish and quality obtainable in a production item.

TEST REQUIREMENTS:

- a) as close to the environment encountered in operation as possible (table 3.4)

BEST SIMULATION TECHNIQUES TO USE:

Rocket sleds, ballistic ranges and in-flight tests.

REFERENCES

- Adler W.F. and James T.W. "Particle impact damage in ceramics", Office of Naval Research Technical Report for Contract No. N00014-76-C-0744, (1979)
- Adler W.F. "Single water drop impacts on polymethylmethacrylate", Proc. of the Fifth Int. Conf. on Erosion by Liquid and Solid Impact, (ed. J.E. Field), Paper 9, (1979)
- Adler W.F. and Flavin J.W. "Surface launched weaponry materials technology (SURFMAT) program, single particle impact damage on MTP composite ceramic insulation materials", General Research Report for NSWC Contact No. N60921-85-C-1327, Sept. (1987)
- Adler W.F. "Evaluation of the particle impact resistance of advanced radome materials", General Research Report CR-87-1003, Jan. (1987)
- Adler W.F. "Rain Erosion Testing", SPIE Vol.1112 Window and Dome Technologies and Materials, (ed. Klocek), (1989a)
- Adler W.F. "Projectile impact test capabilities", Advanced Technologies Division of General Research, Brochure produced Jan. (1989b)
- Adler W.F. "Multiparticle supersonic impact test program", Window and Dome Technologies and Materials III, Vol. 1326, Paper 32, pp.268-279, (1990)
- Adler W.F. "Supersonic waterdrop impacts on materials", Unpublished paper (1991)
- Adler W.F., Flavin J.W., Richards J.P. and Boland P.L. "Multiple simulated waterdrop impact damage in zinc sulfide at supersonic velocities", SPIE Vol.1760 Window and Dome Technologies and Materials III, (ed. Klocek), (1992)
- Alderson M. "Rain erosion testing in support of engine design", Proc. of the Third Int. Conf. on Rain Erosion and Ass. Phen., (ed. A.A. Fyall and R.B. King), Aug. (1970)
- Anon. "A study of rain erosion of aircraft materials at supersonic velocities", WADC TR 55-195, Aug., (1956)
- Armand C. and Fugain G. "Rain erosion studies in the S3-MA transducer wind tunnel at O.N.E.R.A.", Proc. of the Fifth Int. Conf. on Erosion by Liquid and Solid Impact, (ed. J.E. Field), Sept. (1979)
- Barr K. and Steeger E.J. "Supersonic rain erosion testing of missile radomes", Jet Propulsion, pp.1034-1037, Sept. (1957)
- Behrendt A. "Investigation of parameters of aircraft materials in the velocity range up to 1000 m s^{-1} ", Proc. of the Fourth Int. Conf. on Rain Erosion and Ass. Phen., (ed. A.A. Fyall and R.B. King, RAE Farnborough), pp.425-448, (1974)
- Bigg F.J., McNaughton I.I, and Methven J.J. "The measurement of rain erosion from an aircraft in flight", Royal Aircraft Establishment, M.O.A. Report (1956)
- Blair P.W. "The liquid impact behaviour of composites and some infra-red transparent materials", PhD Cavendish Labs, University of Cambridge, (1981)
- Bowden F.P. and Brunton J.H. "Damage to solids by liquid impact at supersonic speeds", Nature, Vol.181, pp.873-875, (1958)
- Bowden F.P. and Brunton J.H. "The deformation of solids by liquid impact at supersonic speeds", Proc. Roy. Soc. Lond. A, Vol.263, pp.433-450, (1961)
- Brunton J.H. "High speed liquid impact", PhD Cavendish Labs, University of Cambridge, (1959)
- Camus J.J. "High speed flow in impact and its effect on solid surfaces", PhD, Cavendish Labs., University of Cambridge, (1971)
- Campbell A. "Assessment of the rain erosion resistance of composite materials for radome applications", Proc. of Sixth Int. Conf. on Erosion by Liquid and Solid Impact, (ed. J.E. Field and N.S. Corney), Paper 23, Sept. (1983)

- Cook S.S. "Erosion by water-hammer", Proc. Roy. Soc. Lond. A., Vol.119, pp.481-488 (1928)
- Corney N.S. and Minter E.M. "The rain erosion resistance of some transparent materials for aerospace applications", Proc. of Seventh Int. Conf. on Erosion by Liquid and Solid Impact, (ed. J.E. Field and J.P. Dear), Paper 6, (1987)
- Davise P.N.H. "Multiple Impact Jet Apparatus", PhD, Cavendish Labs., University of Cambridge, (1988)
- De Haller P. "Untersuchungen über die durch Kavitation hervorgerufenen Korrosion", Schweizerische Bauzeitung, Vol.101, pp. 243-246, 260-264 (1933)
- De Haller P. Schweizerische Archiv., Vol.6, pp.61, (1940)
- Déom A., Devezeaux de Lavergne D. and Balageas D.L. "Hypervelocity erosion of carbon-carbon composites by laser simulation", Proc. of the Sixth Int. Conf on Erosion by Liquid and Solid Impact, (ed. J.E. Field and N.S. Corney), Paper 65, (1983)
- Déom A., Laturelle F. and Gardette G. "Rain erosion resistance characterization of pure and reinforced slip-cast fused silica by laser simulation", Proc. of the Seventh Int. Conf. on Erosion by Liquid and Solid Impact, (ed. J.E. Field and J.P. Dear), Paper 9, (1987)
- Déom A., Balageas D. and Gardette G. "Rain Erosion and Induced Optical damages of infrared materials - characterization by unique curves", Proc. 7th Int. Conf. on Erosion by Liquid and Solid Impact, (ed. J.E. Field and J.P. Dear), Paper 8, (1987)
- Déom A., Balageas D., Laturelle F., Gardette G. and Freydefont G. "Sensitivity of rain erosion resistance of infrared materials to environment conditions such as temperature and stress", Third Workshop on Passive IR Optical Materials, Brussels, Belgium, Paper 37, 27 - 30 March (1990)
- Dittman W.L., Feldman A.L. and Holmes R.F. "A study of rain erosion testing methods for supersonic speeds", WADC-TR 53-173, Nov. (1953.a)
- Dittman W.L., Holmes R.F., Steeger E.J. et al. "A study of rain erosion testing methods for supersonic speeds", WADC TR 53-173 (1953.b)
- Edwards J. "Comparison of nylon sphere and water jet impact upon glass", Part II Project, Cavendish Laboratory, University of Cambridge, April (1987)
- Eskilsson S. "Rain erosion testing facilities at SAAB and some test results", Proc. Rain Erosion Conf., (ed. A.A. Fyall and R.B. King), 5 - 7 May, (1965)
- Eskilsson S. "Design rules for neoprene coatings", Proc. of the Second Meersburg Conf. on Rain Erosion and Allied Phen., (ed. A.A. Fyall and R.B. King), pp. 319-329, (1967)
- Fasso G. "Wind tunnel rain experiments in the research center at Modane", Proc. of the Rain Erosion Conf. held at Meersburg, (ed. A.A. Fyall and R.B. King), May (1966)
- Fasso G., Leclere G. and Pletin M., "First results of rain erosion tests in the S3 intermittent wind tunnel of the O.N.E.R.A. Modane Test Center", Proc. of the Second Meersburg Conf. on Rain Erosion and Allied Phen., (ed. A.A. Fyall and R.B. King), Aug. (1967)
- Field J.E., Sun Q. and Liu J. "Comparison between nylon sphere impact and liquid impact", Report for British Aerospace, Feb. (1991)
- Fyall A.A. and King R.B. "Rain Erosion Part V: Development of the artificial rainfield on the high speed track at P. & E.E. Pendine", Royal Aircraft Establishment, Report No. Chem 536, Sept. (1962)
- Fyall A.A. and Strain R.N.C. "A 'whirling arm' test rig for the assessment of the rain erosion of materials", Royal Aircraft Establishment, Farnborough, Report No: Chem. 509, Dec. (1956)

- Fyall A.A. "XII. Practical aspects of rain erosion of aircraft and missiles", Phil. Trans. of the Roy. Soc. of Lond., A, No.1110, Vol.260, pp.161-167, (1966)
- Fyall A.A. "Single impact studies with liquids and solids", Proc. of the Second Meersburg Conf. on Rain Erosion and Allied Phen., (ed. A.A. Fyall and R.B. King), pp. 563-591, (1967)
- Fyall A.A. "Radome engineering handbook", (ed. J.D. Walton Jr.) Dekker, New York (1970)
- Gardner F.W. "The erosion of steam turbine blades", The Engineer, Vol.153, pp.146-147, (1932)
- Hackworth J.V. "A mechanistic investigation of the rain erosion of infrared transmitting materials at velocities to Mach 2", Proc. of the Fifth Int. Conf. on Erosion by Liquid and Solid Impact, (ed. J.E. Field), Sept. (1979)
- Hammitt F.G., Hwang J.B., Linh Do, Hammitt F.G. Jr., Huang Y.C., Timm E.E. and Hughes R.D. "Experimental and theoretical research on liquid droplet impact", Proc. of the Fourth Int. Conf. on Rain Erosion and Ass. Phen., (ed. A.A. Fyall and R.B. King), pp. 319-345, May (1974)
- Hancox N.L. "The deformation of solids under repeated liquid impact", PhD Cavendish Labs, University of Cambridge, (1962)
- Hand R.J. "Impact and fracture properties of infra-red and optically transmitting materials", PhD, Cavendish Labs, University of Cambridge, (1987)
- Hengstenberg T.F. Power, Vol.76, pp.118, (1932)
- Heyman F.J. "Conclusions from the ASTM interlaboratory test program with liquid impact erosion facilities", Proc. 5th Int. Conf. on Erosion by Solid and Liquid Impact, Cavendish Labs, University of Cambridge, (1979)
- Hoff G., Langbein G. and Rieger H. "Material destruction due to liquid impact", Erosion by Cavitation or Impingement ASTM STP 408, Am. Soc. Testing Mats., pp.42-69, (1967)
- Honegger E. Brown Bov. Rev., Vol.12, pp.263 (1924)
- Honegger E. Brown Bov. Rev., Vol.14, pp.95 (1927)
- Hurley C.J. and Schmitt G.F. "Development and calibration of a Mach 1.2 rain erosion test apparatus", Technical Report AFML-TR-70-240, Oct. (1970)
- Jenkins D.C. "Erosion of surfaces by liquid drops", Nature Vol. 176, No.4476, pp.303-304, Aug. (1955)
- Jenkins D.C., Booker J.D. and Sweed J.W. "An experimental method for the study of the impact between a liquid drop and a surface moving at high speed", Aeronautical Research Council R & M No. 3203, London, (1961)
- Kenyon H.F. and Scoles G.J. "Erosion by Water Jet Impacts", Associated Electrical Industries Ltd., Research Report, T.P. / R. 5587, Jan (1967)
- King R.B. "Multiple impact rain erosion studies at velocities up to 450 m s^{-1} ($M=1.3$)", Proc. of the Second Meersburg Conf. on Rain Erosion and Allied Phen., (ed. A.A. Fyall and R.B. King, RAE Farnborough), pp. 201-215, (1967)
- Krupovage D.J. Private communication (1991)
- Kunz W. "Design and construction of a rain erosion test facility for velocities up to 1000 m s^{-1} ", Proc. of the Fourth Int Conf. on Rain Erosion and Ass. Phen., (ed. A.A. Fyall and R.B. King), pp.187-198, May (1974)
- Lane W.R. Industr. Eng. Chem., Vol.43, June (1951)
- Lankford J.L. "Final technical report NOL 1000 ft hyperballistics range program, Period Oct 1968, Optical instrumentation and rain program", U.S. Naval Ordnance Laboratory, White Oak, Maryland, (1968)
- Lapp R.R., Stutzman R.H. and Wahl N.E. Wright Air Development Center, Technical Report 53 - 185 Part II (1955)
- Lesser M.B. "The impact of compressible liquids", Ann. Rev. Fluid Mech., Vol.15, pp.97-122, (1983)

- Letson K.H.** "Influence of fiber loading on rain erosion behaviour of polytetrafluoroethylene (PTFE)", Proc. of Fifth Int. Conf. on Erosion by Liquid and Solid Impact, (ed. J.E. Field), Sept. (1979)
- Marriott J.B. and Rowden G.** "The erosion of a cobalt-chromium alloy by liquid impact", Phil. Trans. A., Vol.260, pp.144-149, (1966)
- Morris J.W. and Bates C.H.** "Rain erosion of aluminium at velocities of 730 - 2240 ft/s", Proc. of the Third Int. Conf. on Rain Erosion and Ass. Phen., (ed. A.A. Fyall and R.B. King), pp.261-302, Aug. (1970)
- Mortenson R.B.** "Rain erosion testing from 1 to 6 km s⁻¹", Proc. of the Third Int. Conf. on Rain Erosion and Ass. Phen., (ed. A.A. Fyall and R.B. King), pp.65-106, Aug. (1970)
- Mortenson R.B.** "Advanced erosion test facilities", Proc. of the Fourth Int. Conf. on Rain Erosion and Ass. Phen., (ed. A.A. Fyall and R.B. King), pp.155-185, May (1974)
- Mortenson R.B.** "Erosion testing on wheels", Proc of the Fifth Int. Conf. on Erosion by Liquid and Solid Impact, (ed. J.E.Field), Paper 21, Sept. (1979)
- Mousson J.M.** Trans. Amer. Soc. Mech. Eng., Vol.59, pp.399, (1937)
- Nicholson J.E.** "Drop breakup by airstream impact", Proc. Second Meersburg Conf. on Rain Erosion and Allied Phen., pp.263-298, (1967)
- Phillips L.N.** "The protection of Durestos and glass fibre laminates from high speed rain erosion", RAE Tech. Note Chem. 1159, Dec. (1951)
- Pirri A.N.** The Physics of Fluids, Vol. 20, No.2, pp.221-228, (1983)
- Rickerby D.G.** "High velocity liquid impact and fracture phenomenon", PhD Cavendish Labs., University of Cambridge, (1976)
- Rieger H.** "Investigation of the influence of various test parameters on material destruction at drop impact", Proc. of the Third Conf. on Rain Erosion and Ass. Phen., (ed. Fyall and King, RAE Farnborough), pp.147-205, (1970)
- Robertson R.McG., Lobisser R.J. and Stein R.E.** "High speed rain abrasion of glass cloth laminates", Ind. Eng. Chem., Vol.38, pp.590-591, (1946)
- Schaefer W., Koidl P. and Sah R.E.** "Rain erosion resistance of hard carbon coated germanium", Report to AC/243 (Panel III, RSG2), Third Workshop on Passive Infrared Optical Materials and Coatings, NATO Headquarters, Brussels, (1990)
- Schmitt G.F.** "Current investigations in rain erosion by the U.S. Air Force", Proc. U.S.A.F. - Georgia Inst. Tech. Symp. Electromagnetic Windows, (1966)
- Schmitt G.F.** "Polyurethane coatings for rain erosion protection", Proc. of the Second Meersburg Conf. on Rain Erosion and Allied Phen., (ed. A.A. Fyall and R.B. King), pp.329-357, (1967)
- Schmitt G.F.** "Erosion behaviour of polymeric coatings and composites at subsonic velocities", Proc. of the Third International Conf. on Rain Erosion and Ass. Phen., (ed. A.A. Fyall and R.B. King), pp.107-128, (1970)
- Smith A.** "XVIII. Physical aspects of blade erosion by wet steam in turbines", Phil. Trans. A., Vol.260, pp.209-215, (1966)
- Steeger E.J., Sedlund F.R., Dittman W.L. and Holmes R.F.** "Rain erosion tests of radome materials mounted on supersonic rocket sleds", WADC TR 57-203, (1957)
- Sullivan R.J. and Hockridge R.R.** "Simulation techniques for hypersonic erosion phenomena", Proc. of the Fourth Int. Conf. on Rain Erosion and Ass. Phen., (ed. A.A. Fyall and R.B. King), pp. 109-154, May (1974)
- Tattershall P.** Private communication
- Tattershall P. and Minter E.M.** "The rainfield conditions of the DRA aerospace division whirling arm rain erosion facility", DRA Aerospace Division, Tech. Report 91063, (1991)

- Tatnall G.J., Foulke K.W. and Schmitt G.F.** *"The United States Air Force - Navy supersonic rain erosion program for 1966"*, Proc. of the Second Meersburg Conf. on Rain Erosion and Allied Phen., (ed. A.A. Fyall and R.B. King), pp. 239-262, Aug. (1967)
- Taulbee D.B.** *"Aerodynamic and drop breakings in the rain erosion testing facility"*, Bell Report No.9153-940013, March (1965)
- Thomas G.P.** *"Deformation of metals by the repeated impact of liquids"*, PhD Cavendish Labs., University of Cambridge, (1966)
- Vater M.** Zeit. des Ver. Deut. Ing., Vol.81, pp.1305, (1937)
- Vater M.** Zeit. des Ver. Deut. Ing., Vol.82, pp.672, (1938)
- Vater M.** Zeit. des Ver. Deut. Ing., Vol.20, pp.171, (1944)
- Vogel** Private communication (1991)
- Von Schwarz M and Mantel W.** Zeit. des Ver. Deut. Ing., Vol.80, pp.863, (1936)
- Wahl N.E.** Air Force Technical Report No. 5686, (1948)
- Wahl N.E.** *"Study and design of supersonic rotating arm test apparatus"*, Proc. of the Second Meersburg Conf. on Rain Erosion and Allied Phen. (ed. Fyall and King, RAE Farnborough), pp.215-237, (1967)
- Wahl N.E.** *"Supersonic rain and sand erosion research: Design, construction, and operation of a Mach 3 rotating arm apparatus"*, AFML TR-69-287, Pt I, (1969)
- Wahl N.E.** *"Design and operation of Mach 3 rotating-arm erosion test apparatus"*, Proc. of the Third Int. Conf. on Rain Erosion and Ass. Phen., (ed. A.A. Fyall and R.B. King), pp.13-42, Aug. (1970)
- Walton J.D. and Gorton C.W.** *"Evaluation of ceramic coatings for rain erosion protection"*, Proc. of the Third Int. Conf. on Rain Erosion and Ass. Phen., (ed. A.A. Fyall and R.B. King), pp. 209-217, Aug. (1970)

Threshold Evaluation For A Brittle Material

This chapter briefly describes the impact of a liquid drop with a solid, and some of the more important damage mechanisms that this impact produces in a brittle material. In particular the concept of a threshold velocity for damage is explored, and the first attempts to evaluate this with MIJA are presented.

4.1 THE IMPACT OF A LIQUID

The impact of a spherical drop of water onto a solid surface has been carefully analysed by a number of authors (Bowden and Field, 1964, Lesser, 1981, and Lesser and Field, 1983a,b). The impact process is typically broken down into two distinct stages. In the first stage the liquid behaves in a compressible manner, whilst the edge of the contact area between the impacting liquid and the solid moves supersonically with respect to the speed of sound in the liquid. The pressure generated in this stage is known as the water-hammer pressure and is given by the expression:

$$P = v \frac{\rho_1 C_1 \rho_2 C_2}{\rho_1 C_1 + \rho_2 C_2} \quad (4.1.1)$$

where v is the impact velocity, and $\rho_{1,2}$ and $C_{1,2}$ are the densities and the shock wave velocities in the liquid and solid respectively.

After this stage there is a period of incompressible flow, in which the pressure drops to the Bernoulli 'stagnation' pressure given by:

$$P = \frac{1}{2} \rho_1 v^2 \quad (4.1.2)$$

For a 2 mm spherical drop (radius, r) travelling at 500 m s^{-1} the water-hammer pressure is 10 times the stagnation pressure, but its duration given by $(3rv/2C_1^2)$, is only $0.1 \mu\text{s}$.

As a result of the impact with a brittle solid three types of stress waves are generated: a compressional wave, a shear wave, and a Rayleigh surface wave (figure 4.1.1). The damage produced on the brittle solid is primarily a result of the interaction of the Rayleigh waves with pre-existing flaws (Bowden and Field, 1964). This waves peak intensity decreases with distance from the damage site, but at the same time the pulse broadens (Blowers, 1969). The cracks formed are therefore typically short and circumferential, but the longest ones are actually a little way out as a result of the changing shape of the Rayleigh pulse. Cracks opened up in this way typically have a lip facing the impact site. This can be exploited subsequently by the lateral outflow jetting which may be travelling at several times the velocity of the incoming drop, and scabs of material may be removed from the outside of a crack. Finally if there is water trapped in the crack or in a pit there can be a strong hydrodynamic effect which can increase the level of damage (Field, 1967).

The impact of a jet of water can be used to simulate the water-hammer pressure generated during the initial stage of the impact of a spherical drop. It is this pressure

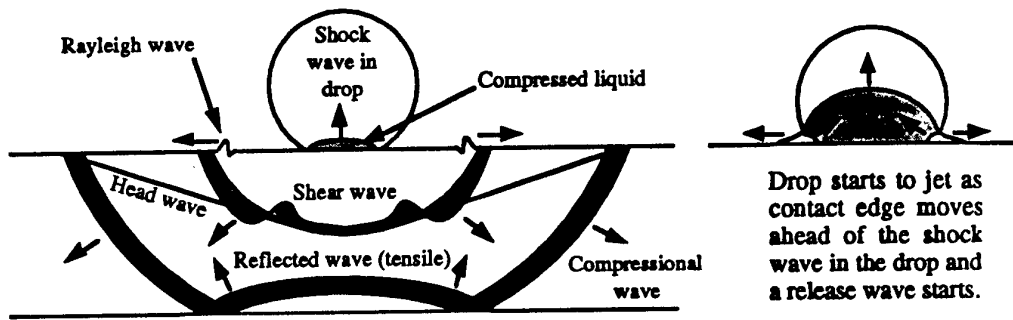


Figure 4.1.1 Impact of a spherical drop on a material showing the shock wave in the drop and the stress waves in the material. The shaded width of the shear and compressional waves represent the relative amplitudes of particle motion. (Woods, 1968)

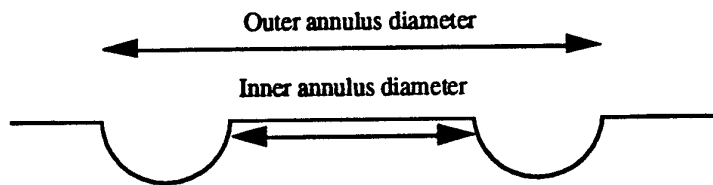


Figure 4.1.2 Cross section of the damage annulus obtained on PMMA showing the inner annulus diameter measured by Rickerby (1976) to obtain his equivalent drop sizes, and the outer annulus diameter used by Hand (1987).

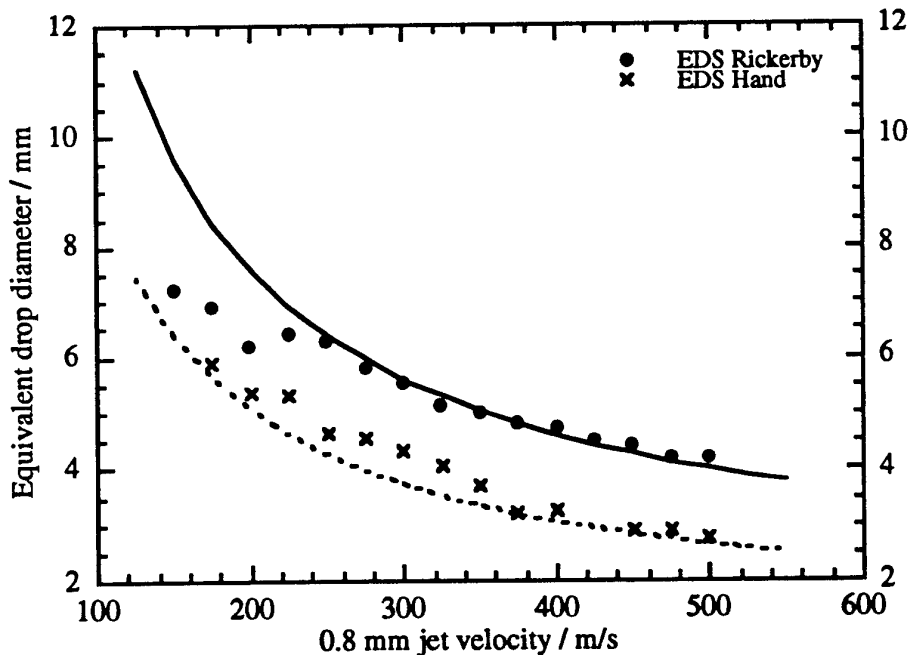


Figure 4.1.3 Equivalent drop data produced using the correlations of Hand (1987) and Rickerby (1976).

that causes the most damage during an impact with a brittle material, and the fact that the incompressible flow phase is longer with a jet impact is relatively unimportant at impact velocities close to the threshold. Equivalence curves for comparing the impact of a jet and a spherical drop, have been constructed by comparing the damage marks produced by jets and drops of identical velocities on PMMA. The first attempt to create such an "equivalent drop curve" was performed by Rickerby (1976) and involved comparing measurements of the inner radius of the damage annulus produced by jets on PMMA, with those of spherical drops (figure 4.1.2). The more recent attempt of Hand (1987) instead compared the total damage area of the two impacts (figure 4.1.3), this appears to be more appropriate for brittle materials.

4.2 THE THRESHOLD VELOCITY FOR DAMAGE

4.2.1 Definition of Damage Threshold

Following a liquid impact on a solid, Rayleigh waves emanate from the contact site and pass over surface flaws in the material. As these waves travel the pulse magnitude decreases and broadens, and its energy is hence dispersed. However if as they pass over a crack these stress waves are of a suitable magnitude and duration that the stress intensity factor reaches its critical value, the crack will grow in length. Whether this condition is met depends on the material fracture toughness, the elastic wave velocity, and the size distribution of preexistent surface flaws, as well as the water drops size and velocity. If no flaws of a suitable size exist on a site to allow growth as a result of a particular impact, then the material should be able to stand repeated impacts of that type on the same site without suffering damage.

For the sake of comparison a spherical 2 mm drop is typically chosen for standardisation of threshold values in the literature. To convert a threshold velocity from one drop diameter to another a relation given by Field et al (1979) can be used: $U_2/U_1 = (d_1/d_2)^{1/3}$ where $U_{1,2}$ are the old and new threshold velocities and $d_{1,2}$ the relevant drop diameters (figure 4.2.5). The threshold velocity therefore refers to the maximum velocity at which a 2 mm drop can hit a specified material without increasing the flaw sizes. Because of the statistical distribution of cracks in the material, this velocity may vary from site to site, however experience has shown that for a well-polished material a threshold velocity can be defined that is applicable to impact anywhere on its surface.

4.2.2 Correlation with Material Properties

An attempt was made to model the threshold velocity theoretically by Evans (1978) and Evans et al. (1980). The relation they produced showed the threshold velocity could be related to the material's properties by the equation $K_c^{2/3} C_t^{1/3}$, where K_c was the critical stress intensity factor, and C_t the wave speed in the material given by $(\text{Youngs modulus} / \text{density})^{1/2}$. This relation was used by Tustison and Gentilman (1988) as a 'damage parameter' for the material, and a graph of this 'damage parameter' plotted against the threshold velocity results for materials tested on the whirling arm rig can be seen in figure 5.4.1.

The threshold values produced using MJA have also been plotted against various different material properties, and combinations of these properties. The best fit has been obtained by plotting the threshold velocity against the log of the fracture toughness as seen in figure 4.2.2, and the fit obtained using the expression of Evans is not quite as good (figure 4.2.1).

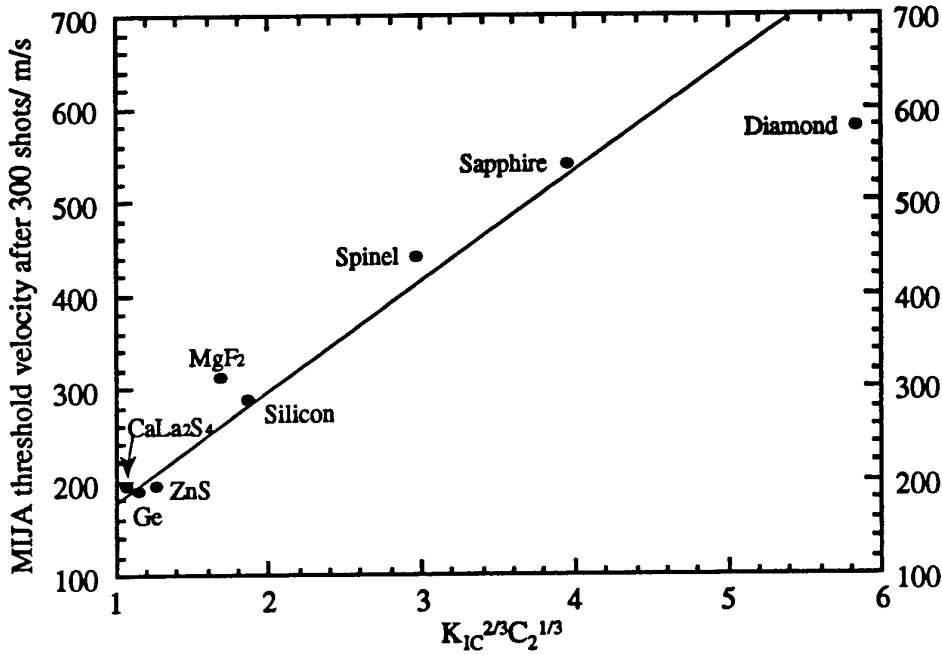


Figure 4.2.1 MIJA threshold velocities for circumferential damage compared to the theoretical threshold velocities predicted using the expression of Evans (1978).

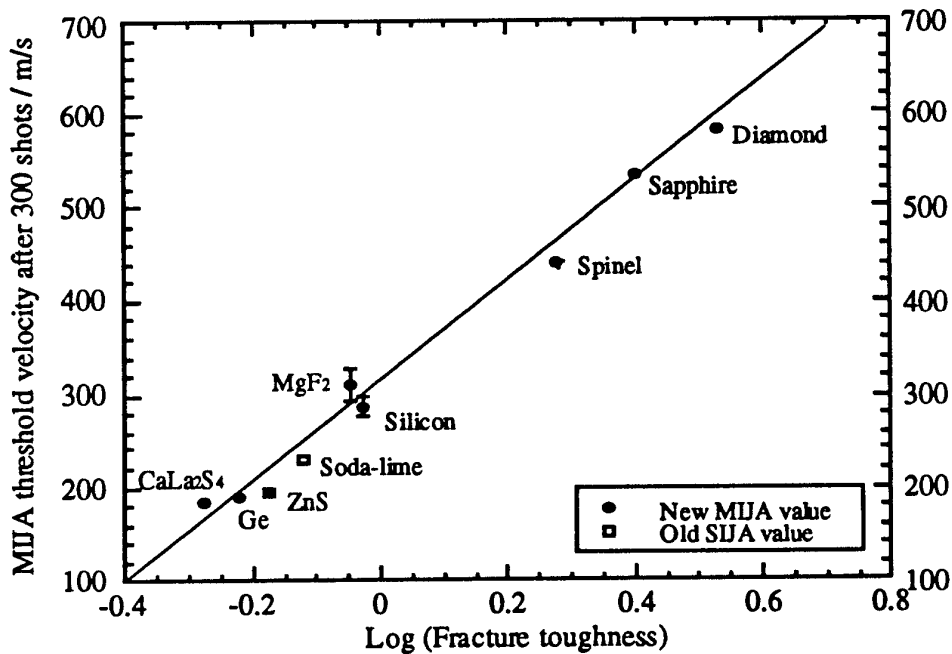


Figure 4.2.2 MIJA and SIIA threshold velocities for circumferential damage plotted against the log of the fracture toughness (Seward, 1993).

Whirling arm data is more commonly plotted using a relation of the form $t = kV^{-n}$, where t is the incubation time, V the impact velocity and k and n experimentally determined parameters. When plotted on a log - log scale this relation produces a straight line that suggests that damage can be obtained at any velocity if sufficient impacts are performed. The results from whirling arms that appear in the literature are consistent with this expression, however this is not irreconcilable with the idea of a threshold, as it is conceivable that the damage proceeds according to this relation until it reaches the threshold value, and that whirling arm tests are not normally performed for long enough, or with carefully controlled enough conditions to demonstrate this.

It is hoped that with MIJA a set of experiments might be performed to try and indicate whether a threshold really exists or not. In the meantime a threshold velocity criteria has been chosen as the maximum velocity that can be fired on a site 300 times without creating any circumferential damage. Other types of impact damage such as central pits, radial scuffing and radial cracks are now also known to occur, however these are currently not used in the definition of the threshold velocity for damage. Future studies of their cause and effects may result in a change in this definition.

4.2.3 SIJA Threshold Evaluation

The most sensitive way to measure the threshold velocity using SIJA is by using a mechanical strength test after five impacts. However to complete a single threshold evaluation using this technique requires approximately 20 one inch discs. To start with three discs are broken in a hydraulic pressure tester to determine their undamaged fracture stress (figure 4.2.3). The remaining discs are then impacted five times each in their centre with a water jet of a selected velocity. The velocities are chosen so that two or three discs are tested for each velocity near to the estimated threshold. This allows an average fracture stress for that velocity to be determined. The values of average fracture stress for the velocities tested are then plotted on a graph as shown in figure 4.2.4, and the threshold estimated from the drop in strength.

This evaluation method relies on the fact that once a material is impacted above its damage threshold, each impact will cause an extension of the microcracks in the surface. These microcracks may still be too small to be visible, but they should cause a deterioration of the mechanical strength of the specimen once they have grown to a size larger than the biggest naturally occurring scratch. This may take several shots for velocities near the threshold, and partly explains why the residual strength curve becomes sharper as larger numbers of impacts are used.

Although strength testing is probably the more sensitive method of damage assessment in the evaluation of a threshold, many SIJA users prefer to carry out a microscopic examination after just 5 - 10 impacts instead. As will be seen in section 6.4, such a method can result in a large overestimate of the threshold velocity, and the value obtained is therefore not the 'absolute' threshold velocity for damage. Nevertheless this additional information is useful in understanding the erosion characteristics of the material, particularly with regard to transmission loss.

Although the SIJA mechanical threshold evaluation technique is a useful one, its main drawbacks are that it is time consuming; has an accuracy of 5 - 10 %; uses large numbers of discs which are often exotic or expensive; and the different methods of damage assessment can lead to a variation in the threshold value quoted.

4.3 MIJA THRESHOLD EVALUATIONS

A method of evaluating a threshold with MIJA was sought so that the maximum amount of information could be extracted out of the smallest number of discs, and so that the threshold value obtained would be as reproducible as possible. The basic idea

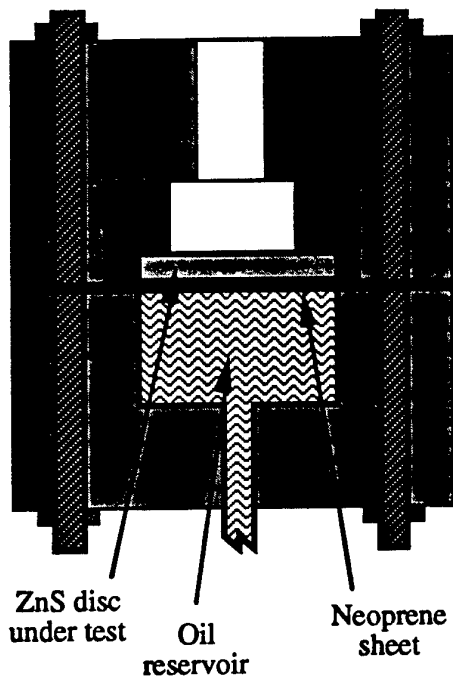


Figure 4.2.3 Bursting disc apparatus, showing a ZnS disc being pressurised by the oil reservoir underneath until it breaks.

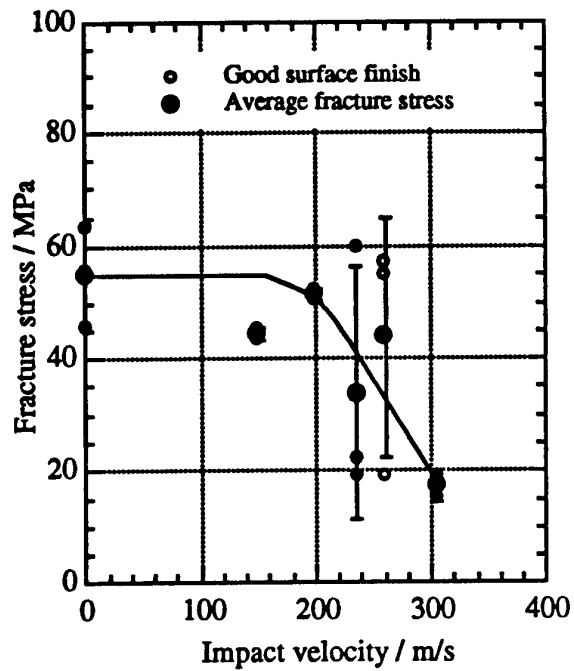


Figure 4.2.4 Plot of the residual fracture stress obtained from the bursting disc test against the water jet impact velocity.

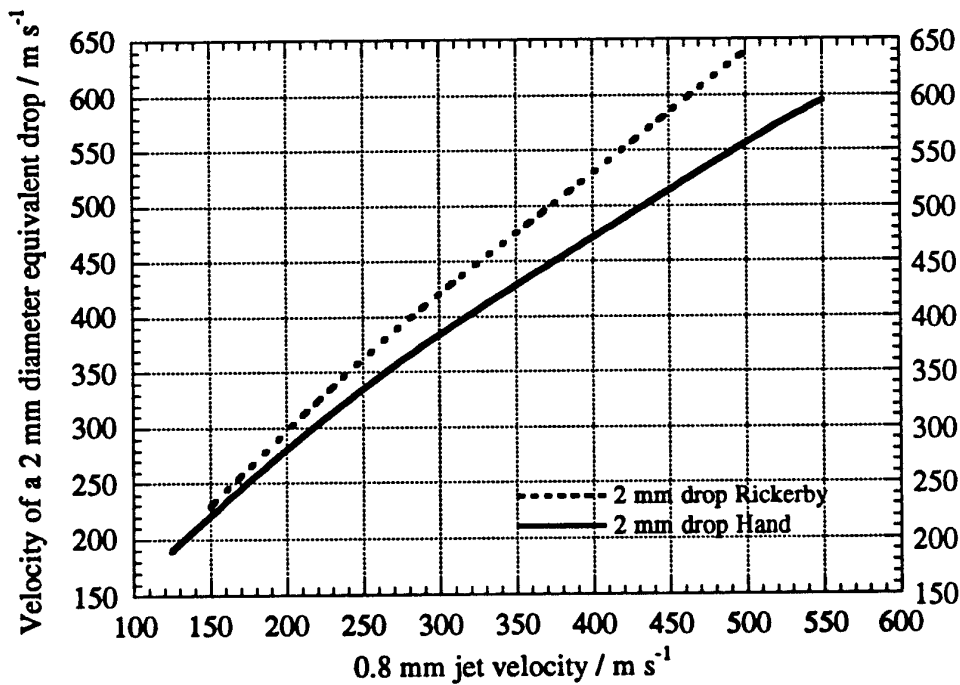


Figure 4.2.5 Conversion chart from a 0.8 mm jet threshold velocity to that of a 2 mm drop using the correlations obtained by Hand (1987) and Rickerby (1976).

behind all four test techniques outlined below, is that initially only an impact with a velocity above the damage threshold will extend microcracks and these cracks will be too small to see. However if repeated impacts occur at that velocity then the microcracks will continue to grow until they become visible. This means that the 'absolute' threshold velocity can be estimated without the need for a destructive residual strength test, and the test thus requires fewer samples.

4.3.1 The 'Petal' Test

The first threshold evaluation technique involved firing 30 shots at each of six sites around a hexagon as shown in figure 4.3.1. Each set of 30 impacts was performed at a higher velocity than the last one, and the sites were positioned so that they overlapped. After these impacts had been performed, 10 further impacts were positioned on a site in the centre of the hexagon. These final 10 impacts had a velocity known to be above the threshold so that damage was guaranteed, and were intended to enable any microcracks grown by the previous impacts to extend to a size where they would become visible, but to do so in a manner that preserved their original orientation. The result can be seen in plate 8.3.1 where the top 'petal' pattern is mostly just below the threshold, and the bottom 'petal' pattern just above (figure 4.3.1). In the bottom 'petal' pattern damage can be seen crossing the central impact site for all six hexagon sites, even though it is not visible elsewhere.

At the time when this test was used the spread in jet velocities was 3 - 5 %. Even so the threshold value obtained for zinc sulphide was 125 m s^{-1} , which is extremely close to the value obtained by the present method (section 5.5). An attempt to determine the threshold for germanium carbide coated zinc sulphide using the same technique, was less successful, because detailed overlap damage could not be seen through the opaque coating, and a different technique was therefore needed.

4.3.2 Statistical Threshold Evaluation

Four discs of germanium carbide coated zinc sulphide were available for testing. Known as PPZ-23, two of the samples had coatings that were well bonded and two had coatings that were poorly bonded. The specimens were 25 mm in diameter, and 56 impact sites were selected for damage assessment on each disc. The test procedure consisted of firing 30 shots at each impact site, and recording the maximum velocity fired and whether damage was visible or not. The results were plotted on the graphs shown in figure 4.3.2. The bar graph shows the number of impact sites tested at a particular velocity, and the points indicate the fraction of the sites that survived.

The probability for survival for the two batches of coated samples had the same initial drop-off value of 130 m s^{-1} , and there appeared to be no differences between the well bonded and poorly bonded specimens. The problem with this test, was that 30 impacts per site was a fairly arbitrary number, and as is shown in chapter 5, two materials may share the same threshold after 30 impacts, but one may be better than the other after just 1, or after 300 impacts.

4.3.3 Threshold Evaluation For Large Samples

The current technique for threshold evaluation has been made possible by the reduction in the velocity spreads. In this technique the specimen is initially impacted once on a number of different sites, each at a different velocity (figure 4.3.3). The impact sites are then examined microscopically and the velocity at which damage

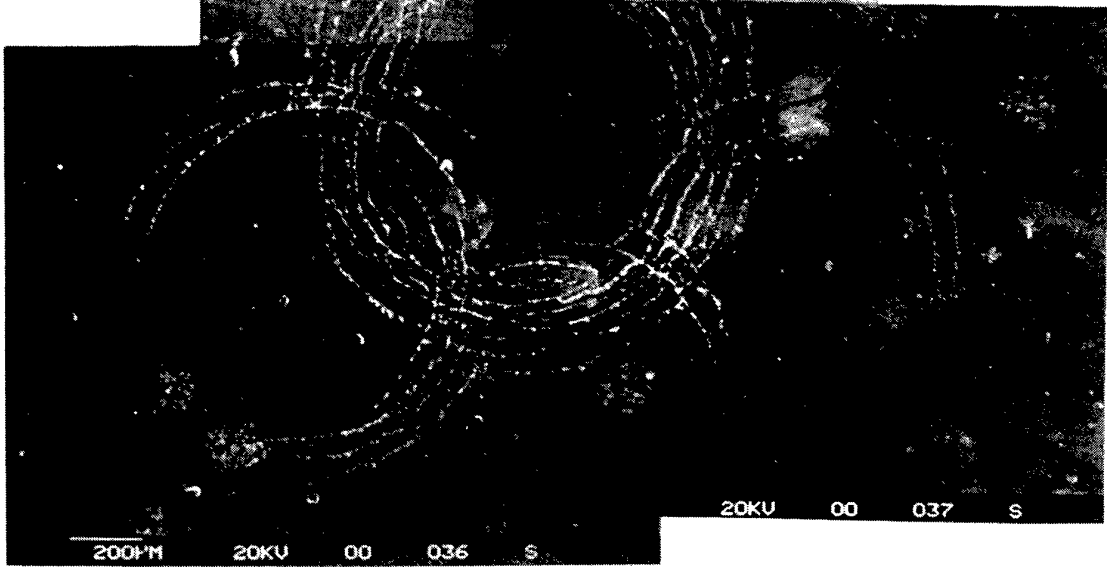
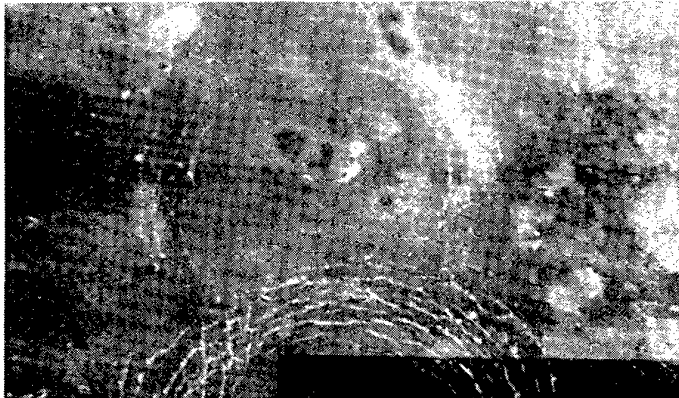
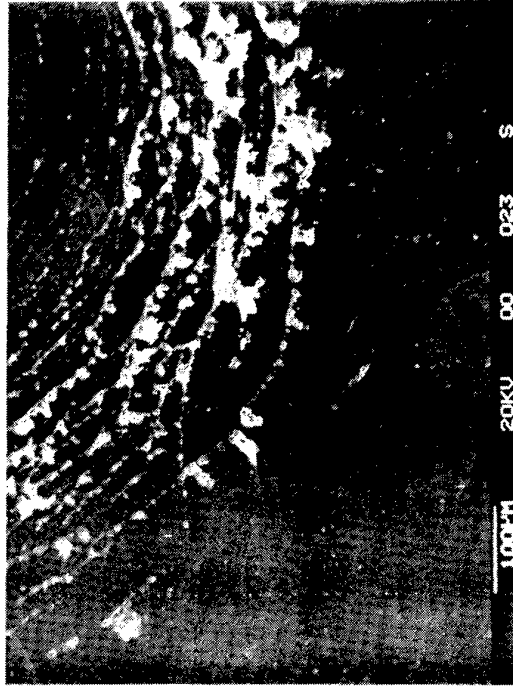
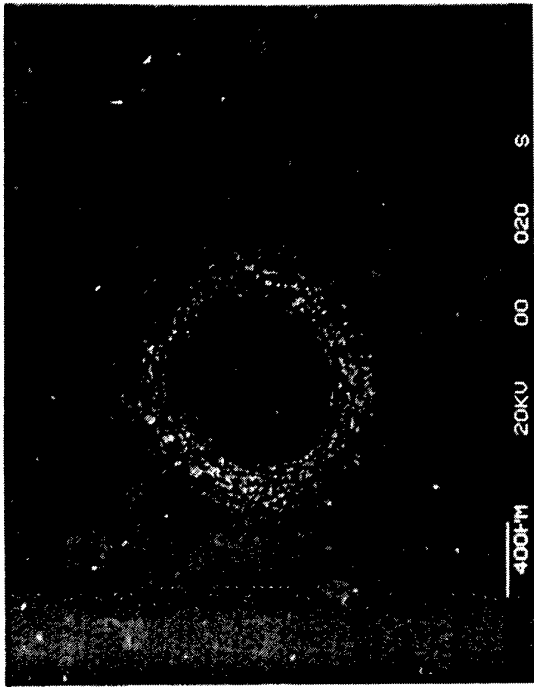


Plate 8.3.1 Interaction of damage sites in the "petal" test (see section 8.3.1).

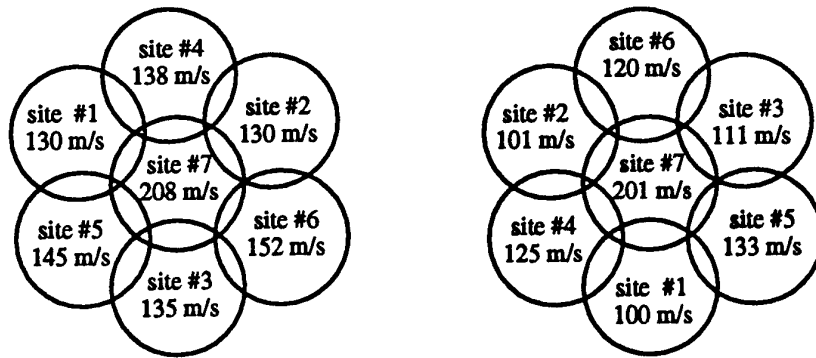


Figure 4.3.1 Patterns and velocities used for the 'petal' test. The petal on the left is the petal on the bottom of plate 8.3.1 and the one on the right is at the top of the plate.

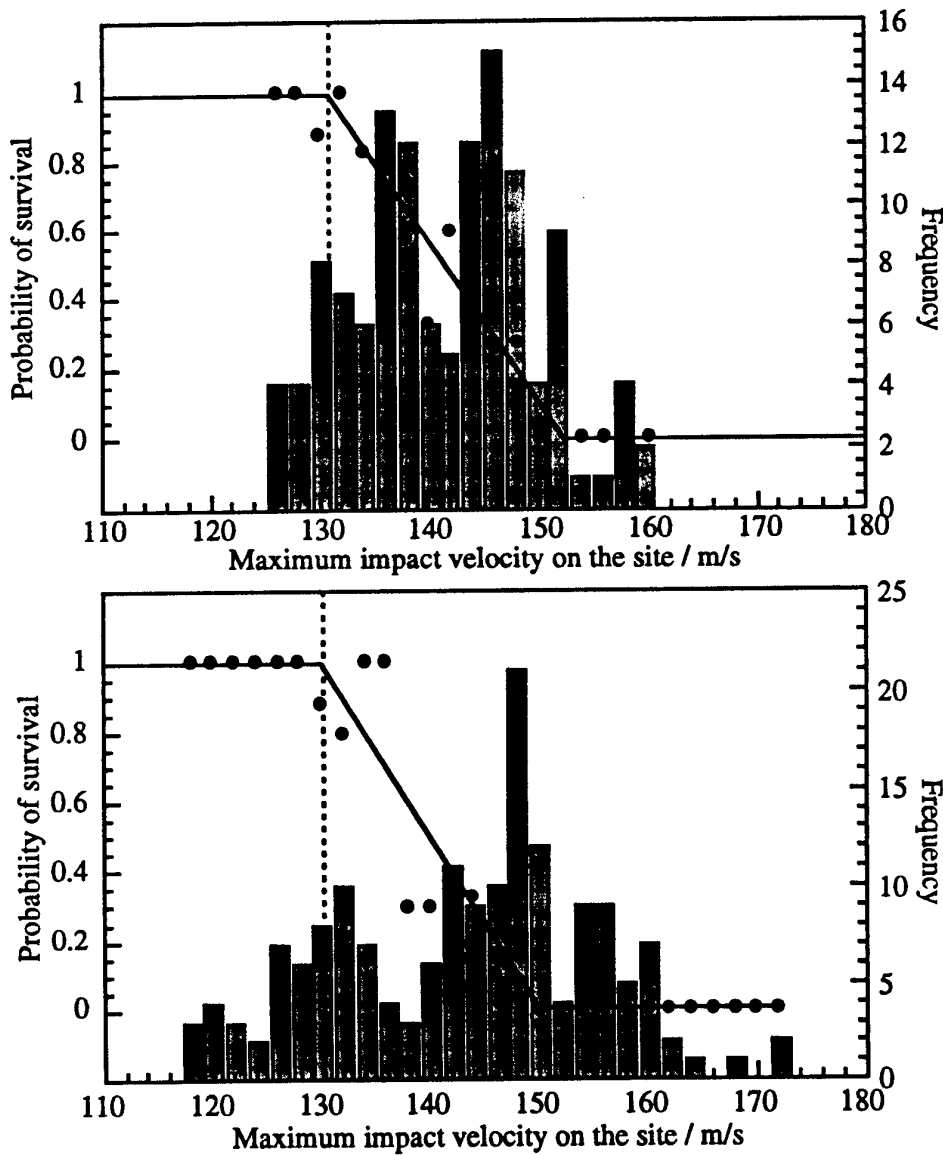


Figure 4.3.2 GeC coating on ZnS - (top) well bonded (bottom) poorly bonded.

becomes visible is noted. The specimen can then be relocated on MIJA so that a second array of impact sites can be fired on top of the first, with each site being impacted at the same velocity as on the first run. The sample is then inspected for damage again, and this procedure is repeated for 1, 2, 3, 5, 10 etc. impacts and a graph of the threshold velocity for visible damage as a function of increasing number of impacts can hence be obtained. This graph appears to flatten out as the visible threshold velocity approaches the mechanical value determined by SIJA (Seward, 1992). The number of impact sites that can be fitted onto one disc depends on the spacing required between impact sites to ensure that damage on adjacent sites does not interact. On some materials impacted at low velocity, such as ZnS, seventeen sites can be fitted onto a single 25 mm disc, and thus a whole threshold curve can be extracted from one sample. On other samples where the impact velocity required is higher the sites need to be spaced out further, and therefore, for example, it is only possible to fit 5 or 6 impact sites on a 25 mm disc of sapphire.

4.3.4 Threshold Evaluation For Small Samples

When a sample is only large enough to fit one impact site on it then a different approach to that of section 4.3.3 has to be used and a full threshold curve cannot be obtained. Testing in this case commences at a velocity below that of the expected threshold, and the number of impacts is gradually increased as before. The specimen is examined regularly, as with the threshold evaluation for a larger sample, and if no damage is detected after 300 impacts then the velocity is incremented and the process repeated. This procedure continues with the velocity being incremented after each 300 impacts until damage is eventually detected. The velocity at which damage is finally detected, and the velocity just below it, should therefore bound the threshold velocity for damage. The data in the bottom graph of figure 4.3.3 would therefore be gradually building up in horizontal rows, and no information would eventually be obtained for the samples performance above the threshold.

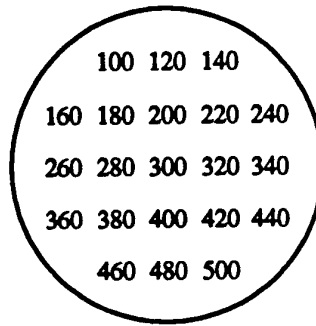
4.4 CONCLUSION

Every brittle material has a damage threshold velocity (DTV) above which impacts will lengthen existing micro-flaws, and therefore reduce the strength of the sample. Providing sufficient impacts are applied to one site above the threshold velocity the micro-flaws will eventually grow to become visible, and they will then also cause transmission loss. Using SIJA the most sensitive method of finding the threshold velocity is by assessing the strength loss. However because of the number of samples and time required this is rarely done in practice. Instead with SIJA a visual threshold velocity evaluation is often carried out after just 5 - 10 impacts.

It is essential to differentiate between visual determinations of the threshold velocity carried out using small numbers of impacts on SIJA, and those carried out with MIJA using 300 impacts which should be a better approximation to the 'absolute' mechanical value. A method of notation has therefore been introduced (see p1) so that all threshold values obtained indicate if they were obtained using a water jet technique and the method of damage assessment. For example 0.8 mm jet DTV (10 impacts) = $130 \pm 10 \text{ m s}^{-1}$, or 0.8 mm jet DTV (mechanical) = $210 \pm 20 \text{ m s}^{-1}$.

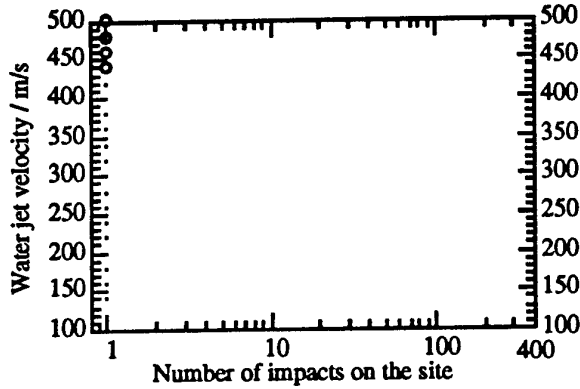
The standard MIJA tests are described in section 4.3.3 and 4.3.4. The 0.8 mm jet DTV (X impacts) is the average of the highest velocity that was fired for X impacts without causing damage and the lowest velocity that was fired for X impacts that caused circumferential cracking. Other damage mechanisms have now also been seen on a number of materials, and these mean that the threshold definition may have to be altered, however for the time being only circumferential cracking is being considered.

Disc with 21 impact sites defined on it.
The location of each site is indicated by
the velocity that is to be fired on it.

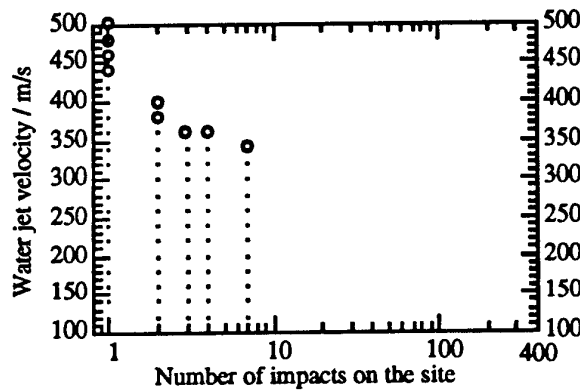
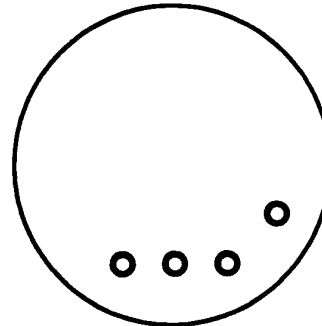


KEY for graphs below

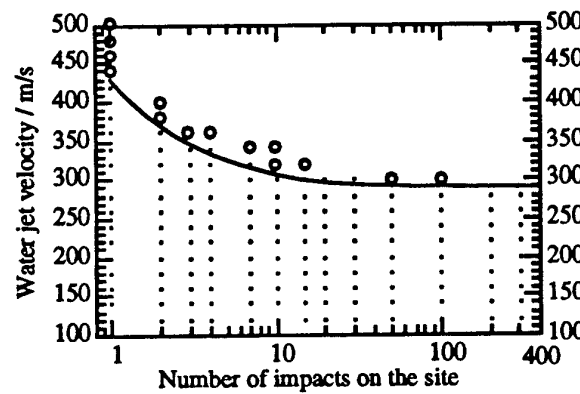
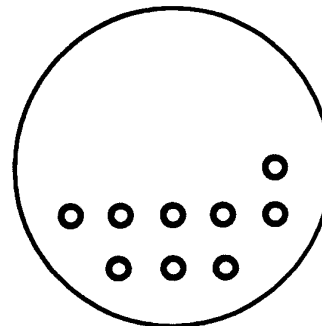
• No damage ○ Circumferential cracking



1 shot per site



7 shots per site



300 shots per site

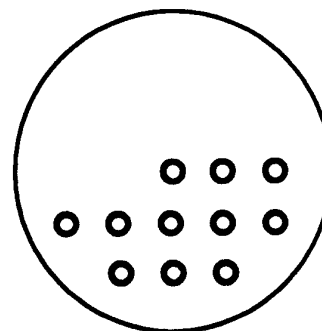


Figure 4.3.3 Illustration of how a threshold velocity curve is constructed for a specimen (Seward, 1992)

REFERENCES

- Blowers R.M. "On the response of an elastic solid to droplet impact", J. Inst. Maths Applcs., Vol.5, pp.167-193, (1969)
- Bowden F.P. and Field J.E. "The brittle fracture of solids by liquid impact, by solid impact and by shock", Proc. Roy. Soc. Lond. A, Vol.282, pp.331-352, (1964)
- Evans A.G. "On impact damage in the elastic response regime", J. Appl. Phys., Vol.49, pp.3304-3310, (1978)
- Evans A.G., Ito Y.M. and Rosenblatt M. "Impact damage thresholds in brittle materials impacted by water drops", J. Appl. Phys., Vol.51, No.5, pp.2473-2482, (1980)
- Field J.E. "The importance of surface topography on erosion damage", Proc. of the Second Meersburg Conf. on Rain Erosion and Allied Phen., (ed. A.A. Fyall and R.B. King), RAE Farnborough, pp.593-604, (1967)
- Field J.E., Gorham D.A. and Rickerby D.G. "High speed liquid jet and drop impact on brittle targets", ASTM STP 664, Erosion: Prevention and useful applications, (ed. W.F. Adler), pp.298-319, (1979)
- Hand R.J. "Impact and fracture properties of infrared and optical transmitting materials", PhD, Cavendish Labs., University of Cambridge
- Lesser M.B. "Analytic solutions of liquid-drop impact problems", Proc. Roy. Soc. Lond. A, Vol.377, pp.289-309, (1981)
- Lesser M.B. and Field J.E. "The impact of compressible liquids", Ann. Rev. Fluid Mech., Vol.15, pp.97-122, (1983a)
- Lesser M.B. and Field J.E. "The geometric wave theory of liquid impact", Proc. 6th Int. Conf. on Erosion by Solid and Liquid Impact (eds. J.E. Field and N.S. Corney), Cavendish Labs., Cambridge, U.K. paper 17, (1983b)
- Rickerby D.G. "High velocity liquid impact and fracture phenomena", PhD, Cavendish Labs., University of Cambridge, (1976)
- Tustison R.W. and Gentilman R.L. "Current and emerging materials for long wavelength infrared external windows", SPIE Vol.968, Ceramics and Inorganic Crystals for Optics, Electro-Optics, and Nonlinear Conversion, pp.25-34, (1988)
- Woods R.D. "Screening of surface waves in soils", J. Soil Mech. Founds Div. Am. Soc. Civ. Engrs., Vol.94, pp.951-979, (1968)

Chapter 5

Liquid Impact of IR Materials

This chapter investigates the response of a variety of infrared transmitting materials to impact by a liquid. Nearly all of the testing has been carried out on MIJA, however a comparison with SIJA results has been performed for completeness.

INTRODUCTION

In this chapter the method of threshold evaluation outlined in section 4.3.3 was used to investigate the rain erosion properties of 14 different IR transmitting materials. The materials investigated were as follows:

1. Sapphire
2. Spinel
3. Magnesium Fluoride
4. Silicon
5. Zinc Sulphide
6. Natural Type IIA Diamond
7. Germanium
8. Calcium Lanthanum Sulphide
9. CVD Diamond
10. Zinc Sulphide with an Amorphous Diamond coating
11. A composite of Zinc Sulphide with Diamond particles
12. BK7 glass with a Silicon Nitride coating
13. Zinc Sulphide with a Germanium Carbide coating
14. Boron Phosphide coatings on Zinc Sulphide, Germanium and Sapphire

For each material investigated the results section is broken down into five parts:

1. Material Characteristics

This lists some of the mechanical, thermal and physical properties of the material that are important in its use as an IR window or radome. In this section the thermal shock figure of merit used is that developed to rank materials for their resistance to a mild thermal shock by Hasselman (1970).

2. Material Description

In this section some of the manufacturing processes currently used to fabricate the material are described, along with the materials main limitations in its use as an IR window. This is done so that the origin of some of the materials quoted in the literature can be better understood, and comparisons of rain erosion results only made where appropriate.

3. Published Rain Erosion Work

This presents some of the results already published in the literature on the material under investigation.

4. MIJA Results

The threshold curves and SEM photos of the material investigation on MIJA are presented, along with observations on the different features that can be seen in the impact damage marks.

5. Conclusion

The MIJA results are compared to those of other experimenters where appropriate, and points requiring further investigation are noted.

N.B. All threshold velocities from MIJA and SIJA have been evaluated and written using the notation described in section 4.4 and p.1 i.e. "0.8 mm jet DTV (X impacts)" where X indicates the number of impacts before microscopic inspection of damage

5.1 SAPPHIRE (ALUMINIUM OXIDE)

5.1.1 Material Characteristics

The values given below are those for a 0^0 cut with the (0001) plane normal to the surface. The data is taken from Savage (1985), Gentilman et al. (1986, 1989), Fisher et al. (1990) and Klocek (1991).

Mechanical

Knoop hardness : 1,800 - 2200 kg / mm²

Fracture stress : 360 - 400 MPa

Fracture toughness : 2.5 MPa m^{1/2} at 25 °C
drops to 1.8 MPa m^{1/2} at 600 °C

Shear modulus : 148.14 GPa

Youngs modulus : E_c 436 GPa
 E_a and E_m 384 GPa

Poissons ratio : 0.27

Weibull modulus : 3.3 - 4.0

Rain erosion resistance (see section 4.4)

0.8 mm jet DTV (300 impacts): 485 ± 5 m s⁻¹

Thermal

Melting point : 2,040 °C

Thermal conductivity : 24 W m⁻¹ K⁻¹

Thermal expansion : $5.6 - 8.8 \times 10^{-6}$ K⁻¹

Heat capacity : 418 J Kg⁻¹ K⁻¹

Thermal shock resistance : 2.1 kW m⁻¹

Physical

Density : 3.98×10^3 Kg m³

Crystal structure : Hexagonal

Grain size : single crystal

Optical

Transmits 3 - 5 μ m wavelength

Sample Used

Source : Barr and Stroud Ltd. and others

Dimensions : discs 25 mm diameter, 3 mm thick, and 6 mm diameter, 1 mm thick

5.1.2 Material Description

Sapphire has a broad transmission band spanning the ultraviolet, visible and infrared. It has very good mechanical and physical properties, but its major drawbacks from a radome point of view are that it is birefringent, and expensive to fabricate. The birefringence can be minimised by using thin components oriented along the [0001] direction, and the introduction of new production techniques is gradually reducing the fabrication cost.

The two main methods of fabrication currently used are the Heat Exchange Method (HEM) (Schmid and Viechnicki, 1970, Schmid and Khattak, 1989, Khattak and Schmid, 1992), and the Edge-Defined Film-Fed Growth technique (EFG) (LaBelle, 1980, Locher et al., 1990, 1992). Excellent reviews of these methods are given in Savage (1985) and Harris (1993), and two methods of polishing after fabrication are described in Gentilman et al. (1989) and Pazol et al. (1992).

5.1.3 Published Rain Erosion Work

A list of some of the early studies performed on Sapphire is presented in Springer (1976). One of these studies was carried out by Behrendt (1974) on the Dornier whirling arm using 1.2 mm diameter drops. This study showed a variation in the incubation time for mass loss that could be fitted to an expression of the form $t = kV^{-n}$ as described previously in section 4.2.2. Similar work was later repeated at Dornier by Steinheil and Schmidberger (1979) who investigated both mass and transmission loss

for impact with 0.5 mm diameter drops. They obtained incubation times for mass loss that varied from 3,000 s at 510 m s^{-1} , to complete fracture in just 10 s at 800 m s^{-1} (figure 5.1.1). These Dornier results are important since neither identified the existence of an absolute threshold velocity for damage, however by using the conversion formula put forward by Field et al. (1983) the more recent data would suggest that if a threshold existed it would at least be below 320 m s^{-1} for a 2 mm diameter drop. (This assumes no drop distortion in the whirling arm rig.)

The first claim to a damage threshold evaluation on sapphire was made by Hackworth (1979), using the Bell Aerospace whirling arm rig, with 2 mm diameter drops. Hackworth's samples for this study were oriented so the c-axis made an angle of 60° with the normal to the specimen surface. In this orientation the fractures took place preferentially on the {1011} rhombohedral planes whose intersection with the surface resulted in the formation of foreshortened hexagons. Hackworth found that no damage occurred in sapphire impacted at 457 m s^{-1} and extensive cracking occurred at 533 m s^{-1} . He therefore concluded that the damage threshold lay in the range $457 - 533 \text{ m s}^{-1}$. It should be noted however that this figure for the threshold refers to that for just one impact, and as MIJA's results show, the threshold after larger numbers of impacts is invariably lower.

Townsend (1985) performed the first sapphire damage threshold evaluation using SIJA with a mechanical strength test. This evaluation was carried out on 1.5, 2 and 2.5 mm thick specimens and the results indicated a threshold between 350 and 400 m s^{-1} (0.8 mm jet DTV (mechanical) = $375 \pm 25 \text{ m s}^{-1}$, $\sim 450 \pm 20 \text{ m s}^{-1}$ for a 2 mm equivalent drop). This threshold has been quoted as 455 m s^{-1} by Field et al. (1983, 1989). The crystal orientation used for this study was different to that used by Hackworth, with the impacts performed at normal incidence to the basal plane (0001), and fracture taking place preferentially along the {1010} cleavage planes. There was some suggestion that the longitudinal stress wave reflected from the rear of the sample was affecting the damage threshold in the thinner discs due to its high wave speed ($11,200 \text{ m s}^{-1}$), but despite this it was claimed that no damage was seen from a single jet impact below 700 m s^{-1} . Further shots were performed on a sapphire sample acoustically backed with a thicker piece of sapphire, and from this Townsend concluded that the bulk sapphire threshold was $\sim 400 \text{ m s}^{-1}$ for a 0.8 mm jet.

Cassaing et al. (1989) attempted to verify the erosion rate equations of Springer (1976) using the SAAB rotating arm. However they obtained no transmission loss after several hours exposure to 1.2 mm diameter drops at 300 m s^{-1} .

The most recent whirling arm test was performed by Locher (1992) at Wright Patterson, Dayton with an impact velocity of 210 m s^{-1} in a 1"/hr rain of 1.8 - 2.2 mm diameter drops for 20 minutes. Locher reported that there was no damage or pitting visible after the test, and that measurements for optical scatter made before and after were essentially unchanged.

Finally the results presented below have been described fully in Seward et al. (1992a), Seward et al. (1993c) and Coad et al. (1993)

5.1.4 MIJA Results

So far four main batches of sapphire have been supplied and tested on MIJA using the threshold evaluation technique described in chapter 4.

Batch 1: Two 25 mm diameter, 3 mm thick discs supplied in the first half of 1992 so that a threshold curve for bulk sapphire could be found on MIJA. This was a preliminary stage to the natural diamond work described in section 5.6.

- Batch 2: Eight 6 mm diameter, 1 mm thick discs produced with the same orientation and surface finish as the discs in batch 1 for assessment of any size effects (ie diameter or thickness) on the threshold velocity value, in preparation for the natural diamond work. (Also supplied in 1992.)
- Batch 3: Two 25 mm diameter sapphire discs for each of 4 different surface finishes, supplied for testing at the beginning of 1993:
- i) conventional polish and annealed
 - ii) conventional polish, annealed and DLC coated
 - iii) conventional polish, annealed and "super polished"
 - iv) conventional polish, annealed, "super polished" and ion implanted.
- Batch 4: Two further 25 mm diameter sapphire discs supplied from the same source as batch 1, as part of a project to assess the effect of adding a coating of Boron Phosphide on the threshold velocity curve for sapphire. (Supplied towards the end of 1993.)

5.1.4.a Batch 1

Two 25 mm discs of similar orientation to those used by Townsend (1985), were used for the first MJA threshold evaluation for sapphire. The results obtained from these are shown in figures 5.1.2 - 5.1.5. The damage threshold velocity (DTV) from disc 1 side 1 suggested the 0.8 mm jet DTV (300 impacts) = $410 \pm 15 \text{ m s}^{-1}$ (figure 5.1.2). The threshold evaluation was repeated on side 2 of disc 1 and this suggested the 0.8 mm jet DTV (300 impacts) = $430 \pm 10 \text{ m s}^{-1}$ (figure 5.1.3). The conclusion from disc 1 was therefore that sapphire probably had a 0.8 mm jet DTV (300 impacts) of $\sim 425 \pm 5 \text{ m s}^{-1}$. Disc 2 however produced slightly different results (figure 5.1.4). The first circumferential crack was observed on the 530 m s^{-1} site after 75 impacts, however in contrast to disc 1 even after 300 impacts on the 487 and 505 m s^{-1} no circumferential cracking had been seen, however the central damage had become so large that the experiments had to be aborted. These impact velocities were repeated on the second side of disc 2 (figure 5.1.5), and this time 2 of the 4 attempts to complete the experiment at 505 m s^{-1} had to be aborted because of central damage. The remaining experiments at 505 m s^{-1} produced circumferential cracks before the central damage became too large, as did the experiment repeated at 487 m s^{-1} . At this point there was no further space left on disc 2 to continue the threshold evaluation, but from the results obtained it was concluded that the threshold velocity for circumferential damage was $< 487 \text{ m s}^{-1}$ (0.8 mm jet DTV (300 impacts) $< 487 \text{ m s}^{-1}$). While this result was consistent with the threshold value obtained from disc 1, it was not very conclusive when compared to the results obtained for other IR materials.

Some SEM photos of the damage sites on disc 1 can be seen in plate 9.1.1. The ring cracks are generally long and don't show many scab marks on the outside of the cracks, however where scabs have been removed their size is quite large. In contrast to the results of Townsend (1985) and Hackworth (1979) the cracking on these sites didn't seem to follow any particular grain orientation.

5.1.4.b Batch 2

The results for the 6 mm diameter, 1 mm thick sapphire specimens are described fully in section 5.6. The method for threshold evaluation for small specimens described in section 4.3.4 was used and this produced an extremely reproducible value of 0.8 mm jet DTV (300 impacts) = $430 \pm 10 \text{ m s}^{-1}$.

5.1.4.c Batch 3

Two 25 mm discs of each of the following four surface finishes were supplied for evaluation on MJA:

- i) conventional polish and annealed
- ii) conventional polish, annealed and DLC coated

- iii) conventional polish, annealed and "super polished"
- iv) conventional polish, annealed, "super polished" and ion implanted.

The strength improvements possible by these different polishing methods are evaluated in McHargue and Snyder (1992). The results from the threshold evaluations on MIJA can be seen in figures 5.1.6 - 5.1.10 and are described fully in Seward et al. (1993c). For surface finishes i, iii and iv the threshold velocity for circumferential cracking after 300 impacts appears to be almost independent of the surface finish of the substrate. The surface finish only appears to effect the reproducibility of the results, and the incubation time before damage initiates when impacted *above* the threshold velocity. The conventional polished sapphire therefore shows the widest variability in results together with the lowest incubation times above the threshold velocity. The addition of a "super polish" raises the incubation times for impact velocities greater than the threshold value, while the addition of ion-implanting after the "super polish" produces incubation times at least as long as the sapphire treated with the "super polishing" alone, and sometimes even longer. The benefits of ion implanting however appear to vary over the disc surface, and work remains to be done to optimise this technique. If ion implanting were eventually to be used in production tight quality control of the material produced would have to be maintained. This may be another area where MIJA will be useful in the future.

The DLC coated sapphire looked at in this work (surface finish ii) appeared to have worse erosion resistance than the other three surface finishes (0.8 mm jet DTV (300 impacts) $< 420 \text{ m s}^{-1}$). This may be due to stress in the substrate produced by the coating deposition process, and it is therefore interesting to compare the results with those obtained with a coating of BP on sapphire in sections 5.14.4.d and 5.14.5.d, where it is known that the deposition has left the substrate surface in tension.

5.1.4.d Batch 4

The final batch of sapphire specimens tested on MIJA came from exactly the same source as batch 1 in section 5.1.4.a. These were supplied together with two discs of sapphire coated with Boron Phosphide to allow confirmation of the threshold curve for the uncoated substrate. During the course of the investigation it was found that an impact site could be located by applying a fine mist onto the surface (hydro-analysis). After the application of this mist, the impact sites appeared in the form of a hatched ring, with water droplets in the spaces created by the straight lines. This process was found to be highly reproducible between successive applications of the mist, and similar "hatched" patterns were also obtained at other impact sites.

The results obtained are shown in figure 5.1.11 and give a threshold velocity for circumferential cracking of: 0.8 mm jet DTV (300 impacts) = $490 \pm 10 \text{ m s}^{-1}$.

5.1.5 Discussion

All the threshold curves obtained for uncoated bulk sapphire are summarised in figure 5.1.12, and the threshold values produced are given in the table on the next page.

The curves shown in figure 5.1.11 suggest the threshold for bulk sapphire is 0.8 mm jet DTV (300 impacts) $\sim 485 \pm 5 \text{ m s}^{-1}$. The only results that don't agree with this are the results from batch 1 sapphire #1 sides 1 and 2 and from the smaller diameter discs tested in batch 2. Of these the results of batch 1 may be inaccurate because the sites were separated by the same distance used for experiments on ZnS, and in the testing of the sapphire for batch 3 it was found necessary to spread the impact sites further apart to avoid any interactions between them. It is therefore conceivable that the damage recorded at 425, 445 and 460 m s^{-1} was actually initiated by the damage

	Description	0.8 mm jet DTV (300 impacts) / m s ⁻¹
Batch 1	Sapphire #1 side 1 Sapphire #1 side 2 Sapphire #2 (Provided for comparison with 6 mm diameter sapphire specimens as part of the natural diamond work - see 5.6)	410 ± 15 430 ± 10 < 487
Batch 2	6 mm diameter sapphire specimens	430 ± 10
Batch 3	Conventional polish and annealed Conventional polish, annealed and DLC coated Conventional polish, annealed and "super polished" Conventional polish, annealed, "super polished" and ion implanted	490 ± 10 < 420 475 ± 15 475 ± 15
Batch 4	sapphire substrate for comparison with BP coated sapphire	490 ± 10

generated on the 490 m s⁻¹ site, and this might possibly explain the sudden sharp drop in the threshold curve following the first signs of damage on the 490 m s⁻¹ site. It is equally possible that this lower threshold value may have been the result of a damaged or poorly polished disc.

The lower threshold velocity of batch 2 is reasonable when the effects of stress wave reflections due to the specimens smaller dimensions are taken into consideration. All the other sapphire results are extremely consistent.

The new figures for the visible damage threshold velocity of sapphire after 300 impacts are considerably higher than those produced by Townsend (1985) using a mechanical strength assessment of damage. This could be accounted for by the improvements in control of the water jet velocity with MIJA, together with the uncertainty due to the scatter in the strength measurements in Townsends' work.

A comparison with whirling arm data is more difficult since Hackworth's threshold velocity results (457 - 533 m s⁻¹) were obtained for single impacts and values for the threshold velocity due to a single impact have not yet been obtained using MIJA because it is > 600 m s⁻¹. With SIJA Townsend reported the single impact threshold as being > 700 m s⁻¹.

Finally, it should be remembered that the work carried out at Dornier in 1979 with smaller drop sizes suggested that the absolute threshold was as low as 320 m s⁻¹. Insufficient details are available of the specimen type or experimental technique used to be able to comment further on this particular result.

5.1.7 Conclusion

The early results obtained for bulk sapphire using MIJA and already published in Seward et al. (1992a), have been revised in view of more recent evidence. The published result of a 0.8 mm jet DTV (300 impacts) = 425 ± 5 m s⁻¹ appears to be too low, and a more accurate value is probably 485 ± 5 m s⁻¹. The initial lower value may be due to the impact sites having inadequate separation to avoid interference between damage sites.

This revised result suggests an effect of specimen size on the threshold velocity, since the 6 mm diameter, 1mm thick discs tested in batch 2 had a 0.8 mm jet DTV (300 impacts) = 430 ± 10 m s⁻¹, and this is ~ 10% less than the threshold value for a 25 mm diameter, 3mm thick disc of 485 ± 5 m s⁻¹. The consequences of this for the natural diamond work are discussed in more detail in section 5.6.

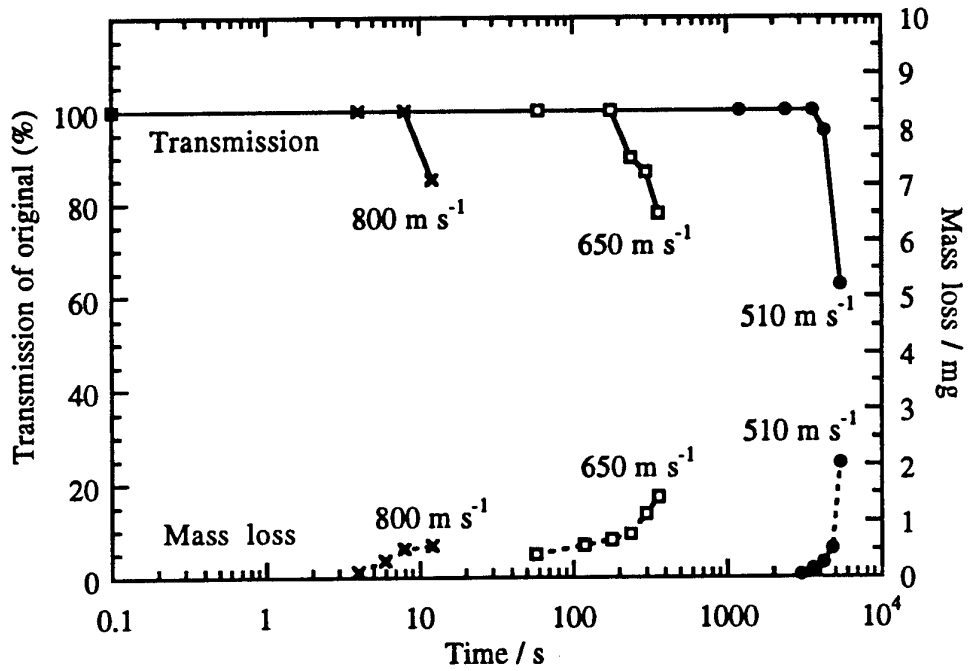


Figure 5.1.1 Rain erosion of sapphire at 3 different velocities. (Steinheil and Schmidberger, 1979)

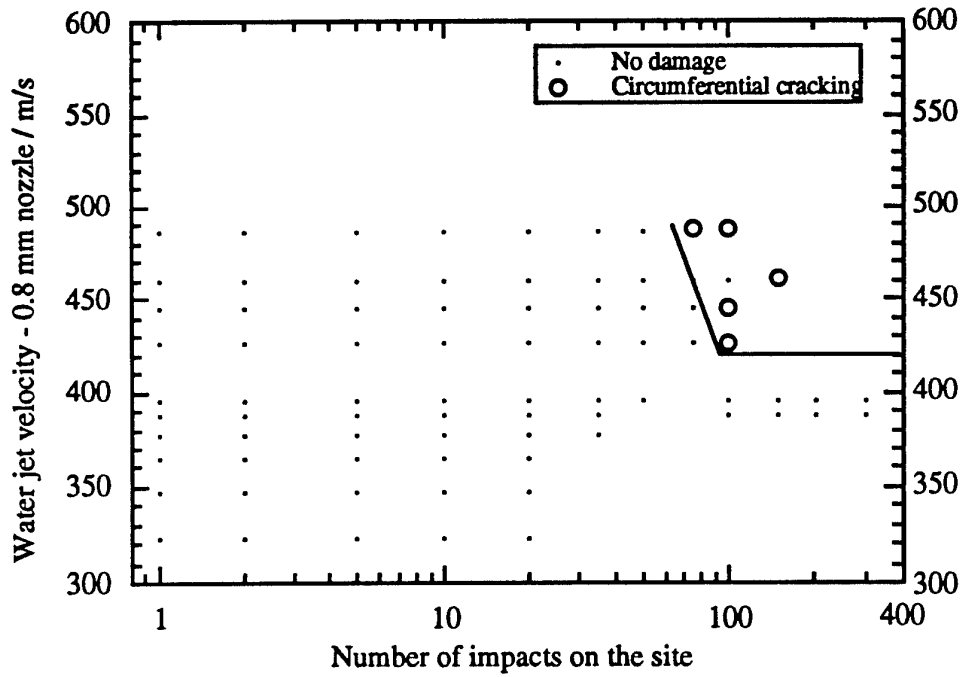


Figure 5.1.2 Threshold curve for batch 1 sapphire disc 1 side 1.

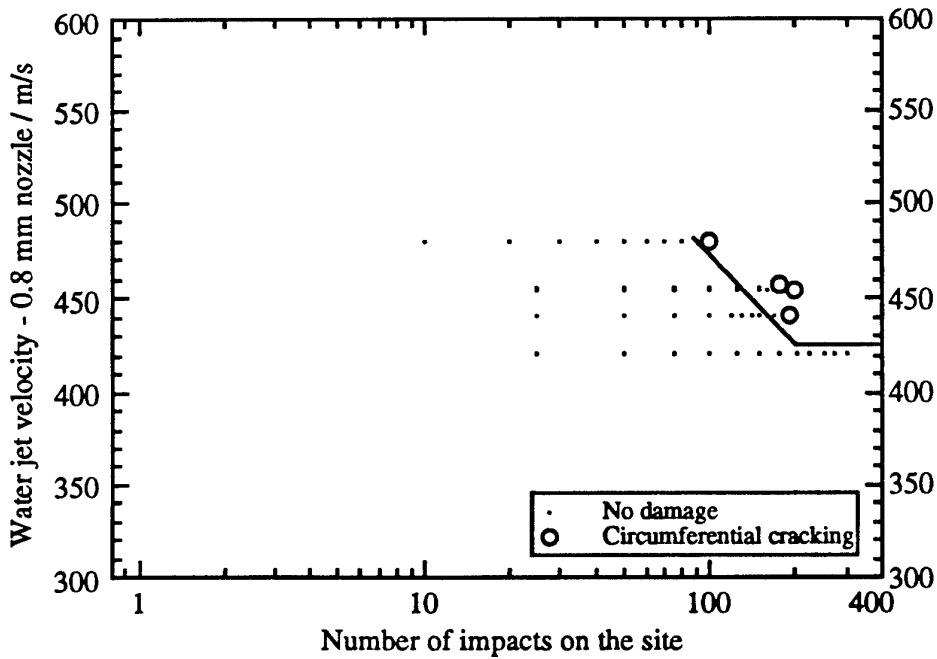


Figure 5.1.3 Threshold curve for batch 1 sapphire disc 1 side 2.

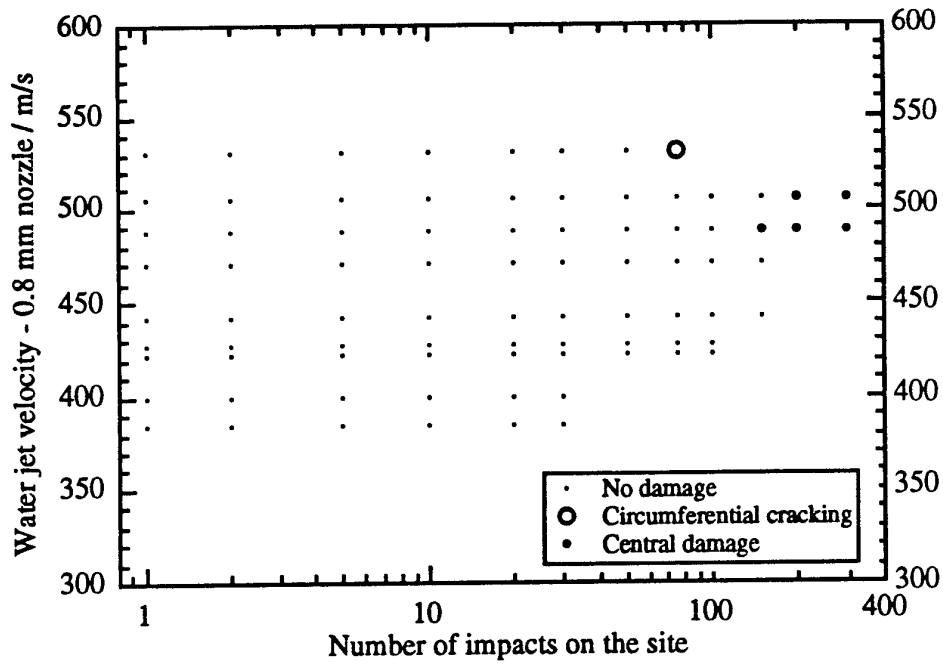


Figure 5.1.4 Threshold curve for batch 1 sapphire disc 2

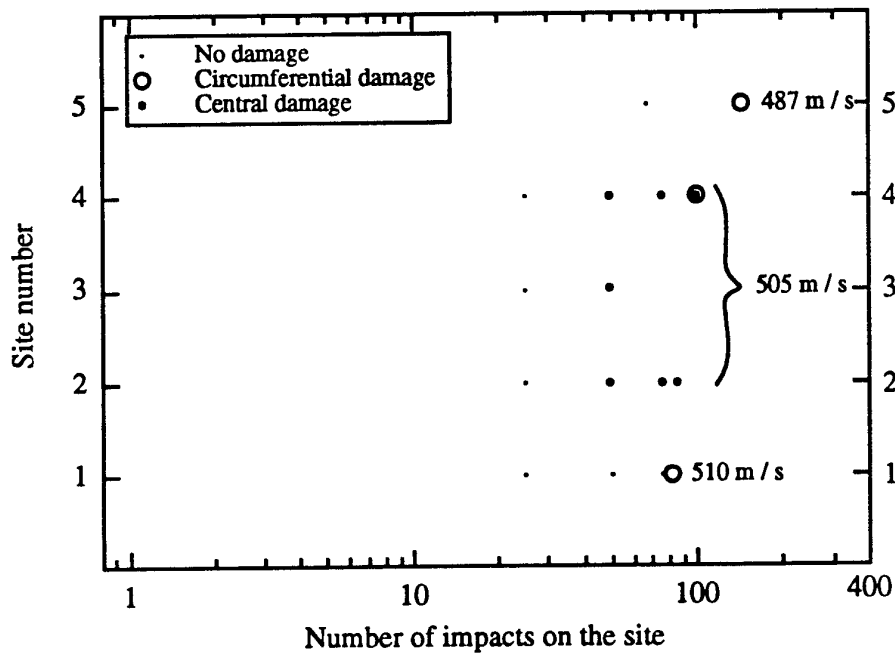


Figure 5.1.5 Check of threshold for batch 1 sapphire disc 2

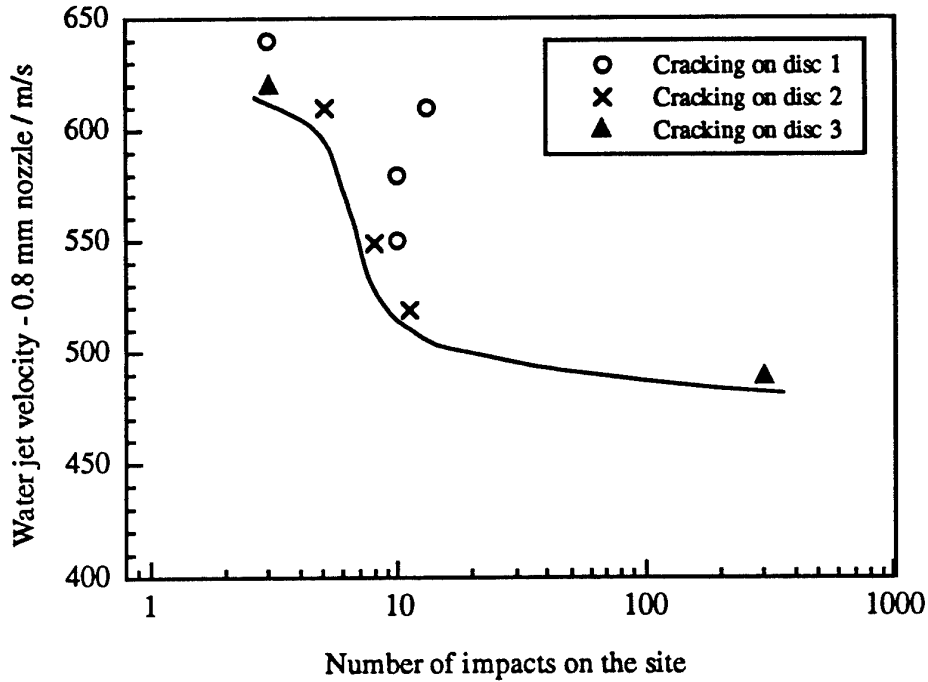


Figure 5.1.6 Summary of data for initiation of circumferential cracking on batch 3, conventional polished sapphire discs 1,2 and 3.

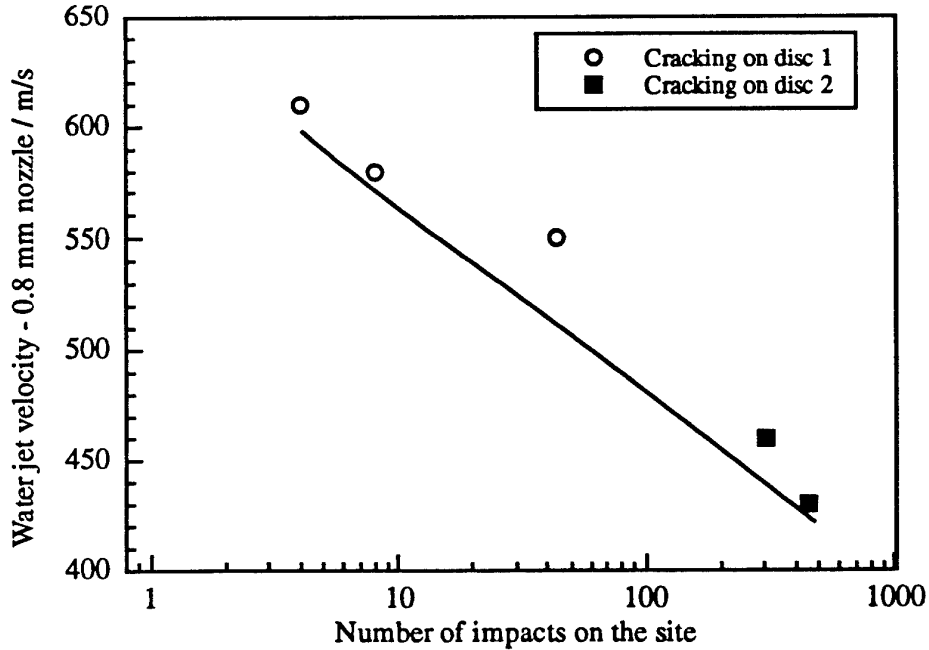


Figure 5.1.7 Summary of data for initiation of circumferential cracking on batch 3, DLC coated sapphire discs 1 and 2.

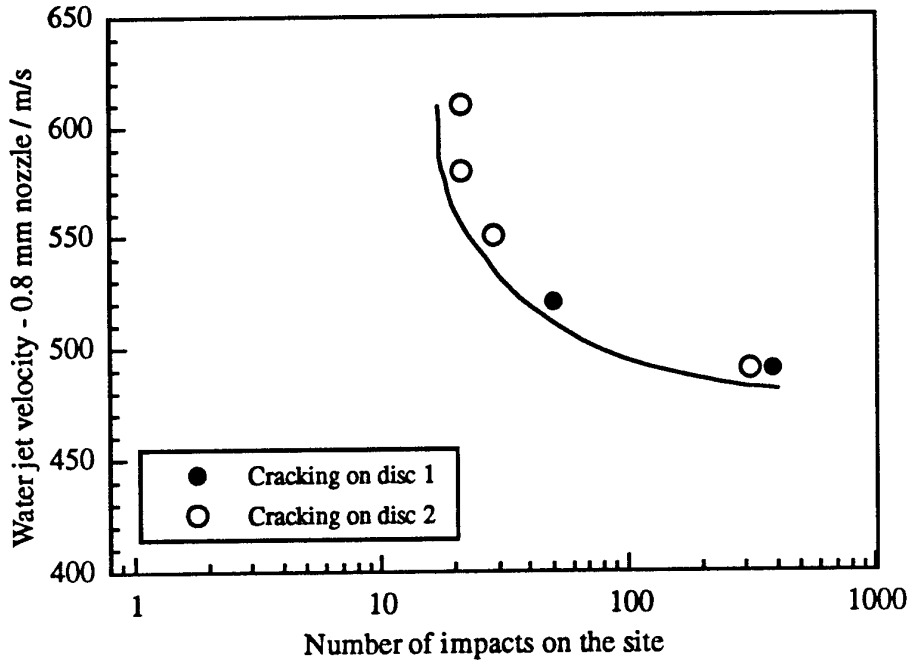


Figure 5.1.8 Summary of data for initiation of circumferential cracking on batch 3, non-contact polished sapphire discs 1 and 2.

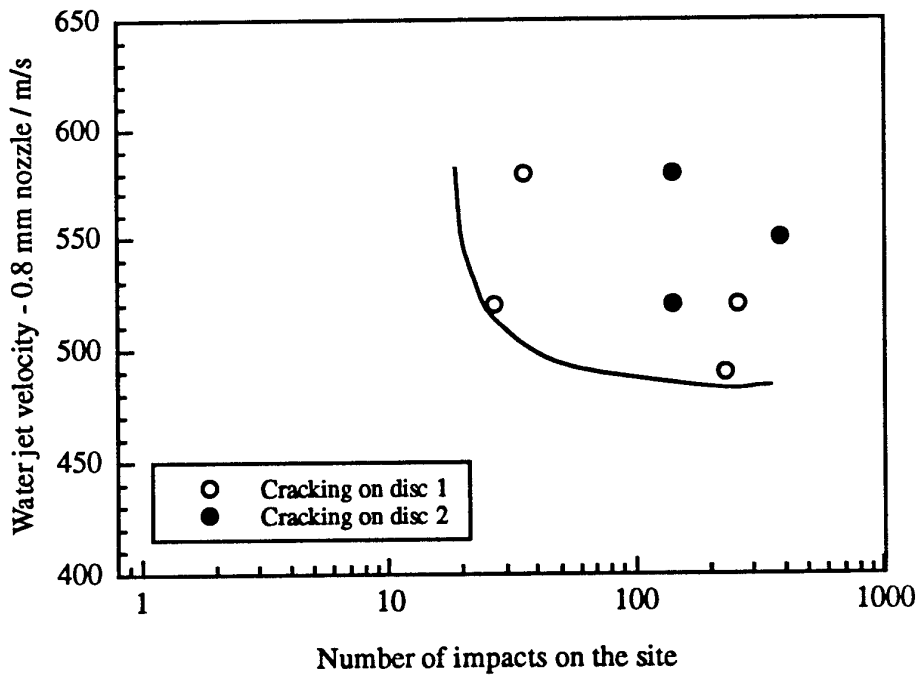


Figure 5.1.9 Summary of data for initiation of circumferential cracking on batch 3, ion implanted sapphire discs 1 and 2.

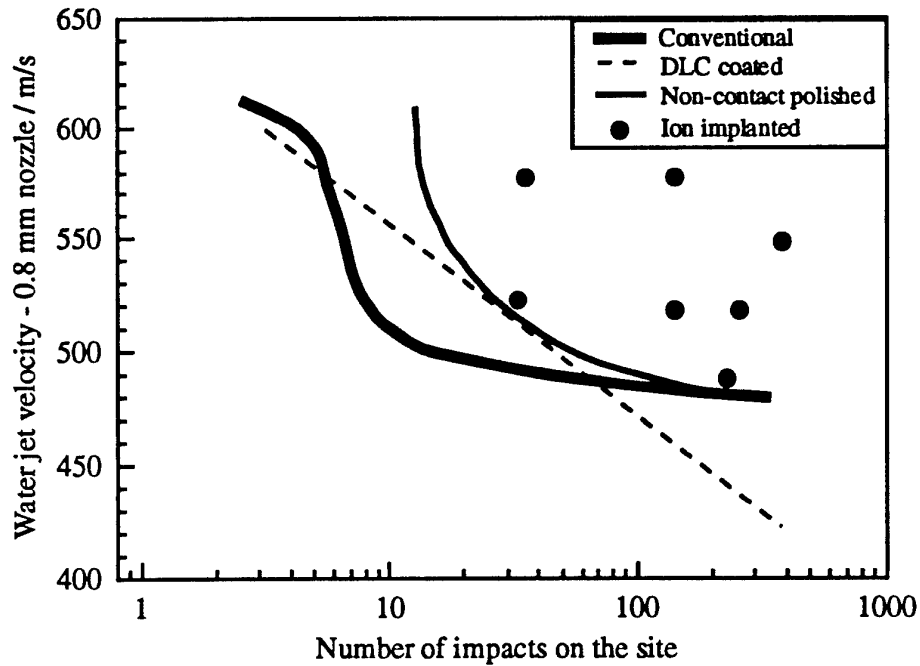


Figure 5.1.10 Summary of the threshold velocity curves for the four different sapphire surface finishes investigated for batch 3.

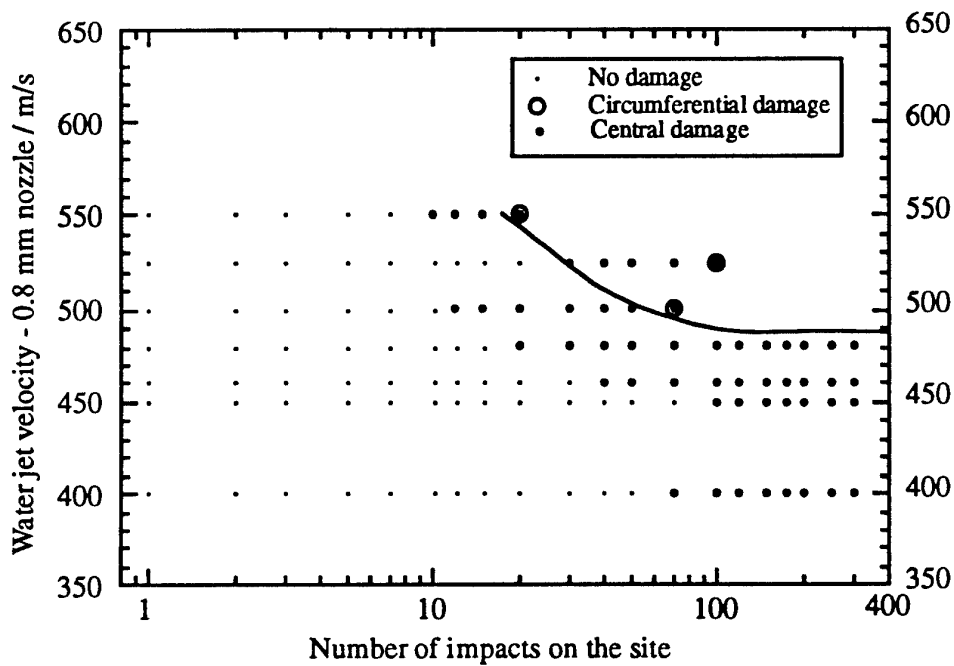


Figure 5.1.11 Threshold velocity curve for sapphire from batch 4.

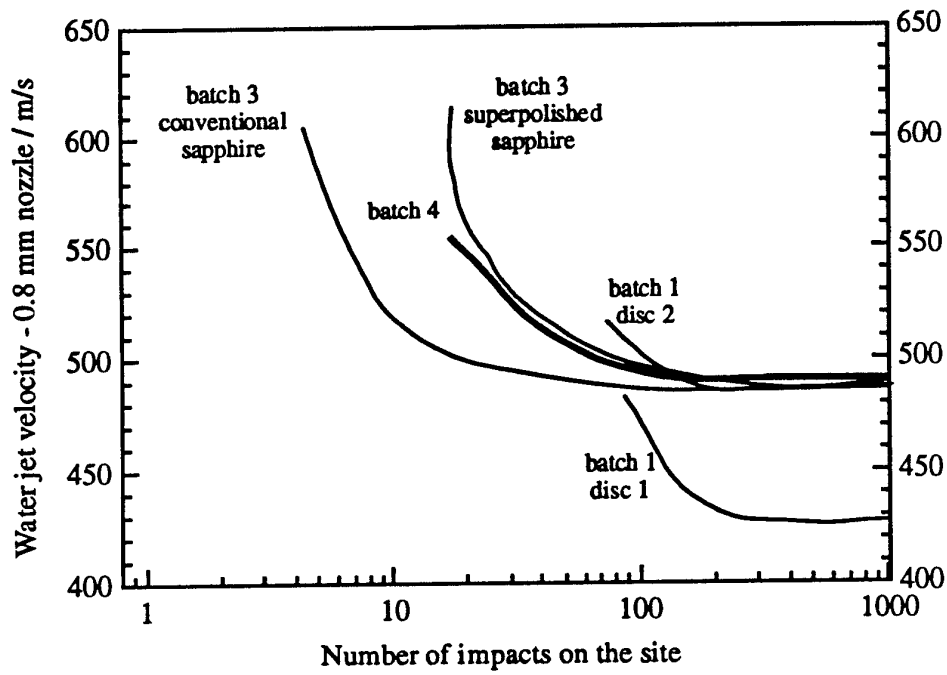


Figure 5.1.12 Summary of threshold velocity curves for uncoated bulk sapphire substrates.

5.2 SPINEL (MAGNESIUM ALUMINATE)

5.2.1 Material Characteristics

The data is taken from Stewart and Bradt (1980), Stewart et al. (1981), Savage (1985), Gentilman (1986) Roy and Green (1989), Klocek (1991) and Pickles (1991) and refers to the polycrystalline spinel.

Mechanical

Knoop hardness : 1,300 - 1,650 kg mm⁻²

Fracture stress : 190 MPa

Fracture toughness : 1.9 MPa m^{1/2}

Youngs modulus : 190 GPa

Poissons ratio : 0.26

Rain erosion resistance (see section 4.4)

0.8 mm jet DTV (1, 3, 10, 300 impacts):

490 ± 10, 415 ± 5, 375 ± 5, 355 ± 5 m s⁻¹

Optical

Transmits 3 - 5 µm wavelength

Thermal

Melting point : 2,135 °C

Thermal conductivity : 15 W m⁻¹ K⁻¹

Thermal expansion : 8.0 x 10⁻⁶ K⁻¹

Heat capacity : 837 J Kg⁻¹ K⁻¹

Thermal shock resistance : 1.2 kW m⁻¹

Physical

Density : 3.55 x 10³ Kg m³

Crystal structure : Cubic

Grain size : 5 µm

Sample Used

Source : SAT, Paris, France.

Dimensions : 29 mm diameter disc, 4.0 mm thick

5.2.2 Material Description

Spinel is cubic and optically isotropic; thus polycrystalline shapes may be fabricated without the scattering problems inherent in non-cubic materials (e.g. sapphire). Mechanically spinel is exceptionally strong and hard for an optical material, and has good thermal shock resistance. The polycrystalline structure results in blunting and redirecting of cracks at grain boundaries, and thus offers greater toughness than spinel single crystals. The high strength of spinel allows thinner windows to be made with a resultant reduction in thermal stresses and improved optical performance. Some spinel grades offer greater transmission in the 3 - 5 µm waveband than sapphire, however trapped water may cause an absorption band at 2.8 µm.

The main methods of fabrication for the single crystals are flame fusion and the Czochralski techniques (Wickersheim and Lefever, 1960, Cockayne and Chesswas, 1967). For flat polycrystalline discs press-forging (Becher, 1977) and fusion-casting (Gentilman, 1981) have both been used to produce excellent optical quality. Attempts to produce domes through these methods have however been limited, and the best fabrication method for domes so far appears to be hot pressing (Roy, 1981a,b, Berges et al., 1990). A good review of these and other fabrication methods is contained in Savage (1985).

5.2.3 Published Rain Erosion Work

Hackworth (1979) investigated a single crystal spinel with (111) planes forming the outer surface, and found a threshold for single impact with a 2 mm drop of slightly below 396 m s⁻¹, using the Bell Aerospace whirling arm. Normally the {100}

planes are the preferential cleavage planes for single crystal spinel, however in this experiment they were not favourably oriented and therefore the fracture was instead due to cleavage of the cubic face planes. This meant that the fracture patterns produced exhibited threefold symmetry as a result of the intersection of the cleavage planes with the surface.

Hackworth (1982) later repeated the whirling arm tests with 2 mm drops on fusion cast spinel. The fracture patterns obtained in this case were square, and his results suggested a damage threshold of slightly below 457 m s^{-1} for a single impact.

Two further reported rain erosion tests of spinel are presented in Roy and Green (1989), however the type of spinel used is not stated. The first of these were rocket sled tests performed in 1972 at speeds of 487 m s^{-1} (Potts, 1972). The second were whirling arm tests performed on both the NADC and the Wright-Patterson rigs (Schwartz, 1989). These tests supposedly demonstrated that "the equivalent of a lifetime of impact with rain drops at 223 m s^{-1} generated minimal damage"

The final set of data published on this material is by Seward et al. (1992a) and Pickles et al. (1992). These experiments were performed on hot-pressed spinel and the results are presented below.

5.2.4 MIJA Results

The MIJA threshold results from two separate experiments are shown in figure 5.2.1 and 5.2.2. These experiments were both performed on the same disc and gave similar threshold results for circumferential cracking; 0.8 mm jet DTV (300 impacts) 355 ± 5 and 0.8 mm jet DTV (150 impacts) $365 \pm 5 \text{ m s}^{-1}$. Central damage can still be obtained at lower velocities, however as can be seen from figure 5.2.3 the number of shots it takes to appear is not so predictable. The MIJA threshold results can be compared to that obtained using SIJA with the bursting disc (described in section 4.2.3) as seen in figure 5.2.4. The agreement between the two techniques is fairly good, with the SIJA 0.8 mm jet DTV (mechanical) $\sim 325 \pm 25 \text{ m s}^{-1}$. The data shown in figure 5.2.4 illustrates one of the difficulties of obtaining more accurate DTV values with SIJA and the bursting disc, the variation in the strength after impact being greatly influenced by the natural variation in strength of the brittle ceramic test samples.

Photographs of some of the damage sites can be seen in plate 9.2.1. After 4 shots at 460 m s^{-1} a series of very fine, long cracks can be seen around the impact circle (photos 1 and 2). The undamaged material in photo 2 can be seen to contain a large number of voids, and some of these may be exploited by the lateral jetting to form the chipping outside the circumferential fractures. As the number of impacts on each site is increased the cracks extend in length around the impact circle. In all three photos 1, 3 and 5 the inner circle has a diameter of 1.3 - 1.4 mm for a nozzle orifice size of 0.8 mm. With larger numbers of impacts the extent of the chipping increases dramatically (photo 5).

The central damage site is shown in photo 7, and a close-up in photo 8. In this photo it appears that grains have become loosened before being removed. The damage here may have initiated by the water pressure under the centre of the damage causing failure at dislocations or grain boundaries, or merely by the exploitation of the existing pits. In any case once a pit has been formed it can fill with water and the large hydrostatic pressures then exerted on the walls of the hole during the next impact can lead to further material loss, and eventually to radial cracking.

5.2.5 Conclusion

The damage thresholds evaluated for spinel independently using both SIJA and MIJA give similar values, with the 0.8 mm jet DTV (300 impacts) = $355 \pm 5 \text{ m s}^{-1}$ ($\sim 430 \pm 10 \text{ m s}^{-1}$ for a 2 mm diameter equivalent drop) and the SIJA value from residual strength measurements after impact, 0.8 mm jet DTV (mechanical) of $325 \pm 25 \text{ m s}^{-1}$. However the MIJA single impact threshold, 0.8 mm jet DTV (1) = $490 \pm 10 \text{ m s}^{-1}$ ($\sim 550 \pm 10 \text{ m s}^{-1}$ for a 2 mm equivalent drop) is rather higher than Hackworth's single impact result for a 2 mm drop of 'slightly below' 457 m s^{-1} . This discrepancy may be because of a difference between the two samples, or it may be a consequence of the way Hackworth conducted his test, the full details of which are not available.

The close agreement between the two MIJA results obtained on the same specimen is extremely encouraging. Such a good agreement may seem surprising once the spread in jet velocities, jet profiles, and flaw sizes, has been taken into consideration, however it is an excellent indication of the reliability and reproducibility that may be possible with the MIJA threshold evaluation technique.

The possibility of sub-threshold central damage is obviously of great interest to a radome designer. Further research is therefore now being carried out in order to identify the exact mechanism for this new damage mode, including time-lapse video analysis to look at the role played by the voids in the spinel surface.

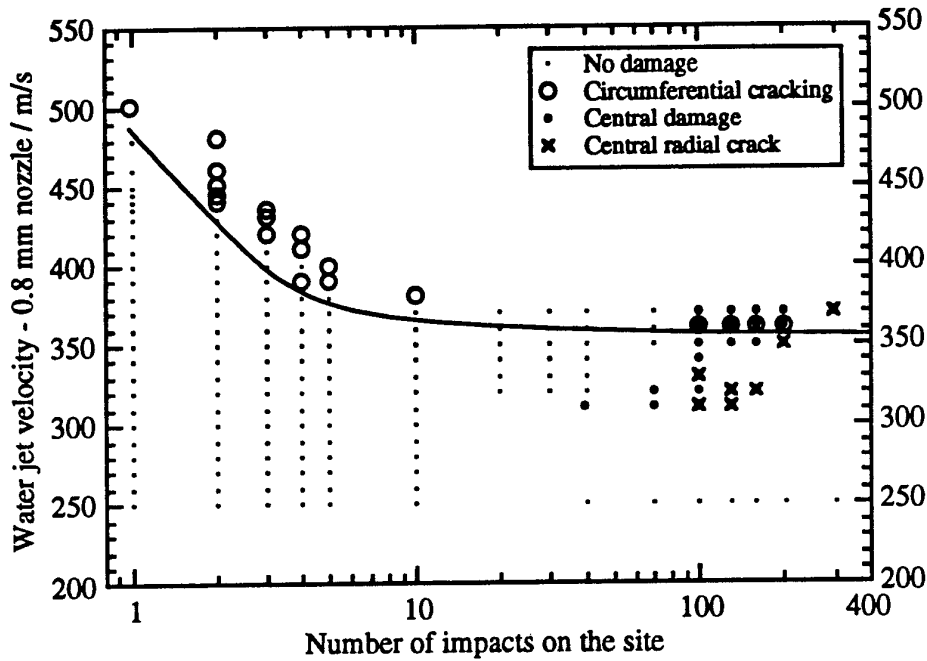


Figure 5.2.1 Threshold curve for spinel.

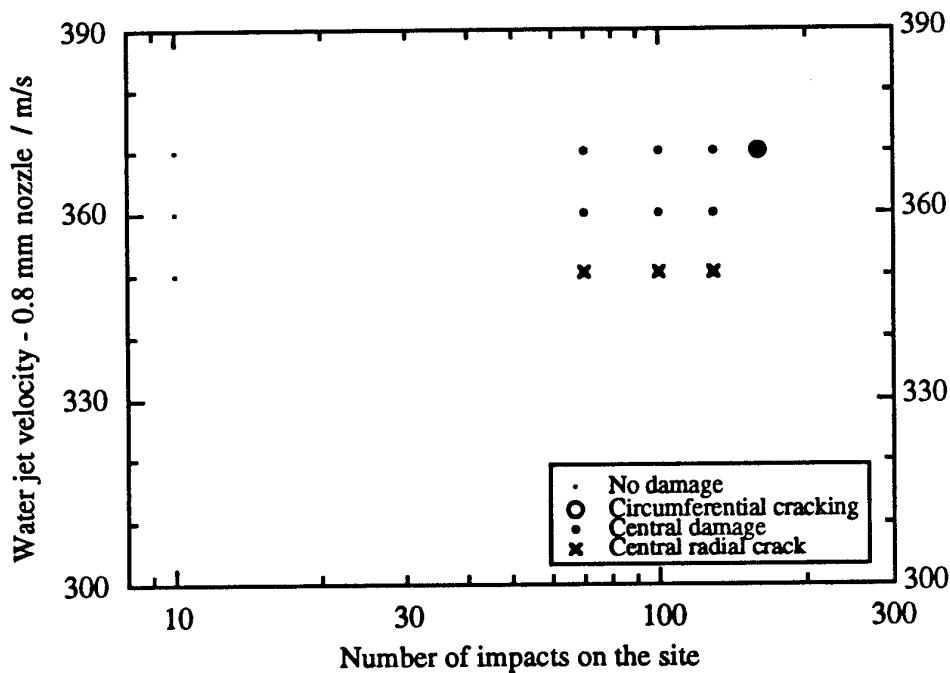


Figure 5.2.2 Second threshold curve for spinel

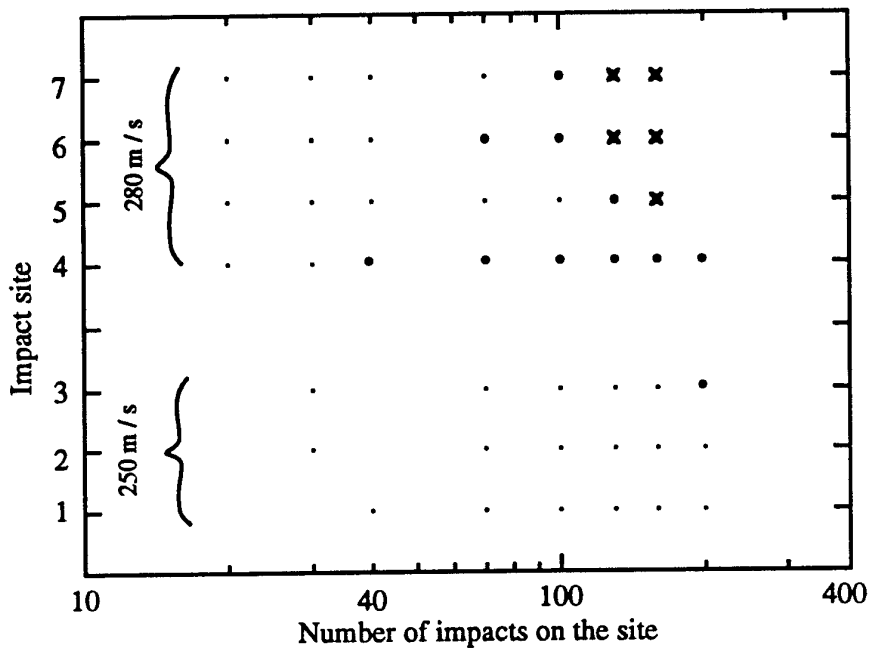


Figure 5.2.3 Assessment of the number of impacts required for the appearance of sub-threshold central damage.

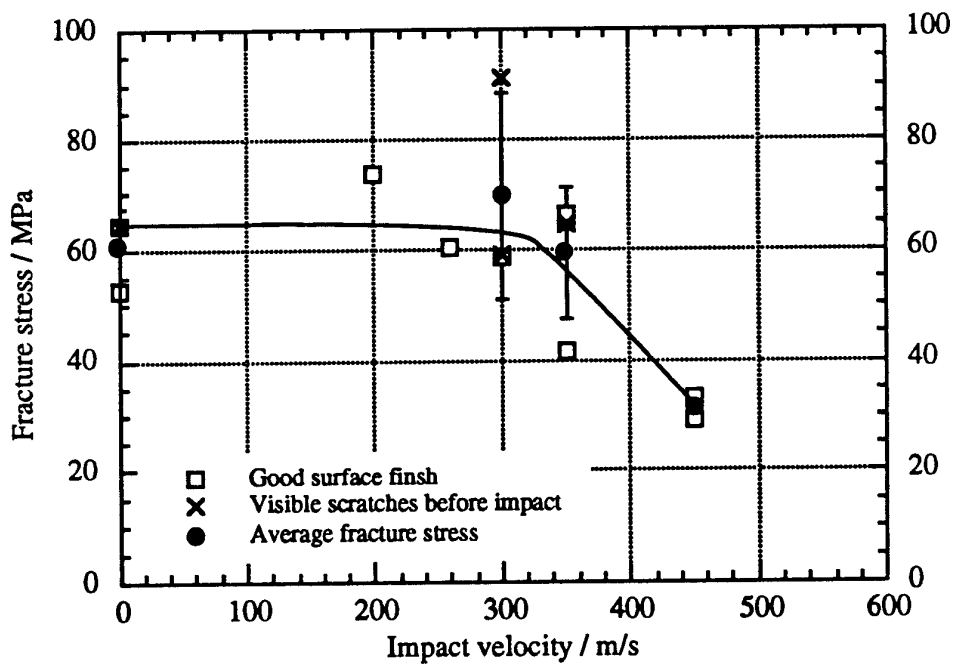


Figure 5.2.4 SIJA evaluation of the spinel threshold velocity.

5.3 MAGNESIUM FLUORIDE

5.3.1 Material Characteristics

The data below is taken from Savage (1985), Gentilman (1986), Klocek (1991) and Pickles (1991) and relates to the polycrystalline material.

Mechanical

Knoop hardness : 576 kg mm⁻²
Fracture stress : 100 MPa
Fracture toughness : 0.9 MPa m^{1/2}
Youngs modulus : 115 GPa
Poissons ratio : 0.30
Rain erosion resistance (see section 4.4)
0.8 mm jet DTV (1, 3, 10, 300 impacts):
320 ± 10, 300 ± 10, 245 ± 5, 245 ± 5 m s⁻¹

Optical

Transmits 3 - 5 µm wavelength

Sample Used

Source : SAT, Paris, France
Dimensions : 25 mm diameter disc, 3.1 mm thick

Thermal

Melting point : 1,255 °C
Thermal conductivity : 16 W m⁻¹ K⁻¹
Thermal expansion : 11.0 x 10⁻⁶ K⁻¹
Heat capacity : 1,004 J Kg⁻¹ K⁻¹
Thermal shock resistance : 0.89

Physical

Density : 3.18 x 10³ Kg m³
Crystal structure : Tetragonal (rutile)
Grain size : ≤ 1 µm

5.3.2 Material Description

Magnesium fluoride is available as a single crystal produced by the Stockbarger process (1936), or as a polycrystalline material produced by hot-pressing into the desired shape (Buckner et al., 1962). The polycrystalline material has found extensive use as an airborne infrared window because of its low cost, and also its infrared absorption edge occurring at longer wavelengths than that of either sapphire or spinel. Adequate optical resolution can be achieved with polycrystalline magnesium fluoride by maintaining a grain size below 1 µm, however because of its tetragonal crystal structure it has a birefringence which whilst small (0.9%), is unacceptable for some of the improved optical resolution required for future systems (Gentilman, 1986). The birefringence is not the only possible cause for scatter, any contamination in the mix or non-uniformity in density can also add to the scatter, and these are inherent problems with the hot-pressing process. The other problems with the material is its low hardness and strength; although the low hardness does have a benefit in that it makes polishing easier and therefore cheap. Even with these limitations, magnesium fluoride was reported by Gentilman (1986) to be one of the most widely used window materials, with approximately 100,000 domes being produced compared to 300 for sapphire and only 60 for spinel!

5.3.3 Published Rain Erosion Work

Despite its extensive use as an infrared window material, little data appears to have been published on magnesium fluoride's rain erosion resistance. Hackworth (1979) conducted experiments on single crystal magnesium fluoride with the (001) plane as the specimen face. The results he obtained showed no damage from a single 2 mm drop impacting at 274 m s⁻¹, but produced two short cracks from an impact at

320 m s⁻¹. The fracture pattern observed above 340 m s⁻¹ was a square ring caused by cleavages of the {100} and {010} planes. The experiment was later repeated for hot-pressed magnesium fluoride and on this Hackworth (1982) reported a threshold value for damage from a single impact of between 340 and 381 m s⁻¹ for a 2 mm drop.

A more comprehensive study of magnesium fluoride using both the SAAB and the Dornier whirling arm rigs was conducted by Deom et al. (1987). This study measured both the optical transmission loss and the mass loss for a variety of different velocities. The results failed to verify the existence of an absolute threshold velocity for damage, and losses were recorded with 2 mm drops even at 208 m s⁻¹ (figure 5.3.1). The results obtained showed that the mass loss initiated soon after the optical loss (figure 5.3.2), and that both losses had an incubation time that had a velocity dependence of $t=kV^{-n}$ (figure 5.3.3). Cassaing et al. (1989) compared the mass and transmission loss results from SAAB with the theory of Springer (1976) for monocrystalline magnesium fluoride, and obtained a reasonable agreement for the mass loss incubation time, and erosion rate. Deom et al. (1990) attempted a further study on the SAAB whirling arm, to investigate the effects of stress on MgF₂, however even with only low stresses, all five samples tested broke before a quantitative result could be obtained. This result is of particular interest because stresses may be developed even during ordinary use on the whirling arm, and this may account for part of the discrepancy between their results and those of SIJA and MIJA.

A flight test through rain carried out in the UK, exposed an uncoated magnesium fluoride sample for 30 minutes at 134 to 144 m s⁻¹ on the wing pod of a mirage jet. At the end of the flight the sample was essentially undamaged with the front and rear surfaces having identical roughnesses, with no sign of any cracking. Like all flight test results the difficulty of defining the rainfield experienced by the sample limits further interpretation of these results.

5.3.4 MIJA Results

The MIJA results are shown in figures 5.3.4 and 5.3.5. The threshold velocity for circumferential damage for disc #1 was 245 m s⁻¹ (0.8 mm jet DTV (300 impacts) = 245 ± 5 m s⁻¹), while the threshold for disc #2 was 210 m s⁻¹ (0.8 mm jet DTV (300 impacts) = 210 ± 5 m s⁻¹). The undamaged surface of disc #2 can be seen in photo 1 on plate 9.3.1. The surfaces of both discs were clearly still very scratched even after polishing, with disc #2 having a worse finish than disc #1. This surface finish variation may be the reason why the two discs produced slightly different threshold values.

The results obtained using SIJA and the bursting disc test are shown in figure 5.3.6. These also exhibit a variability due to the poor surface finish of the specimens. Despite this there is still a good agreement between the two techniques, with SIJA giving a 0.8 mm jet DTV (mechanical) of 217 ± 17 m s⁻¹.

The photos in plate 9.3.1 show the familiar short cracks after just 2 impacts (photo 2), and the extension of these to longer cracks as the number of impacts increases (photo 5). The overlapping circles seen in photo 5 are the result of a shift in the position of the specimen during the experiment, and a more accurate and reliable specimen relocation method therefore appears to be necessary. An enlargement of one of these cracks is shown in photo 3 and its granular nature is very evident.

The role played by the surface scratches in determining the direction of growth of the cracks is not clear from the SEM observations made so far (e.g. photos 4 and 6), and further attention needs to be paid to the role of surface finish in initiation and propagation of the circumferential cracks.

As with spinel, central damage is an important feature of the impact site, however on magnesium fluoride this damage initiates after just 1 or 2 impacts (photo 7). The central damage appears different to that seen on spinel, with a number of cracks forming and no obvious pit, however it should be remembered that the centre of the impact may have shifted during this experiment.

5.3.5 Conclusion

The two magnesium fluoride discs evaluated on MIJA gave slightly different values for the threshold velocity for circumferential cracking because of the poor surface finish of the samples provided. The better polished disc had a 0.8 mm jet DTV (300 impacts) = $245 \pm 5 \text{ m s}^{-1}$, while the other had a 0.8 mm jet DTV (300 impacts) = $210 \pm 5 \text{ m s}^{-1}$. These results compare well with the threshold velocity obtained using SIJA and a residual strength test as described in section 4.2.3, (0.8 mm jet DTV (mechanical) = $217 \pm 17 \text{ m s}^{-1}$).

Hackworth's threshold value for a single 2 mm drop impact of 320 m s^{-1} is once again lower than the 2 mm equivalent drop value for the DTV obtained from MIJA of $400 \pm 10 \text{ m s}^{-1}$ (0.8 mm jet DTV (1 impact) = $320 \pm 10 \text{ m s}^{-1}$). However of more cause for concern is the damage obtained at even lower velocities (208 m s^{-1}) by Deom et al. (1987). Whether in this instance damage is initiated by central damage, as seen with MIJA, deserves further investigation, as does the cause of the central damage itself.

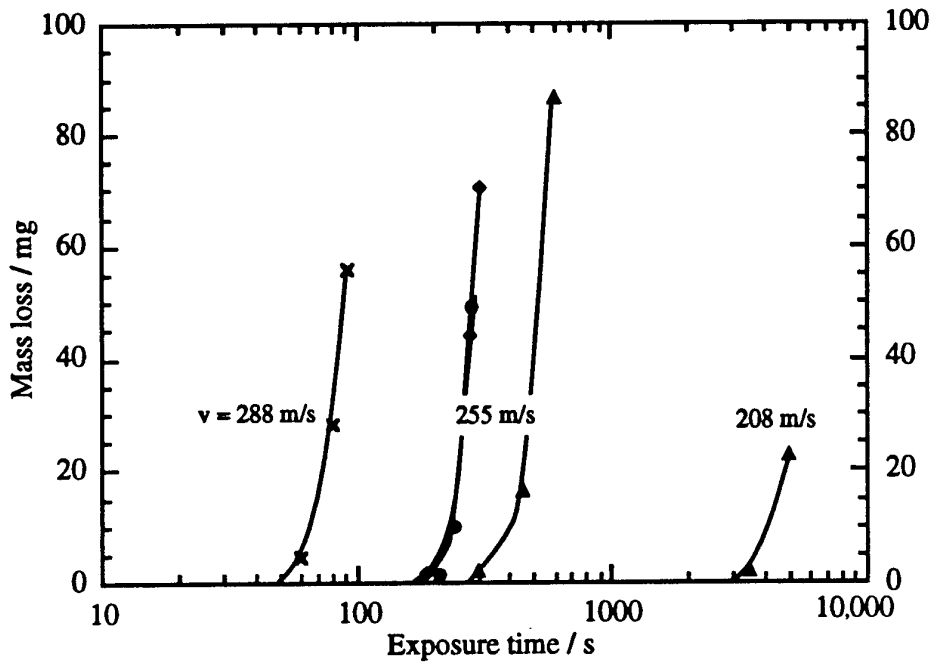


Figure 5.3.1 Mass loss of magnesium fluoride against exposure time. (Deom et al., 1987)

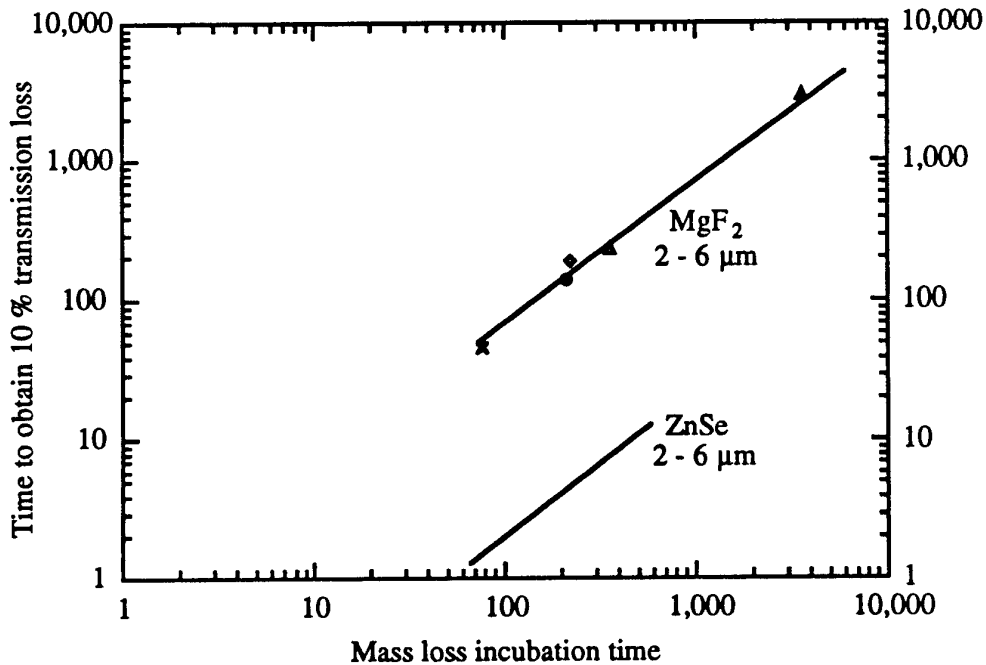


Figure 5.3.2 Variation of the incubation time for mass loss and transmission loss for magnesium fluoride and zinc selenide. (Deom et al., 1987)

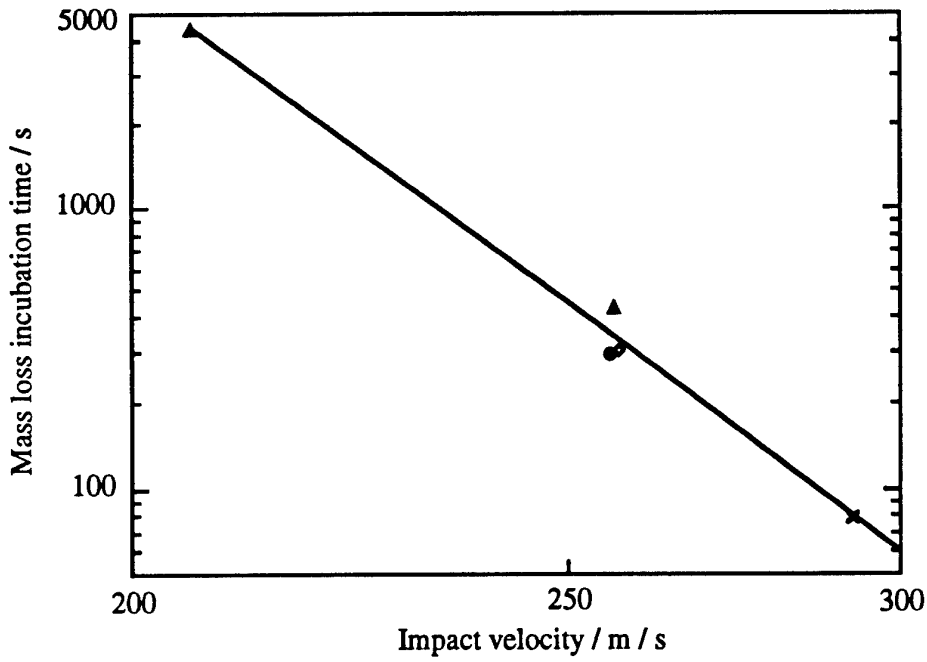


Figure 5.3.3 Variation in the incubation time for mass loss with impact velocity for magnesium fluoride . (Deom et al., 1987)

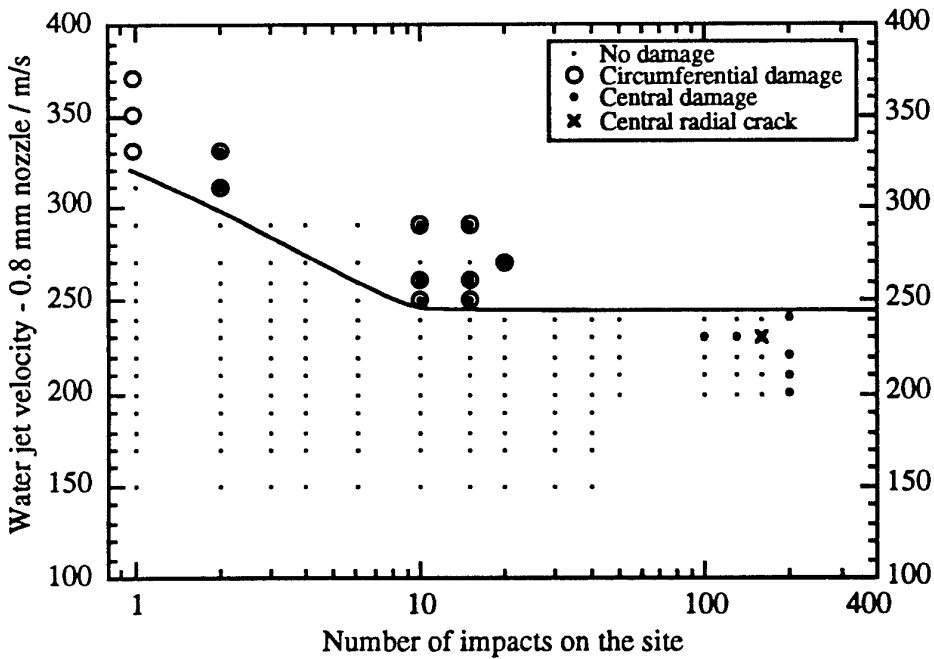


Figure 5.3.4 Threshold curve for magnesium fluoride disc #1.

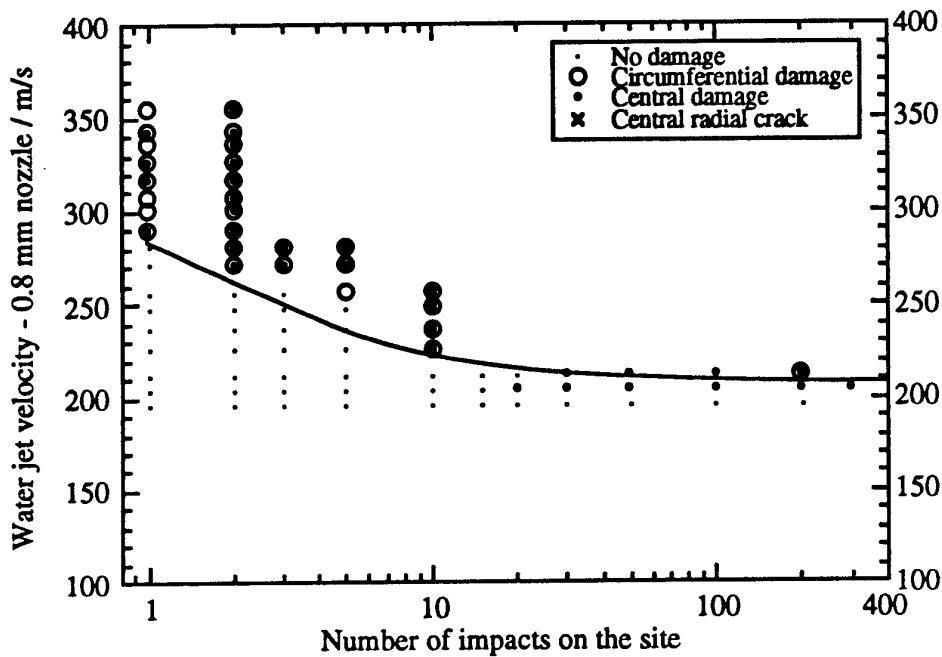


Figure 5.3.5 Threshold curve for magnesium fluoride disc #2.

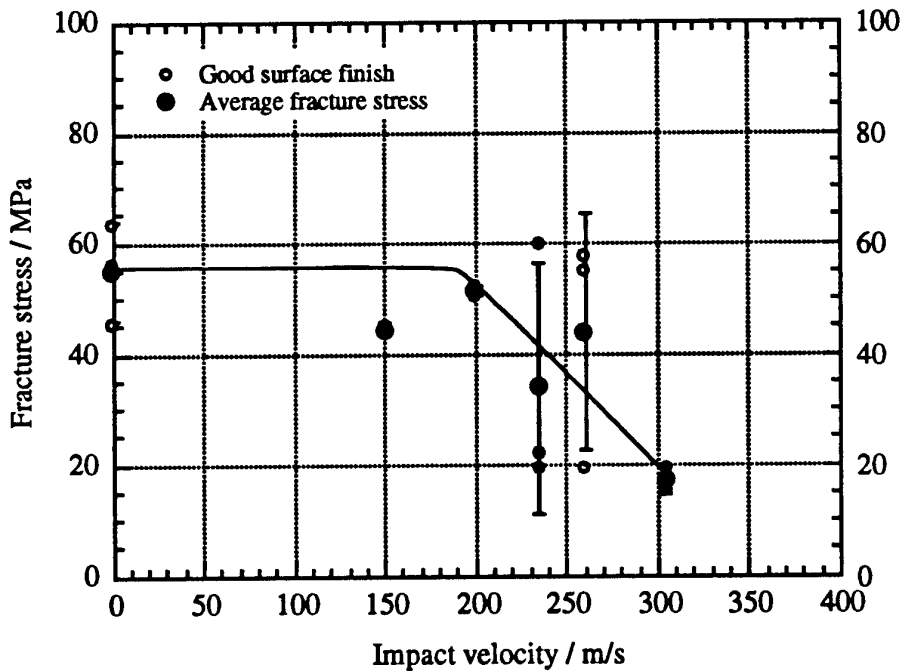


Figure 5.3.6 SIJA evaluation of the threshold velocity for magnesium fluoride.

5.4 SILICON

5.4.1 Material Characteristics

The data below is taken from Anthony and Hopkins (1981), Savage (1985) and Klocek (1991).

Mechanical

Knoop hardness : 1,100 kg mm⁻²
Fracture stress : 117 - 138 MPa
Fracture toughness : 0.94 MPa m^{1/2}
Shear modulus : 79.92 GPa
Youngs modulus : 130 GPa
Poissons ratio : 0.28
Rain erosion resistance (see section 4.4)
0.8 mm jet DTV (1, 3, 10, 300 impacts)
410 ± 10, 310 ± 10, 275 ± 5, 215 ± 5 m s⁻¹

Thermal

Melting point : 1,420 °C
Thermal conductivity : 163 W m⁻¹ K⁻¹
Thermal expansion : 2.6 x 10⁻⁶ K⁻¹
Heat capacity : 753 J Kg⁻¹ K⁻¹

Physical

Density : 2.33 x 10³ Kg m³
Crystal structure : Cubic
Grain size : single crystal

Optical

Transmits 3 - 5 µm wavelength

Sample Used

Source : Auburn University, original source unknown
Dimensions : 25 mm diameter disc, 3.1 mm thick

5.4.2 Material Description

The physical and chemical properties of silicon are very similar to those of germanium. It can be used in both single crystal or polycrystalline form, with minimal scattering, and because of its use as a semiconductor material it is readily available in high quality. The effect of temperature can however be a problem with silicon. For example a 3 mm thick sample of a high resistivity material has a transmission that is reduced from 52 % at 240 °C to 20 % at 400 °C. This property has made silicon unfavourable for use in window applications (Savage, 1985), however its use is currently being re-evaluated by Poznich and Richter (1992).

5.4.3 Published Rain Erosion Work

Eskilsson (1974) described erosion work on silicon using 2 mm diameter drops, on the SAAB whirling arm rig. After 60 minutes damage had been obtained at 260 m s⁻¹ but not at 210 m s⁻¹. Unfortunately no further information was given as to the type of silicon used or its orientation. The motivation behind this study was to compare the time to failure for stressed and unstressed silicon discs. As with the study of Déom (1990) a large drop in the erosion resistance was noted for the stressed disc.

A few further experiments on silicon conducted by various institutes in the 60's and 70's, at velocities ranging from 200 - 850 m s⁻¹ are mentioned by Springer (1976), however no mention is made of their results.

Hackworth (1979) made the first damage threshold evaluation for silicon, using single crystal material with the (100) plane as the face, and 2 mm diameter drops produced in the Bell Aerospace whirling arm rig. Hackworth found a single crack was

formed at 274 m s^{-1} , and a square ring fracture pattern at 340 m s^{-1} , and concluded that the threshold for single impact was $\sim 274 \text{ m s}^{-1}$.

The most recently reported tests on silicon are presented in Tustison and Gentilman (1988) and Cassaing et al. (1989). Tustison used the Wright-Patterson whirling arm, with 2 mm diameter drops, and a rainfall of 1" / hr, and reported damage after a 5 minute exposure at just 135 m s^{-1} (figure 5.4.1) ! Cassaing et al. (1989) used the SAAB rig with 1.2 mm drops at velocities from 200 to 300 m s^{-1} . He compared his results with the theory of Springer (1976), and recorded optical degradation after 40 mins at 186 m s^{-1} .

5.4.4 MIJA Results

The MIJA threshold evaluation on silicon was carried out in order to be able to make a comparison between the damage produced on a silicon substrate, with the damage produced on a silicon substrate with a CVD diamond coating.

Two discs were tested, the first was polished, while the second was already scratched ready for deposition¹. The exact grain orientation of the two discs has not been determined, however an indication is given by the fact that the damage patterns obtained show three-fold rather than four-fold symmetry.

The two results from MIJA can be seen in figures 5.4.2 and 5.4.3. The polished silicon disc had a threshold of $\sim 215 \text{ m s}^{-1}$ (0.8 mm jet DTV (300 impacts) = $215 \pm 5 \text{ m s}^{-1}$), while the scratched disc had a threshold of $\sim 195 \text{ m s}^{-1}$ (0.8 mm jet DTV (300 impacts) = $195 \pm 5 \text{ m s}^{-1}$).

The photos shown in plate 9.4.1 are taken from the polished disc. Initially some of the damage sites only showed a central fracture as seen in photos 1 and 2. However some complete rings of damage were also obtained as seen in photos 3 and 6 with a central undamaged area ~ 1.1 - 1.2 mm in diameter. These two photos both show the hexagonal fracture patterns obtained due to the intersection of the $\{111\}$ cleavage planes with the sample surface. Further fractures can often be seen running parallel with these sides as shown in photos 7 and 8, and stripping of scabs of material can be seen to have taken place by the action of the lateral spreading of the water jet as shown in photo 6 and 8.

5.4.5 Conclusion

As with the previous materials the appearance of central damage and the lower threshold values obtained on the whirling arm rigs require further investigation.

The surface finish appears to have had an effect on the value of the threshold velocity, and it is probably this that caused the final threshold value to drop on the scratched sample from 0.8 mm jet DTV (300 impacts) $\sim 215 \text{ m s}^{-1}$ to $\sim 195 \text{ m s}^{-1}$ ($\sim 300 \text{ m s}^{-1}$ to 275 m s^{-1} for an equivalent 2 mm drop). This effect is even more evident after only one shot has been fired, where the threshold appears to have dropped from 0.8 mm jet DTV (1 impact) $\sim 410 \text{ m s}^{-1}$ to $\sim 290 \text{ m s}^{-1}$ as seen in figure 5.4.4 ($\sim 480 \text{ m s}^{-1}$ to 375 m s^{-1} for an equivalent 2 mm drop). Until the crystallographic orientations are obtained for both discs it is not however possible to say how much of this difference is ascribable to surface finish, and how much to a difference in orientation of the cleavage planes to the surface.

¹ The disc was abraded with diamond powder so that small diamond fragments were left in the surface to act as nuclei for CVD diamond growth

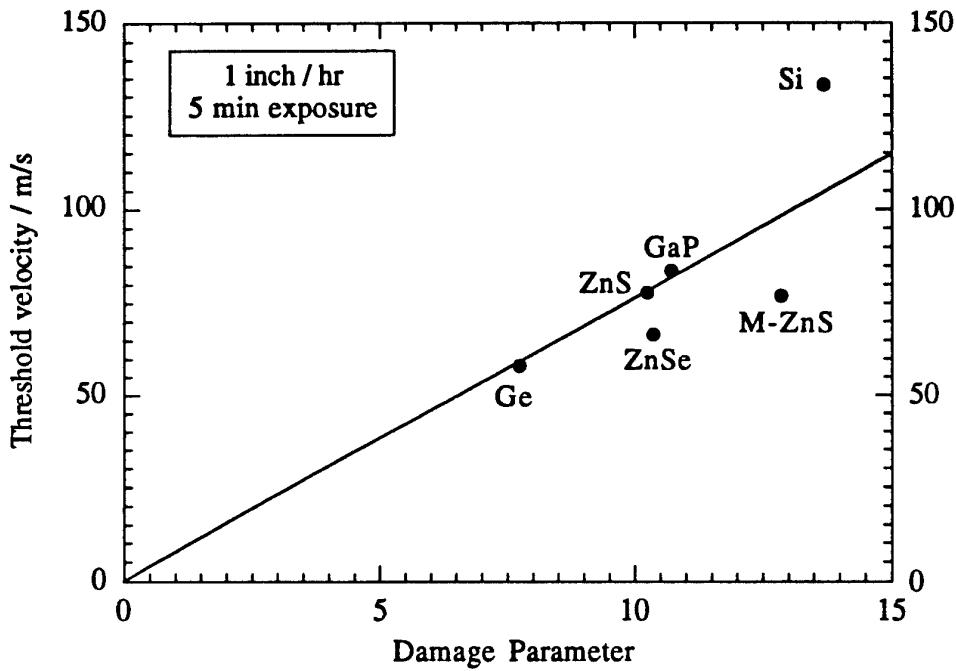


Figure 5.4.1 Multiple drop (2,000 to 4,000 impacts) rain erosion damage threshold for various materials as a function of damage parameter ($K_c^{2/3}c_t^{1/3}$). (Tustison and Gentilman, 1988)

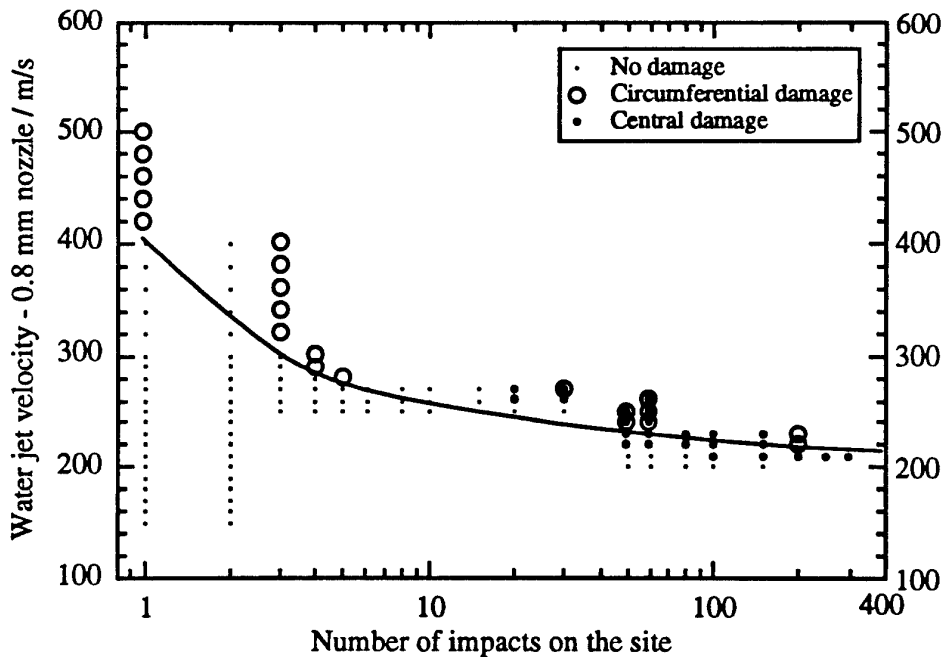


Figure 5.4.2 Threshold curve for a polished silicon disc.

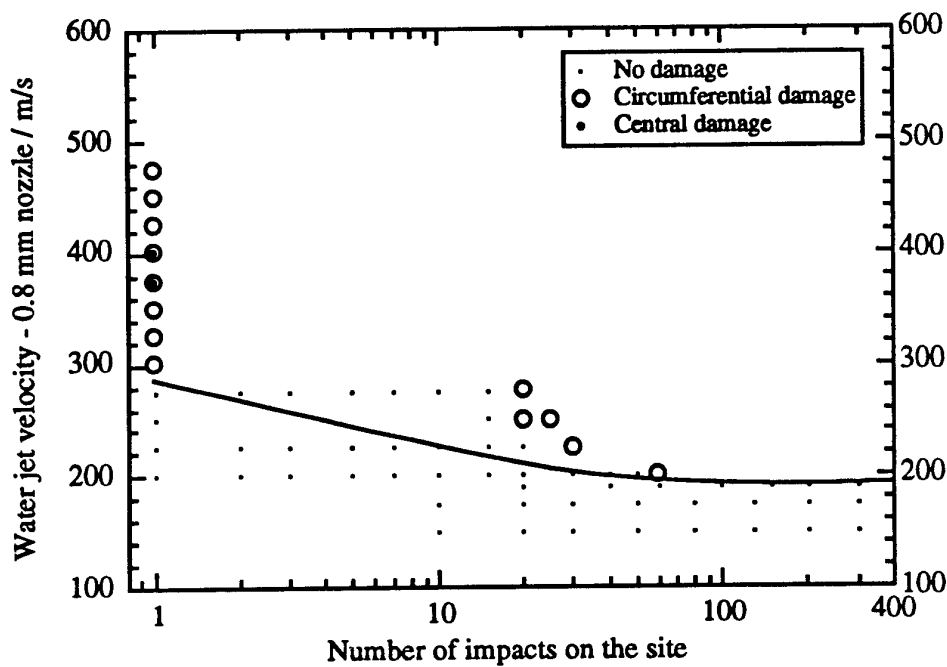


Figure 5.4.3 Threshold curve for a silicon disc scratched ready for deposition of CVD diamond.

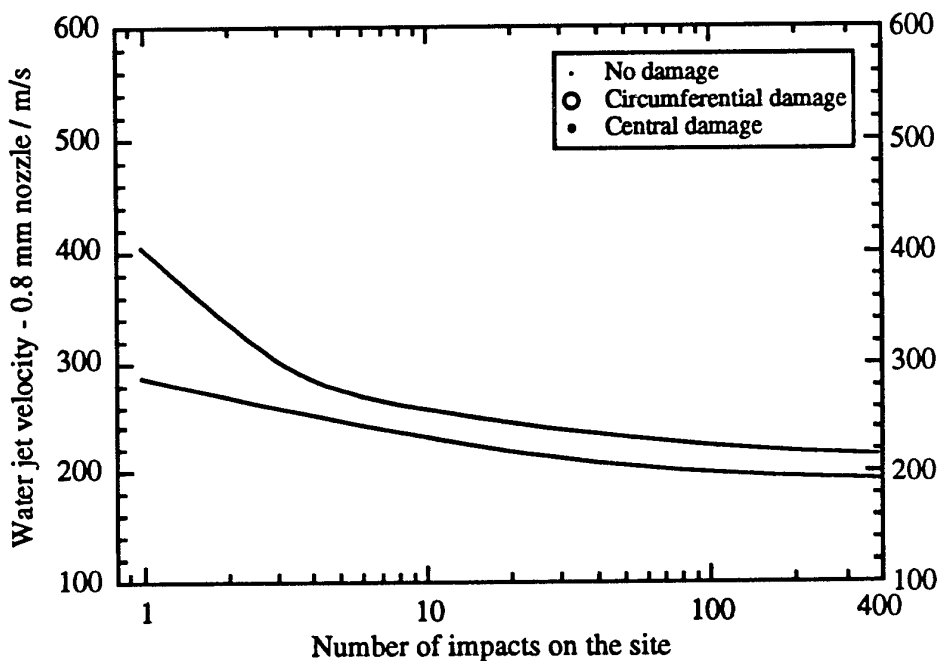


Figure 5.4.4 Summary of the threshold curves for the two silicon discs tested.

5.5 ZINC SULPHIDE

5.5.1 Material Characteristics

The data below refers to the standard grade of CVD ZnS and is taken from Savage (1985), Klocek (1991), Pickles (1991) and the CVD Ltd materials specification.

Mechanical

Knoop hardness : 230 kg mm⁻²
Fracture stress : 68 MPa
Fracture toughness : 0.67 - 1.0 MPa m^{1/2}
Youngs modulus : 87 GPa
Poissons ratio : 0.29
Weibull modulus : 5.6
Rain erosion resistance (see section 4.4)
0.8 mm jet DTV (1, 3, 10, 300 impacts);
170 ± 5, 155 ± 5, 145 ± 5, 130 ± 5 m s⁻¹

Thermal

Melting point : 1,830 °C
Thermal conductivity : 16.7 W m⁻¹ K⁻¹
Thermal expansion : 7.85 x 10⁻⁶ K⁻¹
Heat capacity : 469 J Kg⁻¹ K⁻¹
Thermal shock resistance : 1.2 kW m⁻¹

Physical

Density : 4.09 x 10³ Kg m³
Crystal structure : Cubic
Grain size : 2 - 8 µm

Optical

Transmits 3 - 5, 8 - 12 µm wavelengths

Sample Used

Source : Plessey Research, Caswell
Dimensions : 25 mm diameter disc, 3 mm thick

5.5.2 Material Description

There are three main types of zinc sulphide used for infrared windows and domes. The first type is Irtran 2 which is made by the Eastman Kodak Company by hot-pressing. During the manufacture of Irtran 2 the prevention of contamination presents the same difficulties as described earlier for hot-pressed magnesium fluoride. The second type is grown by chemical vapour deposition (CVD ZnS). In this process the material is grown on the walls of a reaction chamber from a mixture of zinc vapour and hydrogen sulphide at up to 100 µm hr⁻¹. The third type is known as multi-spectral or water-clear. This is produced by leaching out excess zinc and hydrogen from the CVD zinc sulphide by hot isostatic pressing (HIP) (Donadio et al., 1981, Willingham and Pappis, 1982).

The development of CVD zinc sulphide has provided a cost effective method for the manufacture of arbitrary shapes with the additional benefit of improved optical properties over the hot-pressed material. Two of the major disadvantages of zinc sulphide for use as a window material are its transmittance limitations when hot (8 - 10 µm), and its poor rain erosion resistance unless used at small angles of incidence.

5.5.3 Published Rain Erosion Work

Adler and Hooker (1978) investigated the difference between hot-pressed and CVD ZnS. They found that on impact with 2 mm drops at 212 - 222 m s⁻¹ hot-pressed ZnS suffered intergranular fracture and CVD transgranular. Hackworth (1979, 1982) confirmed that fracture in CVD ZnS was transgranular, and obtained an estimate of 175 m s⁻¹ for the damage threshold for single impact from a 2 mm drop. In addition Hackworth (1979) determined a threshold value of 192 m s⁻¹ for multiple impact with

0.75 mm drops (138 m s^{-1} for a 2 mm drop). With the 0.75 mm drops however, an identical rate of erosion was obtained at 340 m s^{-1} and 296 m s^{-1} so clearly problems existed with using these smaller drop diameters. Hackworth also looked at the rate of transmission loss at different velocities and angles of impact. He attempted to fit the results to the equation, $t = kV^{-n}$, but a reasonable fit to the data was only obtained with an impact angle of 90° , and no absolute value for a damage threshold was determined.

Evans et al. (1980) produced a theoretical value for the damage threshold for 2 mm drops of 128 m s^{-1} , whilst Adler (1981) repeating this calculation obtained $89 - 116 \text{ m s}^{-1}$.

Van der Zwaag and Field (1982) used SIJA to produce a threshold for an equivalent 2 mm drop of 175 m s^{-1} . SIJA was also used by Lewis et al. (1986) who obtained a reasonable agreement with the result of Van der Zwaag, with 190 m s^{-1} for standard CVD ZnS, and 215 m s^{-1} for water clear ZnS. Lewis performed damage assessment by impacting several sites ten times each at a given velocity and finding the % number of sites showing failure. Lewis et al. (1986) also reported work performed with angled impact, and with impacts at 200°C to investigate the effect of temperature. Finally Savage and Edwards (1988) quoted SIJA thresholds for 2mm drops on standard CVD ZnS as 170 m s^{-1} , and for water clear ZnS as 197 m s^{-1} . The broad agreement between all these results for damage threshold evaluation using SIJA is encouraging considering the number of different experimental, and damage assessment techniques being used.

Adler (1987) attempted to evaluate the threshold for ZnS by extrapolation of crack lengths at different velocities as shown in figure 5.5.1. This produced a threshold value for a 2.25 mm drop of $150 - 160 \text{ m s}^{-1}$ ($156 - 166 \text{ m s}^{-1}$ for a 2 mm drop). However the error inherent in this technique is large due to the difficulty of crack length measurement near the threshold.

Several whirling arm transmission loss results have also been published for ZnS (Pappis, 1990). Corney and Pippett (1983) compared the RAE results with those of Hackworth (1979) and found they obtained a better long term performance (figure 5.5.2). Waddell and Monahan (1990) showed the transmission loss for water clear ZnS to be faster than standard ZnS on the RAE rig (figure 5.5.3), while Saunders et al. (1986) counted single impact marks on ZnS using the Wright-Patterson rig and showed that 1.8 mm diameter drops were still causing damage at 110 m s^{-1} (figure 5.8.1). This result has been confirmed by Tustison and Gentilman (1988) who obtained a threshold for both water clear and standard ZnS of $\sim 80 \text{ m s}^{-1}$ on the same whirling arm rig with 1.8 mm diameter drops! (figure 5.4.1). Cassaing et al. (1989) using the SAAB rig with 1.2 and 2.0 mm drops was still able to obtain a 10 % transmission drop with 1.2 mm drops after 30 mins at $\sim 220 \text{ m s}^{-1}$ ($\sim 185 \text{ m s}^{-1}$ for a 2 mm drop). Deom et al. (1990) obtained data on the SAAB rig for the effects of temperature on the rate of transmission loss. They observed that over the temperature range $10 - 130^\circ\text{C}$ the rate of transmission loss for Ge and ZnSe increased while that for ZnS decreased! (figure 5.5.4). Such effects of temperature warrant future investigation as they have importance in the interpretation of both real flight results and those obtained from the whirling arm.

A flight test performed on a mirage jet, exposing zinc sulphide to natural rain for 30 minutes at $134 - 144 \text{ m s}^{-1}$, resulted in a large number of ring cracks. Although the general appearance was similar to that of water jet damage, the impact sizes tended to be smaller. The damage sites didn't always have a central undamaged area, and occasionally exhibited cracking in this region of a similar type to that seen with water jets produced in the lab. In one extreme case a large radial fracture was evident similar to one produced by Adler using a SIJA, however its possible that this may have been caused by dust or ice impact.

Finally two full reviews of the liquid impact properties of ZnS have been published, Adler et al. (1979) and Field et al. (1981).

5.5.4 MIJA Results

Three ZnS discs were tested using MIJA, in order to evaluate the reproducibility of its results. The threshold graphs for these three discs can be seen in figures 5.5.5 - 5.5.7, and are all summarised in figure 5.5.8. The agreement between the curves is outstanding, and appears to be limited by the resolution to which the experiments were performed, the curves giving the threshold for ZnS as 0.8 mm jet DTV (300 impacts) = $130 \pm 5 \text{ m s}^{-1}$. The threshold on ZnS was also evaluated using a 0.6 mm nozzle and this gave the result shown in figure 5.5.9 with a 0.6 mm jet DTV (300 impacts) = $135 \pm 5 \text{ m s}^{-1}$. A further ZnS experiment was conducted with observations of damage made from the front, compared with those made looking through the bulk of the specimen from the bottom. This was done to evaluate the possibility of damage detection for the samples with opaque coatings from the bottom of the disc. The result shown in figure 5.5.10 indicates a large inaccuracy after just a few impacts, but that the final threshold value obtained is identical.

Photos of some of the damage sites can be seen in plate 9.5.1. As the number of impacts on one site increases, the cracks increase in length around the circumference of the damaged area. The appearance is thus similar to both magnesium fluoride and spinel seen earlier. However unlike these two previous materials, the central undamaged area is closer in diameter to that of the nozzle orifice, 0.8 - 0.9 mm, instead of 1.2 - 1.4 mm.

Two different types of central damage have occasionally been produced by impacts on ZnS. They are however both very different in appearance to those seen on spinel and magnesium fluoride, consisting either of small circumferential cracks, or of wispy radial cracks. None of the sites tested with a 0.8 mm nozzle during the threshold evaluations documented here showed any central damage.

The black dots visible in the photos are probably a result of the poor adhesion of the film sputtered prior to SEM examination, and not pores or surface defects.

5.5.5 Conclusion

The threshold results on all three ZnS discs tested, produced similar values of 0.8 mm jet DTV (300 impacts) = $130 \pm 5 \text{ m s}^{-1}$ ($\sim 195 \text{ m s}^{-1}$ for a 2 mm diameter equivalent drop). This compares well with previous SIJA results, and the thresholds obtained using the techniques described in chapter 4. However as with silicon the threshold values obtained by Tustison and Gentilman (1988) and Hackworth (1979) on whirling arm rigs are considerably smaller.

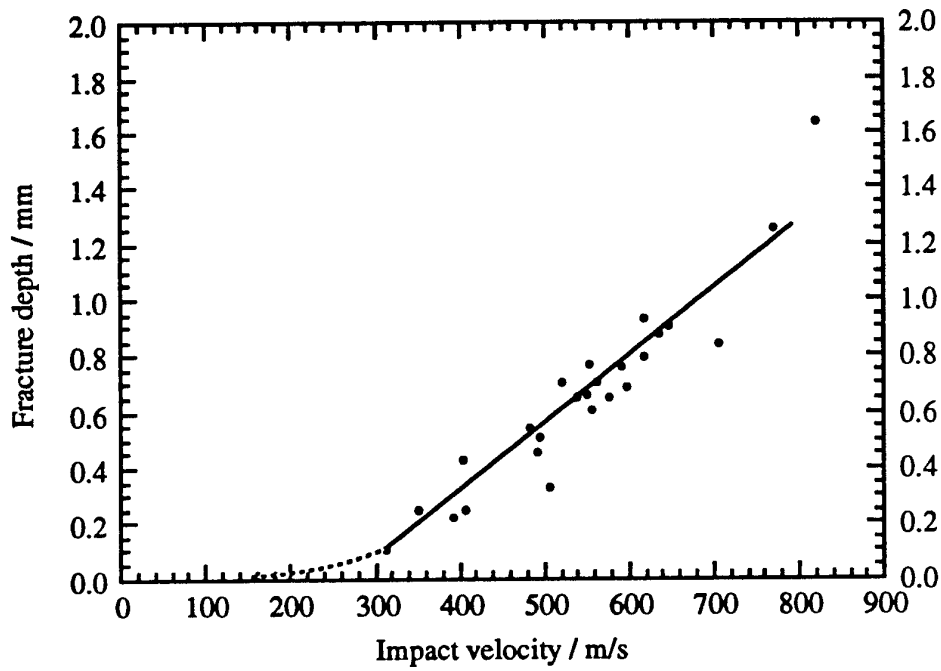


Figure 5.5.1 Penetration depth for type I fractures (see figure 1.3) as a function of impact velocity for water drop impacts on CVD ZnS. (Adler, 1987)

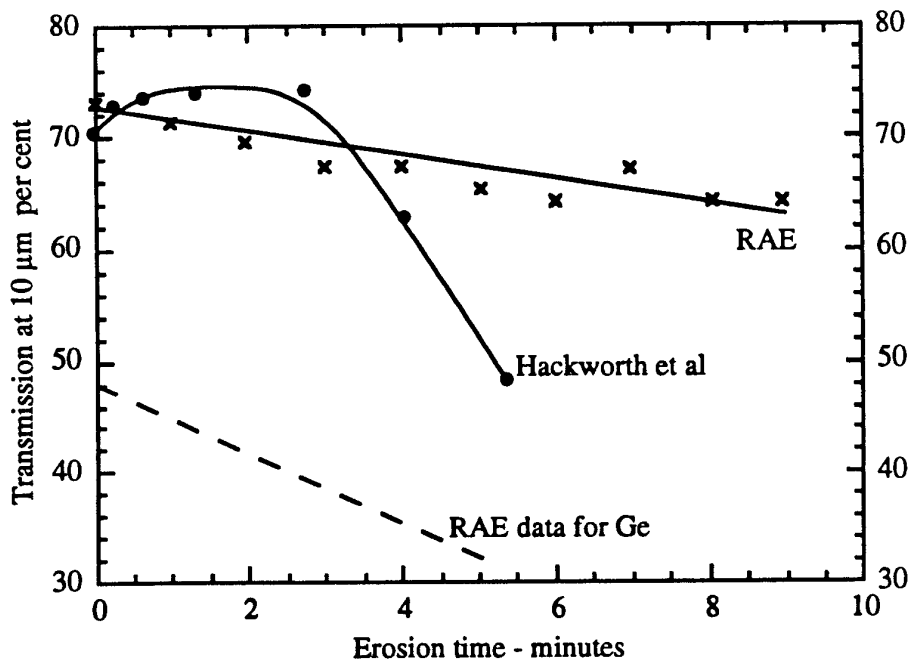


Figure 5.5.2 Whirling arm data for the rain erosion resistance of ZnS and Ge obtained on the RAE and Bell Aerospace rigs at 223 m s^{-1} . (Corney and Pippett, 1983)

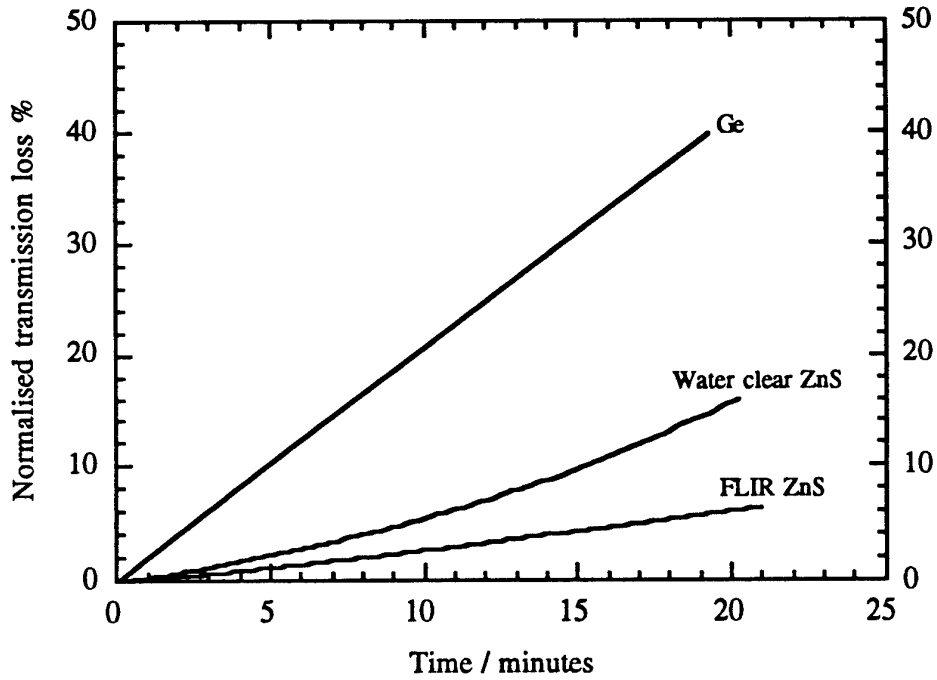


Figure 5.5.3 Normalised transmission loss of FLIR and water clear ZnS, compared to Ge. Performed on the RAE whirling arm rig at 223 m s^{-1} . (Waddell and Monaghan, 1990)

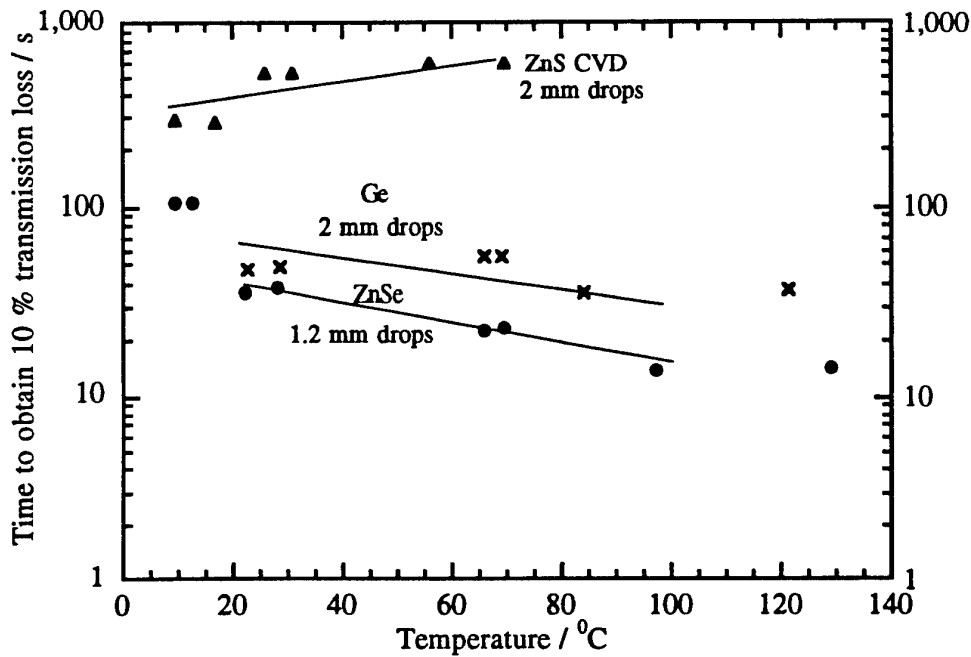


Figure 5.5.4 Variation of the normalised time to obtain 10 % transmission loss for ZnS, Ge and ZnSe at 230 m s^{-1} . (Deom et al., 1990)

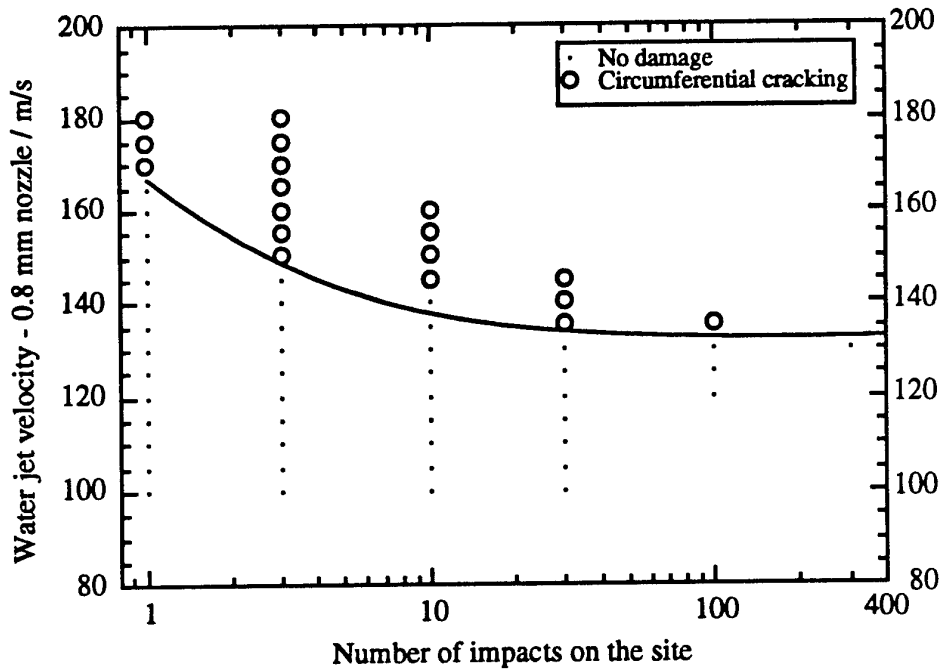


Figure 5.5.5 Threshold curve for zinc sulphide disc #2.

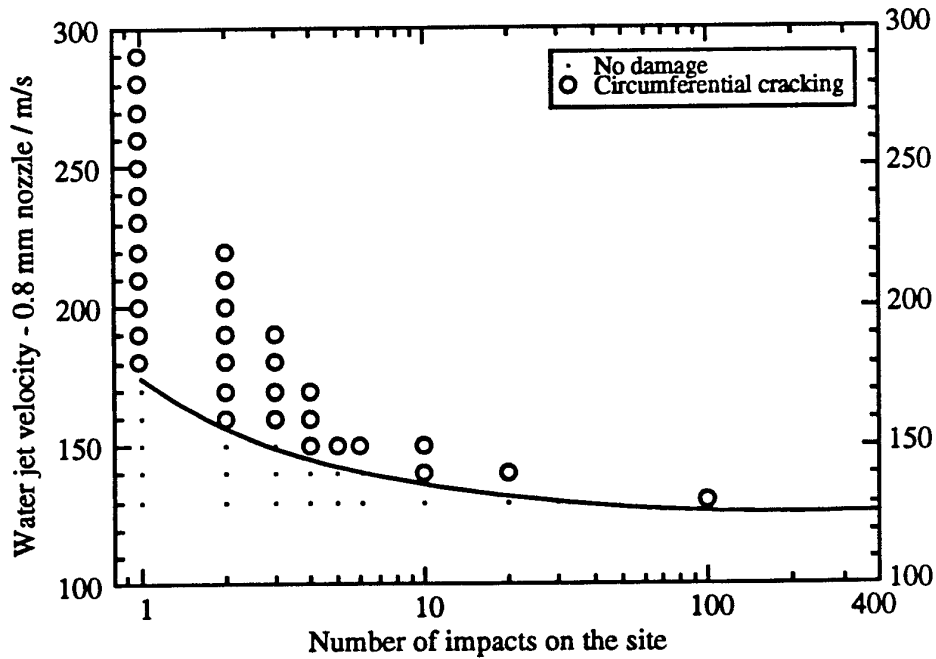


Figure 5.5.6 Threshold curve for zinc sulphide disc #3.

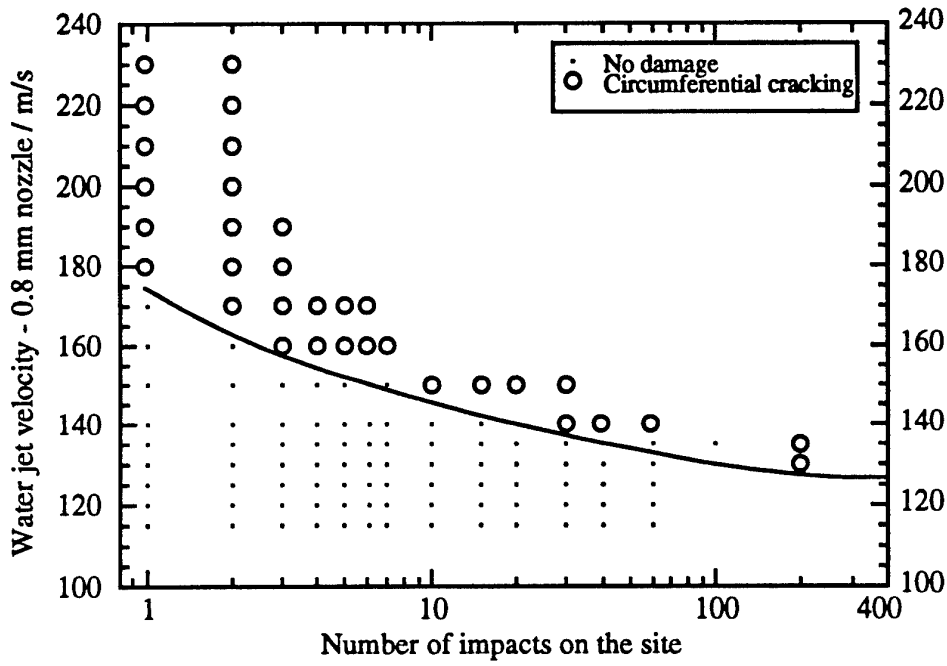


Figure 5.5.7 Threshold curve for zinc sulphide #5.

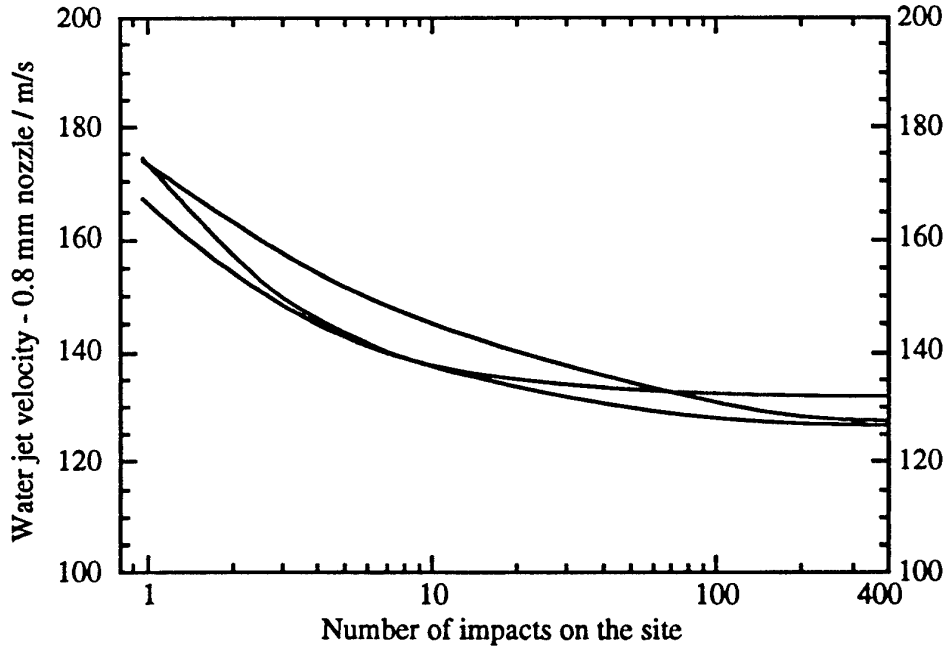


Figure 5.5.8 Summary of the three threshold curves performed on zinc sulphide with a 0.8 mm nozzle.

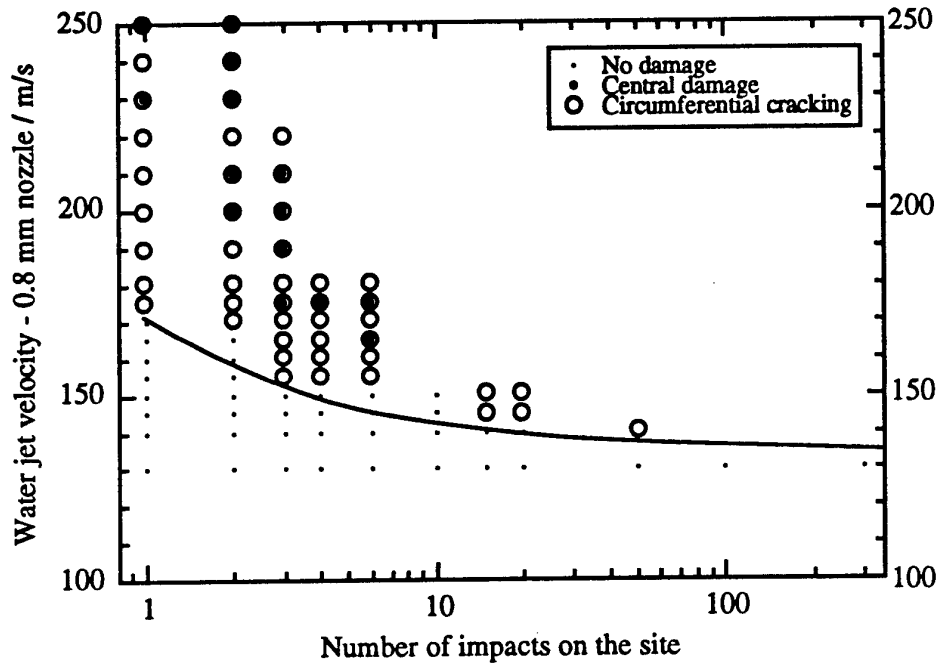


Figure 5.5.9 Threshold curve for zinc sulphide with a 0.6 mm nozzle.

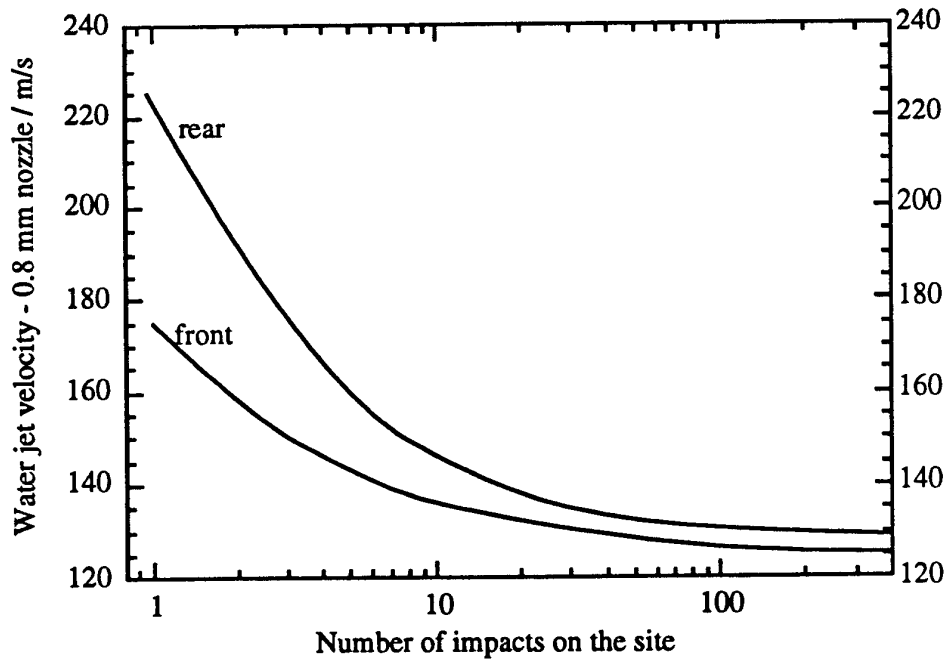


Figure 5.5.10 Comparison of the threshold velocity curve for zinc sulphide produced by looking for damage from the front of the disc, with that obtained by looking through the bulk from the rear.

5.6 DIAMOND II A

5.6.1 Material Characteristics

This material transmits in both the 3 - 5 μm and the 8 - 12 μm wavelengths. The data below is taken from Savage (1985), Klocek (1991), Pickles (1991).

Mechanical

Knoop hardness : 5,700-10,400 kg mm^{-2}
Fracture stress : 2,942 MPa
Fracture toughness : 3.4 MPa $\text{m}^{1/2}$
Youngs modulus : 1,050 GPa
Poissons ratio : 0.07
Rain erosion resistance (see section 4.4)
0.8 mm jet DTV ~ 530 m s^{-1}

Optical

Transmits 3 - 5, 8 - 12 μm wavelengths

Thermal

Melting point : 3,500 $^{\circ}\text{C}$
Thermal conductivity : 2,600 $\text{W m}^{-1} \text{K}^{-1}$
Thermal expansion : $0.8 \times 10^{-6} \text{K}^{-1}$
Heat capacity : 110,000 $\text{J Kg}^{-1} \text{K}^{-1}$
Thermal shock resistance : 12,000 kW m^{-1}

Physical

Density : $3.52 \times 10^3 \text{Kg m}^3$
Crystal structure : Cubic
Grain size : Single crystal

Sample Used

Source : Barr and Stroud
Dimensions : 6 mm diameter disc, 1 mm thick

5.6.2 Material Description

Diamond is the ultimate infrared window material because of its superior optical and mechanical properties. There are four main types of diamond: Ia and Ib contain dissolved nitrogen; IIb contains dissolved boron; and IIa which is effectively free of nitrogen. Research on the fracture and strength properties is difficult because of its high cost, and this has also restricted its use as a window material.

5.6.3 Published Rain Erosion Work

The only previous work on diamond was conducted by Hancox (1962) using a wheel at the Cavendish Labs. After 5×10^6 impacts with a 1.35 mm diameter water jet at an impact velocity of 95 m s^{-1} there was no sign of deformation. This was the maximum impact velocity possible.

The work described below has been published in Seward et al. (1992a, b).

5.6.4 MIJA Results

Because of the expense of the material, only one type IIa bulk natural diamond disc was initially available for this study. This sample was a disc 6 mm in diameter and 1 mm thick.

In order to evaluate the effects of the specimen dimensions on the threshold velocity, two 25 mm diameter, 3 mm thick, specimens of sapphire, and eight 6 mm diameter, 1 mm thick, specimens of sapphire were first tested using MIJA. The threshold produced with the two 25 mm discs has already been discussed in section 5.1.4.a. At the time when the results of the natural diamond work were first published the only sapphire results available were those given in section 5.1.4.a and the

threshold velocity was therefore taken to be 0.8 mm jet DTV (300 impacts) = 425 ± 5 m s⁻¹. Taking into account more recent experiments on other sapphire specimens as presented in section 5.1.4 (including two with the same orientation and finish as the original two) a more accurate value for the threshold velocity for bulk sapphire is probably 0.8 mm jet DTV (300 impacts) = 485 ± 5 m s⁻¹. The analysis that follows has been revised to take into account this new threshold value.

The first three 6 mm diameter discs of sapphire were used to determine a threshold velocity for damage as follows. (See also figure 5.6.1).

DISC ONE

- No damage after 300 shots at 400 m s⁻¹
- No damage after 300 shots at 420 m s⁻¹
- Broke after 200 shots at 440 m s⁻¹

DISC TWO (photo 8, plate 9.6.1 and plate 9.6.2)

- No damage after 300 shots at 400 m s⁻¹
- No damage after 300 shots at 420 m s⁻¹
- Broke after 190 shots at 440 m s⁻¹

DISC THREE

- Broke after 225 shots at 440 m s⁻¹

The first two discs tested suggested a threshold of 430 ± 10 m s⁻¹, and the 3rd disc confirmed that the previous 600 shots on discs 1 and 2 had a negligible effect. The threshold for diamond may however have been outside of the velocity range of MIJA and so an experiment was performed with just ten shots per site to find an estimate of the error that could occur if a smaller number of shots had to be used on SIJA.

DISC FOUR (photos 1 - 3, plate 9.6.1)

- No damage after:
 - 10 shots at 400 m s⁻¹
 - 10 shots at 420 m s⁻¹
 - 10 shots at 440 m s⁻¹
 - 10 shots at 470 m s⁻¹
 - 10 shots at 490 m s⁻¹
- Broke after 3 shots at 505 m s⁻¹

This indicated that with just ten shots per site ~ 15 % error could be produced. The next two discs were tested to find how many shots would be needed to bring this error down to < 10 %.

DISC FIVE (photos 4 - 7, plate 9.6.1)

- Broke after 12 shots at 490 m s⁻¹

DISC SIX

- Broke after 140 shots at 470 m s⁻¹

One of the remaining two discs was tested first to confirm the 0.8 mm jet DTV ~ 430 ± 10 m s⁻¹ threshold and then to confirm the result of disc five.

DISC SEVEN

- No damage after 1,000 shots at 420 m s⁻¹
- Broke after 45 shots at 490 m s⁻¹

The final 6 mm sapphire disc was not tested in case further analysis was needed after the diamond experiment. The results with sapphire obtained at this stage indicated that the thresholds for the 25 mm and 6 mm diameter discs were very close, $425 \pm 5 \text{ m s}^{-1}$, and $430 \pm 10 \text{ m s}^{-1}$ respectively. They also indicated a large error $\sim 15 \%$ if only ten shots were used.

Following the sapphire work the diamond specimen was tested as below:

- No damage after 10 shots at each of 260, 280, 310, 330, 360, 390, 400, 420, 430, 440, 470, 490, 505, 530 m s^{-1}
- Broke after 170 shots at 530 m s^{-1} (plate 9.6.3)

5.6.5 Conclusion

For bulk sapphire the 0.8 mm jet DTV (300 impacts) = $485 \pm 5 \text{ m s}^{-1}$ (as shown in section 5.1) and not $425 \pm 5 \text{ m s}^{-1}$ as first assumed. The threshold velocity for the smaller 6 mm diameter sapphire discs appears to be extremely reproducible, but lower at $430 \pm 10 \text{ m s}^{-1}$. This represents a 10 % difference in the threshold velocity, presumably because of the effects of stress wave interactions. This agrees with work done by Townsend (1985) where an effect of specimen thickness was similarly observed.

The result for diamond was a threshold velocity for damage by a 0.8 mm jet of $\sim 530 \text{ m s}^{-1}$ (a threshold for an equivalent 2 mm drop of $\sim 580 \text{ m s}^{-1}$). If the sapphire result is correct then this value should be adjusted for larger diamond specimens, however the size of the adjustment will probably be different with diamond since it has a higher wave speed. This means that whilst for sapphire the stress waves have travelled $\sim 2 \text{ mm}$ in the time the stresses are still being applied, for diamond they have travelled $\sim 3 \text{ mm}$ and the reflected tensile pulse has arrived back. It should also be noted that because diamond has a higher acoustic impedance there is little transmission out of the specimen. Finally, it is also possible that the natural diamond sample may have been flawed. Because of all these uncertainties a second diamond specimen has now been supplied for evaluation using MIJA, and it is hoped that experiments can be carried out on this sample in such a way that they will help to resolve some of the issues mentioned above.

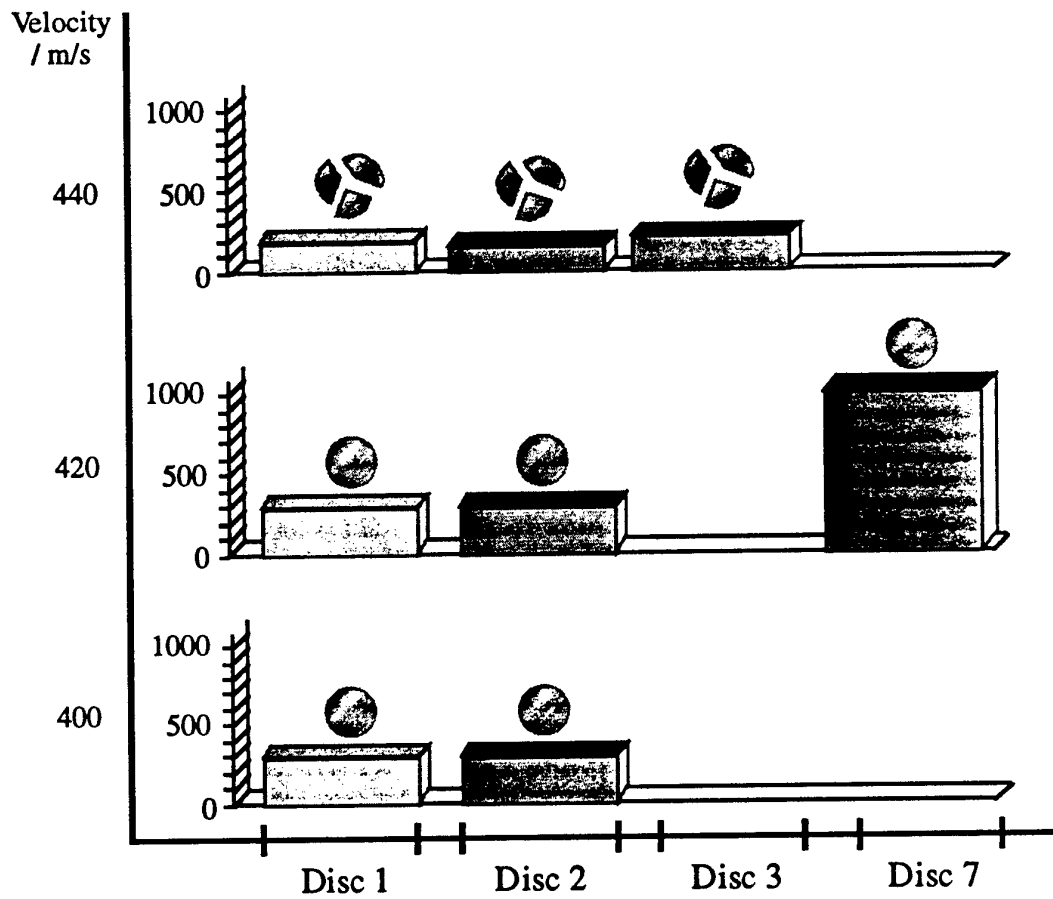


Figure 5.6.1 Pictorial representation of the method used to find the threshold velocity for the 6 mm sapphire discs.

5.7 GERMANIUM

5.7.1 Material Characteristics

The data below is taken from Savage (1985), Klocek (1991) and Pickles (1991). Some variation may occur depending on the crystal orientation (see for example Blair 1981 for K_{IC} measurements).

Mechanical

Knoop hardness : 800 kg mm⁻²
Fracture stress : 93 MPa
Fracture toughness : 0.57-0.67 MPa m^{1/2}
Youngs modulus : 103 GPa
Shear modulus : 67.04 GPa
Poissons ratio : 0.28
Rain erosion resistance (see section 4.4):
0.8 mm jet DTV (1, 3, 10, 300 impacts)
255 ± 5, 195 ± 5, 165 ± 5, 125 ± 5 m s⁻¹

Thermal

Melting point : 937 °C
Thermal conductivity : 59 W m⁻¹ K⁻¹
Thermal expansion : 6.1 × 10⁻⁶ K⁻¹
Heat capacity : 310 J Kg⁻¹ K⁻¹
Thermal shock resistance : 7.4 kW m⁻¹

Physical

Density : 5.32 × 10³ Kg m³
Crystal structure : Cubic
Grain size : Single crystal

Optical

Transmits 3 - 5, 8 - 12 μm wavelengths

Sample Used

Source : RAE
Dimensions : 50 mm diameter disc, 3 mm thick, orientation 7° from [111]

5.7.2 Material Description

Germanium can be used as an optical material in both the polycrystalline and single crystal forms. During the early and mid 1970s most of the optical germanium was grown in the polycrystalline form by the Stockbarger process, however the Czochralski technique then proved successful for growing single crystals (Wilks, 1959) and this offered a better overall performance, producing either single crystal or twinned material in diameters up to 250 mm (Van Goetham et al., 1986). A major asset of germanium is its low dispersion in the 8 - 12 μm range, since this means the small amount of chromatic aberration produced need not be corrected. However germanium is an unsuitable material for applications where aerodynamic heating is likely to occur, since free-electron absorption increases markedly above 70 °C, resulting in a rapid deterioration of its transmission properties.

5.7.3 Published Rain Erosion Work

Hooker (1977) investigated both polycrystalline and (111) single crystal germanium on a whirling arm rig using a 1"/hr rainfall of 1.8 mm diameter water drops at 222 m s⁻¹. Damage initiated through cleavage fractures, from surface pits and scratches, on the {111} planes, and this was extended by fracture on further cleavage planes, hydraulic penetration of existing cracks, and chipping of cracks due to the lateral outflow.

Blair (1981) performed jet impact on germanium at 250 m s⁻¹ and obtained hexagonal fracture patterns due to the (111) cleavage planes. He allegedly found that the hexagonal cracking was not uniformly intense on all six sides, and it alternated between extensive and weak. He attributed this to the fact that on one side of the ring

the planes ran outward making an angle of $\sim 70^\circ$ with the surface, which is near the maximum tensile stress trajectory, while on the other side they ran inwards. Blair also impacted a (100) face and obtained a crack pattern with four-fold symmetry. Van der Zwaag and Field (1983) conducted more jet impact work on coated and uncoated germanium, and Field et al. (1983) gave the 0.8 mm jet DTV (mechanical) as 150 m s^{-1} (205 m s^{-1} for an equivalent 2 mm drop).

A number of more recent investigations of germanium have been carried out on whirling arm rigs. Corney and Pippett (1983) (figure 5.5.2) and Waddell and Monachan (1990) (figure 5.5.3) both used the RAE rig at 223 m s^{-1} to measure transmission loss for 14 minutes. Corney and Pippett tried three different specimen angles 30° , 60° and 90° without detecting an incubation period. Deom et al. (1987) compared results from the RAE, SAAB and Dornier rigs as shown in fig 5.7.1., while Cassaing et al. (1989) investigated the time required to achieve 10 % transmission loss on the SAAB whirling arm for 1.2 and 2.0 mm drops. Wilson (1990) and Tustison and Gentilman (1988) both used the Wright-Patterson whirling arm. Tustison used 2 mm drops for 5 minutes and claimed that a damage threshold velocity of 60 m s^{-1} was obtained (figure 5.4.1). Wilson meanwhile used 1.8 mm drops for 20 minutes and reported some pitting at 130 m s^{-1} (125 m s^{-1} for a 2 mm drop), but no observable fracture until 170 m s^{-1} (164 m s^{-1} for a 2 mm drop). Clearly further clarification is needed for these Wright-Patterson results as to the specimen sources and impact conditions, as such a large difference in results on the same rig is hard to explain. For example Wilson (1993) in further tests on the Wright-Patterson rig found there was a considerable difference in the erosion performance of germanium that was $\langle 111 \rangle$, compared with germanium with 30 % of $\langle 100 \rangle$.

The discrepancy between the liquid jet and whirling arm results may partly be due to the drop size distribution, and the temperatures and stresses imposed on a whirling arm sample. It is therefore worth noting that Deom et al. (1990) investigated the variation in the rate of transmission loss with both temperature and stress for germanium, and found that the rate increased with both parameters as shown in figures 5.5.4 and 5.7.2.

5.7.4 MIJA Results

Two specimens were tested with a surface orientation 7° from [111]. The first threshold was obtained with a nozzle that was not producing round damage marks on PMMA (figure 5.7.3), while the second threshold was obtained after the nozzle had been repolished so the damage produced was once again round (figure 5.7.4). The corresponding 0.8 mm jet DTV (300 impacts) were $155 \pm 5 \text{ m s}^{-1}$, and $125 \pm 5 \text{ m s}^{-1}$ respectively. It is likely that a non-round jet would give a higher threshold because the minimum dimension of the compressed region is smaller, therefore release waves reach the centre quicker.

The SEM photos obtained were very similar to those of silicon in plate 9.4.1, showing hexagonal fracture patterns with increasing amounts of scabbing as the number of shots increased.

5.7.5 Conclusion

For germanium the 0.8 mm jet DTV (300 impacts) = $125 \pm 5 \text{ m s}^{-1}$ ($\sim 190 \text{ m s}^{-1}$ for an equivalent 2 mm drop). As with the results for the previous materials this appears to be slightly high when compared to the whirling arm tests. However it does produce the same material ranking, with the threshold for germanium lower than that of ZnS; in agreement with results found by Tustison and Gentilman (1988), and contrary to those of Field et al. (1983).

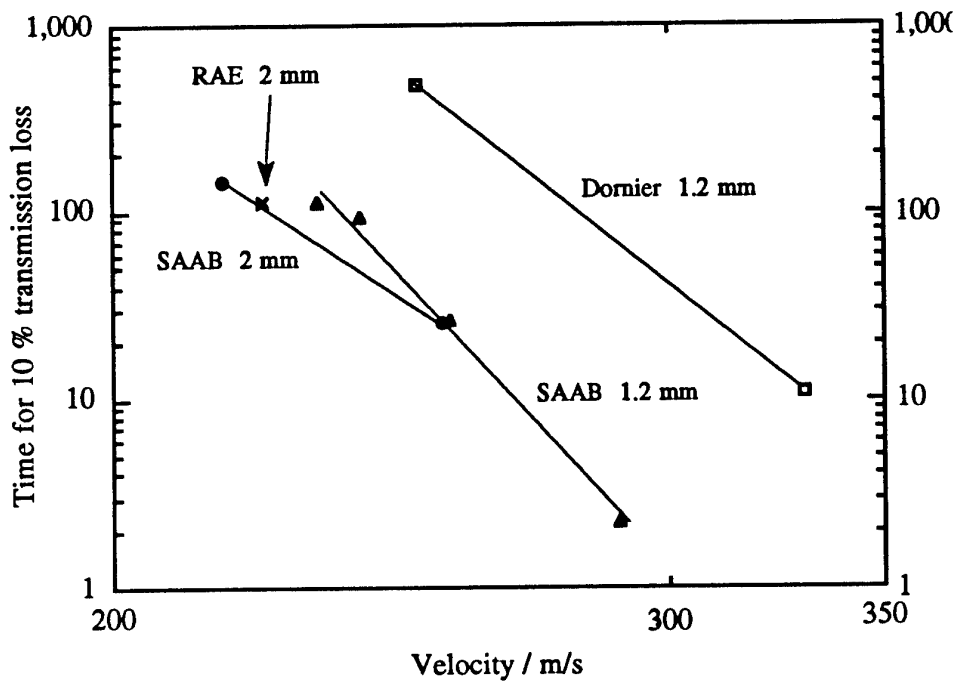


Figure 5.7.1 Scatter in the rain erosion measurements for germanium from three different whirling arm rigs. (Deom et al., 1987)

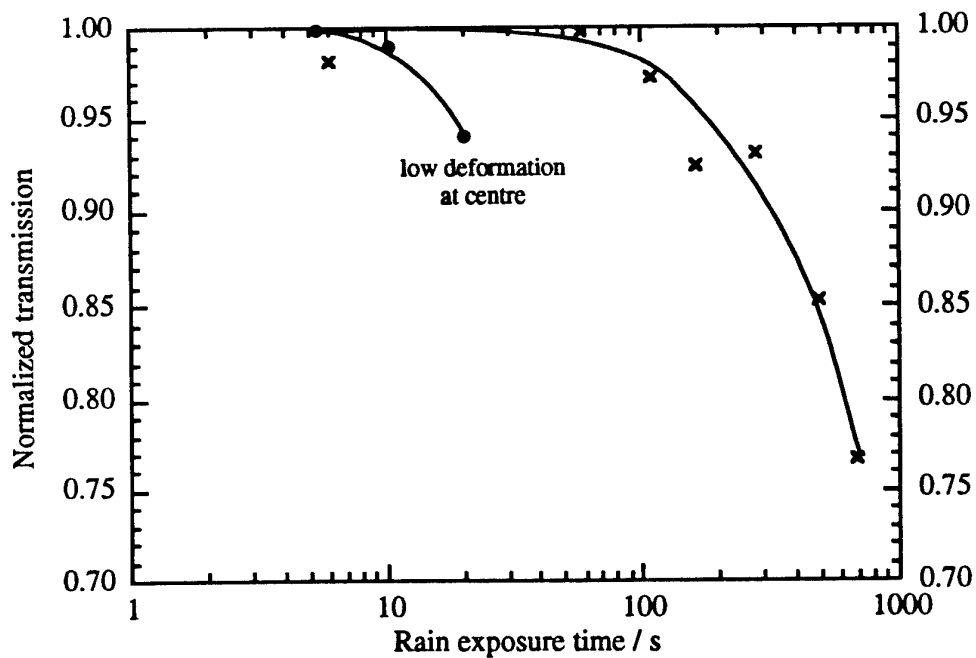


Figure 5.7.2 Variation of normalised transmission of germanium samples for different stresses, using the SAAB whirling arm rig at a velocity of 210 m s^{-1} with droplet diameters of 1.2 mm . (Deom et al. 1990)

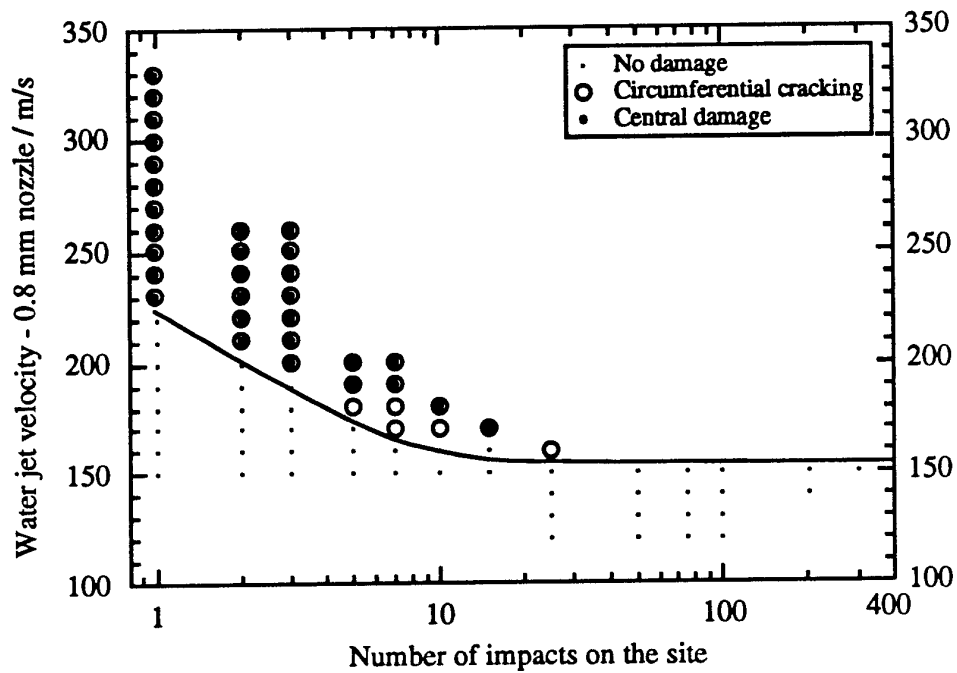


Figure 5.7.3 Threshold curve for germanium disc #1. (produced with nozzle producing non-round damage)

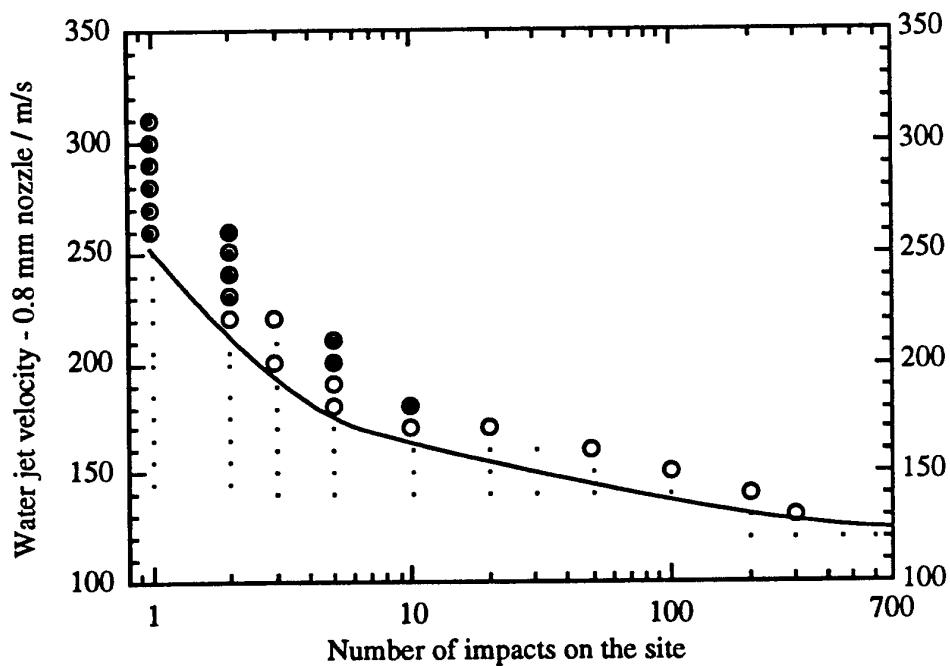


Figure 5.7.4 Threshold curve for germanium disc #2. (produced with nozzle repolished to produce round damage again).

5.8 CALCIUM LANTHANUM SULPHIDE

5.8.1 Material Characteristics

A range of different compositions are obtainable which allow a slight variation in the values given below. The data is taken from Savage (1985), Brierley et al. (1990), Klocek (1991), Pickles (1991).

Mechanical

Vickers hardness : 5.17 GPa
Fracture stress : 37 MPa
Fracture toughness : 0.66 MPa m^{1/2}
Youngs modulus : 90 - 96 GPa
Poissons ratio : 0.25
Rain erosion resistance (see section 4.4)
0.8 mm jet DTV (1, 3, 10, 300 impacts)
245 ± 5, 200 ± 5, 165 ± 5, 110 ± 5 m s⁻¹

Thermal

Melting point : 1,810 °C
Thermal conductivity : 1.7 W m⁻¹ K⁻¹
Thermal expansion : 12 - 14.7 x 10⁻⁶ K⁻¹
Thermal shock resistance : 0.07 kW m⁻¹

Physical

Density : 4.61 - 4.97 x 10³ Kg m³
Crystal structure : Th₃P₄ cubic crystal
Grain size : 50 - 100 µm (?)

Optical

Transmits 3 - 5, 8 - 12 µm wavelengths

Sample Used

Source : GEC, Caswell
Dimensions : 50 mm diameter disc, 3 mm thick

5.8.2 Material Description

Calcium lanthanum sulphide is a rare earth ternary sulphide with the formula CaLa₂S₄. Its structure is described as that of thorium phosphide, that is two cations both 8-fold coordinated, of similar size and occupying similar crystallographic sites. (Savage, 1985). The material was produced by mixing nitrate solutions in the appropriate proportions, in order to yield the stoichiometric oxide mixture after evaporation and firing in air. This oxide was then immediately converted into ternary sulphide by firing in H₂S / N₂. This sulphide was then compacted by uniaxially pressing at 75 MPa with an organic binder that was subsequently removed by heating. The discs were finally sintered by heating in H₂S at 1,200 °C until they reach 95 % of their theoretical density, and then hot isostatically pressed to remove the residual porosity (Roy, 1981a, b, Beswick et al., 1983, Savage and Lewis, 1986, Brierley et al., 1990).

Calcium lanthanum sulphide initially promised improved performance in both the long wavelength infrared transmittance, and also in its rain erosion resistance. However as will be shown in section 5.8.4 the rain erosion resistance is not as good as was initially hoped.

5.8.3 Published Rain Erosion Work

Brierley et al. (1990) conducted a preliminary study of the rain erosion resistance of calcium lanthanum sulphide using two different powder mixtures known as 3 CaS:97 La₂S₃ and 45 CaS:55 La₂S₃. In this study Brierley et al. carried out an evaluation of the threshold velocity for damage using a 0.8 mm nozzle on a SIJA. The results obtained showed a threshold velocity of 180 m s⁻¹ for the first mixture and 190

m s^{-1} for the second. The method of damage assessment used was a visual inspection after 5 impacts (0.8 mm jet DTV (5 impacts)), however it is known from work on MIJA that 5 impacts is not sufficient to determine the absolute threshold velocity for damage for a brittle material with visual inspection alone. Threshold velocity results obtained in this way should therefore be used with caution.

A separate study was carried out by Saunders et al. (1986) using the Wright-Patterson whirling arm rig. In this experiment 22 mm diameter, 2.5 mm thick, acoustically backed, polished discs of CaLa_2S_4 were compared with ZnS by exposing them to 5 minutes of 2 mm water droplet impacts at velocities ranging from 100 - 200 m s^{-1} . The damage was assessed by counting the number of impact sites on which damage could be seen. The results are shown in figure 5.8.1 and indicate that CaLa_2S_4 outperforms ZnS for damage by single impacts. Further work using residual strength tests to find the damage threshold were planned by Saunders, but it appears that this work was never carried out.

5.8.4 MIJA Results

The rain erosion work carried out at the Cavendish during this study can be divided into two main areas. Firstly, samples from each of the three batches were impacted on MIJA to see if there were any obvious differences in the threshold velocity curves produced. Secondly, samples were subjected to higher velocity impacts on SIJA to look at the effect of impact damage above the threshold velocity on samples from different powder mixes.

5.8.4.a Batch 1 - Sample VX239

As the discs used in this study were 50 mm in diameter, there was sufficient space on one disc to perform two threshold velocity curves. The results from these two separate experiments are shown in figures 5.8.2 and 5.8.3. The threshold velocities obtained were 0.8 mm jet DTV (300 impacts) = $105 \pm 5 \text{ m s}^{-1}$ and $115 \pm 5 \text{ m s}^{-1}$, giving an average threshold velocity for batch 1 of $\sim 110 \text{ m s}^{-1}$.

5.8.4.b Batch 2 - Samples VX262 and VX263

As with batch 1 two threshold velocity curves were obtained for batch 2 (figure 5.8.4 and 5.8.5). However this time they were obtained from two different discs from the same batch rather than from one disc. The results showed good agreement both with each other, and also with the earlier results of batch 1. Sample VX262 appeared to have a 0.8 mm jet DTV (300 impacts) $\sim 110 \text{ m s}^{-1}$, and VX263 of $\sim 115 \text{ m s}^{-1}$ giving an average value of $\sim 112.5 \text{ m s}^{-1}$ for a 0.8 mm nozzle. (This compares with a DTV of $\sim 110 \text{ m s}^{-1}$ for batch 1.)

5.8.4.c Batch 3 - Sample VX273

Only one disc was tested from batch 3 and the result from this disc is shown in figure 5.8.6. The threshold velocity appears to be slightly higher than the other two batches with the 0.8 mm jet DTV (300 impacts) = $135 \pm 5 \text{ m s}^{-1}$. Unfortunately due to lack of space the threshold curve evaluation couldn't be repeated so this small difference hasn't been confirmed.

5.8.4.d Damage patterns

There was no significant difference between the damage patterns produced on batches 1, 2 and 3 over the velocity range tested. Photographs of the type of damage produced at a range of different velocities can be seen in plates 9.8.1 - 9.8.3.

Photo 1 on plate 9.8.1 shows the damage caused by the highest velocity impact used during the threshold evaluation on batch 2, and was taken with both transmitted

and reflected light on a standard bench microscope. The corresponding SEM photo can be seen in photo 2 and this serves as an important reminder that the SEM photo only shows the surface cracking and often there is considerable sub-surface damage which can only be visualised using transmitted light. Photo 3 shows an enlargement taken on the SEM of the bottom right corner of the ring of damage. Finally the last two photos in this plate are enlargements of two areas of cracking labelled 'A' and 'B' in photo 3, and these suggest that the cracking may take place around grains. No etching has yet been carried out to confirm this however.

Photos 1 and 2 on plate 9.8.2 shows the damage produced by a slightly slower impacting jet at 375 m s^{-1} . The depth of cracking, number of cracks, diameter over which cracking takes place, and the amount of chipping on the outside of cracks have all been dramatically reduced compared to plate 9.8.1.

There is a similar reduction in the extent of damage as the impact velocity drops to 290 m s^{-1} in photos 4 and 5. It is also worth noting that some central damage can just be made out in both photos 1 and 4 on this plate, but cannot be seen in the equivalent SEM photos 2 and 5 because it appears to be predominately a subsurface effect.

The final plate of photos continues the sequence with the velocity dropping to 240, 180 and finally 140 m s^{-1} while the number of impacts required to produce visible damage gradually increases from 1 to 100. With each successive drop in velocity there are fewer cracks apparent in the final damage pattern, however the addition of subsequent impacts before the damage is finally noticed and the experiment terminated drives the cracks that have opened deeper into the substrate. Once again it is important to notice the difference between the damage patterns observed on the SEM and those observed using transmitted and reflected light.

5.8.5 Conclusion

The threshold velocity curves are summarised in figure 5.8.7 and the average curve is compared with those for other IR materials in figure 5.8.8. The 0.8 mm jet DTV (300 impacts) results were as follows:

batch 1: 105, 115 m s^{-1}	->	$110 \pm 5 \text{ m s}^{-1}$	2 samples used
batch 2: 110, 115 m s^{-1}	->	$112.5 \pm 2.5 \text{ m s}^{-1}$	2 samples used
batch 3:		135 m s^{-1}	1 sample used

The results from batches 1 and 2 are essentially identical and it is therefore only batch 3 that appears to be slightly different. This may indicate a true difference between the batches, or it may just be a chance result due to the statistical distribution of microflaws in the specimens. Only a second threshold evaluation of a batch 3 material could clarify the situation, unfortunately there are not enough samples to carry this out.

The results obtained in these MIJA threshold evaluations are consistent with those obtained by Brierley et al. (1990). Using SIJA Brierley found the 0.8 mm jet DTV (5 impacts) = $180 - 190 \text{ m s}^{-1}$, whereas for MIJA the result is 0.8 mm jet DTV (5 impacts) = $175 \pm 5 \text{ m s}^{-1}$. The difference between these values and that of 0.8 mm jet DTV (300 impacts) ~ 110 m s^{-1} underlines the care that needs to be taken in comparing the impact resistance of different materials in ensuring comparable numbers of impacts are used.

With regards to the results produced by Saunders (1986) on the Wright-Patterson whirling arm rig. Even though these experiments were performed on specimens from a different source to the current ones, the results showed that the performance of

CaLa_2S_4 after just one impact was better than that of ZnS which agrees with the MIJA result, but misses the important point shown up by the full threshold curve from MIJA, that the final threshold velocity values of the two materials are in fact very similar.

One further interesting observation which is worth noting at this stage is that the central damage also appears to have a threshold velocity which is 165 m s^{-1} for batch 1, 195 m s^{-1} for batch 2, and 155 m s^{-1} for batch 3. Above these velocities central damage appears by the time circumferential cracking occurs, and below these velocities central damage never occurs even after prolonged exposure. The exact mechanism for this central damage is still not clear although similar effects have also been seen on several other materials. In some instances it appears that surface porosity is a contributory factor in the initiation of central pitting (e.g. spinel), in others it appears that the important effect may be the interaction of the release waves in the solid on the central axis following the impact.

Finally, some of the specimens were found to have blotches on the surface immediately after testing and needed careful cleaning before the SEM photos in plate 9.8 could be obtained. It is interesting to note that some flight trials carried out on a Mirage in Australia witnessed chemical corrosion of the samples before any fracture occurred, and it is conceivable that these observations may be connected.

The major disadvantage with this material for use in windows and domes is it has very poor thermal shock resistance (Savage and Edwards, 1988). This was illustrated during cleaning, where the cooling action of using a can of compressed air to blow dirt off the surface was sufficient to cause a ring crack to appear in the sample. On the Hasselman (1970) order of merit for thermal shock resistance Ge scores 8.0, ZnS 2.1 and CaLa_2S_4 only 0.07 !

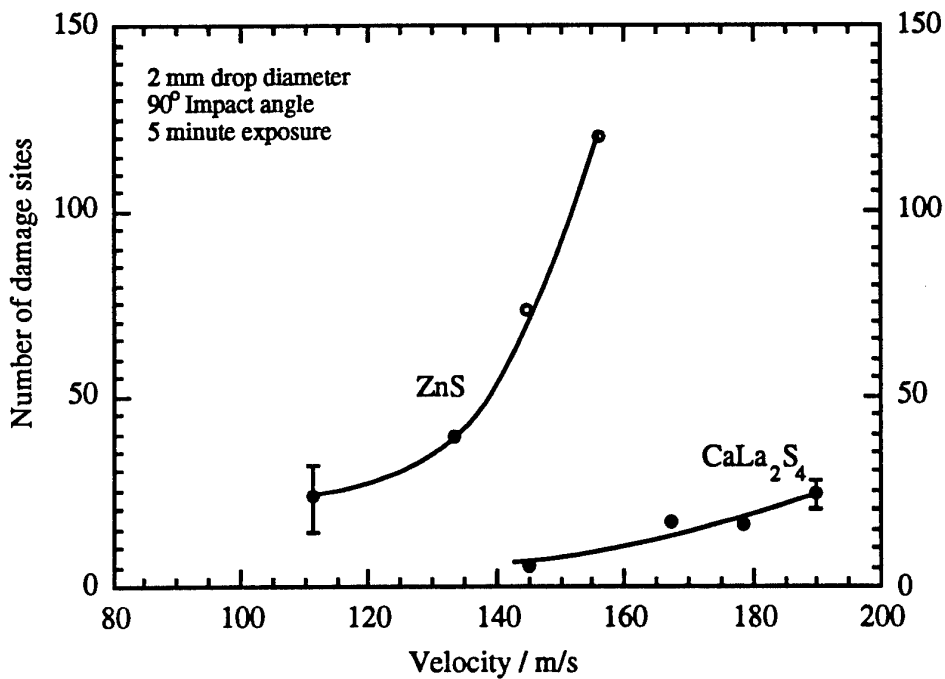


Figure 5.8.1 Number of observed damage sites as a function of impact velocity. Higher velocities are required to induce equivalent damage in CaLa₂S₄ when compared with ZnS. (Saunders *et al.*, 1986)

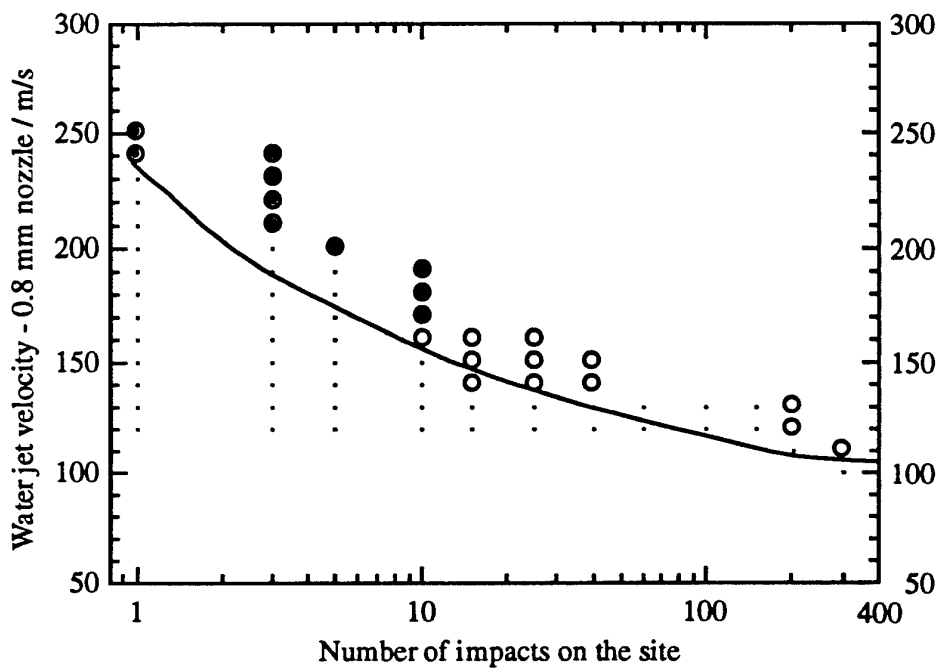


Figure 5.8.2 First threshold velocity curve for specimen VX239 from batch 1 (made from the 68743 powder).

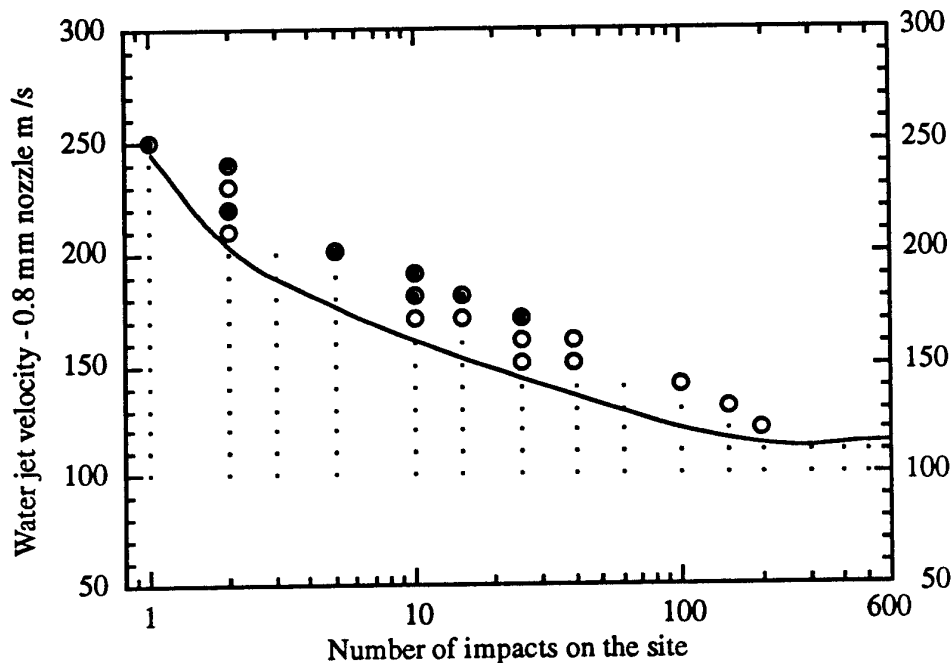


Figure 5.8.3 Second threshold velocity curve for specimen VX239 from batch 1 made from the 68743 powder.

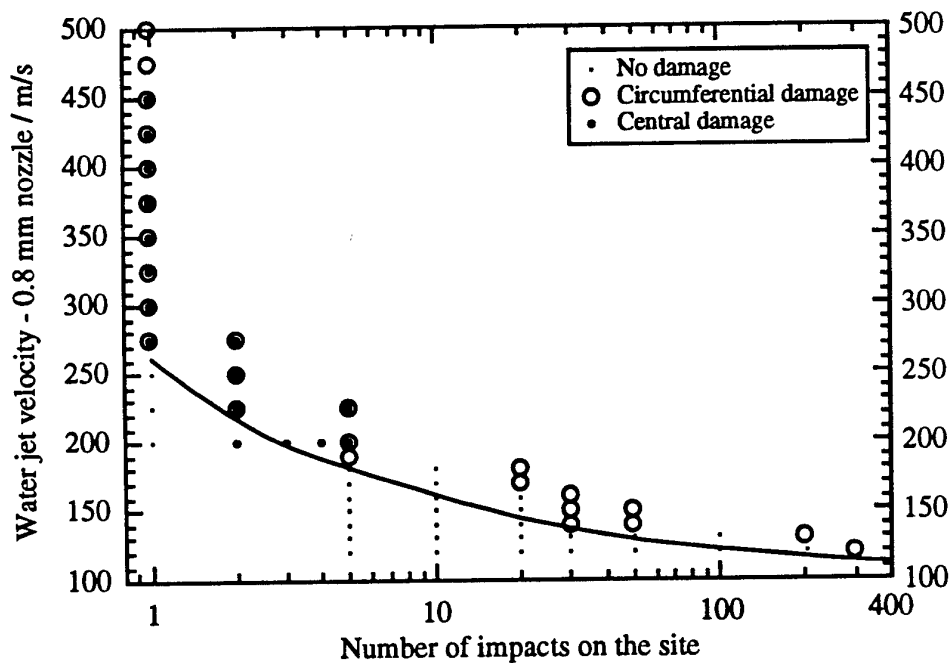


Figure 5.8.4 Threshold curve for calcium lanthanum sulphide, sample VX 262. This was a sample from batch 2 (75% of 68743 powder with 25% of 68799 powder).

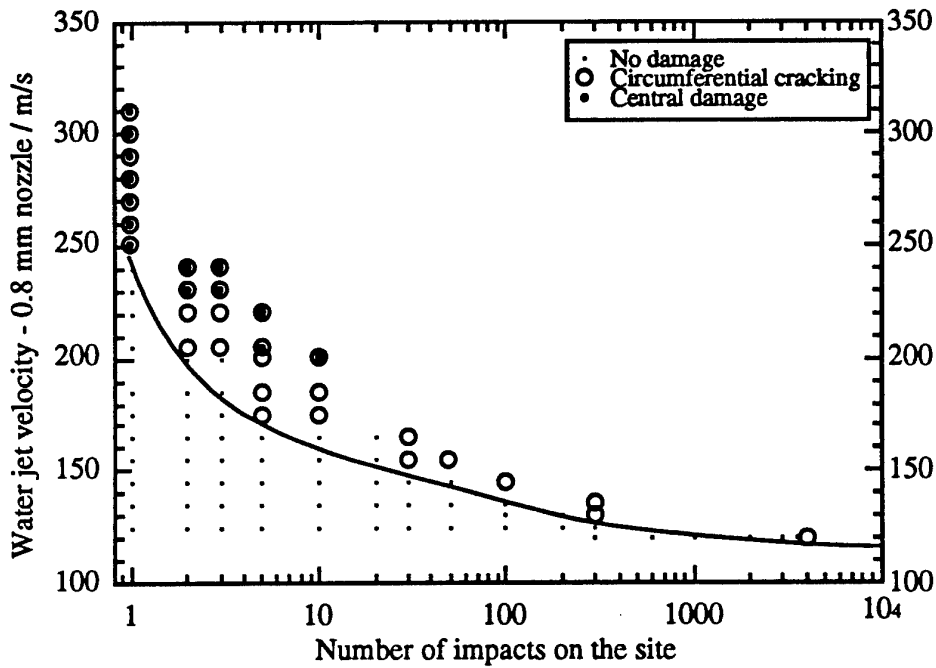


Figure 5.8.5 Threshold curve for calcium lanthanum sulphide, sample VX263. This was a sample from batch 2 (75% of 68743 powder with 25% of 68799 powder).

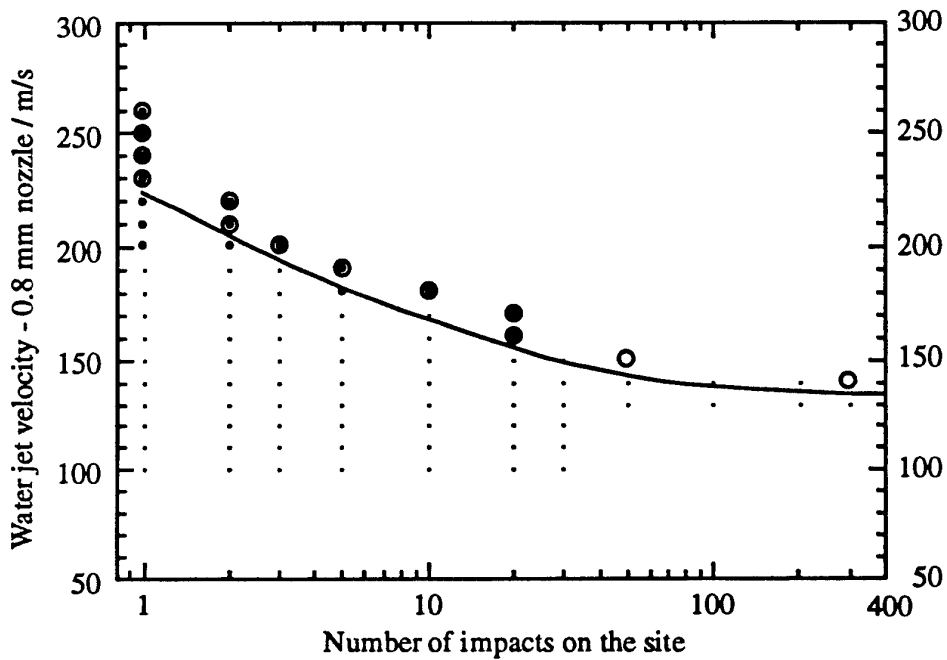


Figure 5.8.6 Threshold velocity curve for specimen VX273 from batch 3 made from the 68799 powder.

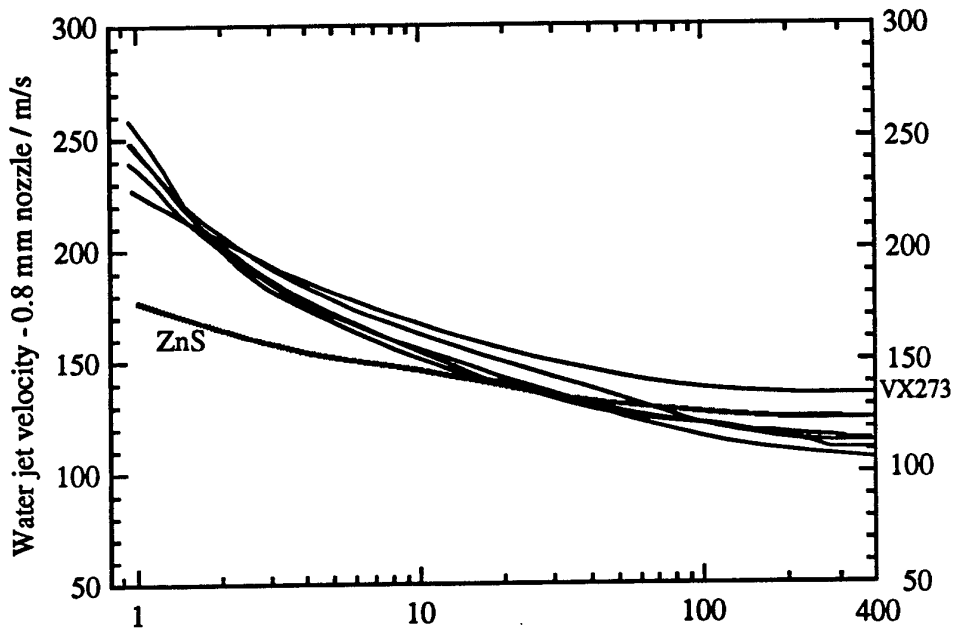


Figure 5.8.7 Summary of the results for the three different batches of calcium lanthanum sulphide tested compared to zinc sulphide. Batch 1: VX239; Batch 2: VX262, VX263; Batch 3: VX273

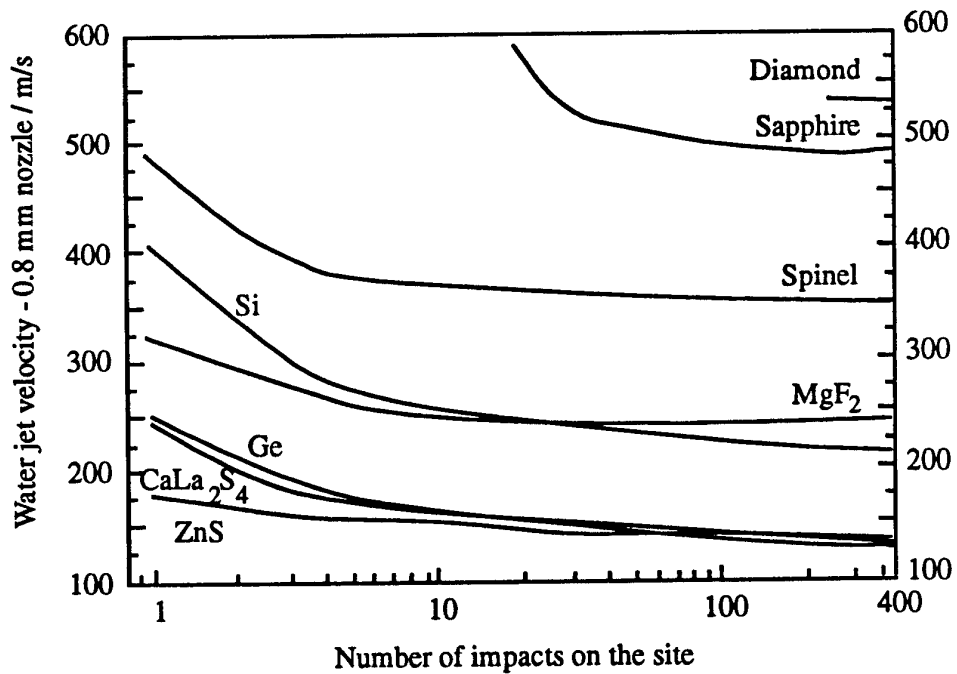


Figure 5.8.8 Summary of the threshold velocity curves for a number of different infrared transmitting substrates, showing how their curves compare to that obtained for CaLa₂S₄.

5.9 CVD DIAMOND

5.9.1 Material Characteristics

Many of the quoted mechanical and thermal properties are still improving as the CVD quality improves.

Mechanical

Vickers hardness :
Fracture stress : 700 - 1,500 MPa
Fracture toughness : 6 - 7 M Pa m^{1/2}
Youngs modulus : 800 - 1,140 GPa
Poissons ratio : 0.07 - 0.10
Rain erosion resistance (see section 4.4):
0.8 mm jet DTV (300 impacts):
best so far 475 ± 25 m s⁻¹

Thermal

Melting point :
Thermal conductivity : 1300-1600 parallel
to plane , 2170 W m⁻¹ K⁻¹ through plane
Thermal expansion : 0.8 x 10⁻⁶ K⁻¹
Heat capacity : 0.54 J g K⁻¹

Optical

Transmits 3 - 5, 8 - 12 μm wavelengths

Physical

Density : 3.5 x 10³ Kg m³
Grain size : Various

Sample Used

Source : Various
Dimensions : Various

5.9.2 Material Description

Several deposition techniques are being used to deposit diamond by CVD. High quality diamond has been made by hot filament CVD (Matsumoto et al., 1982), microwave plasma CVD (Kamo et al., 1983), DC plasma torch (Suzuki et al., 1987), radio frequency plasma torch (Matsumoto, 1985, Matsumoto et al., 1987), microwave plasma torch (Harker and DeNatale, 1991), and oxyacetylene torch (Hirose and Kondo, 1988). The CVD diamond is mainly polycrystalline and still has problems that limit its optical transmission, such as scattering due to roughness, absorption due to defects, non-diamond phases, and impurities, however research is continually improving its optical qualities, and methods for producing single crystal diamond over large areas have recently been reported by Glesener et al. (1991), and Geis et al. (1991).

5.9.3 Published Rain Erosion Work

Only Seward et al. (1992a & b, 1993a & b) and Field et al. (1993) have reported rain erosion work on CVD diamond.

5.9.4 MIJA Results

A variety of different CVD diamond specimens have been tested on MIJA, from a number of different sources around the world. The results described here illustrate the considerable progress that has been made over the last few years in improving the strength and thickness of CVD diamond possible. The exact sources of each specimen have not been disclosed in this account since the processes are always improving and results could therefore not yet be deemed to be typical of one particular source.

5.9.4.a CVD Diamond on Silicon

Sources 1 and 2 (May 1990)

The first CVD diamond coatings on silicon were tested back in May 1990. Before testing these coated samples the threshold curve for the uncoated silicon substrate was evaluated as shown in figure 5.4.2. The testing of each coated disc then commenced by impacting each disc on one site as described in section 4.3.4, with increments of 50 m s^{-1} in velocity between each set of 300 impacts. Although the discs should have been large enough for this procedure to be repeated and information gathered from a number of different sites in order to check the reproducibility of the results, in actual fact all of the experiments either resulted in the silicon substrate shattering, or large areas of the diamond coating peeling off. The final results are shown below:

Source 1

Sample	Velocity / m s^{-1} and number of shots survived						
	150	200	250	300	350	400	450
2.5 μm polished CVD on Silicon	300	300	90	Silicon shattered			
5 μm polished CVD on Silicon	300	300	190	Silicon shattered			

Source 2

Sample	Velocity / m s^{-1} and number of shots survived						
	150	200	250	300	350	400	450
4.5 μm polished CVD on Silicon	300	300	300		Diamond peeled off		
9 μm polished CVD on Silicon	300	300	300	10	Diamond peeled off		
15 μm polished CVD on Silicon	300	300	300	50	Silicon shattered		

Comparing these results with the threshold curve for the silicon substrate in figure 5.4.2, it is clear that the diamond available at this time offered little improvement over the erosion resistance of the substrate, and was therefore of a poor quality.

Source 3 (Feb 1992) and source 4 (August 1992)

In 1992 another two sources supplied some CVD diamond coatings on silicon for evaluation. The sample from the first source was a 5 μm thick unpolished coating, and this was tested in the same way as the specimens from sources 1 and 2 described above. In this case however 2 discrete impact sites were tested on the same disc before the silicon shattered.

Source 3

Sample	Velocity / m s^{-1} and number of shots survived						
	150	200	250	300	350	400	450
5 μm unpolished CVD on Silicon	300	300	300	50		Silicon shattered	
	300	300	300	300	12	shattered	

The second sample tested in 1992 was a 40 μm thick polished coating on silicon. Again the sample was tested by incrementing the velocity impacted on one site, and in this case the experiment was terminated after 200 impacts at 250 m s^{-1} by the coating cracking and debonding.

Source 4

Sample	Velocity / m s^{-1} and number of shots survived						
	150	200	250	300	350	400	450
40 μm polished CVD on Silicon	300	300	200	Cracked and debonded			

Source 5 (Feb 1993)

The next three samples of CVD diamond on silicon arrived at the beginning of 1993, together with two slightly different silicon substrates of the same size (~ 10 mm square). The first of the CVD diamond coatings to be tested was unpolished, and the other two were polished but of different thicknesses. Once again the same testing technique was used so that results could be compared easily with the earlier work described above. The results obtained in this way were as follows:

Source 5

Sample	Velocity / m s ⁻¹ and number of shots survived						
	150	200	250	300	350	400	450
Si-2 untreated	300	300	20				
Si-1 treated	300	300	40				
250 µm unpolished CVD on Si	100						
290 µm polished CVD on Si	300	300	300	300	300	300	10
400 µm polished CVD on Si	300	300	300	300	100		

Several points emerged from this last series of specimens:

1. There was little difference between the untreated and treated silicon substrates and in fact both correlated well with the earlier full threshold evaluation for a silicon disc (figure 5.4.2).
2. The unpolished CVD diamond sample had an extremely low threshold velocity compared to the two polished samples, and was probably badly flawed. The supplier reported that a large number of these CVD samples broke during the polishing process and it is therefore possible that the polishing process itself is acting as a sort of proof testing during the CVD diamond manufacture. Photographs of the unpolished specimen and the cracking in the diamond coating obtained in this experiment can be seen in plate 9.9.1. Photo 6 on this plate clearly shows that the cracking takes place by both transgranular and intergranular fracture, and that the bonding between grains is therefore pretty good.
3. The two polished CVD diamond coatings from source 5 produced quite different results. The thinnest coating (290 µm) had the highest threshold velocity 400 - 450 m s⁻¹, with the impacts resulting in the circumferential cracking seen in photos 1 - 4 on plate 9.9.2. The final crack pattern shown in photo 1 was influenced by the proximity of the impact site to the edge of the sample, however the initiation appeared to have been independent of this and the threshold value for this sample is therefore considered to be reasonably accurate. In contrast to this result the 400 µm thick coating shattered and debonded after just 100 impacts at 350 m s⁻¹. In this case the cracking initiated at a corner after just 10 impacts at 250 m s⁻¹ and this was probably due to defects in the coating.

Summary

The results shown above from the five different sources prove that the strength of CVD diamond coatings on silicon has improved over the last three years, but that there are still problems with maintaining its quality. The results also show that despite these improvements CVD diamond on silicon at its best (0.8 mm jet DTV (300 impacts) = 425 ± 25 m s⁻¹) has still not achieved as high a threshold velocity for damage as natural diamond (section 5.6, 0.8 mm jet DTV ~ 530 m s⁻¹), and further work therefore remains to be done.

5.9.4.b Free standing CVD Diamond

Source 6 (Jan 1992)

The first free-standing CVD diamond specimen was tested in January 1992. This specimen was 15 mm in diameter and 500 μm thick, however it was opaque because of the formation of silicon carbide, and the surface had flaws in it as a result of the polishing process. The testing on the disc commenced at 200 m s^{-1} , however after just 6 impacts the disc shattered into pieces. Even taking into account the fact that it was a thin specimen and therefore that stress wave reflections were a problem, a 0.8 mm jet DTV (6 impacts) $< 200 \text{ m s}^{-1}$ is nowhere near that of natural diamond, and the disc was therefore clearly not of a high quality.

Soon after this test the same manufacturer grew some transparent CVD diamond discs. In these they found that the interior was full of defects and that alterations in the deposition technique were necessary to eliminate them. It is very likely that the opaque sample tested was also riddled with interior defects, and this together with the surface flaws explains the poor result.

Source 7 (Feb 1993)

The next two free standing CVD diamond specimens were tested at the beginning of 1993. The first of these was a disc 10 mm in diameter and 350 μm thick. This disc survived 300 impacts at 150 m s^{-1} and 200 m s^{-1} before a circumferential crack was produced after just 90 impacts at 250 m s^{-1} (0.8 mm jet DTV (300 impacts) = $225 \pm 25 \text{ m s}^{-1}$). The cracking in this case appeared to be largely intergranular with several small chips removed from the outside of the cracks.

The second sample was a 9 mm square, 425 μm thick, and when supplied the sample had two broken corners with a crack extending into the centre from one of them. Despite this crack the sample survived 300 impacts at 150, 200, 250, 300, 350 and 400 m s^{-1} , before a complete ring crack was produced following 180 impacts at 450 m s^{-1} (0.8 mm jet DTV (300 impacts) = $425 \pm 25 \text{ m s}^{-1}$). This ring crack can be seen in photo 5 plate 9.9.2 together with the crack that was there before testing started at 2 o'clock. No grain structure could be seen on the impacted side of the sample, and the cracks produced were extremely fine as shown in photo 6 plate 9.9.2.

The results from these two specimens are given below:

Source 7

Sample	Velocity / m s^{-1} and number of shots survived						
	150	200	250	300	350	400	450
350 μm free standing CVD	300	300	90				
425 μm free standing CVD	300	300	300	300	300	300	180

Source 8, 9 and 10 (May 1993)

Three further CVD diamond specimens were tested in the middle of 1993. These were all 20 mm in diameter, and all about 1 mm thick. Testing on each disc commenced in the manner described in section 4.3.4 for the threshold evaluation of a small disc. The first impact site on each disc was positioned in the middle of one quadrant of the disc so that four impact sites could be evaluated on each. This cautious approach was taken because it was not known whether the discs would shatter after damage initiated on them, or over what area damage would appear on a single impact site. Based on the experience on sapphire described in section 5.1 where experiments were also carried out at a high impact velocity, this separation between sites would hopefully be adequate to avoid significant interactions.

Before testing, each diamond disc was stuck down onto a sapphire substrate using a fast cure epoxy resin. These sapphire discs were then held down onto a rectangular

glass specimen table using a wax that could if necessary be removed with acetone. This method of mounting was not designed to provide an acoustic match with the CVD diamond, but more to ensure that the diamond didn't move during testing, and that all three discs were tested under identical backing and other test conditions so that results were comparable. Two further advantages of this method of mounting are that because sapphire is transparent it doesn't hinder optical examination of the CVD diamond by transmitted light, and secondly the sapphire has a high enough threshold velocity itself that it doesn't crack due to the effects of the transmitted stress pulse in the velocity range of interest.

Source 8

The results for the four impact sites tested on this first specimen are as follows:

Velocity / m s ⁻¹	Number of impacts on each site and the result (if any)			
	site 1	site 2	site 3	site 4
150	300	300	300	300
200	300	300	300	300
250	300	300	300	300
	Central crazing	Central crazing after 3 impacts	Central crazing after 33 impacts	Central crazing after 10 impacts
300	300	300	300	300
350	50	300	300	300
400	50	300	300	300
450	50	300	300	300
500	Ring damage after	Ring damage after	Ring damage after 15 impacts	Ring damage after 10 impacts

Site 1: (0.8 mm jet DTV (300 impacts) = 475 ± 25 m s⁻¹)

Damage was first seen after 300 impacts at 250 m s⁻¹. This damage may have formed earlier during the 300 m s⁻¹ sequence, however because it initiated 200 μm below the surface and was surrounded by black inclusions, it was not noticed immediately. By the time a further 300 impacts at 300 m s⁻¹ had been fired a small network of central crazing had formed under the impact site. During a second series of experiments on this site the damage was extended by another 50 impacts at 350, 400 and 450 m s⁻¹ and a video camera was set up to take a time lapse sequence of the circumferential ring forming around the damage site when impacted at 500 m s⁻¹.

It should be noted that the diameter of the circumferential crack formed was ~4.5 mm although a very faint sign of surface cracking can also be detected with a diameter of ~2 mm. This diameter is far greater than that for ZnS ~1 mm and this may be due to the effects of stress wave reflection off the back surface of the sample reinforcing the Rayleigh surface wave (see analysis in (Bowden and Field 1964)).

Site 2: (0.8 mm jet DTV (300 impacts) = 475 ± 25 m s⁻¹)

Damage on site 2 was first recorded after 3 impacts at 250 m s⁻¹. As with site 1 the damage initiated through crazing 200 μm below the surface. Subsequent increases in velocity then extended this crazing further until a complete ring crack was finally formed at 500 m s⁻¹. As with site 1, the formation of the ring crack has been captured on video using time lapse photography.

Site 3: (0.8 mm jet DTV (300 impacts) = 475 ± 25 m s⁻¹)

Damage on site 3 initiated in a similar manner to on sites 1 and 2 with central crazing in the bulk of the specimen after 33 impacts at 250 m s⁻¹. This crazing grew in size as the velocity was increased until a further 300 impacts had been completed at

300, 350, 400 and 450 m s⁻¹. Then after just 15 impacts at 500 m s⁻¹ the first signs of a circumferential crack were detected.

Site 4: (0.8 mm jet DTV (300 impacts) = 475 ± 25 m s⁻¹)

Central crazing on site 4 started after 10 impacts at 250 m s⁻¹. The extent of this crazing gradually increased as a further 300 impacts were applied to the site at 300, 350, 400 and 450 m s⁻¹ and then circumferential cracking started after 10 impacts at 500 m s⁻¹. This circumferential cracking extended around the circumference of the impact site over the following 10 impacts until the complete ring seen in plate 9.9.3 was formed.

The light patches on the photos are due to bubbles in the wax used to hold the sapphire disc down onto the glass, and are not features of the CVD diamond itself.

Source 9

The undamaged disc from this source had an unusual internal structure. Small grains 50 - 150 μm in size, could be seen ~ 75 μm below the surface, while larger grains 200 - 300 μm in size, could be seen at a depth of 280 μm below the surface. Nothing could be focused on between these depths. Examples of these features can be seen in plate 9.9.5. As with the previous specimen the light patches on the photos are due to bubbles in the wax used to hold the sapphire disc down onto the glass, and are not features of the CVD diamond itself.

Only two sites were impacted on this sample. The results for these are as follows:

Velocity / m s ⁻¹	Number of impacts on each site and the result (if any)			
	site 1	site 2	site 3	site 4
150	300	300	300	
200	300	300	300	
250	300	300	300	
300	300	300	300	
	Central crazing	Central crazing after 3 impacts	Central crazing	
350	300	300	300	
400	300	300	300	
450	Ring damage after 10 impacts	Ring damage after 4 impacts	Ring damage after 50 impacts	
500				

Site 1: (0.8 mm jet DTV (300 impacts) = 425 ± 25 m s⁻¹)

This impact site was initially tested before site 1 on the sample from source 8. Consequently this was the first diamond specimen in which central crazing had been observed, and because of the large grain structure at ~ 200 μm depth in the material, the exact point where damage initiated is not clear. However central crazing was apparent by the end of the 300 impacts at 300 m s⁻¹ and this was extended by the subsequent 300 impacts at 350 and 400 m s⁻¹. Finally at 450 m s⁻¹ a circumferential crack started to open and this formed a complete ring after 10 impacts as shown in plate 9.9.4.

Plate 9.9.5 shows small sections of this circumferential crack in more detail. The photos clearly illustrate the change in the observable grain size with depth through the substrate. From these photos it is possible to conclude that the ring crack produces both inter-granular and trans-granular cracking through the small grains at 75 μm depth, but doesn't penetrate deep enough to have any effect on the larger grain structure at 280 μm depth.

Site 2: (0.8 mm jet DTV (300 impacts) = $425 \pm 25 \text{ m s}^{-1}$)

Central crazing on this site was seen after just 3 impacts at 300 m s^{-1} and extended considerably with the following 300 impacts at 300, 350 and 400 m s^{-1} . As on site 1 the circumferential crack started to form due to impacts at 450 m s^{-1} and after 15 impacts a series of ring sections extended right around the damage site.

Site 3: (0.8 mm jet DTV (300 impacts) = $425 \pm 25 \text{ m s}^{-1}$)

Central crazing was observed in the bulk after the impacts at 300 m s^{-1} , however because of the internal structure it was difficult to say exactly when. As with sites 1 and 2 circumferential cracking started on the surface after 50 impacts at 450 m s^{-1} , and after a further 30 impacts there was a complete ring crack.

Source 10

Because this sample was dark and opaque, damage could not be seen in the bulk of the substrate and it is therefore not known whether central damage was a problem or not. That said under very strong transmitted light some subsurface features could be discerned and it was apparent that these were growing at velocities below that required to generate ring damage.

A summary of the results for the three impact sites tested on this specimen are presented below.

Velocity / m s^{-1}	Number of impacts on each site and the result (if any)			
	site 1	site 2	site 3	site 4
150	300	300	300	Not possible to use because of damage from sites 1, 2 and 3
200	300	300	300	
250	300	300	300	
300	300	300	300	
350	300	300	300	
400	300	300	300	
450	300	300	300	
500	Central crazing? Site abandoned	Ring damage after 10 impacts	Central crazing? Ring damage after 200 impacts	

Site 1:

No clear conclusions could be drawn from this first site.

Site 2: (0.8 mm jet DTV (300 impacts) = $475 \pm 25 \text{ m s}^{-1}$)

The second impact site survived 300 impacts at velocities from $150 - 450 \text{ m s}^{-1}$ then after 10 impacts at 500 m s^{-1} a ring crack started to form. This ring crack however intersected with the edge of the disc, and resulted in a chip being taken off the side of the specimen, and an incomplete ring therefore being formed.

Site 3: (0.8 mm jet DTV (300 impacts) = $475 \pm 25 \text{ m s}^{-1}$)

This impact site was observed with extremely strong transmitted light throughout the course of the experiment in order to try and detect any subsurface damage that may occur. It is possible that some subsurface central damage was seen at velocities below that required for circumferential cracking, however because of the difficulty in observing such cracks it can only be really confidently said that the ring crack initiated after 200 impacts at 500 m s^{-1} .

Source 11 (August 1993), Source 12 (January 1994),

Two further CVD samples were tested in 1993 and a further 5 at the beginning of 1994 from two different sources. Unfortunately the results from these experiments have not yet been cleared for release.

Source 13 (January 1994)

One 20 mm diameter specimen 0.5 mm thick was supplied for testing from a batch of high strength CVD material. Grain boundaries could be seen both on the surface with a microscope and also in the bulk of the substrate. The results from this disc are shown below:

Velocity / m s ⁻¹	Number of impacts on each site and the result (if any)				
	site 1	site 2	site 3	site 4	site 5
150	300	300	300	300	
200	Central crazing after 20 impacts	Central crazing after 10 impacts	300	Central crazing after 10 impacts	
250	300	300	Central crazing after 10 impacts	300	
300	300	300	300	300	Central crazing after 1 impact
350	300	Ring damage after 10 impacts	300		Ring damage after 80 impacts
400	Ring damage after 10 impacts		Ring damage after 10 impacts	Ring damage after 1 impact	
450					
500					

Site 1: (0.8 mm jet DTV (300 impacts) = 375 ± 25 m s⁻¹)

Central crazing was seen in the bulk of the sample after just 20 impacts at 200 m s⁻¹. The crazing appeared to follow the grain boundaries visible in the middle of the sample, however it is not clear whether it initiated at these boundaries or just propagated along them. As with earlier specimens the extent of the crazing increased with the first few impacts of each velocity used and then stabilised. Circumferential cracking on the surface started after 10 impacts at 400 m s⁻¹. As with the central crazing the cracking seemed to follow grain boundaries i.e. it appeared to be mostly inter-granular.

Site 2: (0.8 mm jet DTV (300 impacts) = 325 ± 25 m s⁻¹)

Once again central crazing initiated after just a few impacts at 200 m s⁻¹. However the ring damage on this site initiated earlier, after 10 impacts at just 350 m s⁻¹. No obvious difference could be seen between sites 1 and 2, and the variation is therefore likely to be due to inconsistent properties across the disc.

Site 3: (0.8 mm jet DTV (300 impacts) = 375 ± 25 m s⁻¹)

Central crazing on this site was not obvious until 10 impacts at 250 m s⁻¹, and circumferential cracking only initiated after 10 impacts at 400 m s⁻¹. Once again a variability in properties across the disc is apparent.

Site 4: (0.8 mm jet DTV (300 impacts) = 350 ± 50 m s⁻¹)

On this site central crazing initiated after 10 impacts at 200 m s⁻¹. Unfortunately a rogue jet velocity of 410 m s⁻¹ started the test sequence at 350 m s⁻¹. Circumferential cracking appeared immediately as a result. Although this gives a more inaccurate threshold value it is still informative because it shows that the initiation of ring damage at 400 m s⁻¹ is not dependent on the impacts with 350 m s⁻¹ previously.

Site 5: (0.8 mm jet DTV (300 impacts) = $325 \pm 25 \text{ m s}^{-1}$)

An additional impact site was attempted on the disc to try and define the threshold velocity for circumferential cracking more accurately. Additional impact velocities between 350 and 400 m s^{-1} were to be tested if the disc survived 350 m s^{-1} , however ring damage actually started on this site after 80 impacts at 350 m s^{-1} , once again illustrating the variability in properties across the disc.

In order to confirm that the 0.5 mm thick disc from source 13 really did have a lower threshold velocity than the 1 mm discs, despite its higher strength, a further impact site was attempted on the 1 mm thick disc from source 9. The results from this are given as site 3 on the source 9 disc, and are extremely consistent with the previous two sites evaluated thus lending support to the argument that this thinner disc both has a lower threshold velocity, and is more variable in its properties across the disc.

5.9.5 Conclusion

The results given above for sources 1 - 13 can be broadly summarised by the following two tables:

CVD Diamond on Silicon:

Year	Thickness / μm	Threshold velocity / m s^{-1}
1990	2.5 - 15	250 - 300
1992	5 - 40	200 - 350
1993	290 - 400	300 - 450

Free Standing CVD Diamond:

Year	Thickness / μm	Threshold velocity / m s^{-1}
1992	500	< 200
1993	500 - 1000	350 - 500*

* Central damage may occur after $200 - 300 \text{ m s}^{-1}$

A number of important points can be seen from this summary:

1. The thickness and strength of CVD diamond has increased significantly over the last three years.
2. There is still a wide variation in the threshold velocity for CVD diamond, showing an inconsistency in the quality of the material both from the same source as well as from different sources.
3. Inclusions in the material are a great problem and significantly weaken the CVD diamond.
4. Central damage is also a big problem and could restrict the operational velocity more than that due to circumferential cracking. This central subsurface crazing often initiates in the bulk of the substrate at a depth of $200 - 300 \mu\text{m}$ and extends along a plane at this depth without penetrating the sample surface. The exact cause of this damage is now under investigation, however without any information on the manner in which the samples were produced it is difficult to draw any conclusions at this stage. It should be mentioned at this point that the production of the central crazing in the CVD diamond may be accelerated under the test conditions used, because all the impacts are located on one site. In a whirling arm test, or under real flight conditions these impacts would of course be randomly positioned, and as the stresses generating the central damage appear to be very localised under the centre

of the impact site it may take longer for this mechanism of damage to generate cracking with randomly positioned impacts. Nevertheless the existence of any secondary damage mechanism is of obvious concern to the strength and performance of CVD diamond material, and further investigation is therefore imperative.

N.B. CVD diamond *has* been tested that doesn't appear to suffer from central damage.

5. None of the samples tested so far have yet achieved the threshold velocity of the natural diamond sample described in section 5.6, although they are getting closer. This result suggests that the fracture toughness values for the best CVD diamond samples tested in this study are close to that of natural diamond. However the central damage in the CVD diamond appears to suggest things may not be quite so simple and deficiencies may still exist in the internal strength of many samples.
6. The effect of sample thickness has not been properly investigated yet, although the drop in threshold velocity from the 1 mm thick specimens of sources 8, 9 and 10 to the 0.5 mm thick specimen of source 13 indicates that it may be an important factor.

5.9.5 Future Research

Clearly it is important that further samples are investigated as the initiation of central crazing in the bulk of the substrate at such low impact velocities is unacceptable. However it would be helpful if possible in future if more information on the grain orientation, method of polishing, etc. could be supplied with the samples so that a more complete scientific study of the damage mechanism can be conducted based on a knowledge of any unusual internal microstructures that may be present in the specimen under study. The current future research plans into CVD diamond are limited by the availability of specimens. However future work already planned includes the evaluation of a second natural type IIa diamond sample which will be used to try and establish a more accurate target strength and benchmark for CVD threshold velocities.

5.10 AMORPHIC DIAMOND COATING ON ZINC SULPHIDE

5.10.1 Material Characteristics

The following values are for the amorphous diamond coating. The data is taken from Collins et al. (1992).

Mechanical

Vickers hardness : 37 GPa
Youngs modulus : 369 GPa
Rain erosion resistance of a 1 μm coating
0.8 mm jet DTV (3, 10, 300 impacts):
205 \pm 5, 195 \pm 5, 175 \pm 5 m s⁻¹

Physical

Density : 3.2 - 3.5 g cm⁻³
Crystal structure : Amorphous
Nodule size : 0.04 μm

Optical

Transmits 3 - 5, 8 - 12 μm wavelengths

Sample Used

Source : University of Texas at Dallas
Dimensions : 25 mm diameter disc, 3 mm thick

5.10.2 Material Description

Four structures of carbon atoms can be formed entirely with sp^3 bonding. Two are crystalline, cubic and hexagonal, the third is amorphous diamond composed of a random network of sp^3 -bonded carbon atoms, and the fourth are fullerenes. Because of the internal stresses produced by distortions of the bond angles in a truly random net, it is unlikely that amorphous diamond could exist as a bulk material (Angus and Hayman, 1988).

At low energy states carbon and hydrogen form aromatic rings. These rings can have more constraints put on the motion of the carbon atoms by cross linking with additional bonds. When the number of bonds is sufficient to quantize all degrees of freedom, the material is said to be a fully constrained net of aromatic rings. These nets however still have dangling bonds and these are taken up with hydrogen. The increasing fraction of hydrogen from 20 - 60 % correlates with increasing ratios of sp^3 to sp^2 bonding of the carbons in the nets and gives greater transparency to the material, but lessened hardness. These materials have become known as diamondlike carbon (DLC).

In the absence of hydrogen another possibility exists. In this structure 74 % of the volume consists of localised nodules or clusters of carbon linked by sp^3 bonds, and the remaining 26 % is filled by a matrix of mixed sp^2 and sp^3 bonding to reduce the stress. This structure is known as amorphous diamond and it offers an ability to form chemical bonds with substrates, together with a high hardness and Youngs modulus, that make it an attractive option as a coating material for infra-red windows.

A description of the deposition process for amorphous diamond can be found in Davanloo et al. (1990), and the bonding to substrates such as ZnS, Ge and Si is described in Davanloo et al. (1992). Most notably with Ge the bonding process generates a layer of GeC, which itself is currently being investigated as a coating for rain erosion protection.

5.10.3 Published Rain Erosion Work

Three experiments on rain impact on these coatings have been mentioned in Collins et al. (1992). The first involved a 1 μm thick amorphous diamond film on a ZnS substrate "subjected to a few minutes of exposure to the high speed impact of water droplets", the results from this experiment showed slight debonding due to the presence of unconverted zinc hydride. The second test involved two quartz discs coated with 3 μm of amorphous diamond and rotated on a whirling arm at 208 m s^{-1} , with a drop size of 1.8 mm. In this test the protection afforded was said to be "clearly apparent". The third test involved ZnS with a 4 μm coating under the same impact conditions. In this test the coating offered "complete protection". No further quantitative details are available.

The work described below on MIJA has also been mentioned in Seward et al. (1992a,b).

5.10.4 MIJA Results

Two different coating thicknesses of amorphous diamond on ZnS were examined, 1 μm and 3 μm , however a threshold curve was only obtained for the 1 μm coating (figure 5.10.1). In these experiments liquid impact may have initiated damage either at the coating or on the surface of the substrate. Because the coating was opaque, damage had to be assessed by looking for cracks in the coating by transmitted and reflected light, and by attempting to look for substrate damage from the rear i.e. through the 3 mm thick FLIR grade zinc sulphide. Observation from the rear is clearly not as effective as direct observation on the substrate, and an experiment performed on ZnS in damage assessment from the rear compared to the front shows it produces $\leq 15\%$ error (figure 5.5.10).

The threshold curve for damage to the 1 μm coated ZnS suggests an improvement in the rain erosion resistance over that of the bare substrate. However it should be noted that the threshold curve is still dropping for the coated system even after 500 impacts so that the final threshold velocity may be below 160 m s^{-1} for a 0.8 mm jet. This system was also impacted once at 290 m s^{-1} and both the substrate and the coating remained intact.

The SEM photos of damage sites after just a few high velocity shots show the familiar short circumferential cracks, and after a large number of shots nearer the threshold the longer ring cracks appear. The majority of the coating loss shown in the SEM photos is a result of the substrate cracking first, and then fingers of coating being stripped off by the lateral outflow of the jet. The crack in the coating that results from this substrate damage appears to follow paths both through and around the nodules. Pinholes of light are also seen when the system is viewed with transmitted light in an optical microscope (plate 9.10.2). These appear to be more numerous inside the ring of damage than on the unimpacted coating, indicating there is also some coating loss without substrate cracking. These pinholes appear even at impact velocities as low as 100 m s^{-1} and whether they have an effect on the damage threshold needs further investigation.

The amount of coating stripping that occurs by subsequent impacts is illustrated by comparing the photos 4, 6 and 8 on plate 9.10.1, and also by looking at the damage after 500 shots at 170 m s^{-1} (photo 1). The damage resulting from the 500 impacts seems to have initiated from the crack at ~ 2 o'clock on the ring (seen in photo 2), and the circumferential ring to have grown round from there. This is suggested by the fact that the amount of coating stripping from the outside of the crack decreases in both directions moving away from this feature.

When compared to the damage on the ZnS substrate it is clear that the circumferential cracks require higher velocities and more impacts to initiate, but that once they have started, the area of substrate effected by the coating removal is greater. This means that transmission loss in the coated material may progress faster once damage has been initiated than it does for just ZnS.

In contrast to the above, the 3 μm coating was still undamaged after 2 impacts at 290 m s^{-1} . However after 4 shots at 200 m s^{-1} large fingers of coating were stripped from the circumferential cracks, and subsequent impacts resulted in the disc fragmenting into several pieces. The cause of this catastrophic failure is not yet known since Collins et al. (1992) claim very low residual stresses in the coating.

5.10.5 Conclusions

This coating offers an attractive possibility to the radome designer particularly since it appears to bond very easily to the more popular IR substrates. The 1 μm coating appeared to offer a considerable improvement on the impact performance of uncoated ZnS (figure 5.10.2). The 3 μm coating seemed to offer even more protection for the first couple of shots, however it subsequently failed catastrophically thus preventing the evaluation of a threshold. The cause of the pinholes is not yet understood and requires further investigation. In addition a more general experimental investigation into coating response to impact is needed to validate some of the theoretical work performed by Hand et al. (1989).

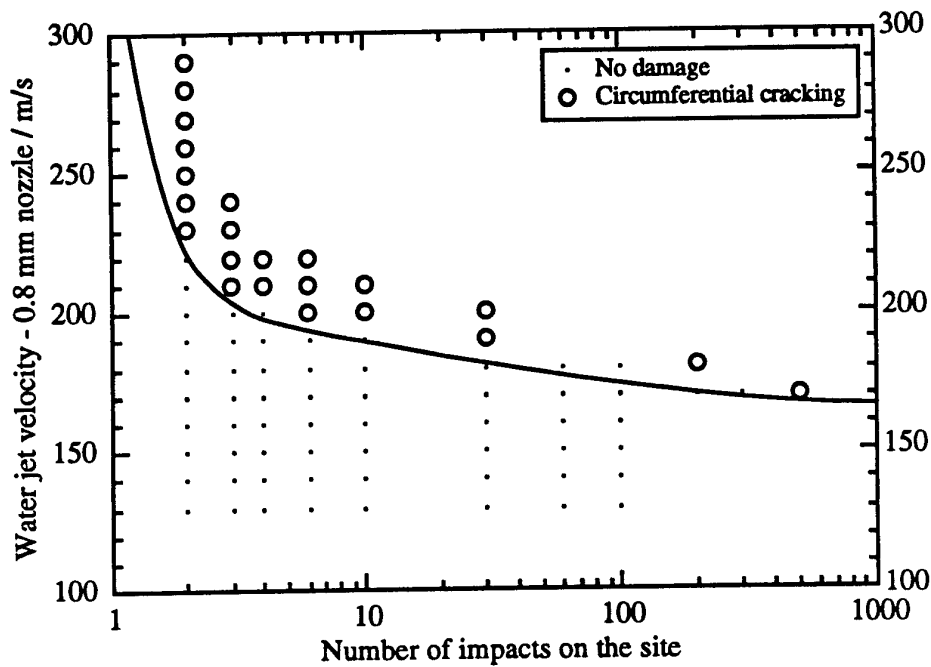


Figure 5.10.1 Threshold curve for a 1 μm thick coating of amorphous diamond on ZnS.

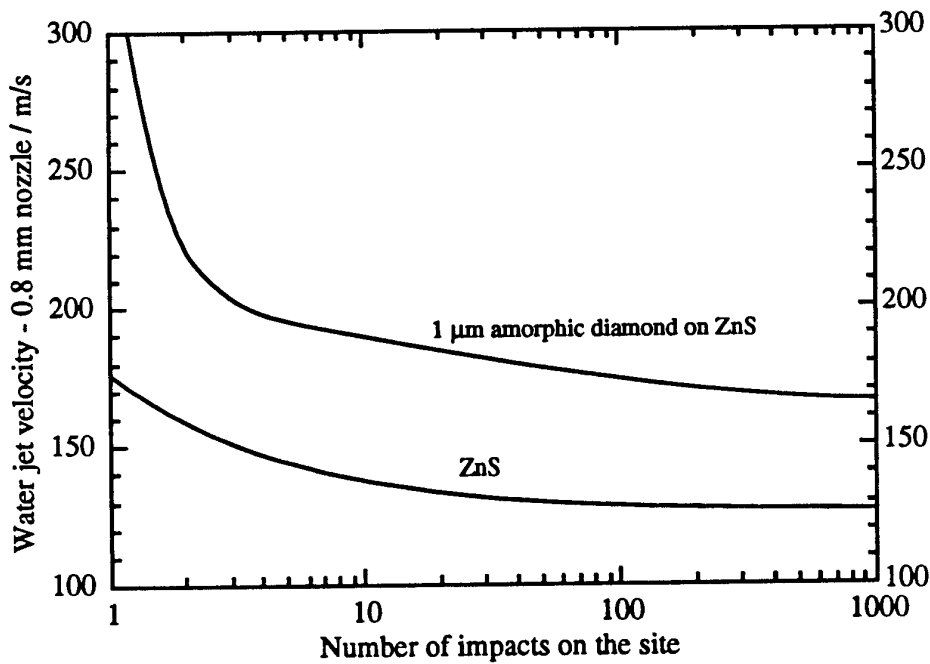


Figure 5.10.2 Threshold curve for a 1 μm thick coating of amorphous diamond on ZnS compared to that for the ZnS substrate.

5.11 PARTICULATE COMPOSITES OF DIAMOND IN ZINC SULPHIDE

5.11.1 Material Characteristics

The following values are for ZnS-10D (0-1 μ m) unless otherwise stated. The data is taken from Farquhar et al. (1990), Schwartz (1990) and Xue et al. (1990).

Mechanical

Vickers hardness : ZnS-10D 2.60 GPa,
ZnS-20D 3.11 GPa,
ZnS-30D 4.11 GPa
Fracture toughness : ZnS-10D 1.20 MPa m^{1/2}
ZnS-20D 1.40 MPa m^{1/2}
ZnS-30D ? MPa m^{1/2}

Youngs modulus : 103.5 GPa

Shear modulus : 39.8 0.6 GPa

Weibull modulus : 4.8

Rain erosion resistance (see section 4.4):

0.8 mm jet DTV (1, 3, 10, 300 impacts)

ZnS-10D (0-1 μ m): 280 \pm 10, 205 \pm 5, 185 \pm 5, 145 \pm 5 m s⁻¹

ZnS-20D (0-1 μ m): 300 \pm 10, 245 \pm 10, 230 \pm 10, 190 \pm 10 m s⁻¹

ZnS-10D (1-3 μ m): 280 \pm 10, 220 \pm 10, 195 \pm 5, 125 \pm 5 m s⁻¹

ZnS-30D (0-1 μ m): 212 \pm 12 m s⁻¹

Physical

Density : 3.99 g cm⁻³

Crystal structure : Composite

Grain size : 1 - 2 μ m

Optical

Transmits 3 - 5, 8 - 12 μ m wavelengths

Sample Used

Source : Department of Materials Science and Engineering, Cornell University.

Dimensions : ZnS-10D and ZnS-20D were 25 mm diameter disc, 3 mm thick

ZnS-30D was 11.5 mm diameter, 0.88 mm thick

5.11.2 Material Description

By embedding diamond particles in hot-pressed zinc sulphide some of the mechanical properties of the zinc sulphide substrate can be improved while preserving its infra-red optical properties. These composite materials are referred to as ZnS-10D or ZnS-20D, where ZnS denotes the zinc sulphide ceramic matrix, D denotes diamond particles, and 10 or 20 refers to the percentage weight of diamond in the composite (Xue et al. 1990, Farquhar et al. 1990). The composites are produced by first mixing to obtain an even distribution of the diamond within the matrix, and then hot-pressing. The best IR transmission is obtained by the diamond particles being uniformly dispersed and less than 1 μ m in size; by reducing the hexagonal phase of ZnS; and by maintaining the grain size of the ZnS below 1.5 μ m. The resulting mechanical properties show an increase in tensile strength and elastic moduli of ~20 %, an increase in the fracture toughness of ~100 % (compared to ZnS with the same grain size), and an identical yield stress (Schwartz, 1990). The intrinsic flaw size in ZnS-10D however, is 2.7 times bigger than ZnS. This means that there is probably an optimum volume fraction of diamond to use since increasing the diamond content might be expected to increase the fracture toughness further, but this might be offset by an increase in the intrinsic flaw size.

5.11.3 Published Rain Erosion Work

Only Seward et al. (1992a, 1993f) have presented rain erosion data for these composites. A more complete account is given in Seward et al. (1992b).

5.11.4 MIJA Results

One 25 mm diameter, 3 mm thick disc was tested for each of the following compositions:-

1. ZnS with 10 % 0 - 1 μm diamond powder
 2. ZnS with 20 % 0 - 1 μm diamond powder
 3. ZnS with 10 % 1 - 3 μm diamond powder
- and a further two 11.5 mm diameter, 0.88 mm discs were tested for the following composition:
4. ZnS with 30 % 0 - 1 μm diamond powder

These last two discs of composition 4 were labelled A and B. Based on the optical transmission data sample A was expected to have superior mechanical properties to sample B (Raj, 1992). Unfortunately due to the smaller disc size a full threshold curve could not be obtained for this last composition and instead only an estimate of the threshold velocity for damage could be made.

The visual damage threshold curves obtained for compositions 1 - 3 can be seen in figures 5.11.1 - 5.11.3, and the three results are summarised compared to plain ZnS in figure 5.11.4. The materials were all dark and opaque so the visual inspection for cracks during the experiment was performed with reflected light rather than transmitted. The results indicate that all three of the composites offer improved rain erosion resistance over plain ZnS for a small number of impacts, however only ZnS-20D appears to have a significantly higher 0.8 mm jet DTV (300 impacts) of $190 \pm 10 \text{ m s}^{-1}$ compared to ZnS-10D (0-1 μm) $145 \pm 5 \text{ m s}^{-1}$, ZnS-10D (1-3 μm) $125 \pm 5 \text{ m s}^{-1}$ and plain ZnS, $130 \pm 5 \text{ m s}^{-1}$. This threshold velocity for a plain ZnS substrate of 130 m s^{-1} , is however based on a grain size of 3 - 5 μm , which has a fracture toughness of $\sim 0.65 - 0.75 \text{ M Pa m}^{1/2}$. The size of the ZnS grains in the composite are usually smaller at 1 - 2 μm , and a ZnS substrate with this grain size would be expected to have a fracture toughness of $\sim 0.5 - 0.6 \text{ M Pa m}^{1/2}$ (Townsend and Field, 1990), and thus should give a lower threshold velocity (see figure 4.2.2). The fracture toughness of the ZnS-10D was quoted by Farquhar et al. (1990) as $\sim 1.20 \text{ MPa m}^{1/2}$, and this would make it stronger than ZnS. From figure 4.2.2 the threshold value for this fracture toughness would actually be expected to be still higher $\sim 350 \text{ m s}^{-1}$. The discrepancy in the threshold velocity might be due to the intrinsic flaw size being considerably larger for a composite (Farquhar et al., 1990) than for the pure substrates plotted in this graph.

There are four pages of SEM photos, two on the ZnS-20D composite with the higher threshold, and one on each of the other two compositions. In the photos the dark areas are generally areas where the diamonds have been torn out of the matrix, while the bright areas often represent diamonds protruding from the surface. The diamond particles are situated between ZnS grains such that lines connecting the dark and bright areas on the micrographs correspond to the grain structure of the matrix. The removal of diamond particles from the matrix may take place in the polishing process, as can be seen in the photos of undamaged specimens, or during the impact and lateral expansion of the jet. The photos of the undamaged materials show that the ZnS-20D had the most voids in the surface, while the ZnS-10D (1 - 3 μm grains) had fewer larger voids, but in addition had diamonds protruding from the surface. The sites with only a couple of impacts before fracture showed the usual short circumferential cracks. However in many photos the ends of these cracks appear

black due to charging up on the SEM (for example plate 9.11.1 photos 6 and 8). This is most often seen on small narrow cracks that don't show the removal of material by scabbing due to the jet outflow after the impact. This observation might suggest there is some crack extension following the coating of the sample ready for viewing on the SEM, or it may be due to the crack being thin and insufficiently coated so the charge accumulates at the crack tips. If the cause is crack extension then there are several possible explanations : it may be residual stresses in the material, or the heating effect of the SEM together with the thermal expansion mismatch between diamond and ZnS, or some form of atmospheric effect such as stress corrosion cracking which is possible in ZnS (Pickles, 1992).

On the sites exposed to large numbers of impacts, long circumferential cracks can be seen. In addition the ZnS-20D impacted 300 times at 170 m s^{-1} shows a ring of radial striations where the lateral flow of the jet after impact has exploited the surface voids (plate 9.11.3, photo 2). This effect can be seen even at supposedly sub-damage threshold velocities, as in photo 7, plate 9.11.4. In this photo a small crack not visible with the optical microscope can be seen at ~ 2 o'clock. This crack either indicates that the damage threshold had not yet in fact been reached, or that the radial striations eventually lead to cracking. The ZnS-10D ($1-3 \mu\text{m}$) shows similar radial striations, however here they initially appear to be generated by a combination of the exploitation of existing voids in the surface, with the ripping out of the remaining diamond particles by the lateral expansion of the jet after impact, (since fewer diamonds are visible on the surface compared to the undamaged material). In contrast to the other two materials, the ZnS-10D ($0-1 \mu\text{m}$) only exhibits a faint trace of this radial stripping with a slightly increased surface porosity after 200 shots.

One final observation regards the central damage mark which is quite obvious after 200 shots at 170 m s^{-1} on the ZnS-20D, very faint on the ZnS-10D ($0-1 \mu\text{m}$) after 200 shots at 150 m s^{-1} , and still not visible on the ZnS-10D ($1-3 \mu\text{m}$) after 300 shots at 130 m s^{-1} . The causes of central damage in different material is not yet fully understood. In these zinc sulphide / diamond composites the damage initially appears to be due to grain removal. This is probably due to hydraulic penetration of the voids generating tensile stresses in the surrounding material during the impact and resulting in grain dislodgement. This process may be velocity dependent, which may explain its absence on ZnS-10D at 130 m s^{-1} , but further work needs to be carried out to confirm this.

The final two discs tested as part of the composite work were the two thinner discs (0.88 mm instead of 3 mm) containing 30 % ($0 - 1 \mu\text{m}$) diamond particles. The first of these, sample A, was impacted once at 150 and 200 m s^{-1} without any sign of damage and then shattered into small pieces after just one impact at 250 m s^{-1} . Sample B meanwhile was impacted 500 times at 150 , 175 and 200 m s^{-1} before shattering after 60 shots at 225 m s^{-1} . For ZnS-30D, 200 m s^{-1} therefore appears to be below the threshold and 225 m s^{-1} above which makes these compositions stronger than the other three tested (0.8 mm jet DTV (300 impacts) = $212 \pm 12 \text{ m s}^{-1}$). In addition when SEM analysis was carried out on the pieces there were hardly any radial striations, and from this point of view the ZnS-30D composition offered an enormous improvement over the others.

5.11.5 Conclusion

ZnS-10D ($0 - 1 \mu\text{m}$), ZnS-10D ($1 - 3 \mu\text{m}$) and ZnS-20D ($0 - 1 \mu\text{m}$) all offered an improved resistance to rain impact after just a few impacts over that of the standard ZnS substrate. However only ZnS-20D appeared to have a significantly improved threshold velocity for circumferential cracking with the 0.8 mm jet DTV (300

impacts) = $190 \pm 10 \text{ m s}^{-1}$ ($\sim 270 \text{ m s}^{-1}$ for a 2 mm equivalent drop) compared to ZnS of $130 \pm 5 \text{ m s}^{-1}$.

A further composite with 30% diamond has also been tested, however its damage threshold has not yet been fully evaluated because the samples provided were not large enough. The initial results however are promising, and no circumferential cracking was seen after 500 impacts at 200 m s^{-1} (0.8 mm jet DTV (300 impacts) = $212 \pm 5 \text{ m s}^{-1}$ or $\sim 290 \text{ m s}^{-1}$ for a 2 mm equivalent drop) making it better than the ZnS-20D which cracked after just 200 impacts at this velocity, and significantly better than ZnS.

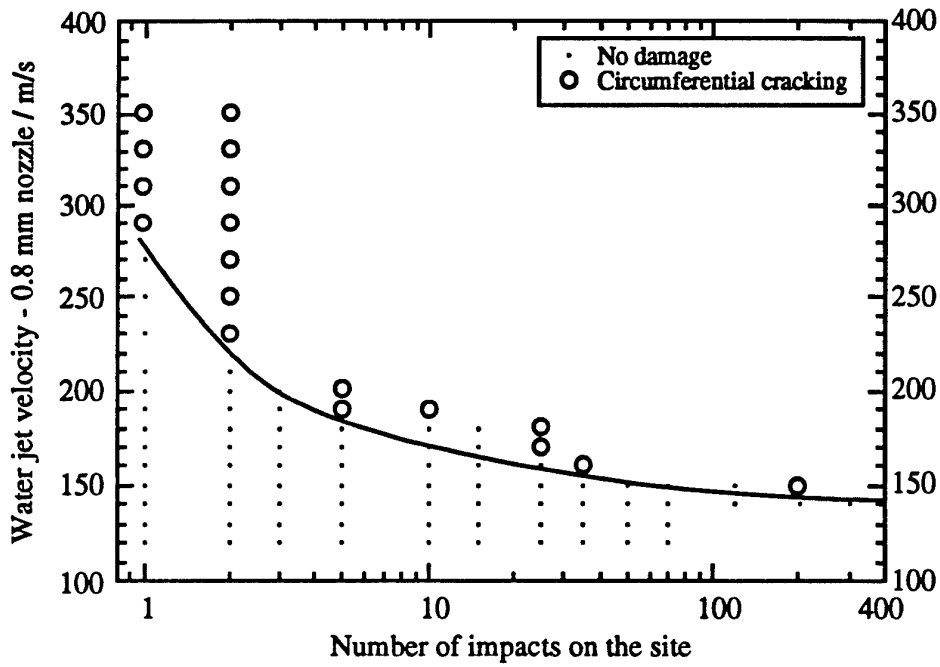


Figure 5.11.1 Threshold curve for ZnS-10D (0 - 1 μm).

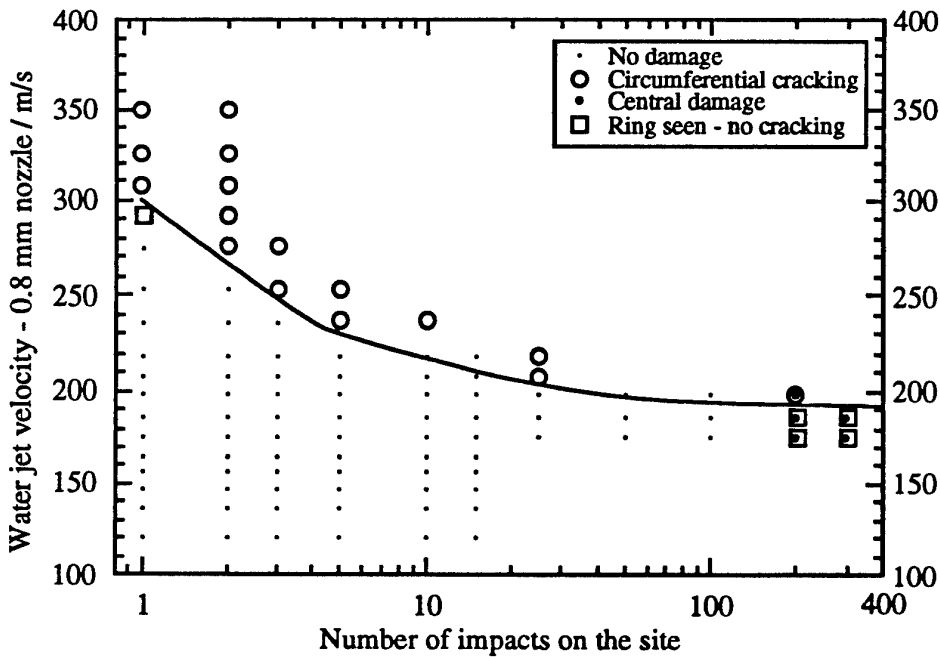


Figure 5.11.2 Threshold curve for ZnS-20D (0 - 1 μm).

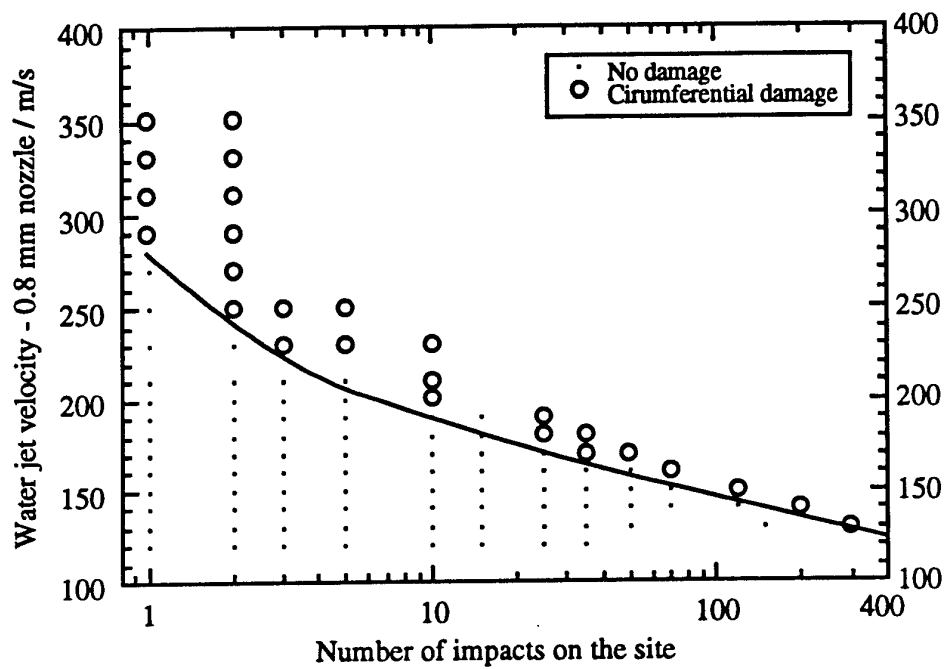


Figure 5.11.3 Threshold curve for ZnS-10D (1 - 3 μm).

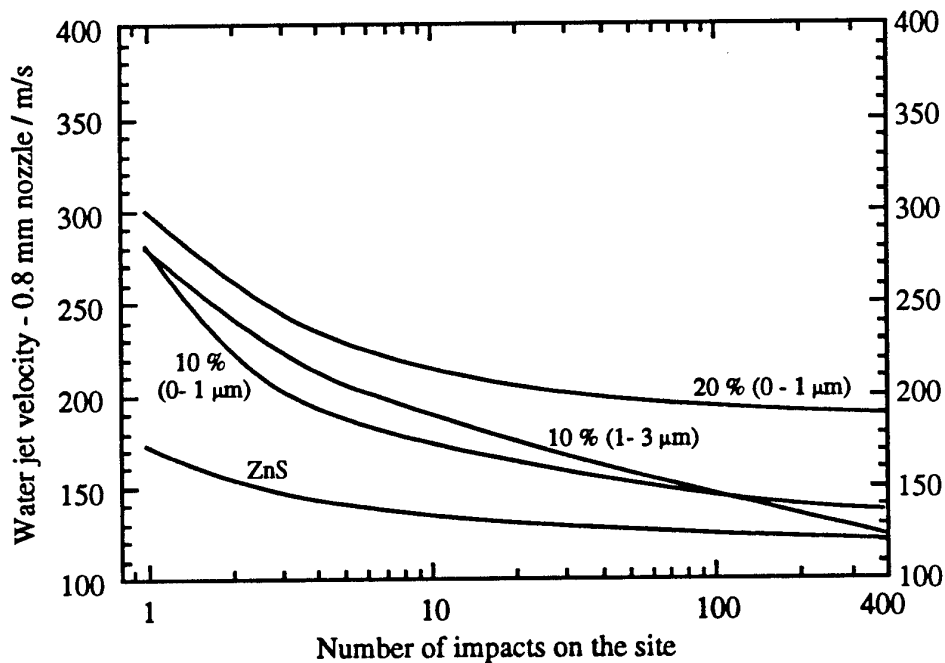


Figure 5.11.4 Summary of the threshold curves for the three ZnS and diamond composites together with that for the ZnS substrate.

5.12 SILICON NITRIDE COATING ON BK7 GLASS

5.12.1 Material Characteristics

This coating is still under development and no data has yet been released for physical, mechanical and optical properties.

Sample Used

Source : GEC Marconi Limited, Hirst Research Centre, Herts
Dimensions : BK7 glass substrate 25 mm diameter, 2mm thick
SiN coatings of thicknesses 1.3, 2.8 and 4.4 μm

5.12.2 Material Description

This coating was selected for development by GEC Marconi for three main reasons. Firstly they could deposit it at low temperatures, secondly they thought it was likely to have hard mechanical properties, and thirdly it was likely to be IR transparent. In order to cover several different applications three substrate materials were to be investigated for use with the coating. These were ZnS, BK7 and sapphire. The coating was to be deposited by a hot MPACVD system as described in Nichols et al (1993).

5.12.3 Published Rain Erosion Work

The only work written on the rain erosion resistance properties of this coating was in a report to GEC Marconi by Seward et al. (1993e).

5.12.4 MIJA Results

In the work covered out on MIJA uncoated discs of BK7 glass were first used to evaluate the threshold curve for the substrate. Three different coating thicknesses 1.3 μm , 2.8 μm and 4.4 μm were then applied to the BK7 and the threshold curve evaluation repeated.

5.12.4 Conclusions

The SiN coatings tested in this study were only in the early development stages. Unfortunately we are not able to present the full results of this work at this time, however a paper presented by Nichols et al. (1993) has reported a 4x improvement in sand erosion resistance, and work on the development of nitride coatings is therefore still continuing.

5.13 GERMANIUM CARBIDE COATING ON ZINC SULPHIDE

5.13.1 Material Characteristics

The following values are taken from Monachan et al. (1989) and Nicholson (1993).

Mechanical

Nano-indentation hardness : 19.8 GPa

Fracture toughness : $1.6 \pm 0.3 \text{ MPa m}^{-3/2}$

Youngs modulus : 260 - 325 GPa

Internal stress : 0.05 GPa

Rain erosion resistance (see section 4.4):

0.8 mm jet DTV (1, 3, 10, 300 impacts)

$205 \pm 5, 175 \pm 5, 155 \pm 5, 125 \pm 5 \text{ m s}^{-1}$

Thermal

Thermal expansion :

$3.3 \times 10^{-6} \text{ K}^{-1}$ at room temperature

$5.1 \times 10^{-6} \text{ K}^{-1}$ at 300 °C

Optical

Transmits 3 - 5, 8 - 12 μm wavelengths

Physical

Structure : Amorphous

Sample Used

Source : OCLI

Dimensions : 25 mm diameter disc, 3 mm thick

5.13.2 Material Description

The investigation into germanium carbide as a potential erosion resistant coating was mentioned by Lettington et al. (1989). The material used in their study was an infrared transparent amorphous hydrogenated alloy of germanium and carbon, deposited in one of two different ways. Firstly, by plasma assisted chemical vapour deposition (PACVD), using germane (GeH_4) and butane (C_4H_{10}) as the feedstocks, and secondly by reactive radio frequency sputtering using a germanium target in a sputtering medium of methane and argon. Using PACVD a deposition rate of 1 $\mu\text{m/hr}$ could be achieved, while the coatings refractive index could be varied in the range of 2 - 4 by changing the flow rates of the two feedstock gases. With sputtering a refractive index range of only 3 - 4 was possible, however far higher deposition rates of up to 10 $\mu\text{m/hr}$ could be obtained.

The germanium carbide coating could be grown in thick layers if necessary (> 100 μm) and promised good adhesion, high durability and low stresses, together with a low absorption coefficient, $<10 \text{ cm}^{-1}$, over the wavelength range 3 - 12 μm .

5.13.3 Published Rain Erosion Work

In order to achieve good rain erosion protection with a hard coating it is necessary to use thick films with a high Young's modulus (Hand et al., 1989). Although this can be achieved with GeC, films with high values of Young's modulus are associated with the carbon rich end of the GeC family where the absorption coefficient is higher than desirable. It therefore becomes necessary to strike a balance to maximise protection while minimising optical absorption loss.

Initial coating systems developed at Barr and Stroud incorporating a layer of GeC had a DLC outer coating. These were known as ARZ5 when on FLIR ZnS, and ARG6 when on Ge. Despite these coatings having excellent durability and easily passing the RSRE sand / water wiper test (Lettington et al. 1989) the whirling arm

results from RAE were disappointing with ARZ5 offering little improvement over the uncoated ZnS, and ARG6 offering little improvement over DLC on Ge (Monachan et al. 1989). SIJA threshold evaluations likewise showed little difference in threshold velocity, with the uncoated water clear ZnS at 0.8 mm jet DTV (5 impacts) = $145 \pm 11 \text{ m s}^{-1}$, and the coated water clear ZnS at $160 \pm 12 \text{ m s}^{-1}$ (Monachan et al. 1989). It should be noted that although DLC is actually harder it cannot be used in place of GeC, as inherent stresses limit its thickness to 1 - 2 μm , and it has a relatively high absorption compared to GeC.

In 1990 Kelly et al. at OCLI claimed to have carried out in-house SIJA tests on a 20 μm thick GeC coating on ZnS, obtaining 0.8 mm jet DTV of 190 m s^{-1} . However neither the method of damage assessment, nor the number of impacts used was stated for this test, and the results therefore cannot be compared to those of Barr and Stroud. OCLI specimens were also tested at RAE (Tattershall and Minter, 1990) and at Wright Patterson (Wilson 1990), and as with the samples from Barr and Stroud little difference was observed between coated and uncoated specimens. Samples of this coating were also supplied to MIJA for testing and these results are described below, however these were on FLIR grade ZnS rather than waterclear ZnS.

Martin (1990a and b) also initiated a testing programme of the rain erosion resistance of GeC, and more recently Mackowski et al. (1992) completed a study of several different GeC alloys with different substrate preparations. As a result of testing on the SAAB whirling arm rig, Mackowski et al. claimed that benefits in erosion performance could be obtained by correct optimisation of deposition conditions for the germanium carbide.

5.13.4 MIJA Results

The results from the MIJA tests can be seen in figure 5.13.1 which shows the threshold curve for a 11 μm thick germanium carbide coating supplied by OCLI. Figure 5.13.2 shows how this result compares with those for the uncoated ZnS, and also with coatings of boron phosphide and amorphous diamond on ZnS. On comparing the uncoated and GeC coated ZnS we see that the addition of the coating has had no significant effect on the threshold velocity, and only slightly increased the incubation time for impact velocities above this threshold. Part of the reason for the increase in incubation time could be attributed to the number of impacts required after crack initiation in the ZnS, to propagate the cracks either through the coating or the bulk, to such an extent that they are visible by either direct observation on the coating surface, or by observation through the bulk of the ZnS.

5.13.5 Conclusions

The erosion results obtained on both the RAE and Wright Patterson whirling arms, together with those of MIJA all lead to the same conclusion. Despite germanium carbides good mechanical properties, low stress and good adhesion the improvements in erosion resistance offered are very small. Consequently interest in GeC as a coating has now virtually disappeared, and testing of further samples of coatings from Battelle and Barr and Stroud on MIJA has become a low priority. The new germanium carbide material produced by Mackowski et al. (1992) has yet to be evaluated by an objective source, however the recent results from the CVD diamond and boron phosphide programmes are so promising that it is unlikely that their GeC will make an impact.

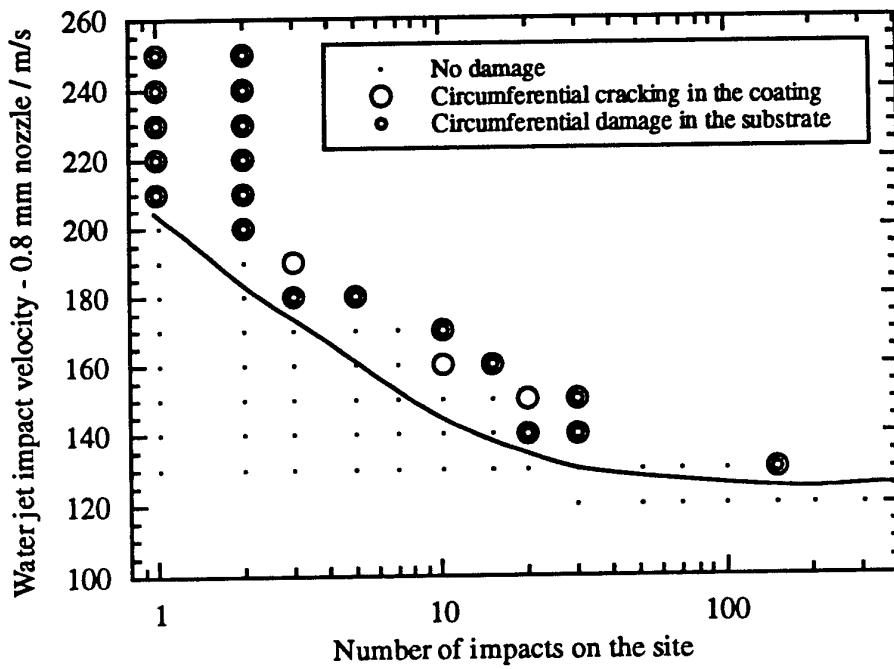


Figure 5.13.1 Threshold velocity data for a 11 μm thick coating of GeC on ZnS

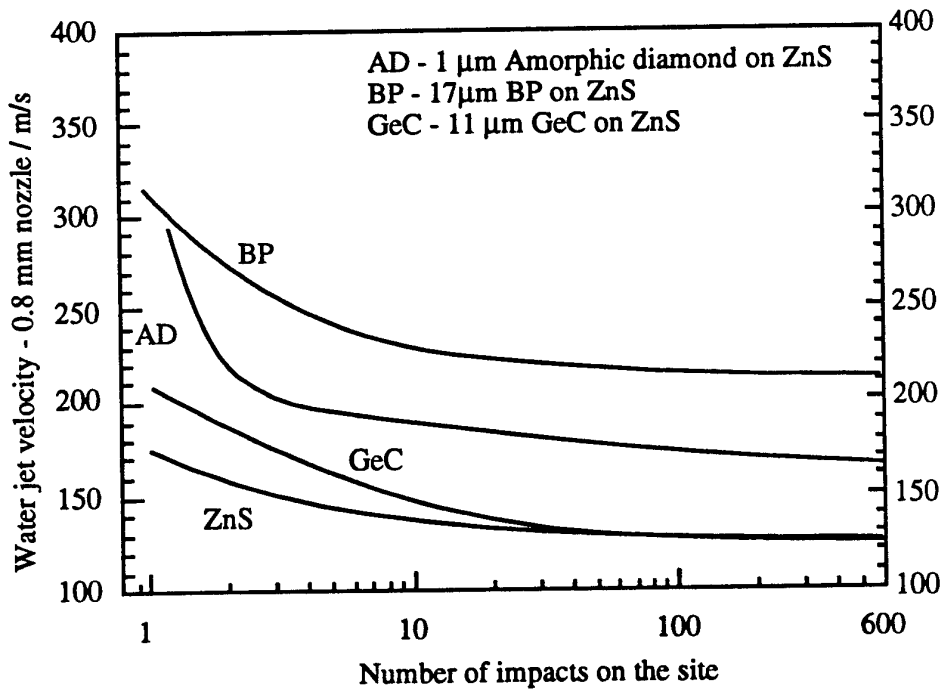


Figure 5.13.2 Comparison of threshold velocity curves for various coatings on ZnS

5.14 BORON PHOSPHIDE COATINGS

5.14.1 Material Characteristics

The following values are taken from Lewis et al. (1989) and Nicholson (1993).

Mechanical

Nano-indentation hardness : 24 GPa

Youngs modulus : 166 GPa

Internal stress : -0.3 GPa (can be varied)

Rain erosion resistance (see section 4.4):

0.8 mm jet DTV (300 impacts) - depends on coating thickness

Optical

Transmits 3 - 5, 8 - 12 μm wavelengths

Physical

Structure : Amorphous

Sample Used

Source : Barr and Stroud, Pilkington Optronics

Dimensions : 25 mm diameter disc, 3 mm thick

5.14.2 Material Description

Boron Phosphide can be prepared by a number of different methods. Chu et al. (1971) tried two CVD methods involving the thermal decomposition of diborane (B_2H_6) and phosphine (PH_3) in hydrogen and the thermal reduction of a boron halide and a phosphorous halide in hydrogen. Both these processes have been widely used and reported along with several other methods, however they all involve temperatures $> 1000^\circ\text{C}$.

The samples tested as part of this work were all grown by PACVD (plasma assisted chemical vapour deposition) using diborane, boron trichloride and phosphine as the feedstock gases. This has the advantage of allowing deposition of films at significantly lower substrate temperatures ($< 500^\circ\text{C}$). In this technique additional energy required to ensure efficient surface mobility of the growing film is provided by energy transfer processes from the RF plasma. The films are really amorphous phosphorous glass containing some boron, hydrogen and oxygen. A typical formula might be $\text{BP}_4\text{O}_{0.1}\text{H}_{0.4}$ with the P:B atomic ratio normally in the range of 2-8:1 (Lewis et al., 1989).

5.14.3 Published Rain Erosion Work

Lewis et al. (1989) evaluated the damage threshold velocity of BP on ZnS using 10 impacts with SIJA, and then Nomarski microscopy to assess damage. They estimated that the uncoated material had a threshold of 0.8 mm jet DTV (10 impacts) = 145 m s^{-1} while a 38 μm thick coating had a threshold of $260 \pm 10 \text{ m s}^{-1}$. They also carried out some whirling arm work and reported pitting in the surface at 60° , and fracture in the underlying ZnS at 90° . At the same conference Monachan et al. (1989) added that the threshold velocity for 18 μm thick BP on ZnS was 220 m s^{-1} , and said that there was no change in the transmission measurement for a BP coating on ZnS even after long exposures on a whirling arm rig.

Monachan (1990) next extended the above work with a graph showing the change in threshold with BP coating thickness for ZnS. He also gave a threshold value of 0.8

mm jet DTV (10 impacts) = 150 m s⁻¹ for uncoated germanium and 245 m s⁻¹ for germanium with a BP coating.

Waddell et al. (1990) reprinted the variation of threshold velocity with BP coating thickness on ZnS, and added a similar graph for BP coating thickness on germanium. He also reported whirling arm results at 470 mph at Wright Patterson, showing the variation in transmission loss after a 20 minute exposure for a range of BP coating thicknesses on Ge (figure 5.14.1).

Gibson et al. (1992) extended the variation in threshold velocity against coating thickness of Waddell et al. (1990) to include GaP on Ge and ZnS, and BP on Ge, ZnS and Tuftran (figure 5.14.3), together with graphs for GaP and BP incorporated into antireflection multilayers on both Ge and ZnS. Gibson (1992) recorded that all of the BP coated substrates had passed the RAE and Wright-Patterson whirling arm tests, with less than 4 % decrease in transmission after 20 minutes exposure at 470 mph.

Gibson et al. (1993) recently updated these results adding a graph for transmission loss after a 20 minute exposure at RAE for a range of BP coating thicknesses on Ge and ZnS as shown in figure 5.14.2

5.14.4 MIJA Results

Boron phosphide coatings have been tested on MIJA on four different substrates, and at various periods in its development..

1. Fused silica substrate	Feb 1989	13 µm BP
2. ZnS substrate	Feb 1990	13 µm BP
	Dec 1992	10.8, 12.5, and 16.8 µm BP
3. Germanium	May 1993	12.9, 13.9 and 16.2 µm BP
4. Sapphire	June 1993	9.8 µm BP

5.14.4.a Fused Silica Substrate (Feb 1989)

A threshold velocity evaluation for the uncoated fused silica substrate was carried out giving a 0.8 mm jet DTV (300 impacts) = 175 ± 10 m s⁻¹.

The first disc with a BP coating was then tested. This disc was impacted over the range 185 - 455 m s⁻¹, and shattered into pieces after one just impact at each of these velocities, the initiation point appearing to be the 455 m s⁻¹ site. Damage was seen on all the sites impacted at velocities above 330 m s⁻¹, with extensive coating debonding being a prominent feature. The sites below 330 m s⁻¹ could not be properly identified because of the disc failure. A second disc was therefore impacted over the range 165 - 345 m s⁻¹ to complete the threshold curve.

The results from the coated and uncoated fused silica are shown in figure 5.14.4. The addition of the BP coating appears to have lowered the rain erosion resistance of the fused silica substrate with the 0.8 mm jet DTV (10 impacts) = 175 ± 10 m s⁻¹ compared to 0.8 mm jet DTV (10 impacts) = 195 ± 10 m s⁻¹ for the uncoated fused silica..

5.14.4.b Zinc Sulphide Substrate (Feb 1990, Dec 1992)

The first batch of ZnS samples coated with BP all had 13 µm thick coatings on them and were supplied in February 1990. Initially an impact template that covered the range 185 - 440 m s⁻¹ was defined. However the first disc tested using this template broke after just one impact at each velocity, and damage could be seen on all of the sites impacted at 295 m s⁻¹ or above. The next disc tested was therefore only subjected to the impact range of 185 - 410 m s⁻¹ and after one impact the same result was achieved as for disc #1, with damage visible on all the sites subjected to impacts

at 295 m s⁻¹ or above. The final threshold velocity curve obtained is compared to that for ZnS in figure 5.14.5 with 0.8 mm jet DTV (300 impacts) = 180 ± 5 m s⁻¹.

It is important to remember in this and other work with opaque coated materials that the methods of damage assessment for coated and uncoated material are often different. For uncoated ZnS examination under the microscope using transmitted light can reveal very small cracks in the substrate surface. Once the opaque boron phosphide coating is applied damage is assessed by checking for coating damage using reflected light under the microscope, and for damage on the surface of the ZnS underneath the BP coating by looking for cracking *through* the bulk of the zinc sulphide, i.e. from the underside of the specimen. This technique of crack detection on the ZnS surface is not likely to be as accurate as direct observation, and therefore if anything the assessment of the protection offered by the coating will be an overestimate.

A second batch of BP on ZnS were supplied for rain erosion and sand erosion testing in December 1992. The three discs evaluated on MIJA had coating thicknesses of 10.8, 12.5 and 16.8 µm. Thirteen impact sites were initially defined onto each of the discs tested to cover the impact velocity range of 160 - 360 m s⁻¹. Assessments were made of substrate damage (by observation from the rear surface), coating damage, central damage on the coating, and chipping on the coating. The results for each of the substrates can be seen in figures 5.14.6 - 8 and are summarised in figures 5.14.9.

The two thinner BP coatings gave a slightly lower threshold velocity value (0.8 mm jet DTV (300 impacts) = 195 ± 5 m s⁻¹) than the 16.8 µm one (0.8 mm jet DTV (300 impacts) = 210 ± 10 m s⁻¹). On both the thinner coated samples damage was detected simultaneously in the coating and in the substrate. However in the thicker sample damage only occurred simultaneously at high velocities > 350 m s⁻¹. Between 225 and 350 m s⁻¹ the damage initiated in the substrate and then extended up through the coating, while between 205 and 225 m s⁻¹ the damage initiated in the coating with no damage observable in the substrate through from the rear side.

The chipping recorded in the threshold graphs at supposedly sub-threshold velocities was very localized, and didn't appear to spread or lead to further damage. The structure within the chipped areas occasionally consisted of spheres packed closely together, of a size similar to those found attached to the surface of the undamaged material. These 'spheres' were more numerous on the surface of this batch of the BP coating compared to those supplied in Feb 1990. The cause or composition of these 'spheres' is unknown.

5.14.4.c Germanium (May 1993)

The germanium sample used to establish a base line curve for the substrate was the uncoated side of one of the samples provided. This gave threshold velocity values for circumferential cracking of 0.8 mm jet DTV (1, 3, 10, 300 impacts) = 230 ± 10, 190 ± 10, 170 ± 10, 110 ± 10 m s⁻¹ which compares fairly well with results from previous experiments on germanium (0.8 mm jet DTV (1, 3, 10, 300 impacts) = 255 ± 5, 195 ± 5, 165 ± 5, 125 ± 5 m s⁻¹).

Four BP coated germanium discs were then evaluated to investigate the effect of the coating thickness on the threshold velocity curve (figures 5.14.10-12 and 5.14.14). These samples had BP coating thicknesses of 12.9, 13.9 and 16.2 µm (2 samples) but all gave 0.8 mm jet DTV (300 impacts) = 250 ± 10 m s⁻¹.

The damage seen on the thickest coated germanium sample after impact took the form of short cracks, complete ring cracks or pits. When pits occurred the damage was not always confined to the impact area, and sometimes cracks appeared to run away from the site suggesting that there was substantial damage in the substrate before it

was observed through the coating. When a complete ring crack was obtained a hexagonal shape was produced as seen previously with the damage on the uncoated germanium. This observation suggests that the damage initiates in the germanium substrate and then propagates up through the coating.

Unlike the damage on the 16.2 μm coated germanium there were no pits formed on the surface of the 12.9 and 13.9 μm coated germanium samples. This suggests that the cracking had spread through the coating before more extensive damage occurred in the substrate.

5.14.4.d Sapphire (June 1993)

The results on the uncoated sapphire discs have already been mentioned in section 5.1.4.d. These results were in good agreement with each other allowing data to be combined to produce a full threshold curve. This gives the uncoated sapphire a 0.8 mm jet DTV (300 impacts) of $490 \pm 10 \text{ m s}^{-1}$, which is in good agreement with previous samples tested, as shown in section 5.1.5 (Seward et al. 1993).

Only two samples of boron phosphide coated sapphire were supplied for threshold evaluation both with BP coatings 9.8 μm thick. These samples were provided in an attempt to evaluate the damage threshold curve for the boron phosphide coating, without the complication of damage initiation taking place in the substrate, as seen previously with germanium and zinc sulphide. This would therefore hopefully give some idea of just how erosion resistant boron phosphide is on its own. Sapphire was chosen as a substrate for this reason, because of its high fracture toughness, so that cracking in the substrate would not be likely to initiate below 490 m s^{-1} .

The first sample tested, number 4, was impacted at a range of velocities below the 490 m s^{-1} threshold value for the uncoated sapphire substrate. Damage of the coating was assessed regularly using both reflected and transmitted light on the microscope, in order to record both the number of impacts required to initiate central damage in the coating, and the number of impacts required to damage the coating sufficiently to reveal the sapphire substrate underneath, (i.e. coating stripping).

Surprisingly this first disc shattered after 155 impacts at 450 m s^{-1} . This was unexpected, since with the uncoated sapphire only central damage was observed to occur at this velocity and the 0.8 mm jet DTV (300 impacts) was $490 \pm 10 \text{ m s}^{-1}$.

As a result of this unexpected result for the first disc, the second disc, number 2, was used not just to assess the damage of the coating, but also to obtain a threshold curve for the damage of the substrate. This curve showed a dramatic reduction in the threshold velocity for the sapphire, as shown in figure 5.14.16 (0.8 mm jet DTV (300 impacts) = $412 \pm 12 \text{ m s}^{-1}$).

This reduction in threshold velocity could be due to the surface of the substrate suffering damage during the deposition process, or due to the surface of the sapphire being put into stress following the deposition of the boron phosphide coating.

Circumferential cracking was observed in the sapphire only when the coating had been stripped away from a small area of the substrate. As with the coated germanium, damage was sometimes observed to extend in the substrate, away from the impact site.

5.14.5 Conclusions

The BP coating produced by Pilkington Optronics appears to offer a considerable degree of rain erosion protection to the zinc sulphide and germanium substrates. However care needs to be taken when discussing such results because damage is only observed after it has propagated through the coating. Despite this reservation BP still appears to be the clear leader out of the protective coatings currently available, and work to characterise it further will therefore be carried out over the next 12 months.

5.14.5.a Fused Silica Substrate

The BP coated fused silica seemed to offer no improvement in rain erosion resistance over that of the uncoated fused silica, in fact the resistance to impact seemed to have got worse. One of the main problems appears to be in the bonding between the coating and the substrate.

5.14.5.b Zinc Sulphide Substrate

Sample number	BP thickness (μm)	SIJA DTV (10) Barr & Stroud / m s^{-1}	MIJA DTV (10) Cavendish / m s^{-1}	MIJA DTV (300) Cavendish / m s^{-1}
Feb 1990 # 1	13		230 ± 10	180 ± 5
Dec 1992 # 1	10.8	> 255	230 ± 10	195 ± 5
Dec 1992 # 2	12.5	235	230 ± 10	195 ± 5
Dec 1992 # 3	16.8	> 270	235 ± 15	210 ± 10

The BP coated ZnS offered an improved rain erosion resistance compared to uncoated ZnS. However it must be remembered that the methods of damage assessment being used were not identical, and therefore the magnitude of this improvement is not well defined.

The new and old batches of BP on ZnS did not have significantly different responses to liquid impact after a short exposure above the threshold velocity, however the more recent samples did have a slightly higher final threshold velocity. This threshold velocity improved still further, although only slightly, with the thicker coating. However once again this made little difference to the incubation period for damage at many of the velocities tested above the threshold.

When damage was first detected on the BP on ZnS supplied in Feb 1990, or from the two thinnest samples supplied in Dec 1992, the damage was seen in both the coating and the substrate at the same time. However after a large number of impacts a complete cone crack could often be seen in the substrate whilst only a partial arc of a circle was visible in the coating.

With the thickest BP coating supplied in Dec 1992 the damage mostly initiated in the substrate after low numbers of impacts, and only after large numbers of impacts (or at velocities above the one impact damage threshold) was any damage detected in the coating.

5.14.5.c Germanium Substrate

Sample number	Dimensions (mm)	Ge thickness (mm)	BP thickness (μm)	MIJA DTV / m s^{-1}
1	25.0 x 25.0	5.0	12.9	250 ± 10
2	25.0 x 25.0	5.0	13.9	250 ± 10
3	25.0 diameter	6.1	16.2	250 ± 10
4	25.0 diameter	6.1	16.2	280 ± 20

The threshold curve for the uncoated germanium was in fairly good agreement with previous results obtained from MIJA. The 0.8 mm jet DTV (300 impacts) of $110 \pm 10 \text{ m s}^{-1}$ also gave a value to compare with subsequent results from the coated samples, see figure 4.1.

From figure 4.1 it can be seen that the 0.8 mm jet DTV (300 impacts) for all the coated germanium samples are approximately the same, at $250 \pm 10 \text{ m s}^{-1}$. This is a considerable improvement compared to the uncoated substrate. There appears to be

no obvious relationship between the final threshold velocity and coating thickness. However there is a thickness dependency in the number of impacts required to observe damage when impacting above the threshold velocity. For the two 16.2 μm thick coated samples at the 400 m s^{-1} site, damage was observed after 7 impacts, this was repeatable for both samples provided. The number of impacts decreased with coating thickness. This suggested that the damage was initiating in the substrate and propagating through the coating. The thicker the coating the more impacts required before cracks were visible on the surface. Further evidence for the damage initiating in the germanium was obtained by examination of the impact sites. These sites had shapes which agree with the damage patterns of the uncoated germanium again suggesting damage initiates in the substrate.

The MIJA results obtained in this work can be compared with those obtained using SIJA by Gibson et al. (1992, 1993). In the SIJA work only 10 impacts were used on each site evaluated, and therefore the final threshold velocity is never actually reached. Using SIJA an 11 μm thick coating of BP on Germanium was recorded by Gibson et al. to have a 0.8 mm jet DTV (10 impacts) of $\sim 370 \text{ m s}^{-1}$. In comparison on MIJA a 12.9 μm thick coating has a 0.8 mm jet DTV (10 impacts) of $300 \pm 20 \text{ m s}^{-1}$ and a 0.8 mm jet DTV (300 impacts) of $250 \pm 10 \text{ m s}^{-1}$. The cause for this discrepancy between the SIJA and MIJA results is unknown, since the uncoated germanium results are fairly close (SIJA 0.8 mm jet DTV (10 impacts) = 150 m s^{-1} and MIJA 0.8 mm jet DTV (10 impacts) = $170 \pm 10 \text{ m s}^{-1}$, with the 0.8 mm jet DTV (300 impacts) = $110 \pm 10 \text{ m s}^{-1}$).

The results obtained from Gibson et al. also try to identify a relation between the coating thickness and the threshold velocity. The results of this study indicate that the threshold increases with coating thickness, however it would be of considerable interest to now repeat this evaluation with MIJA using full threshold curves to see how the 0.8 mm jet DTV (300 impacts) varies.

The boron phosphide coatings tested appear to have offered a substantial improvement to the observed rain erosion resistance of the germanium substrate. However it is important to remember that because germanium is opaque, damage can only be observed when the cracking has extended through the coating.

5.14.5.d Sapphire Substrate

The uncoated sapphire samples gave good agreement with previous results, with a threshold velocity of $490 \pm 10 \text{ m s}^{-1}$. Unlike with germanium or zinc sulphide however, the application of a boron phosphide coating to the sapphire has not improved the threshold velocity for damage after 300 impacts. In fact the addition of the boron phosphide coating seems to have reduced the erosion resistance of the sapphire substrate, to give a 0.8 mm jet DTV (300 impacts) = $412 \pm 12 \text{ m s}^{-1}$. This result would have been missed if the threshold velocity had been taken after just 10 impacts, since at this stage the results in figure 5.14.17 still suggest that the addition of the coating has been beneficial. Once again the importance of evaluating the whole threshold curve is apparent.

The aim of this experiment was to try and find the erosion resistance of the boron phosphide coating itself, without the complication of the substrate cracking first. The experiments on MIJA failed to identify a damage threshold for the coating on its own, since damage was still seen to initiate after large numbers of impacts at 250 m s^{-1} (figure 5.14.14), well below the threshold for damage of the sapphire substrate. In view of these results it may be interesting to try even longer exposures than the normal 300 impacts on the BP coated Germanium and ZnS, and to test another sample of BP on sapphire at even lower velocities to further characterise the coating itself.

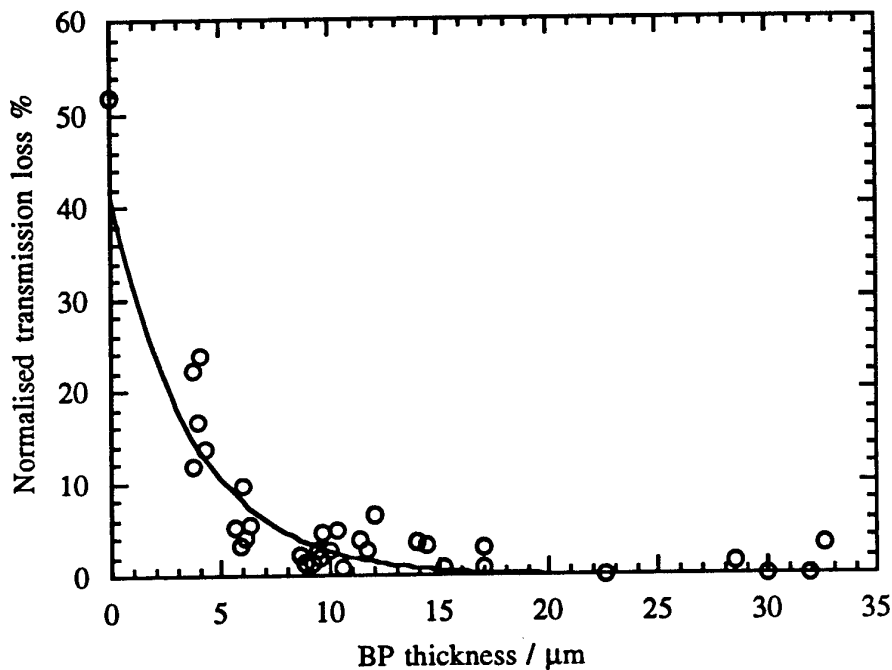


Figure 5.14.1 Loss in transmission as a function of BP thickness on polycrystalline germanium on the UDRI whirling arm. Conditions were 2 mm nominal drop size, 25 mm hr⁻¹, 20 mins exposure at 211 m s⁻¹, transmission averaged 8 - 11.5 μm .

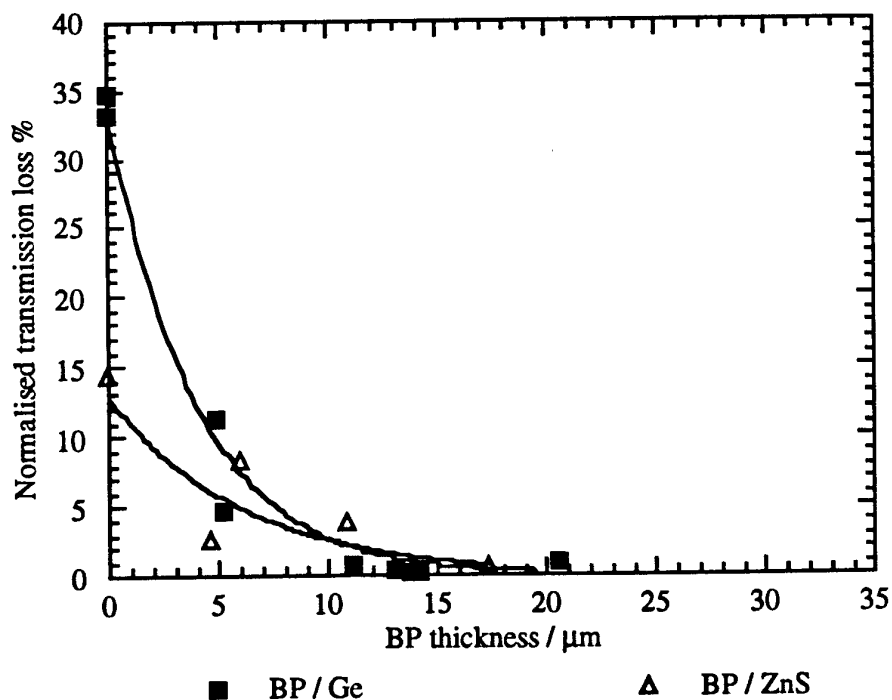


Figure 5.14.2 Loss in transmission as a function of BP thickness on germanium and multispectral ZnS on the RAE whirling arm rig. Conditions were 2 mm nominal drop size, 25 mm hr⁻¹, 20 mins exposure at 211 m s⁻¹, transmission averaged 8 - 11.5 μm .

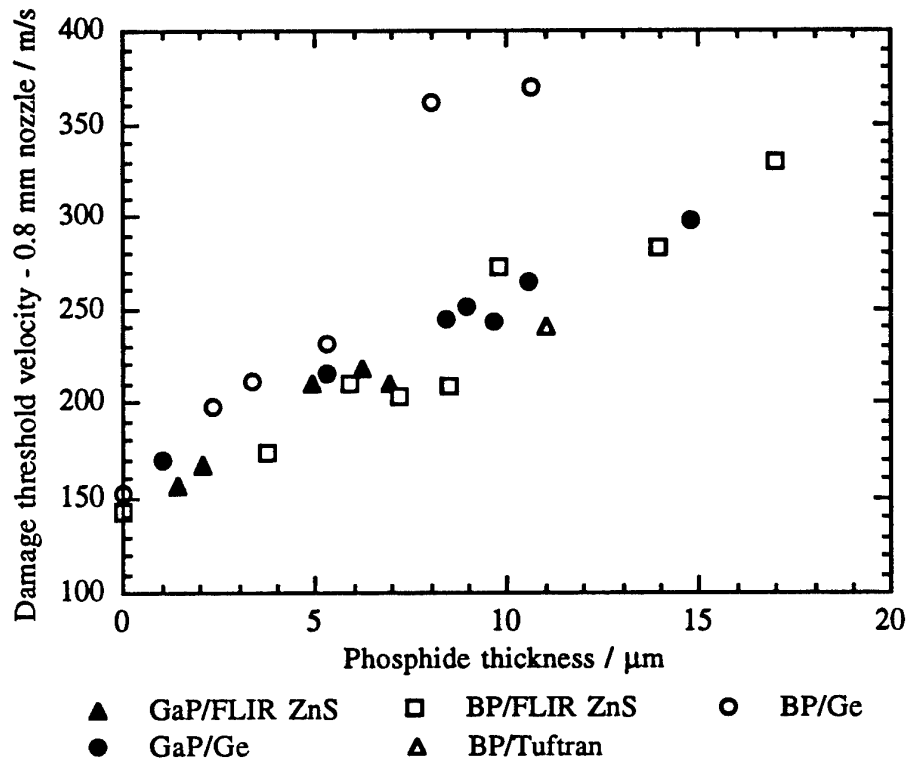


Figure 5.14.3 Damage threshold velocity as a function of phosphide film thickness for BP and GaP deposited on a range of substrate materials.

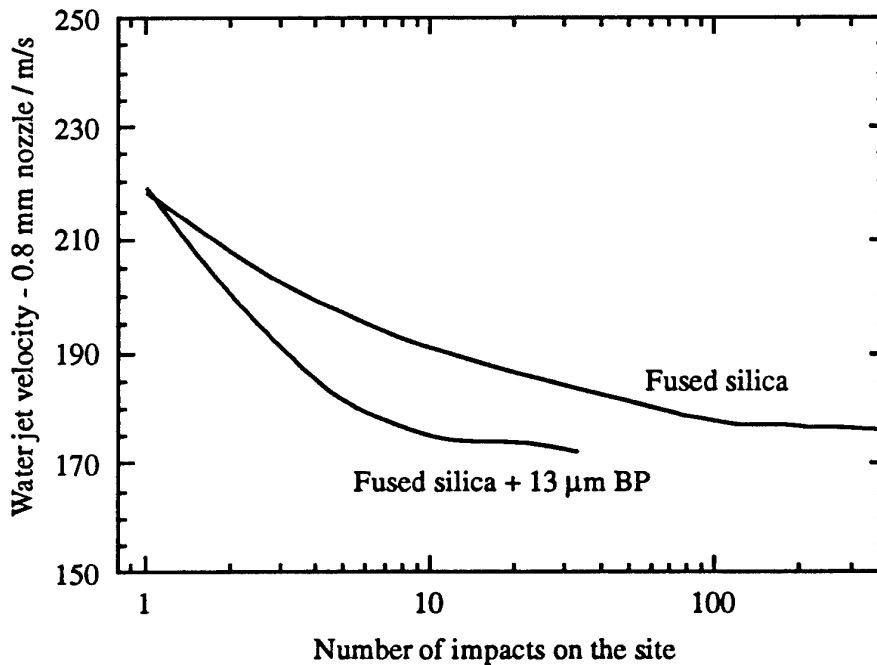


Figure 5.14.4 Summary of the threshold velocity curves obtained for fused silica and for a 13 μm thick BP coating on fused silica.

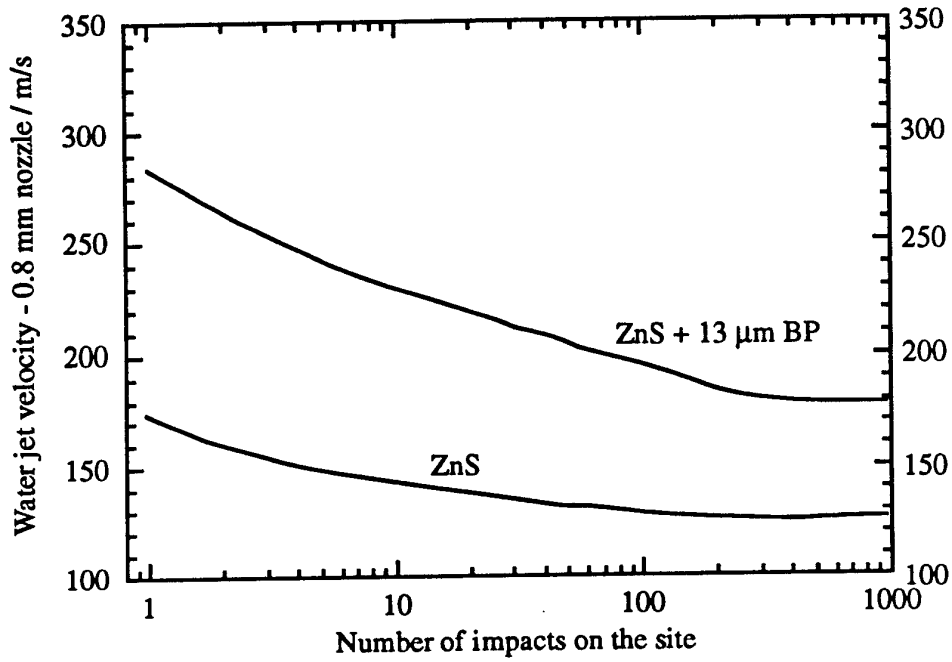


Figure 5.14.5 Comparison of the threshold velocity for uncoated ZnS with that for a 13 μm BP coating on ZnS supplied in Feb 1990.

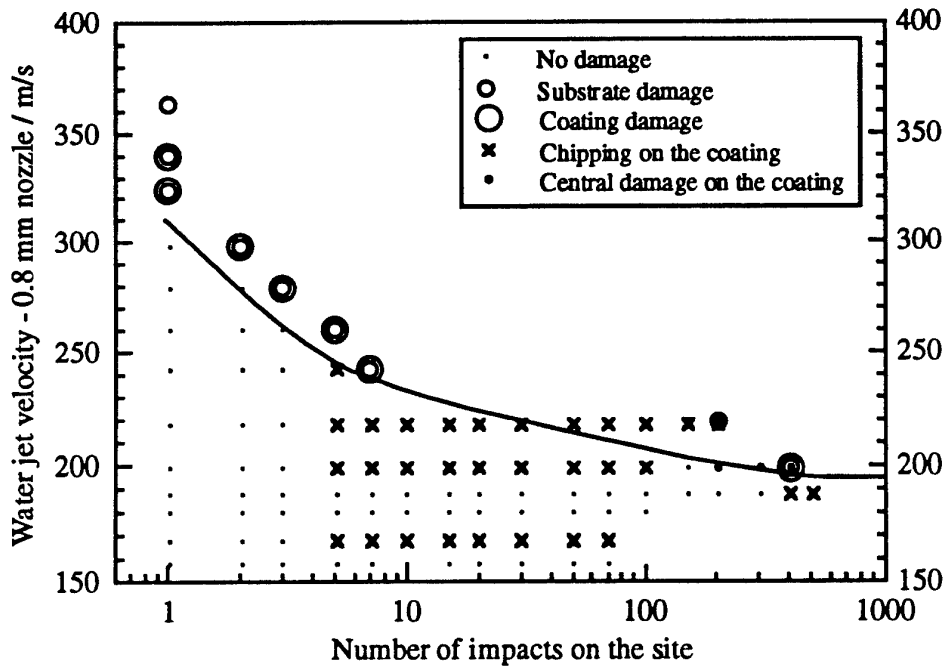


Figure 5.14.6 Threshold velocity data for the 10.8 μm thick BP coating on ZnS supplied in Dec 1992.

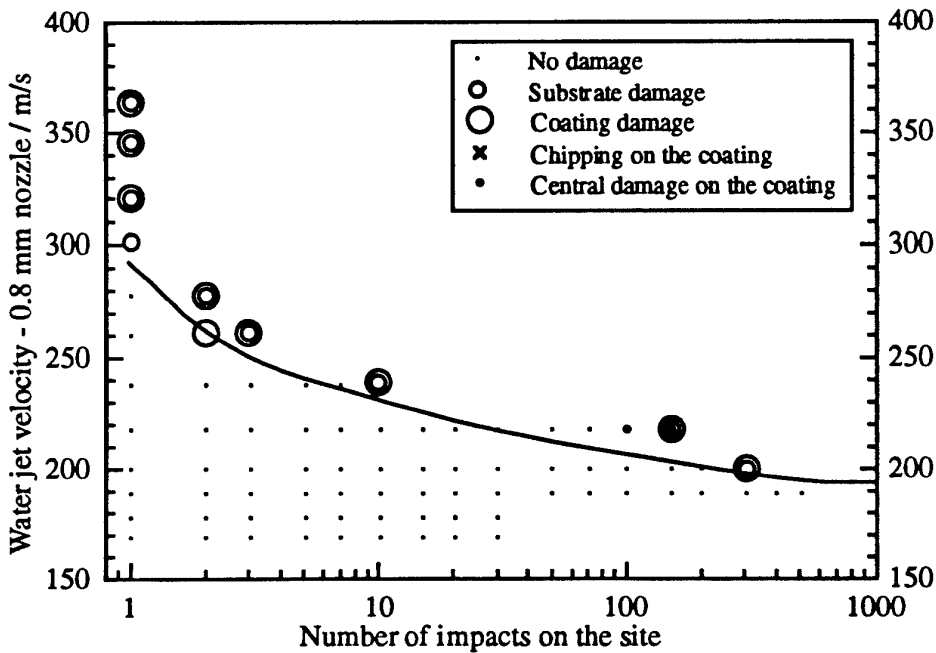


Figure 5.14.7 Threshold velocity data for the 12.5 μm thick BP coating on ZnS supplied in Dec 1992.

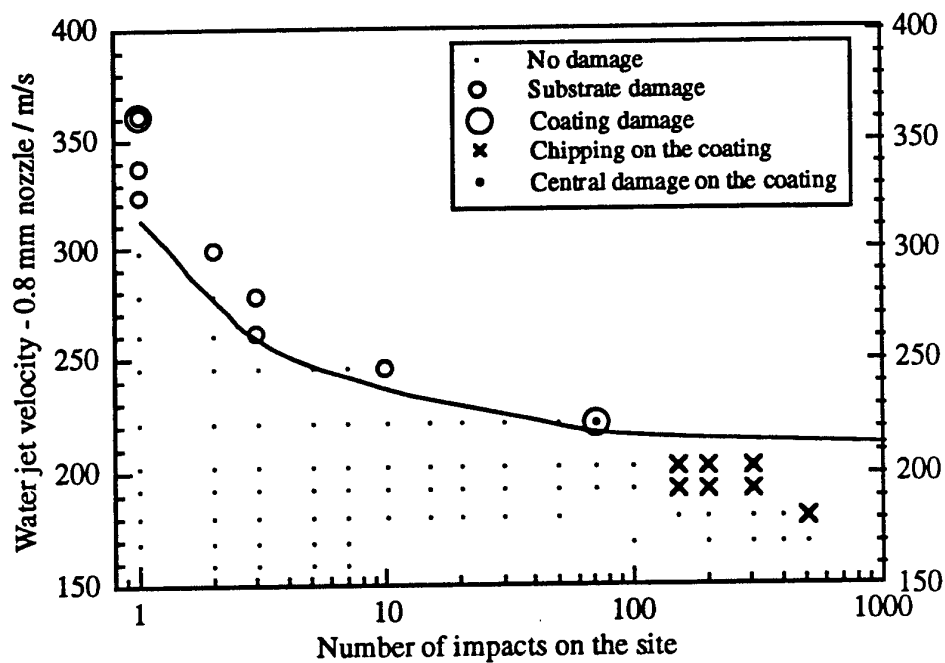


Figure 5.14.8 Threshold velocity data for the 16.8 μm thick BP coating on ZnS supplied in Dec 1992.

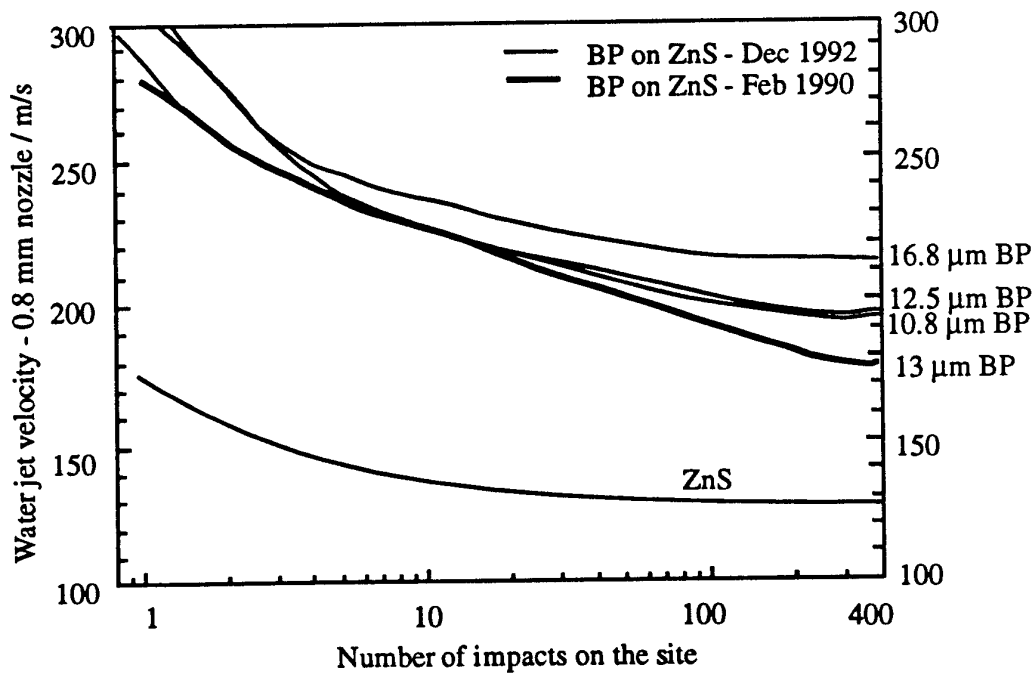


Figure 5.14.9 Graph comparing the threshold curve results from BP on ZnS from the samples supplied in Feb 1990 and Dec 1992 with uncoated ZnS.

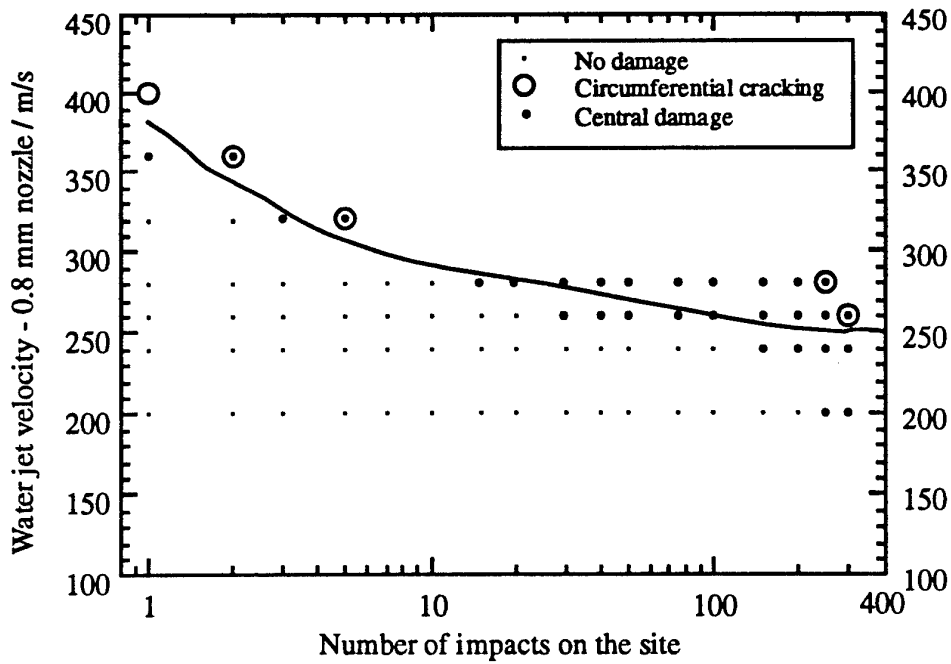


Figure 5.14.10 Threshold curve for the 12.9 μm thick BP coating on Ge

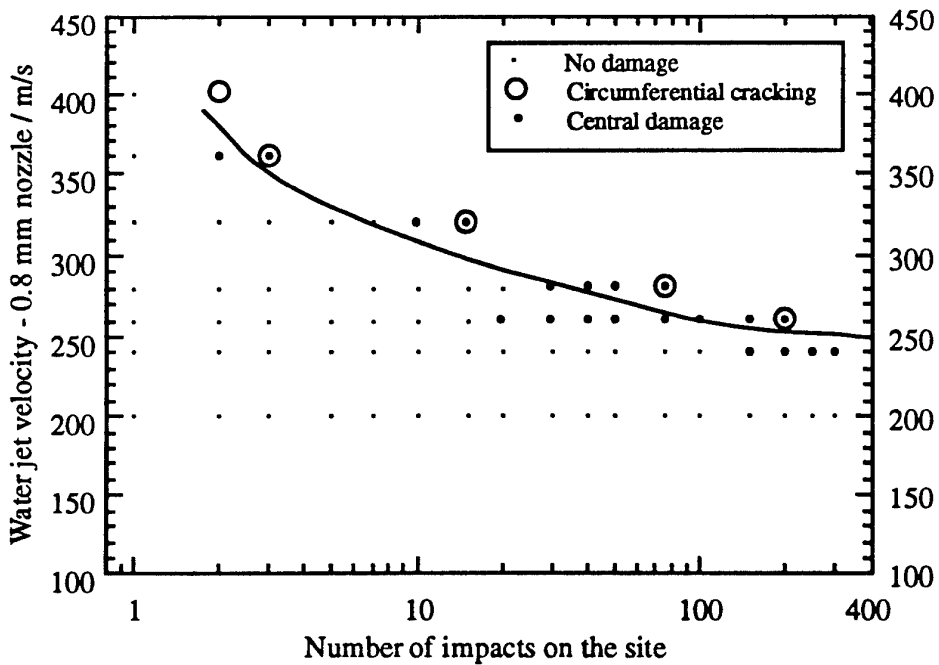


Figure 5.14.11 Threshold curve for the 13.9 μm thick BP coating on Ge

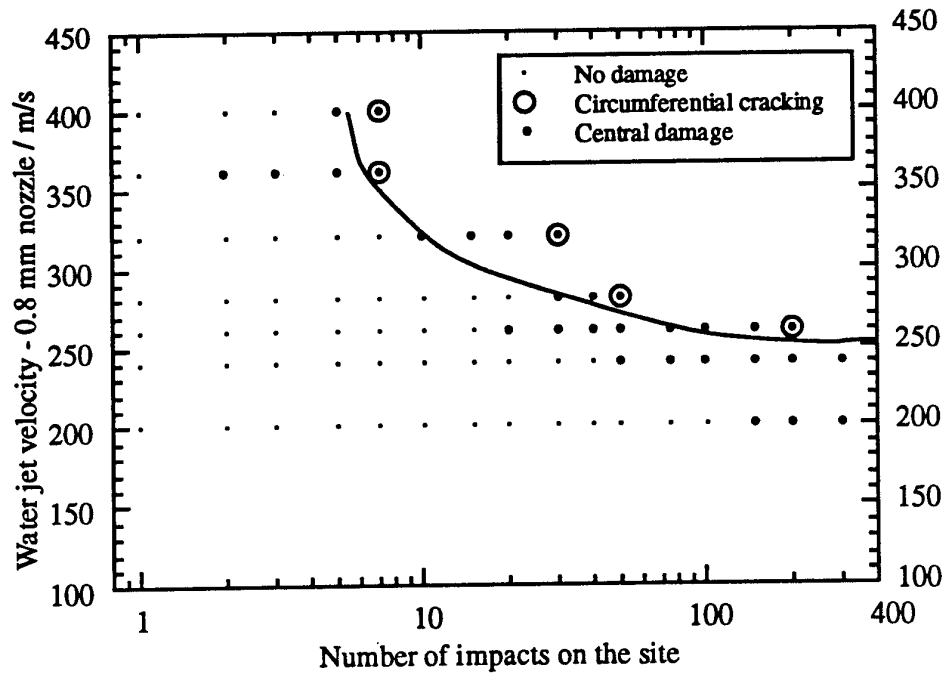


Figure 5.14.12 Threshold curve for the first 16.2 μm BP coating on Ge

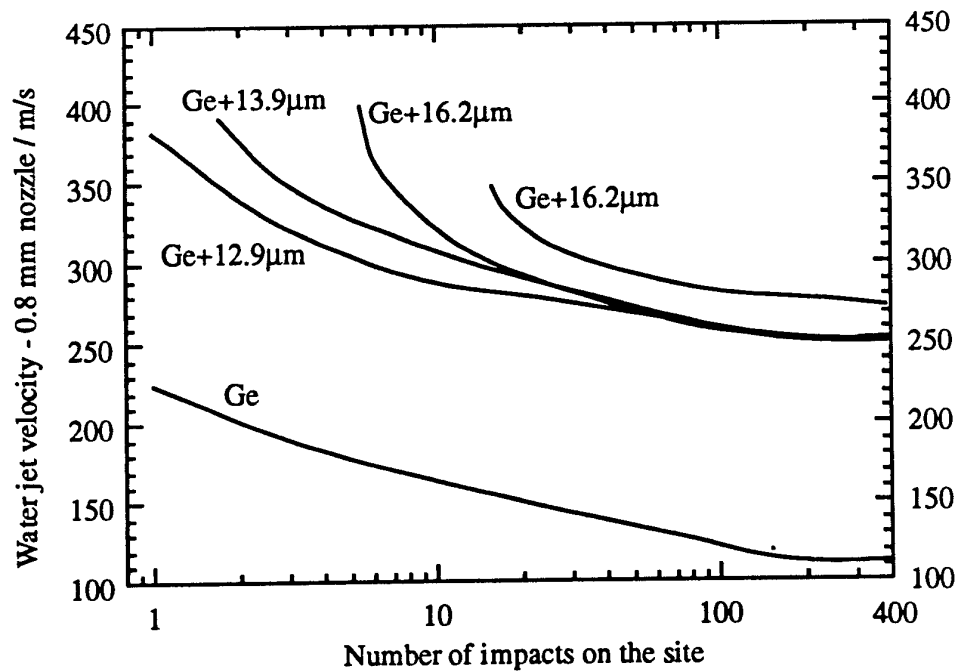


Figure 5.14.14 Comparison of threshold curves for coated and uncoated Ge

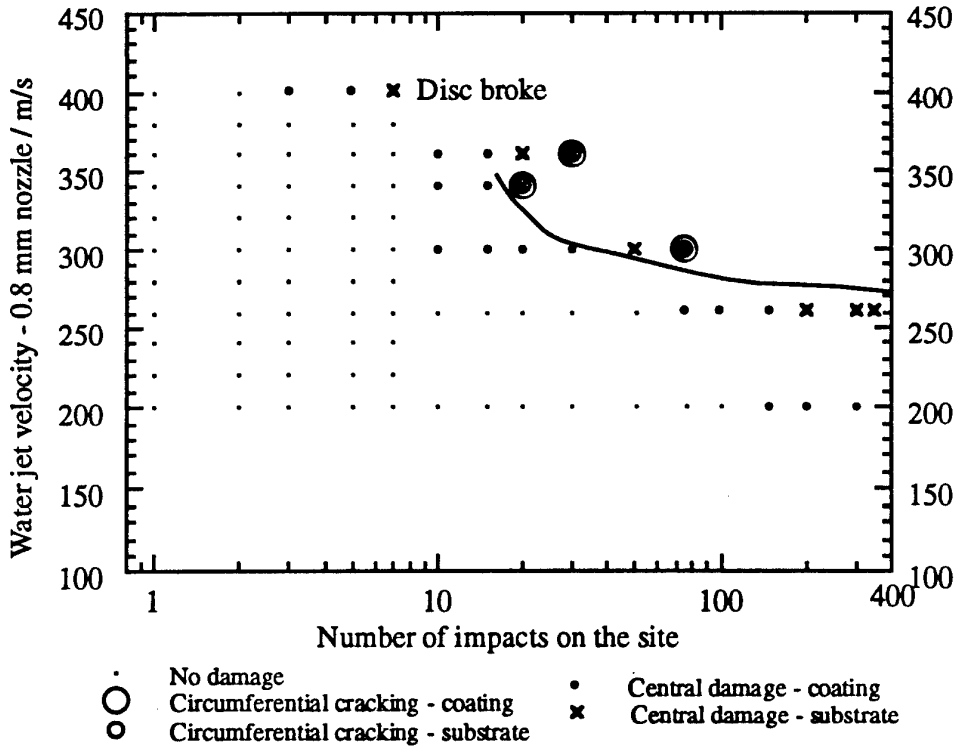


Figure 5.14.13 Threshold curve for the second 16.2 μm BP coating on Ge

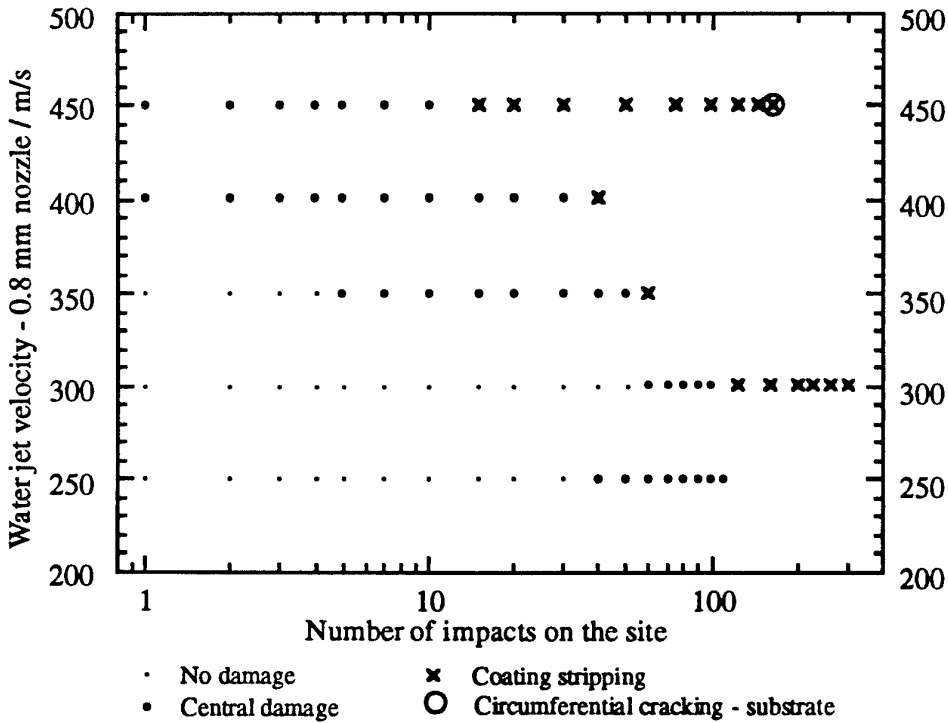


Figure 5.14.15 Damage threshold data for the first BP coated sapphire sample

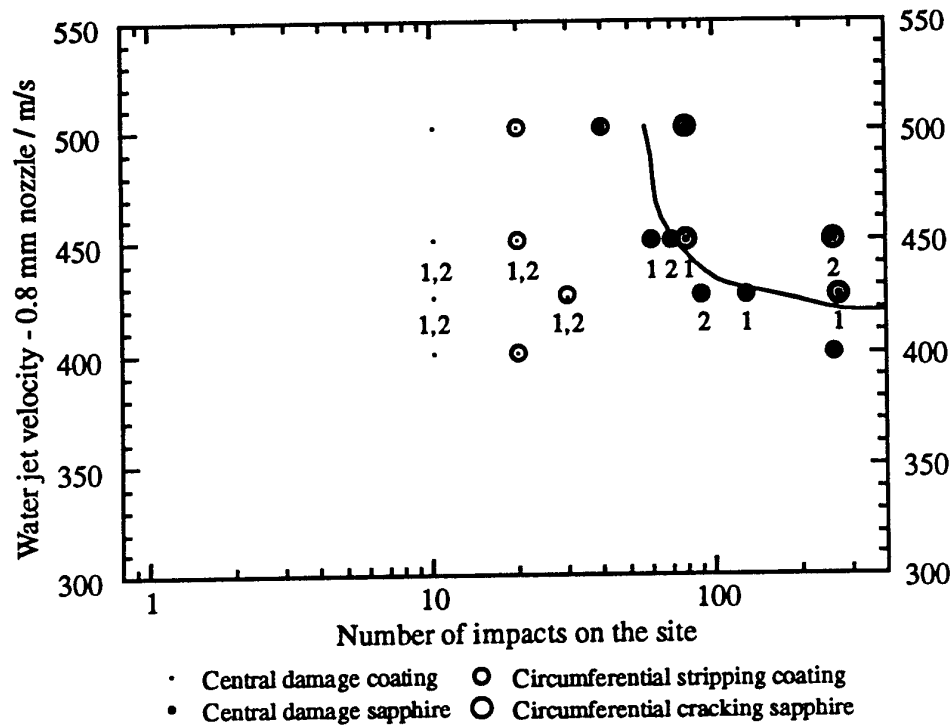


Figure 5.14.16 Threshold curve for second BP coated sapphire substrate. The experiments at 425 and 450 m s⁻¹ were both repeated twice. Both sets of results are shown on the same graph above labelled 1 and 2.

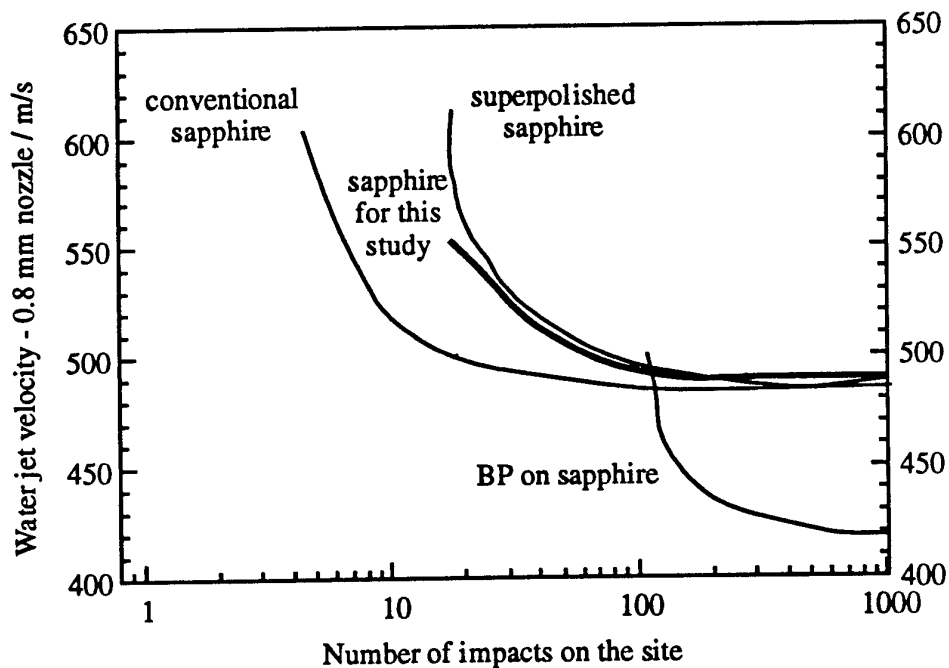


Figure 5.14.17 Comparison of threshold curves for coated and uncoated sapphire samples.

5.15 SOME PARAMETERS INVESTIGATED IN THIS STUDY

1. Repeatability of threshold determination

spinel - used same disc twice, and obtained same value both times.

ZnS - obtained same value from three discs from the same batch.

CaLa₂S₄ - looked at two discs per batch for 3 different batches and got the same values for each batch.

CVD diamond - repeated DTV evaluation on each sample. Same answer obtained each time for good quality CVD specimens

These results demonstrate the excellent repeatability that is possible with this threshold evaluation technique.

2. Correlation with SIJA and bursting disc

MgF₂ - SIJA 0.8 mm jet DTV (mechanical) = $217 \pm 17 \text{ m s}^{-1}$

MIJA 0.8 mm jet DTV (300 impacts) = $245 \pm 5 \text{ m s}^{-1}$

MIJA 0.8 mm jet DTV (central damage - 300 impacts) = ? ($< 200 \text{ m s}^{-1}$)

Fairly good agreement between DTV values, difference may be due to poor quality of samples tested, or due to the occurrence of central damage which can happen after just a few impacts.

spinel - SIJA 0.8 mm jet DTV (mechanical) = $325 \pm 25 \text{ m s}^{-1}$

MIJA 0.8 mm jet DTV (300 impacts) = $355 \pm 5 \text{ m s}^{-1}$

MIJA 0.8 mm jet DTV (central damage - 300 impacts) = ? ($< 250 \text{ m s}^{-1}$)

Once again there is reasonable agreement between the results, the difference is less likely to be due to central damage since this takes a very large number of impacts to develop.

Both materials show a good agreement between the SIJA and MIJA results. The SIJA results would in general be expected to show slightly lower thresholds, because for a 0.8 mm jet on SIJA a velocity of 350 m s^{-1} would have a variation of $\sim 10 \%$, whereas on MIJA it would only be $\sim 1 \%$, so SIJA's highest velocity impacting jet would be faster than MIJA's.

3. Effect of specimen size

sapphire - $\varnothing 25 \text{ mm}$, 3 mm thick, 0.8 mm jet DTV (300 impacts) = $485 \pm 5 \text{ m s}^{-1}$

$\varnothing 6 \text{ mm}$, 1 mm thick 0.8 mm jet DTV (300 impacts) = $430 \pm 10 \text{ m s}^{-1}$

CVD diamond - 0.5 mm thick, 0.8 mm jet DTV (300 impacts) $\sim 325 - 350 \text{ m s}^{-1}$

1 mm thick, 0.8 mm jet DTV (300 impacts) $\sim 425 - 475 \text{ m s}^{-1}$

The effects of stress wave reflections and disc bending should always be taken into account for thin specimens. This is particularly important with samples like diamond which have a high wave speed (section 5.6).

4. Effect of surface finish

sapphire - conventional polish 0.8 mm jet DTV (300 impacts) = $490 \pm 10 \text{ m s}^{-1}$

conventional and super-polished 0.8 mm jet DTV (300 impacts) = $475 \pm 15 \text{ m s}^{-1}$

super-polished, ion implanted, 0.8 mm jet DTV (300 impacts) = $475 \pm 15 \text{ m s}^{-1}$

silicon - a polished disc had a 0.8 mm jet DTV (1 impact) = $410 \pm 10 \text{ m s}^{-1}$, and a 0.8 mm jet DTV (300 impacts) = $215 \pm 5 \text{ m s}^{-1}$

- a scratched disc had a 0.8 mm jet DTV (1 impact) = $290 \pm 10 \text{ m s}^{-1}$, and a 0.8 mm jet DTV (300 impacts) = $195 \pm 5 \text{ m s}^{-1}$.

MgF₂ - both discs had scratches the least scratched had a 0.8 mm jet DTV (300 impacts) = $245 \pm 5 \text{ m s}^{-1}$, the other had a 0.8 mm jet DTV (300 impacts) = $215 \pm 5 \text{ m s}^{-1}$.

5. Effect of a non-round jet damage mark

germanium - using a nozzle creating non-round damage on PMMA gave a 0.8 mm jet DTV (300 impacts) = $155 \pm 5 \text{ m s}^{-1}$
- after repolishing the nozzle a 0.8 mm jet DTV (300 impacts) = $125 \pm 5 \text{ m s}^{-1}$

A non-round jet would be expected to give a higher threshold because the minimum dimension of the compressed region is smaller, so release waves can reach the centre quicker.

6. Effect of a smaller nozzle orifice

ZnS - a 0.6 mm jet DTV (300 impacts) = $135 \pm 5 \text{ m s}^{-1}$
a 0.8 mm jet DTV (300 impacts) = $130 \pm 5 \text{ m s}^{-1}$

The difference in the equivalent drop sizes for a 0.8 and 0.6 mm nozzle is small and this is reflected in a small difference between the threshold values. Of more interest would be the threshold value for a 1.6 mm nozzle, however dripping may be a problem with the vertical loading on MJA.

7. Difference in threshold due to damage assessment from front and rear

ZnS - the difference is only small near the 0.8 mm jet DTV (300 impacts) (~ 2 %) but much larger near the 0.8 mm jet DTV (1 impact) (~ 30 %).

8. Effect of a coating

The effect of a coating is complicated and dependent on thickness, bonding, internal stress and the mechanical properties of the coating and substrate. No firm conclusions on the effects of all these parameters have yet been drawn.

9. Effect of a making a composite

Only one composite mixture has been investigated; ZnS mixed with diamond particles. The threshold for small numbers of impacts was higher than for ZnS, and the ZnS-30D 0.8 mm jet DTV (300 impacts) gave a 63 % improvement over ordinary ZnS. However their surface texture can make them more prone to sub-threshold damage after long exposures.

10. Determination of the existence of an absolute threshold for damage

The existence of an absolute threshold value on MJA will be difficult to determine because of the spread in velocities of 1 %. It will similarly be difficult to prove on a whirling arm rig because of the spread in drop diameters.

11. Both polycrystalline and single crystal materials have been tested.

Cracking in the single crystal materials (silicon, germanium, sapphire, natural diamond) often exhibits preference for cleavage planes, while on polycrystalline materials (ZnS, CaLa_2S_4 , MgF_2 , spinel) both transgranular and intergranular cracking have been seen.

REFERENCES

- Adler W.F. "Investigation of liquid drop impacts on ceramics", CR-82-1075, Office of Naval Research, Contract N00014-76-C-0744 NR032-565
- Adler W.F. and Hooker S.V. "Water drop impact damage in zinc sulphide", *Wear* Vol.48, pp.103-119, (1978)
- Adler W.F., Botke J.C. and James T.W. "Response of infrared-transparent materials to raindrop impacts", AFML-TR-79-4151, Oct. (1979)
- Adler W.F. "Development of design data for rain impact damage in infrared-transmitting materials", SPIE Vol.297, *Emerging Optical Materials*, pp.143-154, (1981)
- Adler W.F. "Development of design data for rain impact damage in infrared-transmitting windows and radomes", *Opt. Eng.*, Vol.26, No.2, pp.143-151, Feb. (1987)
- Adler W.F. "Rain erosion testing", SPIE Vol.1112, *Window and Dome Technologies and Materials*, pp.275-294, (1989)
- Angus J.C. and Hayman C.C. *Science*, Vol.241, pp.913, (1988)
- Anthony F.M. and Hopkins A.K. "Actively cooled silicon mirrors", SPIE Vol.297, *Emerging Optical Materials*, pp.196-203, (1981)
- Becher P.R. "Press-forged Al_2O_3 - rich spinel crystals for IR applications", *Am. Ceram. Soc. Bull.*, Vol.56, pp.1015-1017, (1977)
- Behrendt A. "Investigation of parameters of aircraft materials in the velocity range up to $1000 m s^{-1}$ ", Proc. of the Fourth Int. Conf. on Rain Erosion and Ass. Phen., (ed. A.A. Fyall and R.B. King, Royal Aircraft Establishment, England), pp.425-448, (1974)
- Berges P., Droguet J.C. and Froissart P. "Realization and characterization of spinel", Report to AC/243 (Panel III, RSG2) on the Third Workshop on Passive Infrared Optical Materials and Coatings, NATO Headquarters, Brussels, Belgium, March (1990)
- Beswick J.A., Pedder D.J., Lewis J.C. and Ainger F.W. "New infra-red window materials", SPIE Vol.400, *New Optical Materials*, pp.12-20, April (1983)
- Blair P.W. "The liquid impact behaviour of composites and some infrared transparent materials", PhD, Cavendish Labs., University of Cambridge, (1981)
- Brierley C.J. and Wilson A.E.J. "The development of calcium lanthanum sulphide windows", Report to AC/243 (Panel III, RSG2) on the Third Workshop on Passive Infrared Optical Materials and Coatings, NATO Headquarters, Brussels, Belgium, March (1990)
- Buckner D.A., Hafner H.C. and Kreidl N.J. "Hot-pressing magnesium fluoride", *J. of the Am. Ceram. Soc.*, Vol.45, No.9, pp.435-438, (1962)
- Camus J.J. "High-speed flow in impact and its effect on solid surfaces", PhD. Cavendish Labs., University of Cambridge, (1971)
- Cassaing J.J., Deom A.A., Bouveret A.M. and Balageas D.L. "IR materials and rain damage prediction and tests results", SPIE Vol.1112 *Window and Dome Technologies and Materials*, pp.295-305, (1989)
- Chu T.L., Jackson J.M., Hyslop A.E. and Chu S.C., *J. Appl. Phys.*, Vol.42, pp.420, (1971)
- Cockayne B. and Chesswas M., *J. Mater. Sci.*, Vol.2, pp.498-500, (1967)
- Collins C.B., Davanloo F., Jander D.R., Lee T.J., You J.H. and Park H. "Microstructural and mechanical properties of amorphous diamond", *Diamond Films and Tech.*, Vol.2, No.1, pp.25-48, (1992)
- Corney N.S. and Pippett J.S. "The rain erosion resistance of some radome and irdome materials", Proc. of Sixth Int. Conf. Erosion by Liquid and Solid Impact, paper 24, (1983)

- Davanloo F., Juengerman E.M., Jander D.R., Lee T.J. and Collins C.B. "Amorphous diamond films produced by a laser plasma source", *Jnl. Appl. Phys.*, Vol.67, No.4, pp.2081-2087, 15th Feb. (1990)
- Davanloo F., Lee T.J., Jander D.R., Park H., You J.H. and Collins C.B. "Adhesion and mechanical properties of amorphous diamond films prepared by a laser plasma discharge source", *Jnl. Appl. Phys.*, Vol.71, No.3, pp.1446-1453, (1992)
- Deom A., Balageas D. and Gardette G. "Rain erosion resistance characterisation of pure and reinforced slip-cast fused silica by laser simulation", *Proc. of the Seventh Int. Conf. on Erosion by Liquid and Solid Impact*, Paper 8, (1987)
- Deom A.A., Balageas D.L., Laturrelle F.G., Gardette G.D. and Freydefont G.J. "Sensitivity of rain erosion resistance of infrared materials to environmental conditions such as temperature and stress", *SPIE Vol.1326 Window and Dome Technologies and Materials II*, pp.301-309, (1990)
- Donadio R.N., Connolly J.F. and Taylor R.L. "New advances in chemical deposited (CVD) infrared transmitting materials", *SPIE Vol.297 Emerging Optical Materials*, pp.65-69, (1981)
- Eskilsson S. "Rain drop impact damage dependent on material stress", *Proc. of the Fourth Int. Conf. on Rain Erosion and Ass. Phen.*, (ed. A.A. Fyall and R.B. King), pp.449-453, (1974)
- Evans A.G., Ito Y.M. and Rosenblatt M. "Impact damage thresholds in brittle materials impacted by water drops", *J. Appl. Phys.*, Vol.51, No.5, pp.2473-2482, May (1980)
- Farquhar D.S., Raj R. and Phoenix S.L. "Fracture and stiffness characteristics of particulate composites of diamond in zinc sulfide", *Jnl. Am. Ceram.*, Vol.73, No.10, pp.3074-3080, (1990)
- Field J.E., Van der Zwaag S. and Hagan J.T. "Liquid impact erosion mechanisms in transparent materials", *AFWAL-TR-81-4026*, May (1981)
- Field J.E., Van der Zwaag S. and Townsend D. "Liquid jet impact damage assessment for a range of infra-red materials", *Proc. 6th Int. Conf. on Erosion by Liquid and Solid Impact*, Paper 21, (1983)
- Field J.E., Hand R.J., Pickles C.J. and Seward C.R. "Rain erosion studies of I.R. Materials", *SPIE Proc. Vol.1191, Design and Evaluation of Optical Systems*, (1989)
- Field J.E., Nicholson E., Seward C.R. and Feng Z. "Strength, fracture and erosion properties of CVD Diamond", *Phil. Trans. Roy. Soc. Lond. A*, Vol.342, pp.261-275, (1993)
- Fischer J.W., Compton W.R., Jaegar N.A. and Harris D.C. "Strength of sapphire as a function of temperature and crystal orientation", *Window and Dome Technologies and Materials II*, ed. P. Klocek, *SPIE Vol.1326*, Paper 02, (1990)
- Geis M.W., Smith H.I., Argoit A., Ma G.H.M., Glass J.T., Butler J., Robinson C.J. and Pryor R. *Appl. Phys. Lett.*, Vol.58, pp.2485-2487, (1991)
- Gentilman R., *Ceram. Bull.*, Vol.60, pp.906-908 (1981)
- Gentilman R.L. "Current and emerging materials for 3-5 micron transmission", *SPIE Vol.683, Infrared and Optical Transmitting Materials*, pp.2-11, (1986)
- Gentilman R.L., Maguire E.A., Kohane T. and Valentine D.B. "Comparison of large ALON and sapphire windows", *Window and Dome Technologies and Materials*, ed. P. Klocek, *SPIE Vol.1112*, Paper 05, (1989)
- Gibson D.R., Waddell E.M., Kerr J.W. and Wilson A.D. "Ultradurable phosphide-based antireflection coatings for sand and rain erosion protection", *Window and Dome Technologies and Materials III*, ed. P. Klocek, *SPIE Vol.1760*, Paper 21, pp. 178-200, (1992)

- Gibson D.R., Waddell E.M., Wilson A.D. and Lewis K.L.** "Ultradurable phosphide-based antireflection coatings for sand and rain erosion protection of current IR materials", Report to AC/243 (Panel III, RSG2) on the Fourth Workshop on Passive Infrared Optical Materials and Coatings, DRA Malvern, June (1993)
- Glesener J.W., Morrish A.A. and Snail K.A.** Applications of Diamond Films and Related Materials, pp.347-351, (1991)
- Hackworth J.V.** "A mechanistic investigation of the rain erosion of infrared transmitting materials at velocities to Mach 2", Proc. 5th Int. Conf. on Erosion by Solid and Liquid Impact, Paper 10, (1979)
- Hackworth J.V.** "Damage of infrared-transparent materials exposed to rain environments at high velocities", SPIE Vol. 362, pp.123-136 (1982)
- Hancox N.L.** "The deformation of solids under repeated liquid impact", PhD Cavendish Labs., University of Cambridge, (1962)
- Hand R.J., Field J.E. and Van der Zwaag S.** "High modulus layers as protective coatings for window materials", SPIE Vol.1112, Window and Dome Technologies and Materials, pp.120-129, (1989)
- Harker A.B. and DeNatale J.F.** "Pressure effects in the microwave plasma growth of polycrystalline diamond", SPIE Vol.1534, Diamond Optics IV, pp.2-8, (1991)
- Hasselmann D.P.H.** "Thermal stress resistance parameters for brittle refractory ceramics: A compendium", Bull. of the Am. Ceram. Soc., Vol.49, No.12, pp.1033-1037, Dec. (1970)
- Hirose Y. and Kondo N.** Program and Book of Abstracts, Japan Appl. Phys. (1988)
- Hooker S.V.** "Initiation of rainfield erosion in germanium at subsonic velocities", Wear, Vol.43, pp.253-257, (1977)
- Kamo M., Sato Y., Matsumoto S. and Setaka N.** J. Cryst. Growth, Vol.62, pp.642-644, (1983)
- Kelly C.J., Orr J.S., Gordon H. and Traub L.T.** "Application of germanium carbide in durable multilayer IR coatings", Report to AC/243 (Panel III, RSG2) on the Third Workshop on Passive Infrared Optical Materials and Coatings, NATO Headquarters, Brussels, Belgium, March (1990)
- Khattak C.P. and Schmid F.** "Production of near-net-shaped sapphire domes using the heat exchange method (HEM)", SPIE Vol. 1760, Window and Dome Technologies and Materials III, pp.41-46, (1992)
- Klocek P.** "Handbook of infrared optical materials", Marcel Dekker Inc., ISBN 0-8247-8468-5, ed. P. Klocek, (1991)
- LaBelle H.E.** "EFG the invention and application to sapphire growth", Jnl. of Crystal Growth, Vol.50, pp.8-17, Sept. (1980)
- Lesser M.B.** "Analytic solutions of liquid-drop impact problems", Proc. Roy. Soc. Lond. Ser. A., Vol.377, pp.289-308, (1981)
- Lettington A.H., Wort C.J.H. and Monahan B.C.** "Developments and IR applications of GeC thin films", SPIE Vol.1112, Window and Dome Technologies and Materials, pp.156-161, (1989)
- Lewis K.L., Savage J.A., Pitt A.M., Adams K., Orr J.S. and Weir I.** "Toughening effects induced in zinc sulphide by hot isostatic pressing", SPIE Vol.683, Infrared and Optical Transmitting Materials, pp.64-71, (1986)
- Lewis K.L., Kelly C.J. and Monahan B.C.** "Recent progress in the development of boron phosphide as a robust coating material for infrared transparencies", SPIE Vol. 1112, Window and Dome Technologies and Materials, pp.407-416, (1989)
- Locher J.W., Bennett H.E., Archibald P.C. and Newmyer C.T.** "Large diameter sapphire dome: fabrication and characterization", Window and Dome Technologies and Materials II, ed. P. Klocek, SPIE Vol.1326, Paper 01, (1990)

- Locher J.W., Bates H.E., Pazol B.G. and Defranza A.C. "Optimisation of sapphire processing parameters leads to high-quality low-cost single crystal sapphire domes", SPIE Proc. Vol.1760, Window and Dome Tech. and Materials III, pp.48-54, (1992)
- Mackowski J.M., Cimma B. and Pignard R. "Rain erosion behaviour of germanium carbide (GeC) films grown on ZnS substrates", SPIE Vol.1760 Window and Dome Technologies and Materials III, pp.201-209, July (1992)
- Martin P.M. and Johnston J.W. "Erosion-resistant coatings for optical infrared windows", Report to AC/243 (Panel III, RSG2) on the Third Workshop on Passive Infrared Optical Materials and Coatings, NATO Headquarters, Brussels, Belgium, March (1990a)
- Martin P.M., Johnston J.W. and Bennett W.D. SPIE Vol.1323, Optical Thin Film III: New Developments, pp.291-298, (1990b)
- Matsumoto S., Sato Y., Kamo M. and Setaka N. Jpn. J. Appl. Phys., Vol.21, L183, (1982)
- Matsumoto S. Symp. Proc. 7th Int. Symp. Plasma Chem., pp.79-84, (1985)
- Matsumoto S., Hino M. and Kobayashi T. Appl. Phys. Lett., Vol.51, pp.737-739, (1987)
- McHargue C.J. and Snyder W.B. "Surface modification of sapphire for IR window application", SPIE, (~1992)
- Monachan B.C., Kelly C.J. and Waddell E.M. "Ultra-hard coatings for IR materials" SPIE Vol.1112, Window and Dome Technologies and Materials, pp.129-143, (1989)
- Monachan B.C. "Coatings for the protection of IR optical materials from the effects of rain erosion", Report to AC/243 (Panel III, RSG2) on the Third Workshop on Passive Infrared Optical Materials and Coatings, NATO Headquarters, Brussels, Belgium, March (1990)
- Nichols B.A., Shipley S.P., Greenham A.C., Allen J.J. and Nourshargh N. "Microwave plasma deposition of nitride coatings", Report to AC/243 (Panel III, RSG2) on the Fourth Workshop on Passive Infrared Optical Materials and Coatings, DRA Malvern, June (1993)
- Nicholson E.D. "Measurement of thermal and mechanical properties of thin layer protective coatings for IR Materials", PhD Cavendish Labs, Univeristy of Cambridge, (1993)
- Pappis J. "Issues in commercialisation and production of ZnS and ZnSe", Report to AC/243 (Panel III, RSG2) on the Third Workshop on Passive Infrared Optical Materials and Coatings, NATO Headquarters, Brussels, Belgium, March (1990)
- Pazol B.G., De Vito R., Giguere P.J. and Kiefner P.S. "Development of sapphire windows for use in high-quality IR imaging systems", SPIE Proc. Vol.1760, Window and Dome Tech. and Materials III, pp.55-65, (1992)
- Pickles C.S.J. "Infrared transmitting materials in the high velocity environment", PhD Cavendish Labs., University of Cambridge, (1991)
- Pickles C.S.J., Seward C.R. and Field J.E. "Assessment of aerospace materials to impact; the rain erosion and thermal shock resistance of magnesium fluoride and spinel", Interim Report, Agreement 2029/259, Cavendish Labs., Cambridge (1992)
- Potts D.L. "Rain erosion test of proposed sample materials; preliminary report", NWC, China Lake, CA., (1972)
- Poznich C.R. and Richter J.C. "Silicon for use as a transmissive material in the far IR", SPIE Vol.1760, Window and Dome Technologies and Materials III, (1992)
- Roy D.W. "Hot-pressed MgAl₂O₄ for ultraviolet (UV), visible, and infrared (IR) optical requirements", SPIE Proc. Vol.297, Emerging Optical Materials, Paper 2, pp.13-19, (1981a)

- Roy D.W. "Progress in the development of ternary sulfides for use from 8 to 14 μm ", SPIE Vol.297, Emerging Optical Materials, pp.24-34, (1981b)
- Roy D.W. and Green K.E. "Polycrystalline MgAl_2O_4 Spinel, a broad band optical material for offensive environments", Alpha Optical Systems Report, (1989)
- Saunders K.J., Wong T.Y., Hartnett T.M., Tustison R.W. and Gentilman R.L. "Current and future development of Calcium Lanthanum Sulphide", SPIE Vol.683, Infrared and Optical Transmitting Materials, pp.72-78, (1986)
- Savage J.A. "Infrared optical materials and their antireflection coatings", Adam Hilger Ltd., ISBN 0-85274-790-X, (1985)
- Savage J.A. and Lewis K.L. "Fabrication of infrared optical ceramics in the CaLa_2S_4 - La_2S_3 solid solution systems", SPIE Vol.683 Infrared and Optical Transmitting Materials, pp.79-84, (1986)
- Savage J.A. and Edwards M.J. "Optical, mechanical and thermal properties of calcium lanthanum sulphide compared with the properties of current 8 - 12 μm materials", SPIE Vol.968, Ceramics and Inorganic Crystals for Optics, Electro-optics, and Non-linear Conversion, pp.19-24, (1988)
- Schmid F. and Viechnicki D. Jnl. Am. Ceram. Soc., Vol.53, pp.528, (1970)
- Schmid F. and Khatak C.P. "Current status of sapphire technology for window and dome applications", Window and Dome Technologies and Materials, ed. P. Klocek, SPIE Vol.1112, Paper 04, (1989)
- Schwartz R.W. "Rain erosion tests on candidate dome materials", NWC, China Lake, CA., (1989)
- Schwartz R.W. "U.S. Navy LWIR Materials Research Program", Report to AC/243 (Panel III, RSG2) on the Third Workshop on Passive Infrared Optical Materials and Coatings, NATO Headquarters, Brussels, Belgium, March (1990)
- Seward C.R., Pickles C.S.J., Marrah R. and Field J.E. "Rain erosion data on window and dome materials", Presented at SPIE's 1992 Tech. Symp. "Window and Dome Technologies and Materials III", July 22-23, San Diego, (1992a)
- Seward C.R., Watt M.J. and Field J.E. "Rain erosion results on infrared window materials", Annual Report to the U.S., (1992b)
- Seward C.R., Pickles C.S.J., Watt M. and Field J.E. "The erosion properties of natural and synthetic diamond", Proc. 2nd Int. Conf. on Applications of Diamond Films and Related Materials, August 25-27, Tokyo, Japan, (1993a)
- Seward C.R., Pickles C.S.J. and Field J.E. "The response of diamond films to liquid and solid impact", Proc. of the 4th European Conf. on Diamond, Diamond-like and Related Materials, Sept. 20-24, Algarve, Portugal, (1993b)
- Seward C.R., Watt M.J. and Field J.E. "Rain erosion test results on sapphire and CVD diamond", Report for U.S. / U.K. Joint Optical Materials Program, Contract Number 2029 / 262 / DCVD, May (1993c)
- Seward C.R., Coad E.J. and Field J.E. "The rain erosion resistance of CVD diamond", Report for Contract Number 2029 / 262 / DCVD, October (1993d)
- Seward C.R., Watt M.J. and Field J.E. "The rain erosion resistance of SiN Coatings on BK7", Report for GEC Marconi, February (1993e)
- Seward C.R., Pickles C.S.J., Field J.E. and Feng Z. "Liquid and solid erosion properties of diamond", Diamond and Related Materials, Vol.2, pp.606-611, (1993f)
- Springer G.S. "Erosion by Liquid Impact", Scripta Technica Inc., ISBN 0-470-15108-0, (1976)
- Steinheil E.R. and Schmidberger R. "Liquid impact erosion of structural and window materials in the velocity range up to 1000 m s^{-1} ", Proc. of the Fifth Int. Conf. on Erosion by Liquid and Solid Impact, (ed. D. Tabor), Paper 11, (1979)
- Stewart R.L. and Bradt R.C. "Fracture of polycrystalline MgAl_2O_4 ", Jnl. of the Am. Ceram. Soc., Vol. 63, No.11-12, pp.619-623, (1980)

- Stewart R.L., Iwasa M. and Bradt R.C. "Room-temperature K_{Ic} values for single-crystal and polycrystalline $MgAl_2O_4$ ", J. Am. Ceram. Soc., Vol.64, C22-3, (1981)
- Stockbarger D.C. Rev. Sci. Instrum., Vol.79, pp.133, (1936)
- Sun Q. "Solid particle erosion and ballistic impact", PhD, Cavendish Labs., University of Cambridge (1991)
- Sun Q. and Field J.E. "Spherical projectile impact on aluminas", 2nd Int. Symp. on Intense Dynamic Loading and its Effects, (1992)
- Suzuki K., Yasuda J. and Inuzuka T. Appl. Phys. Lett., Vol.50, pp.728-729, (1987)
- Tattershall P. and Minter E.M. "The multiple drop rain erosion of germanium carbide coated zinc sulphide", Erosion Report No. 72, Royal Aerospace Establishment, Farnborough, June (1990)
- Townsend D. "Liquid impact properties of brittle materials", PhD, Cavendish Labs., University of Cambridge, (1985)
- Tustison R.W. and Gentilman R.L. "Current and emerging materials for LWIR external windows", SPIE Vol.968, Ceramics and Inorganic Crystals for Optics, Electro-Optics, and Nonlinear Conversion, pp.25-34, (1988)
- Van der Zwaag S. and Field J.E. "Liquid jet impact damage on zinc sulphide", J. Mater. Sci., Vol.17, pp.2625-2636, (1982)
- Van der Zwaag S. and Field J.E. "Indentation and liquid impact studies on coated germanium", Phil. Mag. A, Vol.48, No.5, pp.767-777, (1983)
- Van Goetham L., Van Maele. L.Ph. and Van Sande M. "Trade-offs using poly versus monocrystalline germanium for infrared optics", SPIE Vol.683 Infrared and Optical Transmitting Materials, pp.160-165, (1986)
- Waddell E.M. and Monahan B.C. "Rain erosion protection of IR materials using boron phosphide coatings", SPIE Vol.1326, Window and Dome Technologies and Materials II, pp.144-156, (1990)
- Wickersheim K.A. and Lefever R.A., J. Opt. Soc. Am., Vol.50, pp.831-832, (1960)
- Wilks J.G. Proc. IEE, B106 Sup. 17, pp.866-870, (1959)
- Willingham C.B. and Pappis J. UK Patent Application GB 2090237A Raytheon Co. USA, (1982)
- Wilson M. "Characterisation of hard carbon coated and uncoated Ge", Report to AC/243 (Panel III, RSG2) on the Third Workshop on Passive Infrared Optical Materials and Coatings, NATO Headquarters, Brussels, Belgium, March (1990)
- Wilson M. "F-14 dome coatings program overview", Fourth Workshop on passive IR optical materials and coatings, Report to AC/243 (Panel 111, RSG 2), DRA Malvern, 8-10 June 1993
- Xue L.A., Farquhar D.S., Noh T.W., Sievers A.J. and Raj R. "Optical and mechanical properties of zinc sulphide composites", Acta metall. mater., Vol.38, No.9, pp1743-1752, (1990)

Chapter 6

Summary

6.1 RAIN EROSION

As outlined in chapter 1 high velocity flight through rain poses a number of design problems to the radome engineer. The radome is often the foremost component of the aircraft or missile, and for many applications is made of brittle infra-red transmitting ceramics that can become damaged as a result of impact with rain drops at the operational velocities required. Greater protection to the materials can be offered by placing them at an angle to the direction of travel, for example as a flat window on the side of the missile. However this may reduce the missiles operational performance, therefore it is normally necessary for the materials to be able to survive the worst case scenario i.e. normal impact.

There are two performance regimes of particular interest for the radome. Firstly low velocity flight with long exposures to rain similar to those experienced during missile carriage, and secondly high velocity flight with short exposures to rain similar to those that might be experienced following missile launch. The two main problems with the cracking induced by rain on the radome during these regimes are:

1. degradation of the target signal by transmission loss and scattering - this may lead to failure of a missile to identify and track its target.
2. reduction in the radome strength possibly leading to catastrophic failure - this may again lead to failure of the missile to track its target, however in the worst case fragments of the broken radome may be sucked into the jet engines of the plane and cause engine failure seriously effecting the flight safety of the plane itself.

In order to improve the radomes erosion resistance research is needed to select suitable candidate materials, understand the mechanics of the impact and the damage mechanisms of the materials, characterise the material performance and optimise its manufacture. In order to do this the rain environment must be well understood and a suitable simulation technique must be developed.

6.2 THE RAIN ENVIRONMENT

The second section of this report investigated the drop shapes and sizes likely to be encountered by a vehicle flying through rain. The section briefly reviewed three main areas:

1. The drop size distribution - this depends on the season, rain intensity, location and type of cloud.
2. The drop shapes - these are controlled by surface tension, internal hydrostatic pressure, aerodynamic pressure, internal circulation, electric stress, oscillation caused by collision and coalescence, and canting caused by wind shear etc.
3. The drop distortion or breakup due to the approach of the radome - this looked at various different modes of drop breakup due to interaction with a drop, and some calculations attempted to investigate the distortions produced.

With regards to high velocity flight through rain each ceramic material used for the radome has its own threshold velocity above which damage will result from the impact with raindrops. The velocity and number of impacts required to exceed this

damage threshold however depends on the drop diameter, and larger drops may initiate damage at lower velocities than smaller drops. Once damage has initiated propagation of the cracking may occur by impacts below the threshold velocity.

The main conclusions that can be drawn from this review

1. The extent of drop distortions observed in natural rain mean that while the impact with a sphere may be easier to analyse theoretically, the drops actually likely to be encountered are often not spherical.
2. Since it is the radius of curvature of the impacting drop that determines the magnitude and duration of the stress waves that the radome is subjected to, a small distorted drop can potentially cause as much damage as a large spherical one. Because the number of drops of different diameters increases exponentially with decreasing drop diameter it is possible that such distorted drops have a larger role than has previously been recognised.

6.3 SIMULATION OF THE RAIN ENVIRONMENT

Section three of this report reviewed seventeen different rain erosion simulation techniques and outlined some of their advantages and disadvantages. The radome development programme may broadly be broken down into three stages as described in section 3. The first stage is to identify and develop candidate materials, the second to extend the evaluation programme and assess suitability for the proposed application, and the third to evaluate the complete radome. The test requirements for each stage vary. The water jet technique is currently of most use in stage 1; the study of available materials. This stage can be described as follows:

Objectives:

- identification of suitable candidate materials for further development
- investigation into the damage mechanisms important for that material
- characterisation of strength loss and transmission loss with exposure
- optimisation of the material manufacture and surface treatment

Test Requirement:

In order to compare material performance a well controlled, reproducible test is essential. It is not necessary to use a spherical drop except for convenience with linking with theoretical calculations or computer modelling, since as stated already drops in natural rain are often distorted.

Some useful tests:

- Water jet (e.g. SIJA and MIJA) - this has the advantage of being a cheap, quick test that can be performed in any lab and produces results which should be easy to compare. The test is reproducible however the front surface is not spherical being slightly flattened by its passage through the air.
- Whirling arm - this is a more expensive test but it can provide a large number of impacts over relatively big areas in a short space of time. It allows transmission, scatter and mass loss to be measured with exposure time. The impacting drops are not always spheres and the level of distortion may vary from rig to rig, therefore comparison of results between tests and materials has to be carried out with care.
- Suspended drop - Although expensive and slow this test does provide valuable information on the impact with spherical drops.
- Nylon beads - this test technique has been investigated by a number of labs, however while superficially attractive care must still be exercised in its range of application. It has been reported that it is a closer simulation to rain impact

at higher velocities, however it is not known about the accuracy with which it will simulate the stripping seen on many coated substrates.

6.4 THE DAMAGE THRESHOLD VELOCITY (DTV)

In section 4 of this report the theory behind the formation of damage as a result of a high velocity impact with a rain drop is reviewed, and several methods for determining the damage threshold velocity (DTV) are then discussed. The damage threshold velocity of a material can be defined as the minimum impact velocity required for a 0.8 mm jet to extend existing microflaws in the material. There are two main ways to evaluate this threshold with a water jet.

1. Examination of the impact sites under a microscope for visible damage.
2. Measurement of the residual strength of a sample by breaking it in a hydraulic pressure tester after it has been impacted 10 times at a given velocity to look for a reduction in strength.

Method 1 relies on the fact that if the jet impact velocity is above the damage threshold then each successive impact will extend the flaws further and eventually any cracks that are growing should become visible. Method 2 however is probably the more sensitive method since strength loss will soon accompany the extension of flaws, however it is less popular than method 1 because it is slower and requires a larger number of samples. Both techniques should produce the same threshold value providing sufficient impacts are applied to the damage site used for visual damage assessment. However the number of impacts required to achieve this is impractical with SIJA, and care therefore needs to be taken in comparing DTV values in the literature. To illustrate this problem the % difference between the DTV values determined on MIJA after 300 impacts and the DTV values determined on SIJA or MIJA after 1, 3, 10, 30 and 100 impacts is shown in figure 6.4.1.

A further aspect over which care needs to be exercised is the definition of what actually constitutes damage during a visual threshold determination. The discovery of central damage in addition to circumferential cracking on a number of materials has in particular highlighted this area, and further research is urgently needed. The main concern with central damage is that it can occur at velocities that would be considered as sub-threshold for circumferential cracking, and it is not yet clear whether it actually has a threshold velocity at all. For the time being the threshold velocity for damage as determined by method 1 (visual inspection) therefore only refers to the onset of circumferential cracking, and reference to any alternative damage mechanisms are stated clearly.

The consequences of the above complications are that there may appear to be a difference between DTV (mechanical) and DTV (visual) for some materials. However this difference may actually only be in damage assessment, since central damage may cause strength loss but not be considered in the DTV (visual). The justification for this is that central damage may be premature on some materials because in the testing on MIJA and SIJA the impacts are all on one site, whereas in reality they are randomly positioned. This is probably a fair comment for materials such as spinel and sapphire where it often takes several hundred impacts for central damage to appear, however in materials such as calcium lanthanum sulphide, magnesium fluoride and most recently CVD diamond its appearance after just one impact is clearly of much greater cause for concern. Great care is clearly needed in defining what we mean by a threshold velocity for damage. In order to help clarify this a new standard has been introduced for this report which describes exactly how

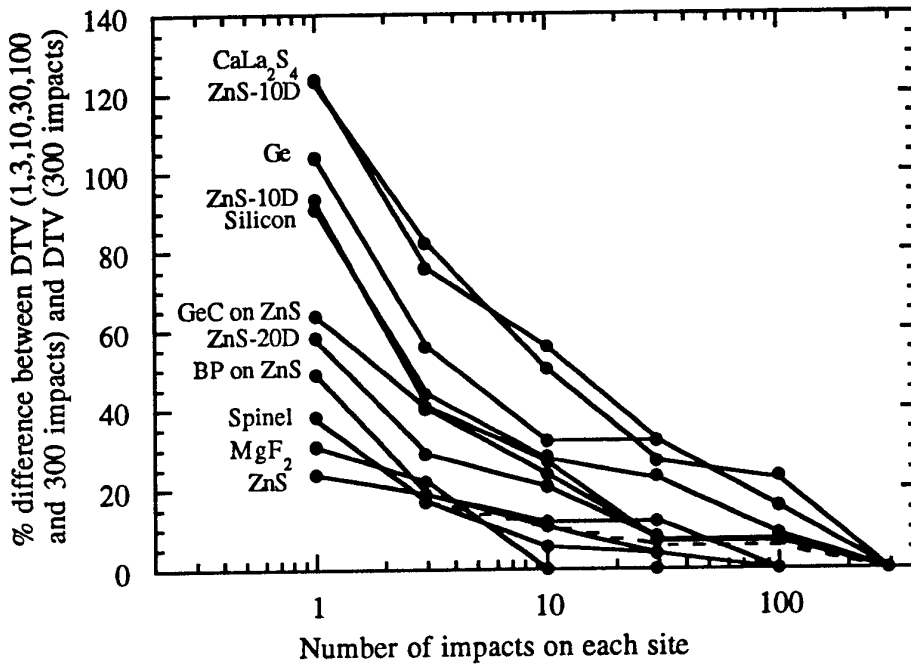


Figure 6.4.1 The % difference between the DTV values determined on MIJA after 300 impacts and the DTV values determined after 1, 3, 10, 30, or 100 impacts.

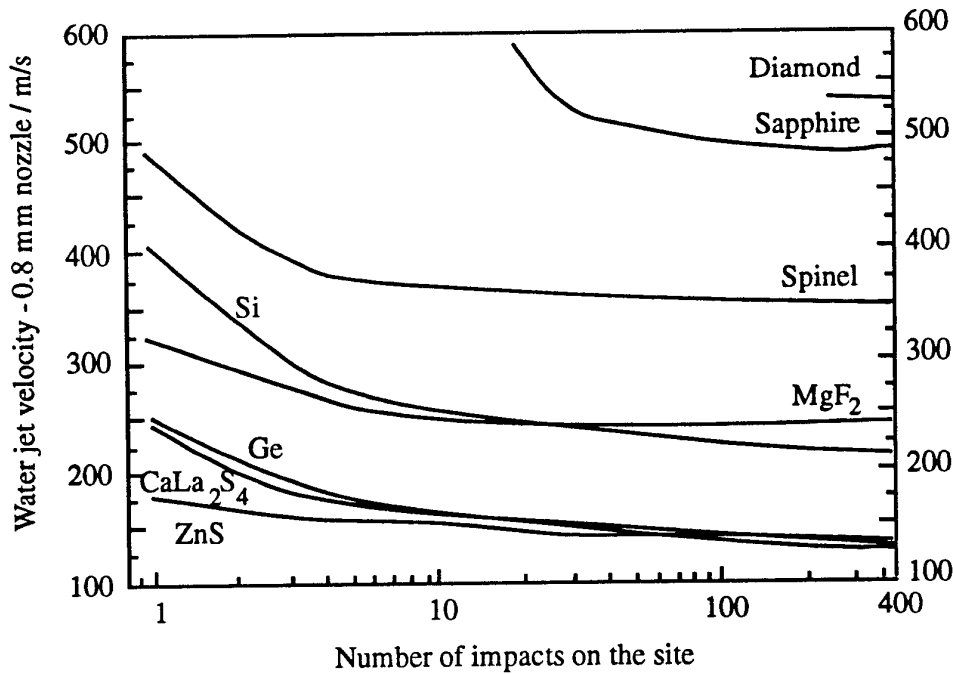


Figure 6.5.1 Summary chart of the threshold velocity curves for the uncoated substrates.

the DTV is defined, and how it should be quoted when written in a paper. This standard is set out on page 1 of this report and will shortly be circulated to all other SIJA users worldwide. This is a first attempt at such a standard and as such it may require revision in the light of new results and also of different users needs, any feedback on the definition is therefore most welcome.

6.5 MATERIAL RESPONSE

A wide range of materials have been tested over the last 18 months using MIJA. These include coated, uncoated and composite materials from a variety of sources and the results document several different modes of damage. The most common of these damage modes are:

- Circumferential cracking** - initiated by the Rayleigh surface wave
- Scabbing** from the outside of cracks - due to the impact of the fast lateral jet as the high water hammer pressure of the drop is released.
- Central damage** - various causes, overlap of tensile release waves in the solid, hydraulic loading of surface voids, defects in the internal structure.
- Coating stripping** - coating torn off the surface by the lateral jetting
- Radial striations** - seen on the composite material due to the lateral jetting impacting against diamond particles left protruding from the surface

6.5.1 Substrates

The following substrates have now been tested at the Cavendish Labs:

- Zinc Sulphide** - this has been tested several times on MIJA, and has been used as a standard reference material to check the velocity calibration
- Germanium** - several samples have now been tested, including both (100) and (111) material.
- Magnesium Fluoride** - looked at material of variable quality, but from only one source so far.
- Sapphire** - tested a number of different surface finishes and sizes.
- Calcium Lanthanum Sulphide** - compared the threshold curves from three different powder sources. These samples were found to have threshold velocities for both circumferential cracking *and* central damage
- Spinel** - looked at samples from one source
- Silicon** - compared the results from polished silicon with those for samples given a pre-diamond deposition treatment.
- Natural diamond** - tested one sample, and a second sample has now been supplied
- CVD Diamond** - tested CVD diamond from a range of U.K. and U.S. sources, different thicknesses, qualities, and growth techniques have been evaluated.

The results from some of these tests are summarised in table 6.5.1 and figure 6.5.1. As stated in section 6.4 the DTV curves are for circumferential cracking only, although some idea of the effect of central damage has been given in table 6.5.1. The effect of surface finish on the threshold curves was most notably demonstrated by the experiments on sapphire and silicon. These demonstrated that although improving the surface finish had little effect on the threshold velocity after 300 impacts, it did cause a significant increase in the incubation period when impacted above this value (figure 6.5.2).

Material	0.8 mm jet DTV (1 impact) / m s ⁻¹	0.8 mm jet DTV (3 impacts) / m s ⁻¹	0.8 mm jet DTV (10 impacts) / m s ⁻¹	0.8 mm jet DTV (300 impacts) / m s ⁻¹	0.8 mm jet DTV (mechanical) / m s ⁻¹	0.8 mm jet DTV (Central damage) / m s ⁻¹
SUBSTRATES						
Sapphire				485 ± 5		? < 400
Spinel (% drop to DTV (300))	490 ± 10 (38 %)	415 ± 5 (17 %)	375 ± 5 (6 %)	355 ± 5 (0 %)	325 ± 25	? < 250
Mg F ₂ (% drop to DTV (300))	320 ± 10 (31 %)	300 ± 10 (22 %)	245 ± 5 (0 %)	245 ± 5 (0 %)	217 ± 17	? < 200
Silicon (% drop to DTV (300))	410 ± 10 (91 %)	310 ± 10 (44 %)	275 ± 5 (28 %)	215 ± 5 (0 %)		? < 200
ZnS (% drop to DTV (300))	170 ± 5 (24 %)	155 ± 5 (19 %)	145 ± 5 (11 %)	130 ± 5 (0 %)	115 ± 10	
Diamond IIa				~ 530		
Germanium (% drop to DTV (300))	255 ± 5 (104 %)	195 ± 5 (56 %)	165 ± 5 (32 %)	125 ± 5 (0 %)	115 ± 10	~ 170
CaLa ₂ S ₄ (% drop to DTV (300))	245 ± 5 (123 %)	200 ± 5 (82 %)	165 ± 5 (50 %)	110 ± 5 (0 %)		160 - 190
CVD Diamond				475 ± 25		200 - 250
COMPOSITES						
ZnS-10D (1-3 μm) (% drop to DTV (300))	280 ± 10 (124 %)	220 ± 10 (76 %)	195 ± 5 (56 %)	125 ± 5 (0 %)		
ZnS-10D (0-1 μm) (% drop to DTV (300))	280 ± 10 (93 %)	205 ± 5 (41 %)	185 ± 5 (27 %)	145 ± 5 (0 %)		
ZnS-20D (0-1 μm) (% drop to DTV (300))	300 ± 10 (58 %)	245 ± 10 (29 %)	230 ± 10 (21 %)	190 ± 10 (0 %)		? < 170
ZnS-30D (0-1 μm) (% drop to DTV (300))				212 ± 12		
COATINGS						
11 μm GeC on ZnS (% drop to DTV (300))	205 ± 5 (64 %)	175 ± 5 (40 %)	155 ± 5 (24 %)	125 ± 5 (0 %)	120 ± 10	
16.8 μm BP on ZnS (% drop to DTV (300))	312 ± 12 (49 %)	250 ± 10 (19 %)	235 ± 15 (12 %)	210 ± 10 (0 %)		? < 200
16.2 μm BP on Ge (% drop to DTV (300))			340 ± 20 (36 %)	250 ± 10 (0 %)		? < 200
1 μm Am.dia. on ZnS (% drop to DTV (300))		205 ± 5 (17 %)	195 ± 5 (11 %)	175 ± 5 (0 %)		

Table 6.5.1 Damage Threshold Velocity values (DTV) for a 0.8 mm jet on a range of materials. The values after 1, 3 and 10 impacts have been presented for comparison with SIJA results. The values after 300 impacts from MIJA are probably closer to the mechanical DTV value determined by impacting the sample 5 times and then finding its residual strength. The last column gives an estimate for the central damage threshold velocity where possible. For most materials this is just expressed as < X m s⁻¹ since the value has not been fully investigated yet, however for some materials such as calcium lanthanum sulphide, germanium and CVD diamond a threshold velocity has actually been identified.

The threshold velocity for circumferential cracking for CVD diamond has improved significantly over the last couple of years. However the threshold is still not on a par with that of natural diamond and there is also still a problem with central crazing in the middle of the sample which occurs at a velocity well below that for circumferential cracking. One source has now provided samples that don't generate central crazing so further improvements are expected.

Finally the threshold velocity values produced using MIJA have also been plotted against various different material properties, and combinations of these properties. The best fit has been obtained by plotting the threshold velocity against the log of the fracture toughness as seen in figure 6.5.3

3.3.3 Coatings Tested

A number of different coatings have so far been investigated on MIJA (figure 6.5.4):

Germanium carbide - several different sources and coating thicknesses

Boron phosphide - several different coating thicknesses on zinc sulphide, germanium, sapphire and fused silica

Amorphous diamond - two coating thicknesses evaluated on zinc sulphide

Silicon nitride - a number of different thicknesses tested on BK7 glass

CVD diamond - a range of different thicknesses and sources, from different deposition techniques.

The samples are examined regularly during testing and five different damage mechanisms are noted. Circumferential cracking, central damage and chipping / debonding in the coating, and circumferential cracking and central damage in the substrate underneath the coating. Damage may initiate either in the coating, or in the substrate and then spread through the coating. Detection of damage initiating in the substrate is however more difficult, and has to be carried out by cross-sectioning the sample, or looking for cracks through the bulk of the substrate.

Although a predictive relationship has been obtained for the threshold velocity for a substrate, much more work is still needed before a similar understanding can be achieved for a coated system. In particular the effects of coating modulus, thickness, internal stress and bonding, on the damage initiation and propagation need to be investigated. Despite the complexity of the problem much useful information has already been learnt, and it is hoped that this and future information will help materials designers in achieving better optimisation of their coating systems.

6.5.3 Composites Tested

Four different composites have been tested that were made of a mixture of diamond particles in zinc sulphide:

ZnS - 10 D (0 - 1 μm) i.e. 10 % of diamond particles with sizes (0 - 1 μm)

ZnS - 10 D (1 - 3 μm)

ZnS - 20 D (0 - 1 μm)

ZnS - 30 D (0 - 1 μm) only one small sample tested with insufficient space for a full threshold curve evaluation

Three different damage mechanisms were seen: circumferential cracking, central damage and radial striations. The radial striations were caused by the interaction of

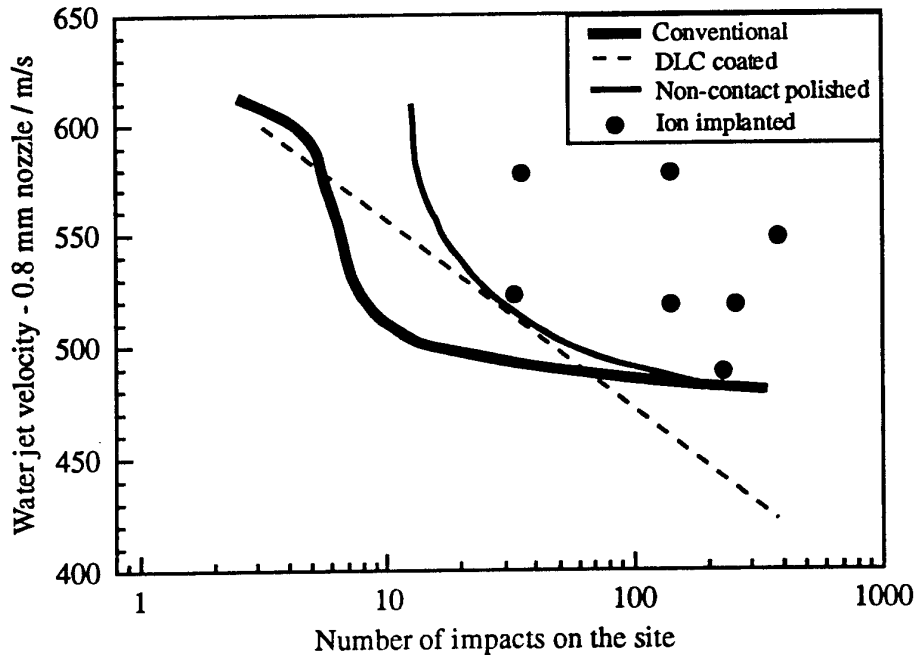


Figure 6.5.2 The effect of surface finish on the threshold curve can be suitably illustrated by the work on sapphire.

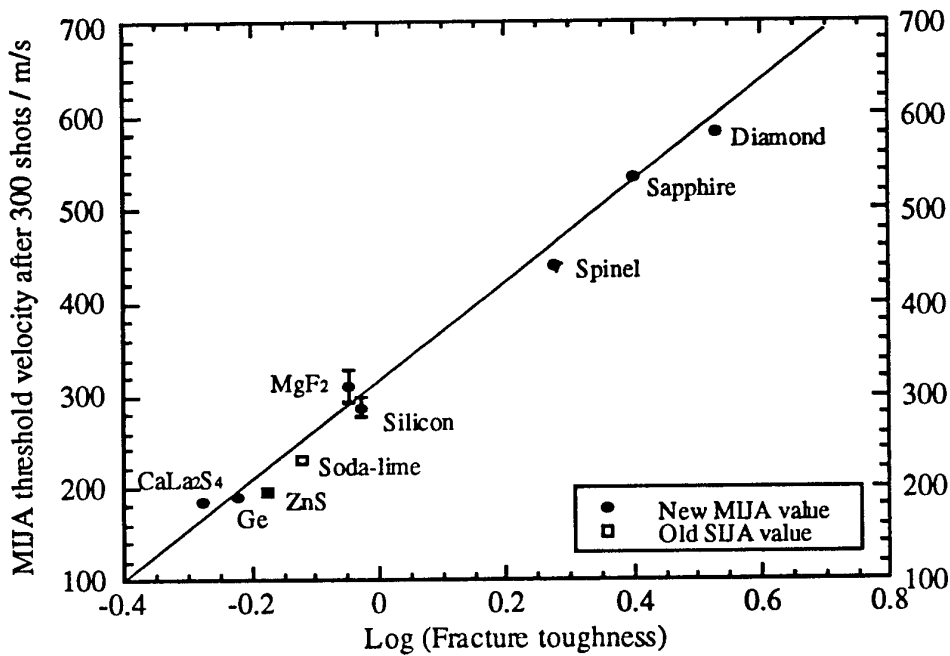


Figure 6.5.3 Relation between the damage threshold velocity for the substrate after 300 impacts and log(fracture toughness).

the lateral jetting with voids in the surface or diamond particles left protruding from the surface. This type of damage was only seen after large numbers of impacts, but could occur at sub-threshold velocities (i.e. below that required to cause circumferential cracking). A summary of the results obtained can be seen in figure 6.5.5

6.6 FUTURE RESEARCH

The objectives for future research are:

1. to update the definition of the damage threshold velocity for brittle materials subjected to high velocity rain impact.
2. to investigate new damage mechanisms discovered recently at the Cavendish Laboratory in ceramic materials subjected to high velocity liquid impact.
3. to evaluate the erosion resistance of new and existing infra-red transmitting materials, and the improvements offered by protective coatings.
4. to produce standard methods of rain erosion testing, and of subsequent damage evaluation for both transparent and opaque materials, coated and uncoated.
5. to carry out a correlation of the data produced using the water jet method of simulation with other methods, and also where possible real test flight results.
6. to look at both the decrease in transmission properties of infra-red transparent ceramics due to crack formation and the decrease in material strength.
7. to investigate the effect of temperature, stress, angle of impact, and residual water on the erosion resistance of brittle materials.

Work in many of these areas has already been started and the results emerging are proving extremely interesting. The main aim behind the work is to try and understand the damage mechanisms at work, so that a simple, cheap reliable test can be defined, and to try and relate the results produced to the real flight situation. This would allow the organisations working on material development to carry out their own testing during their research to identify new materials, and also to check the quality of the domes being produced during manufacture.

6.7 CONCLUSION

A review of the existing rain erosion testing facilities suggests that direct comparison of data produced from different labs is often difficult. The water jet technique used by MIJA (Multiple Impact Jet Apparatus) and SIJA (Single Impact Jet Apparatus) allows much easier comparisons of erosion results to be made between materials and laboratories. After a large amount of design optimisation MIJA now allows jet velocities from 30 - 600 m s⁻¹ to be fired, at a rate of 20 shots per minute, and with a velocity spread of just 0.5 - 1.5 %.

Different techniques for evaluating the damage threshold velocity have been tried, and the final technique chosen has been used to evaluate a range of IR window materials, some of which had never been subjected to rain impact testing before. The results from these tests appear to be very reproducible, and new modes of damage have been discovered which may prove to be important in real flight applications.

A first attempt has been made at standardising the method of testing with MIJA and SIJA, since SIJA is now in use in ~ 20 labs worldwide. In order to complete this work further investigation will be necessary using MIJA at the Cavendish and a comprehensive test programme is therefore to be attempted over the next few years.

1



100 shots at 480 m s⁻¹

2



100 shots at 480 m s⁻¹

3



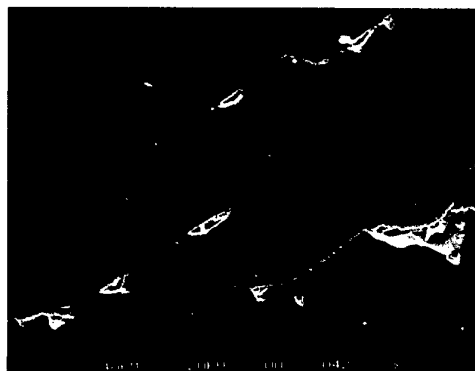
175 shots at 455 m s⁻¹

4



175 shots at 455 m s⁻¹

5



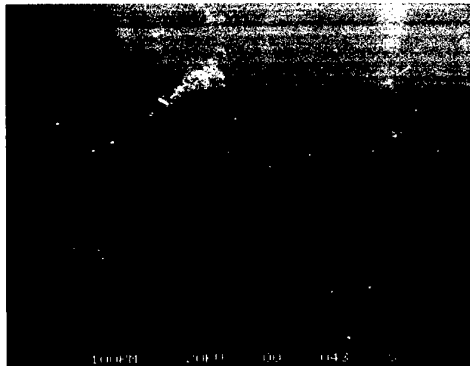
175 shots at 455 m s⁻¹

6



200 shots at 455 m s⁻¹

7

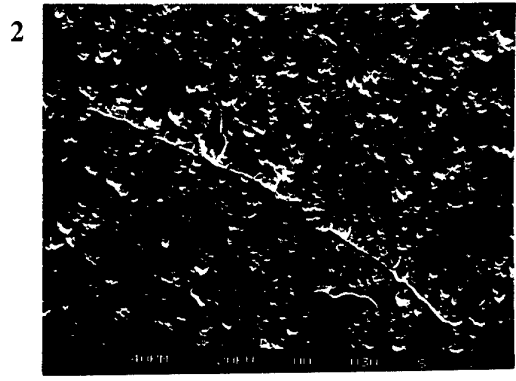


185 shots at 440 m s⁻¹

Plate 9.1.1 Sapphire (Aluminium Oxide)



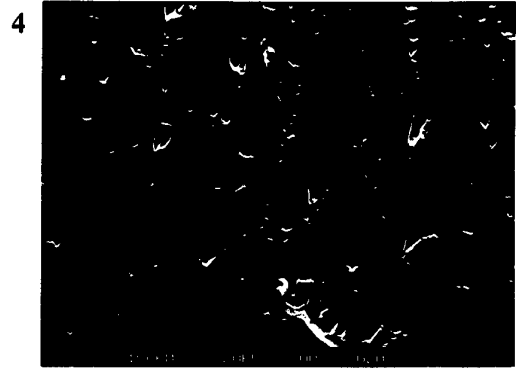
4 shots at 460 m s^{-1}



4 shots at 460 m s^{-1}



160 shots at 370 m s^{-1}



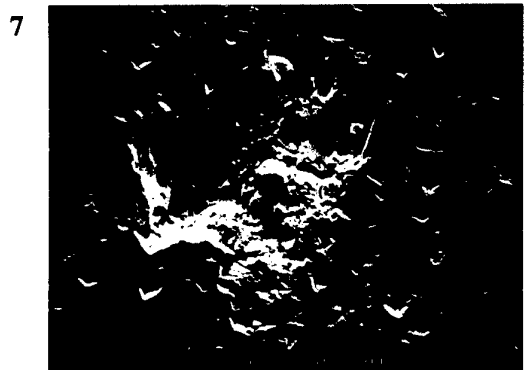
160 shots at 370 m s^{-1}



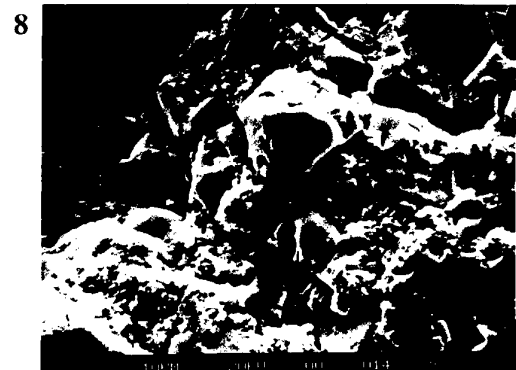
200 shots at 360 m s^{-1}



200 shots at 360 m s^{-1}



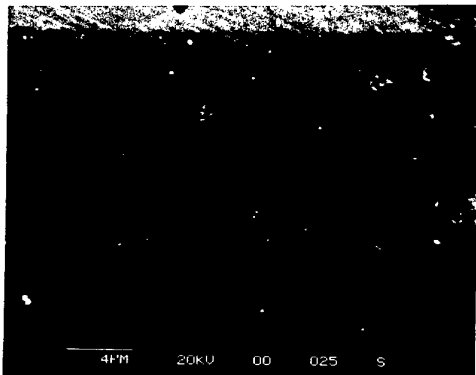
200 shots at 360 m s^{-1}



200 shots at 360 m s^{-1}

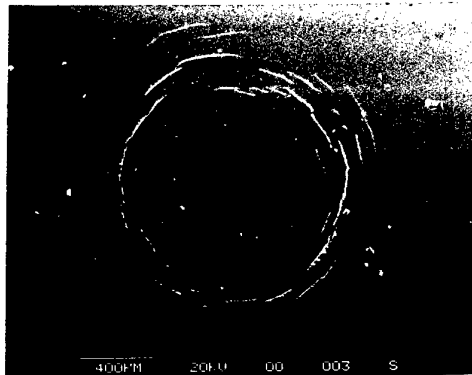
Plate 9.2.1 Spinel (Magnesium Aluminate)

1



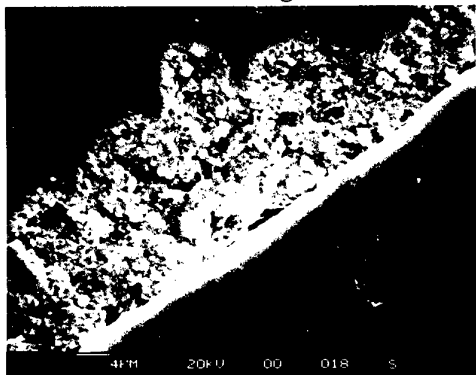
Undamaged

2



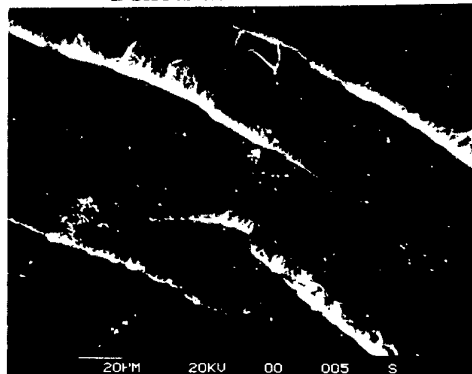
2 shots at 340 m s⁻¹

3



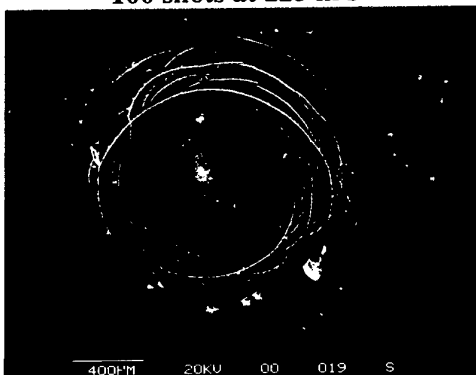
100 shots at 225 m s⁻¹

4



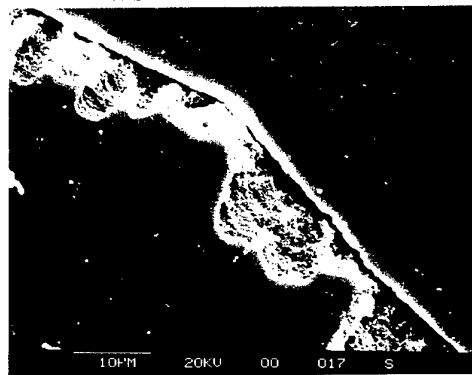
2 shots at 340 m s⁻¹

5



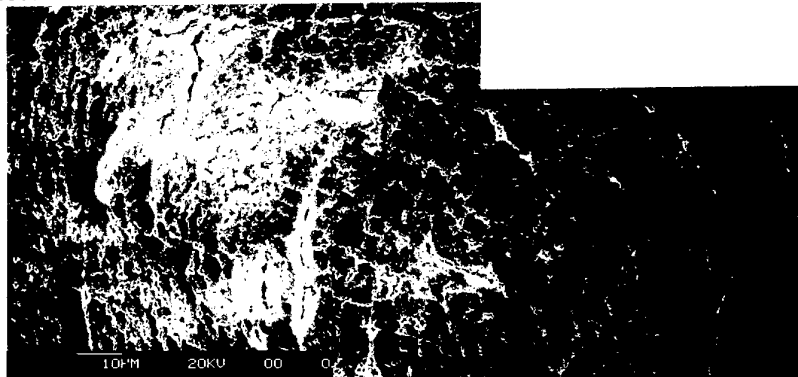
200 shots at 210 m s⁻¹

6



200 shots at 210 m s⁻¹

7



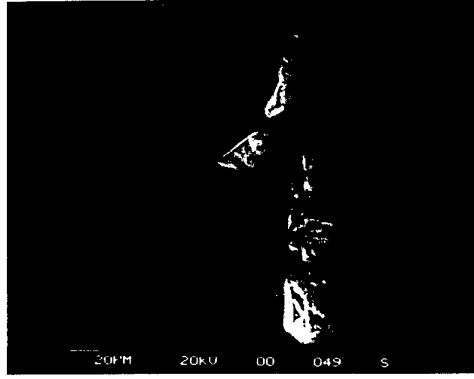
200 shots at 210 m s⁻¹

1



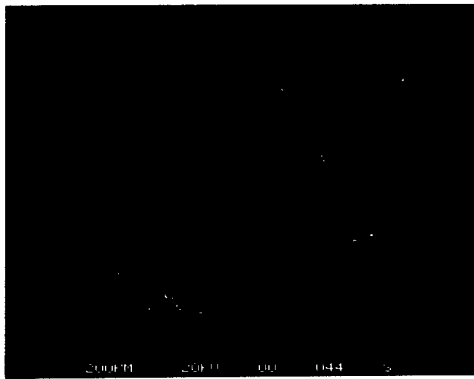
1 shot at 340 m s⁻¹

2



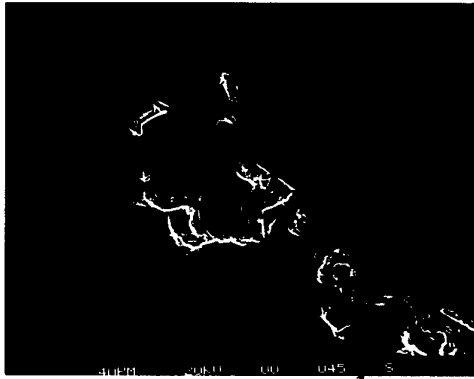
1 shot at 340 m s⁻¹

3



30 shots at 270 m s⁻¹

4



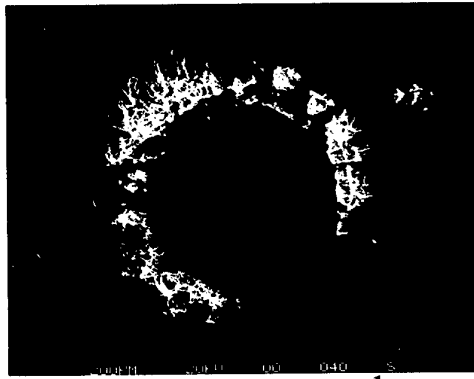
30 shots at 270 m s⁻¹

5



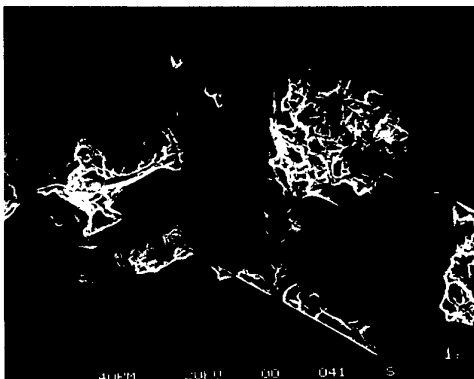
30 shots at 270 m s⁻¹

6



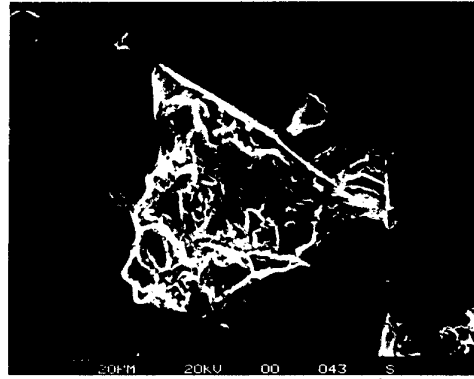
200 shots at 220 m s⁻¹

7



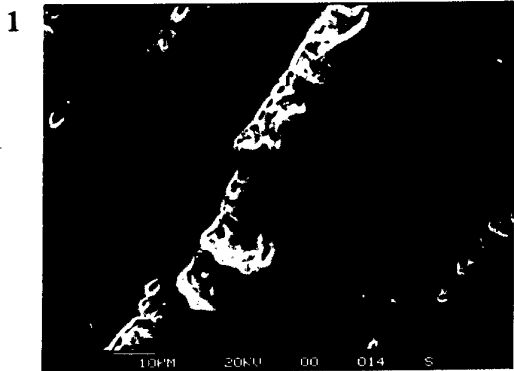
200 shots at 220 m s⁻¹

8

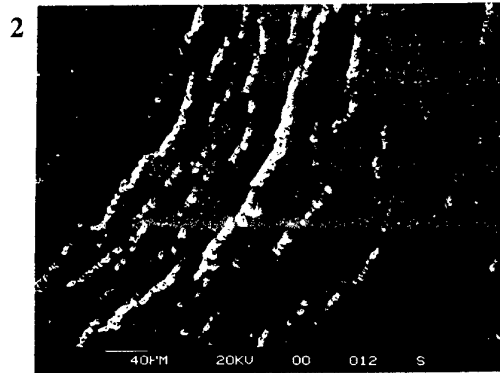


200 shots at 220 m s⁻¹

Plate 9.4.1 Silicon



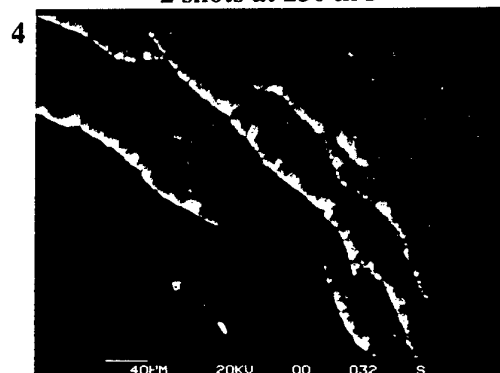
2 shots at 230 m s⁻¹



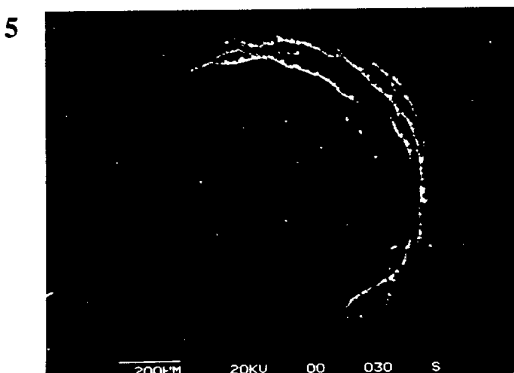
2 shots at 230 m s⁻¹



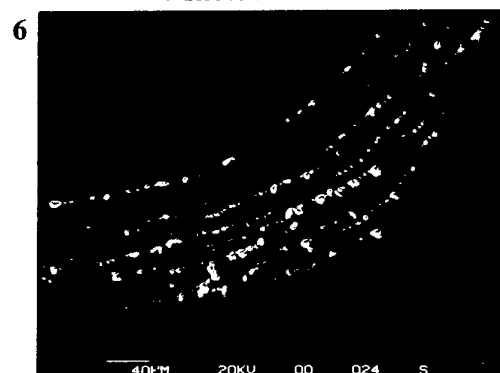
2 shots at 230 m s⁻¹



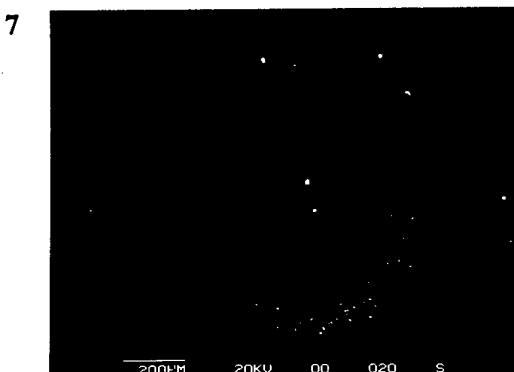
7 shots at 160 m s⁻¹



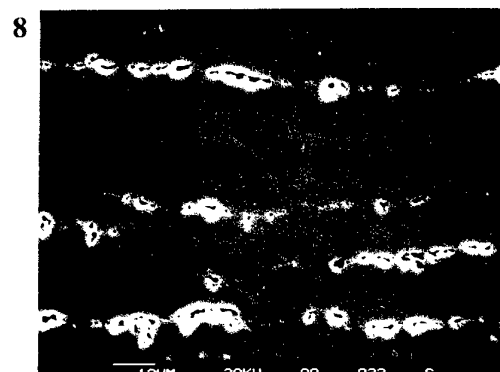
7 shots at 160 m s⁻¹



300 shots at 130 m s⁻¹

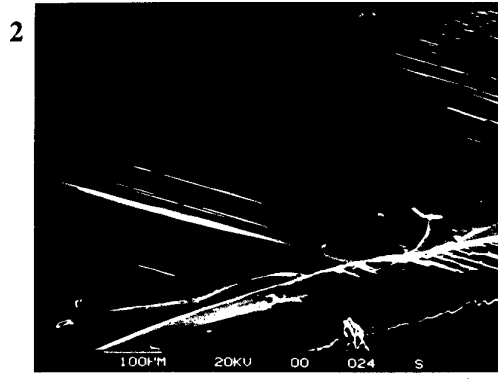


300 shots at 130 m s⁻¹

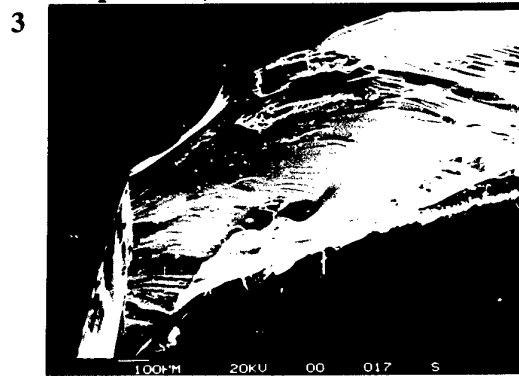


300 shots at 130 m s⁻¹

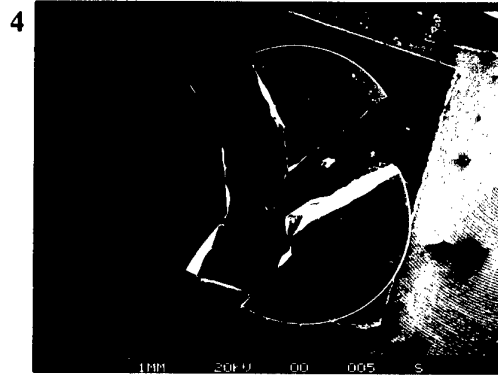
Plate 9.5.1 Zinc Sulphide



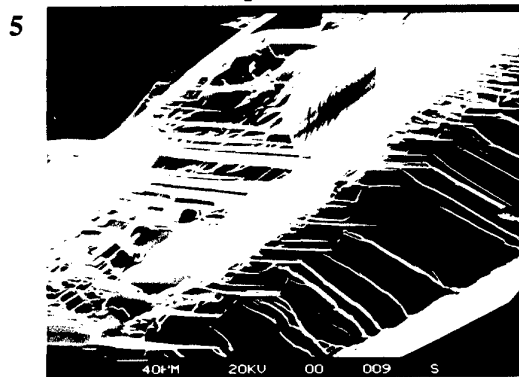
photos 1, 2 and 3: 10 shots at 400,420,440,470,490 $m s^{-1}$, then 3 at 505 $m s^{-1}$



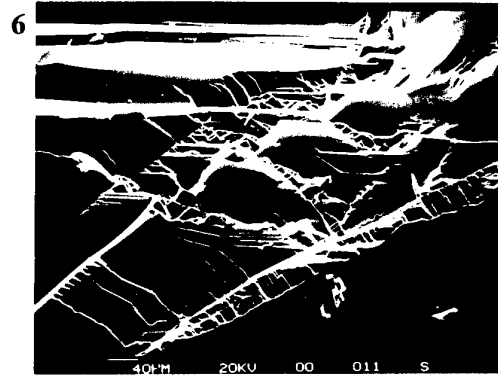
same as photos 1 and 2



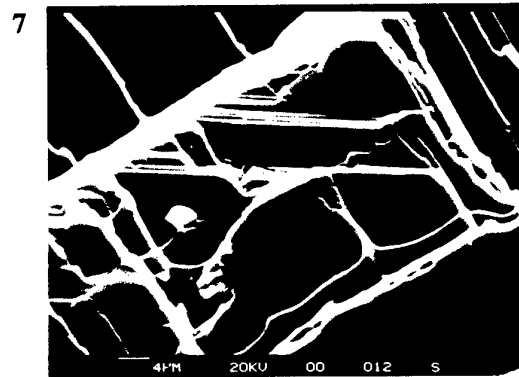
12 shots at 490 $m s^{-1}$



12 shots at 490 $m s^{-1}$



12 shots at 490 $m s^{-1}$



12 shots at 490 $m s^{-1}$



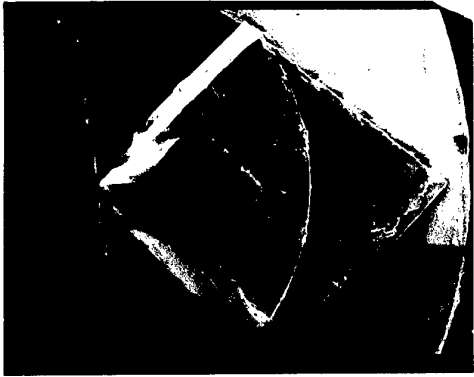
300 shots at 400,420, then 190 at 440 $m s^{-1}$

Plate 9.6.1 6mm Sapphire disc (Aluminium Oxide)



Plate 9.6.2 Fracture surface of the 6 mm sapphire disc seen in photo 8 on plate 9.6.1.

1



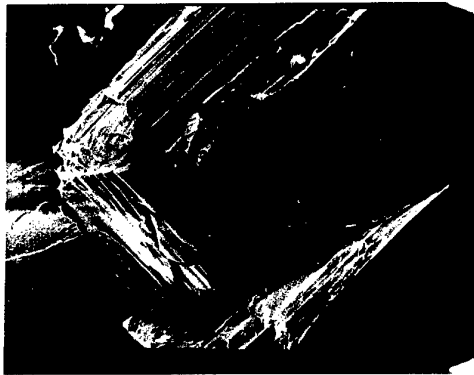
Piece 1

2



Piece 1

3



Piece 1

4



Piece 1

5



Piece 2

6



Piece 2

7



Piece 3

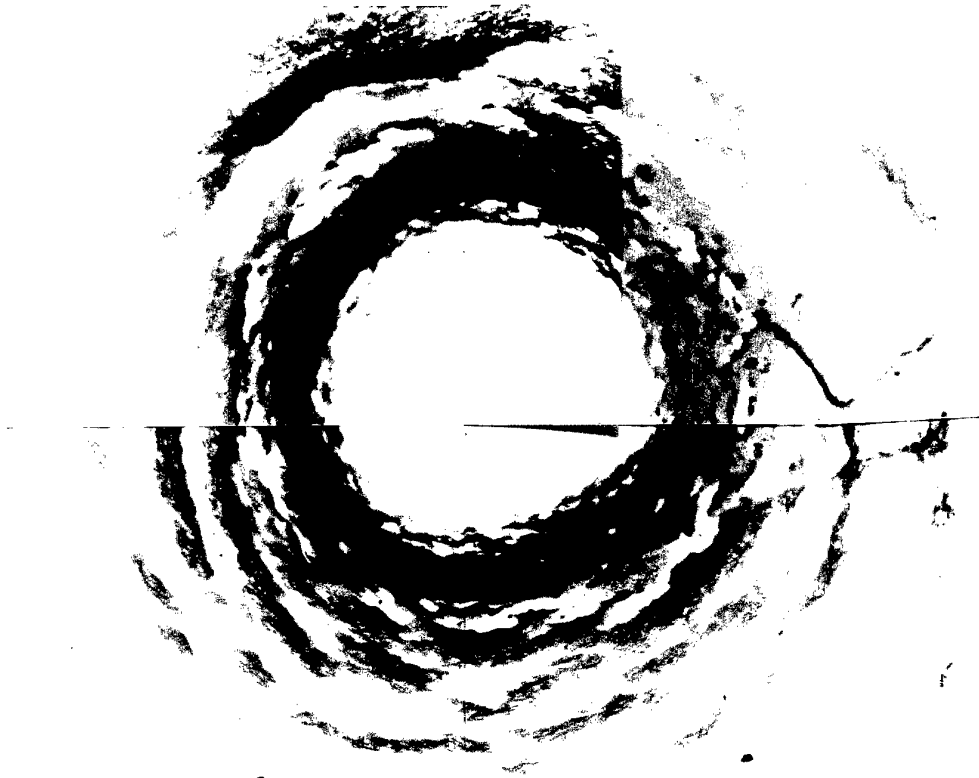
8



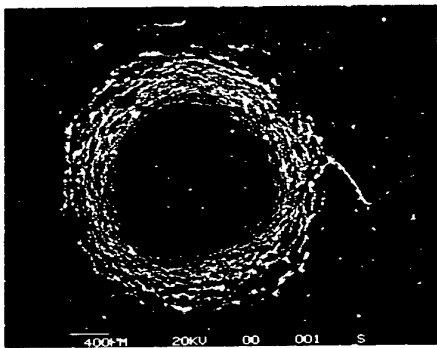
Piece 3

Plate 9.6.3 Type IIA Natural Diamond

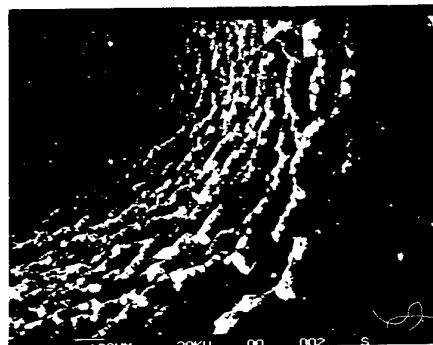
Batch 2 (specimen VX 262) - 1 impact at 500 m s⁻¹



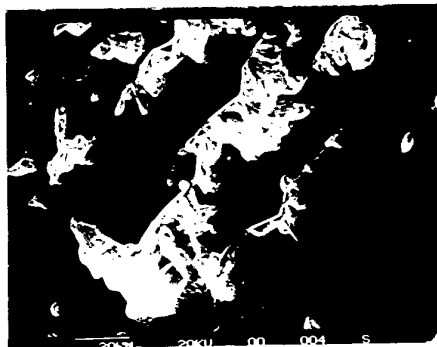
1. Damage viewed with transmitted and reflected light



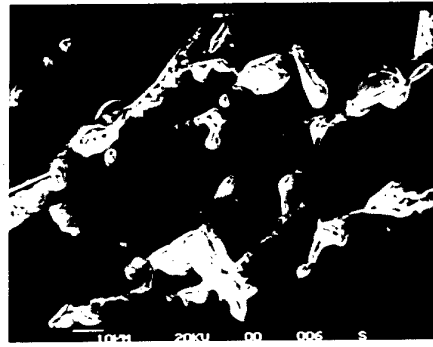
2. SEM of damage site



3. Enlargement of photo 2



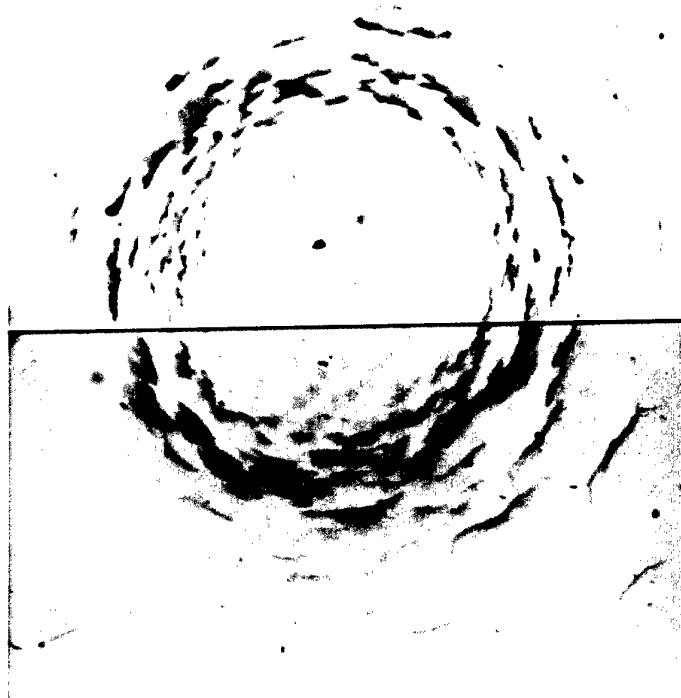
4. Close-up of A in photo 3



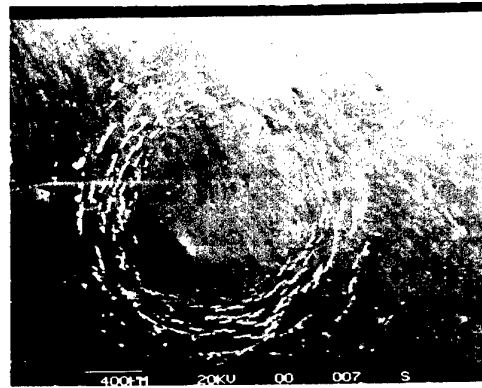
5. Close-up of B in photo 3

Plate 9.8.1 Calcium Lanthanum Sulphide

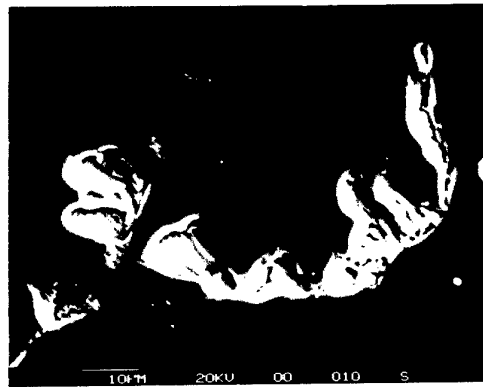
Batch 2 (specimen VX 262) - 1 impact at 375 m s⁻¹



1. Damage viewed with transmitted light



2. SEM of damage site

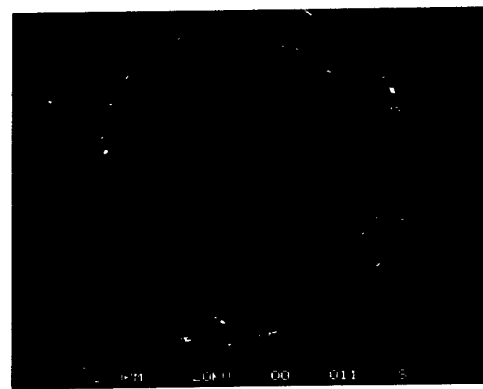


3. Enlargement of cracking

Batch 2 (specimen VX 263) - 1 impact at 290 m s⁻¹



4. Damage viewed with transmitted light



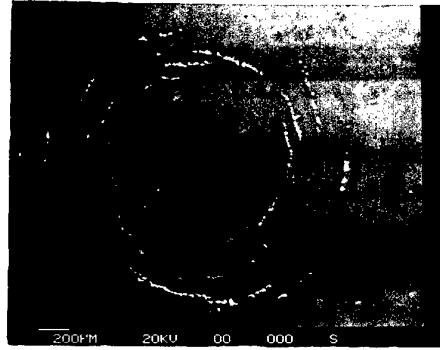
5. SEM of damage site

Plate 9.8.2 Calcium Lanthanum Sulphide

Batch 1 (specimen VX 239) - 2 impacts at 240 m s⁻¹



1. Damage viewed with transmitted light

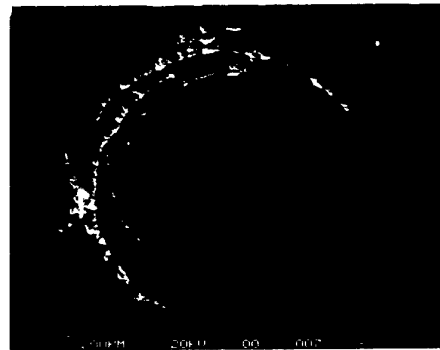


2. SEM of impact site

Batch 1 (specimen VX 239) - 15 impacts at 180 m s⁻¹



3. Damage viewed with transmitted light

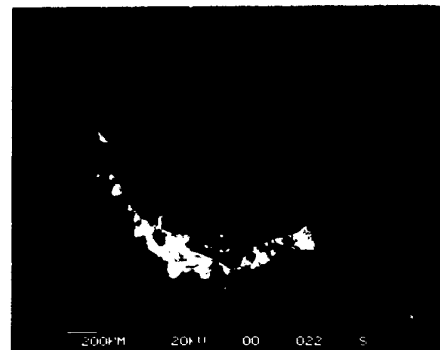


4. SEM of impact site

Batch 2 (specimen VX 263) - 100 impacts at 140 m s⁻¹



5. Damage viewed with transmitted light



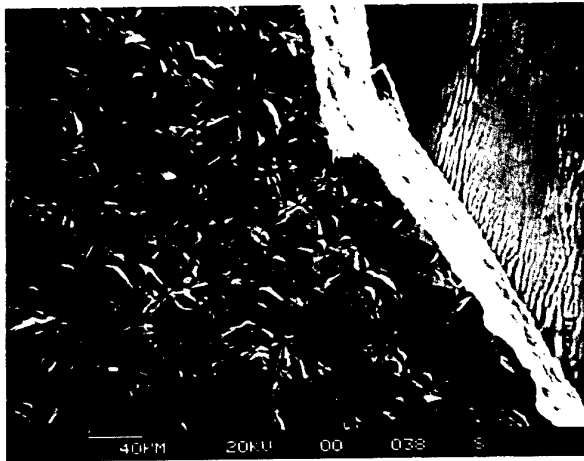
6. SEM of impact site



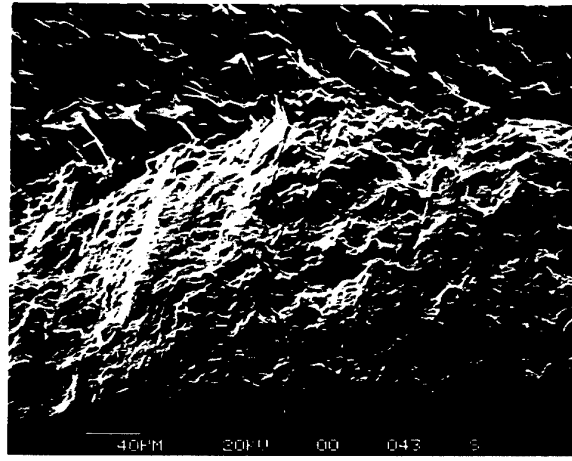
1. Close-up of CVD diamond surface.



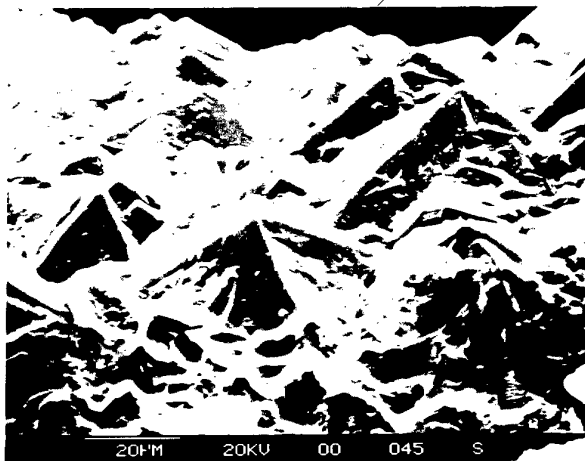
2. Enlargement of photo 1.



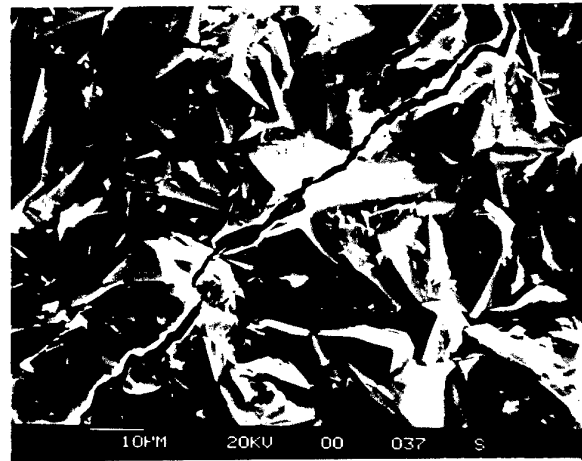
3. Close-up of a crack in the diamond



4. View of the crack at 32°



5. View of the unpolished surface at 32°



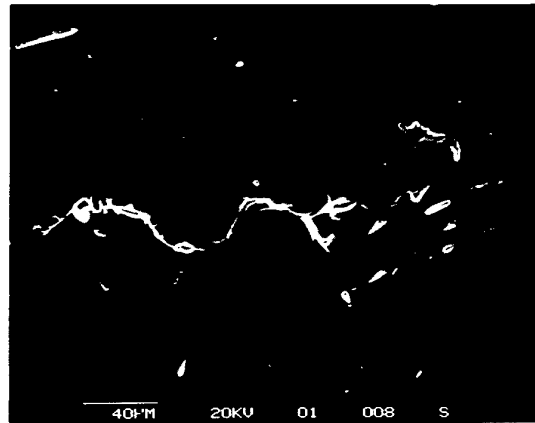
6. Enlargement showing transgranular cracking.

Plate 9.9.1 250 μm Thick, Unpolished CVD Diamond

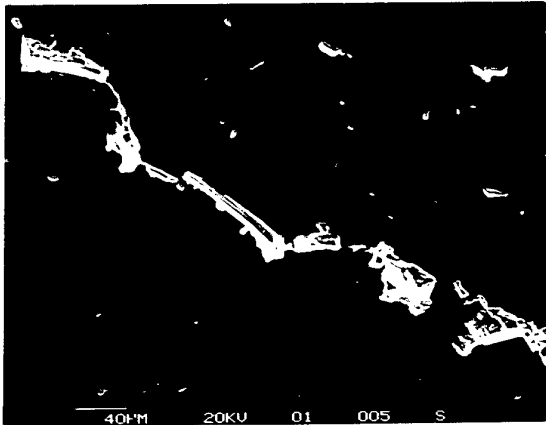
290 μm Thick, Polished, CVD Diamond on Silicon



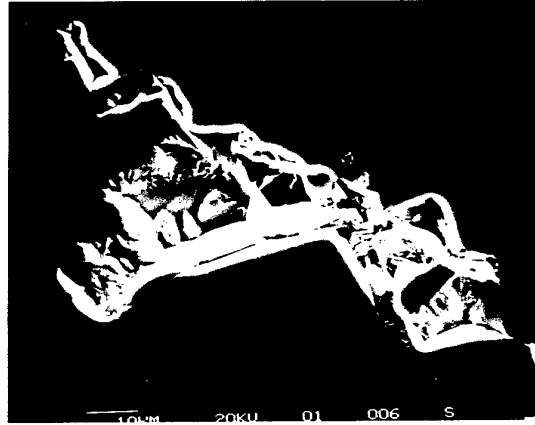
1. View of damage on an optical microscope.



2. Enlargement of cracking.

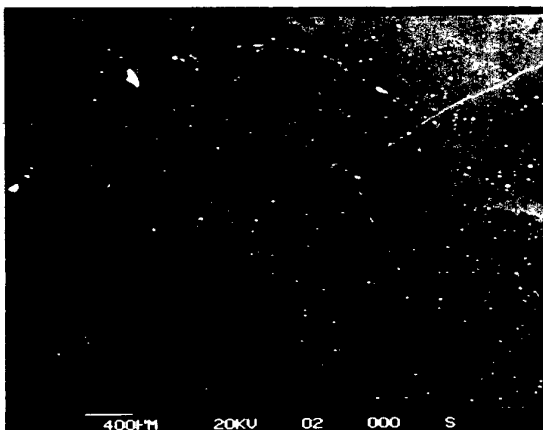


3. Enlargement of cracking.

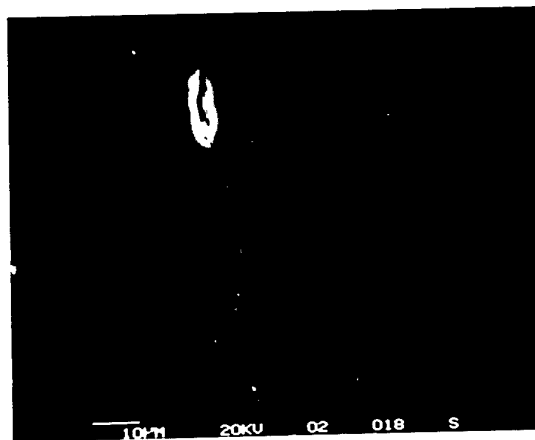


4. Enlargement of C in photo 4.

425 μm Thick, Polished, Free Standing CVD Diamond



5. SEM of damage site.

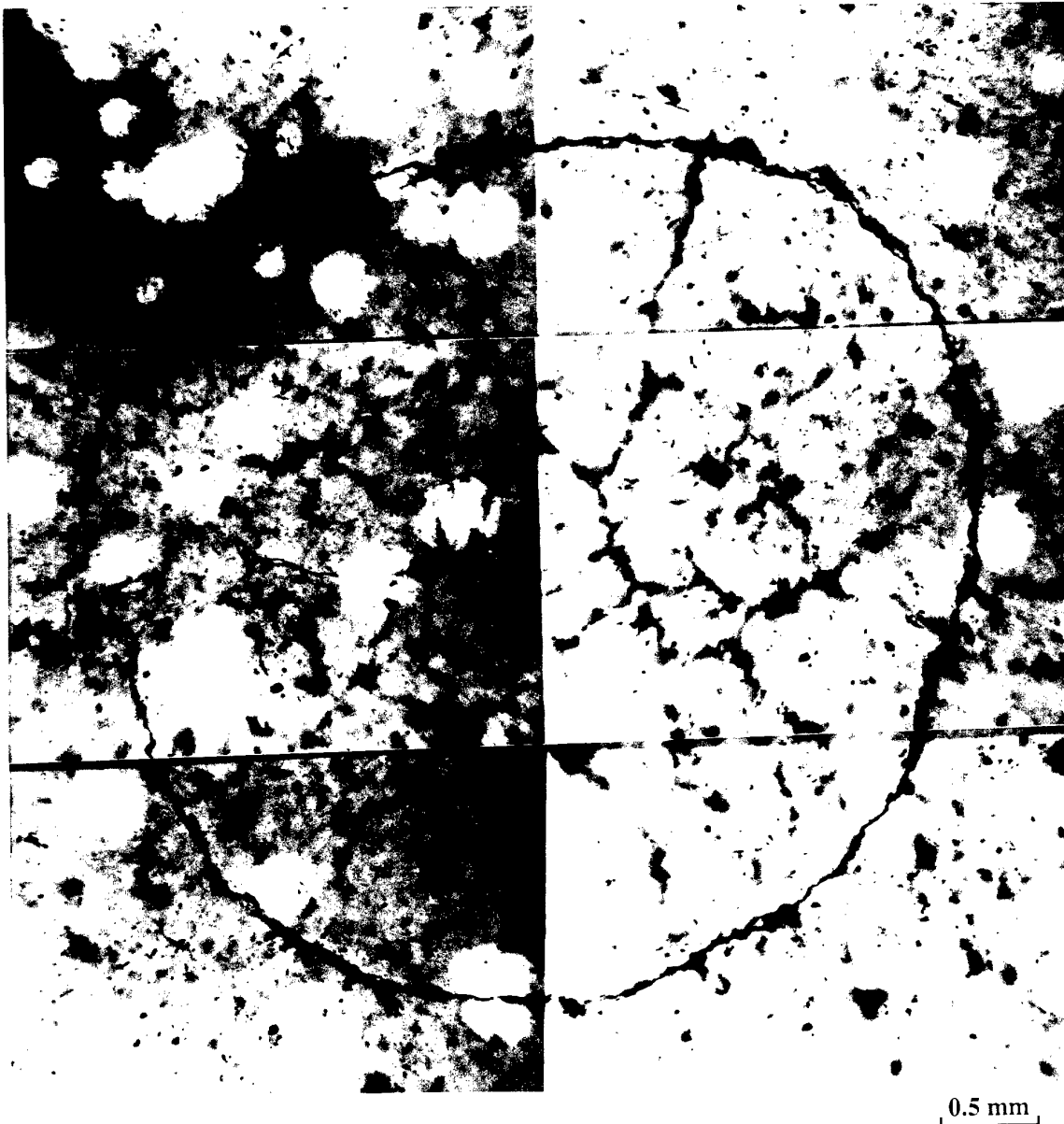


6. Close-up of ring crack.

Plate 9.9.2 CVD Diamond

Photo after 20 impacts at 500 m s^{-1}

Central damage appeared after 10 impacts at 250 m s^{-1}
Circumferential cracking after 10 impacts at 500 m s^{-1}

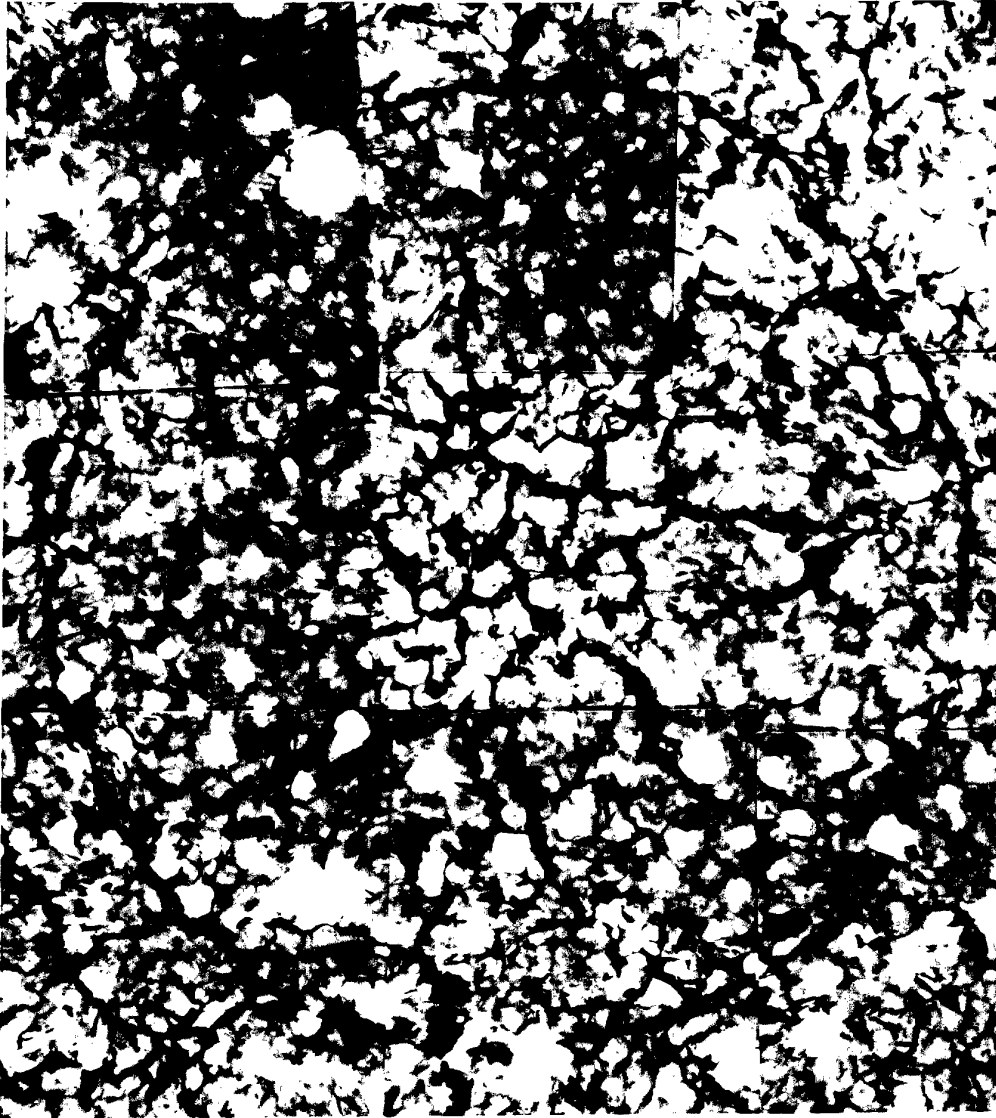


1 mm Thick, Polished, Free Standing CVD Diamond

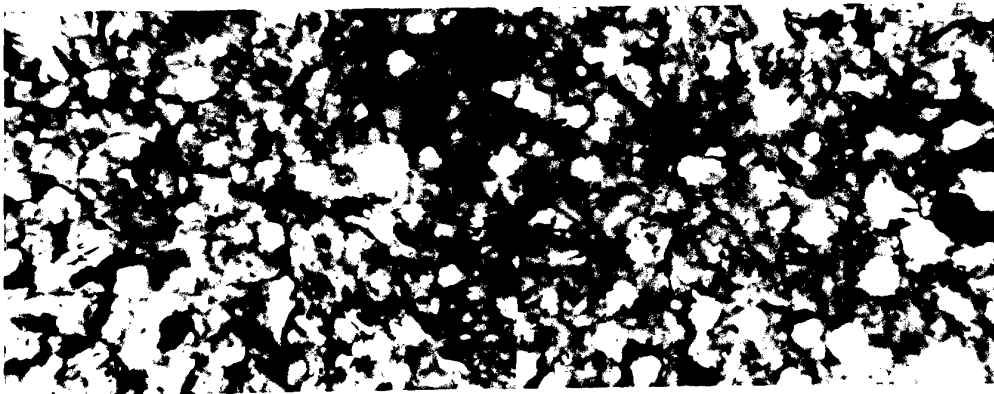
Plate 9.9.3 CVD Diamond

0.5 mm

10 impacts at 450 m s⁻¹



1. Montage of the damage after 10 impacts at 450 m s⁻¹. at 280 μm depth

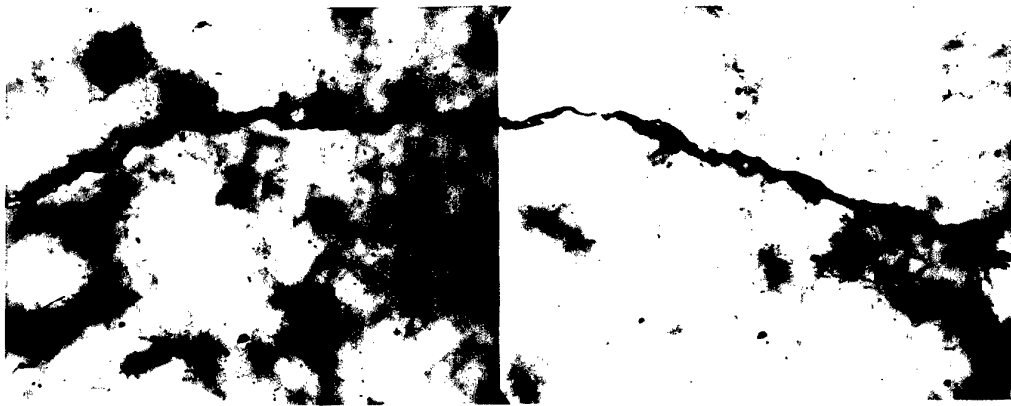


2. Undamaged Material at 280 μm depth

0.5 mm

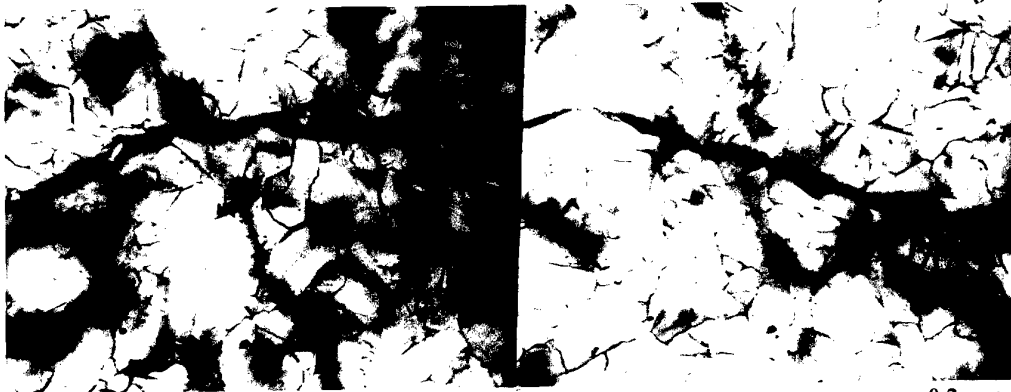
1 mm Thick, Polished, Free Standing CVD Diamond

Plate 9.9.4 CVD Diamond



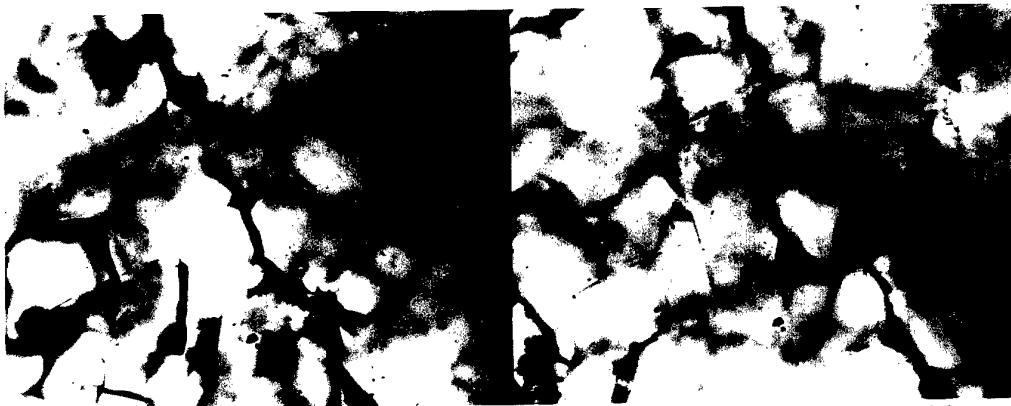
1. Circumferential cracking on surface - depth 0 μm

0.2 mm



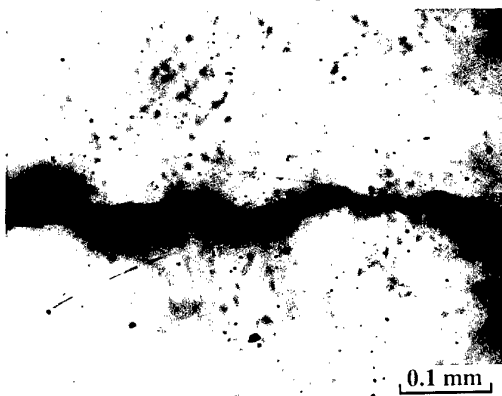
2. Small grain structure in material - depth 75 μm

0.2 mm



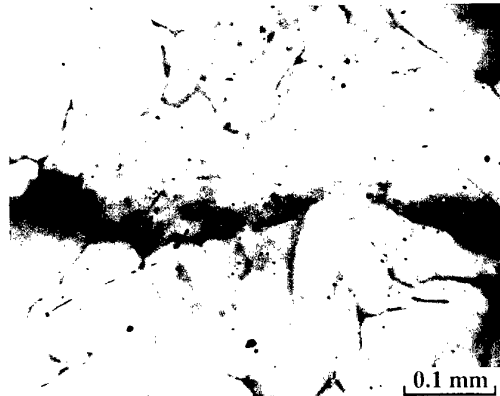
3. Large grain structure in material - depth 280 μm

0.2 mm



0.1 mm

4. Enlargement of crack at 0 μm

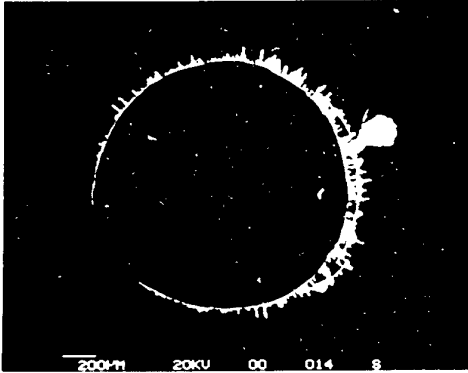


0.1 mm

5. View of small grains at 75 μm

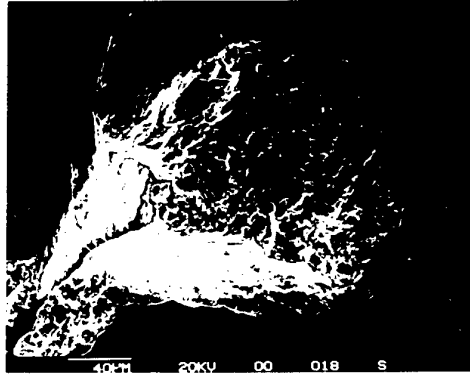
Plate 9.9.5 CVD Diamond - after 10 impacts at 450 m s⁻¹

1



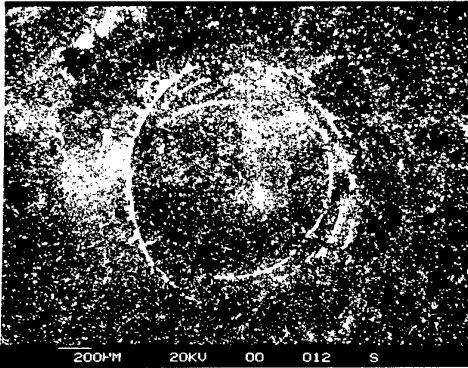
500 shots at 170 m s^{-1}

2



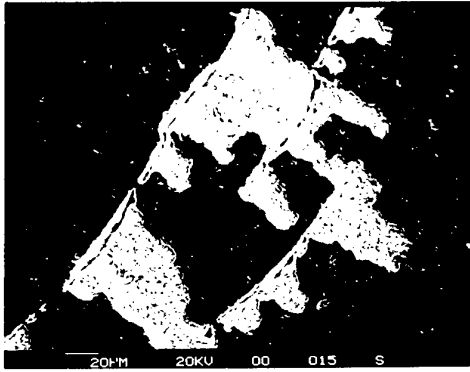
500 shots at 170 m s^{-1}

3



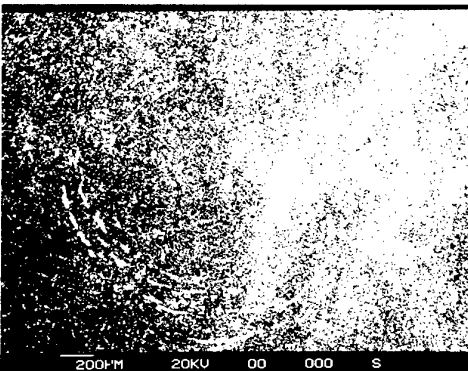
30 shots at 190 m s^{-1}

4



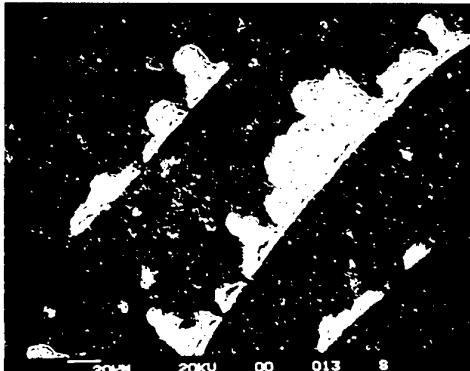
500 shots at 170 m s^{-1}

5



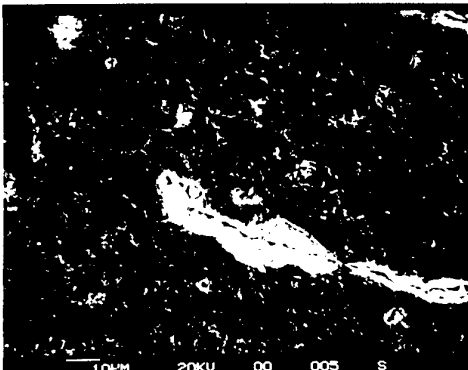
2 shots at 290 m s^{-1}

6



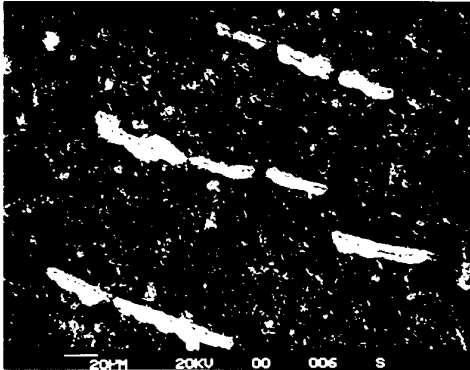
30 shots at 190 m s^{-1}

7



2 shots at 290 m s^{-1}

8



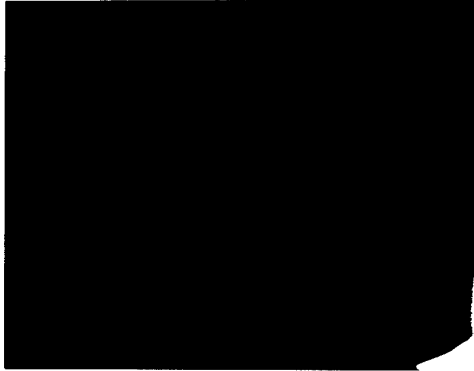
2 shots at 290 m s^{-1}

Plate 9.10.1 Zinc Sulphide with a $1\mu\text{m}$ Amorphous Diamond coating



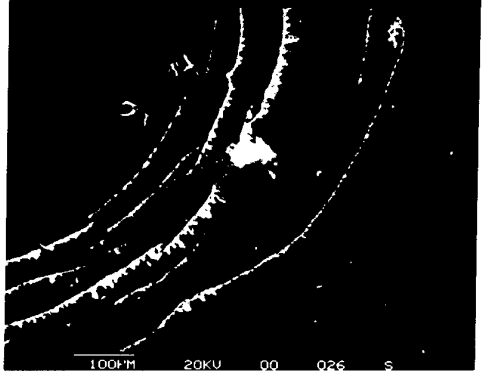
Plate 9.10.2 Zinc Sulphide with a $1\mu\text{m}$ coating of Amorphic diamond viewed with transmitted light on an optical microscope after 500 shots at 170 m s^{-1} .

1



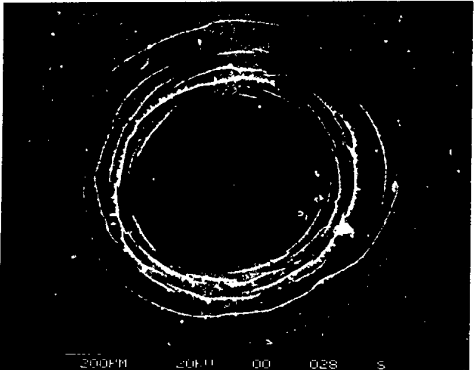
Undamaged

2



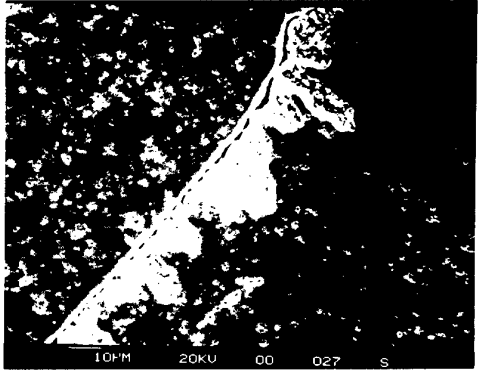
200 shots at 150 m s⁻¹

3



200 shots at 150 m s⁻¹

4



200 shots at 150 m s⁻¹

5



5 shots at 210 m s⁻¹

6



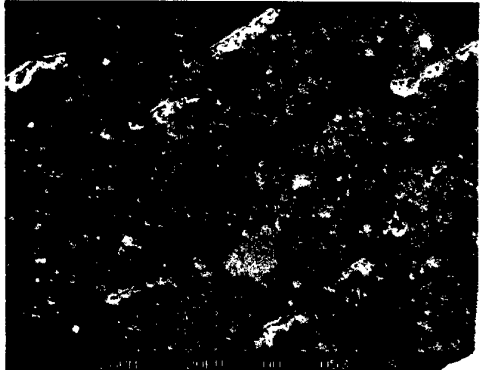
5 shots at 210 m s⁻¹

7



2 shots at 290 m s⁻¹

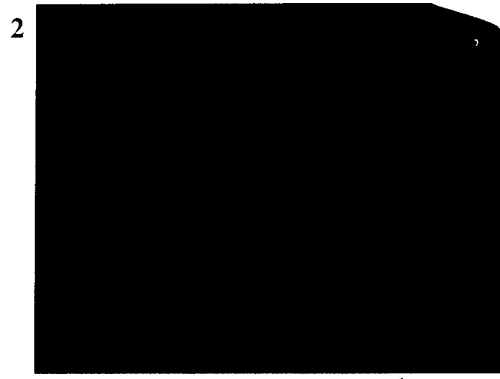
8



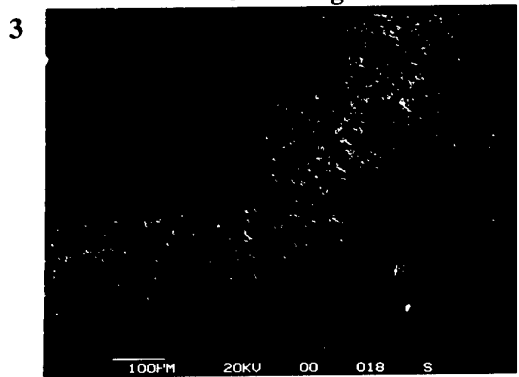
2 shots at 290 m s⁻¹



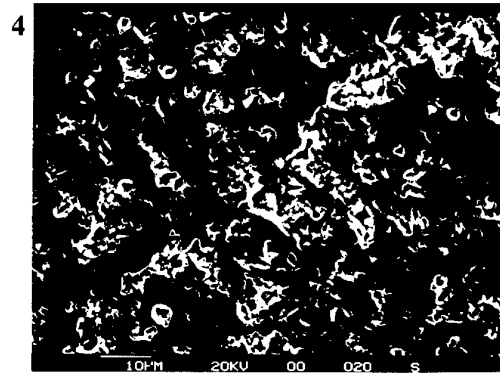
Undamaged



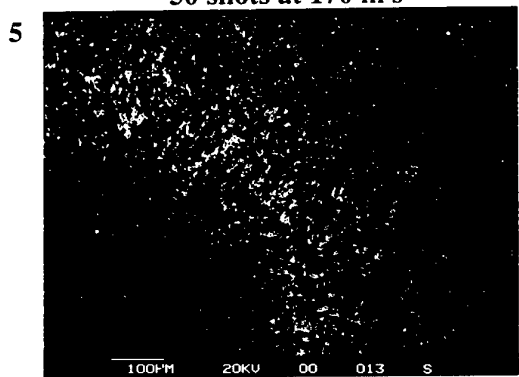
50 shots at 170 m s^{-1}



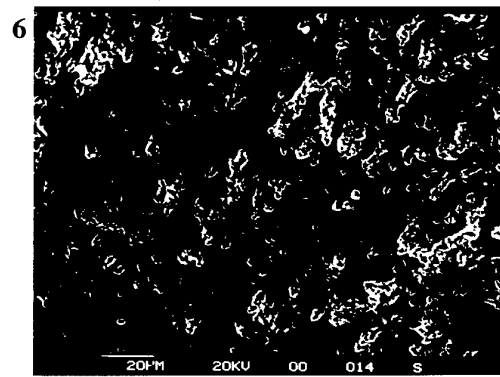
50 shots at 170 m s^{-1}



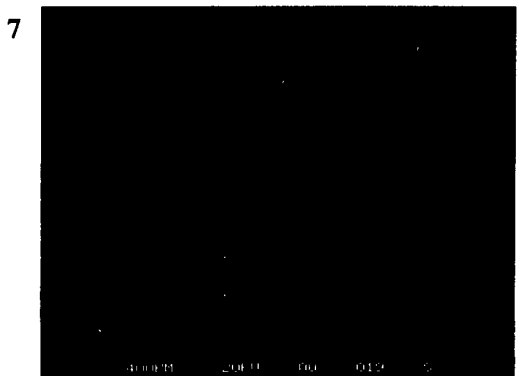
50 shots at 170 m s^{-1}



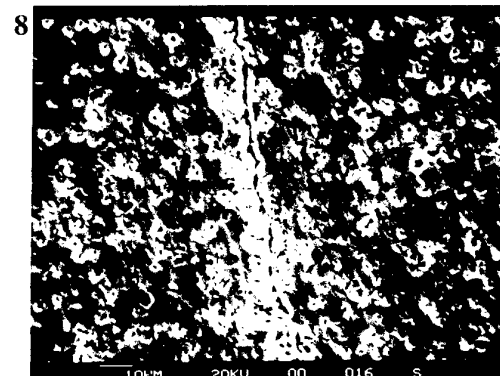
300 shots at 130 m s^{-1}



300 shots at 130 m s^{-1}

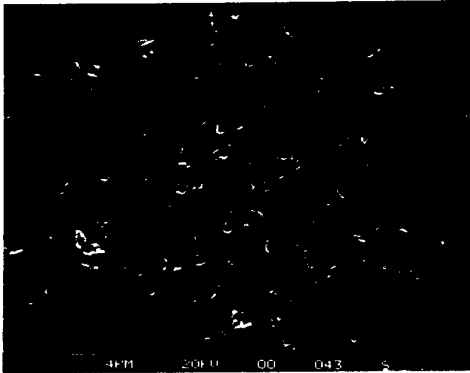


2 shots at 350 m s^{-1}



2 shots at 350 m s^{-1}

1



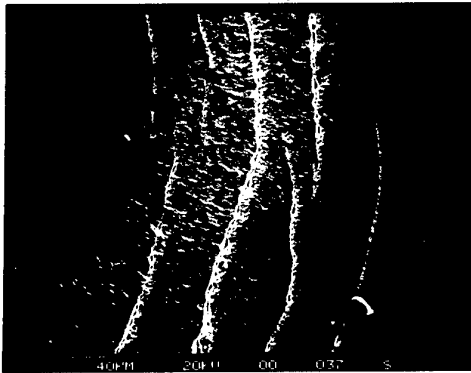
Undamaged

2



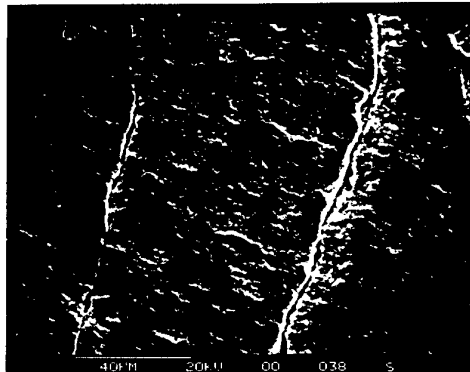
200 shots at 200 m s⁻¹

3



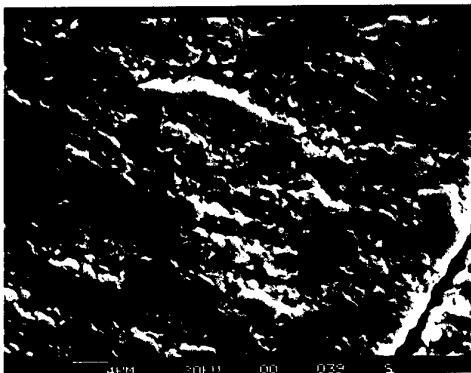
200 shots at 200 m s⁻¹

4



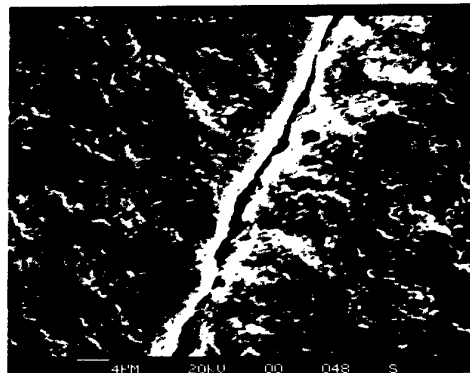
200 shots at 200 m s⁻¹

5



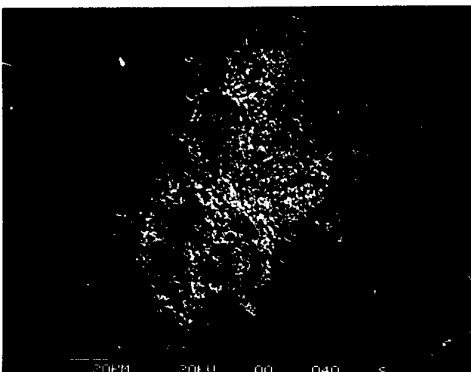
200 shots at 200 m s⁻¹

6



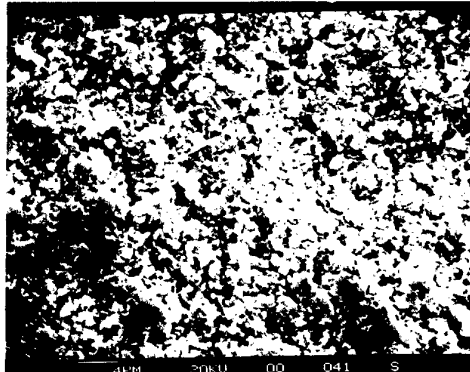
200 shots at 200 m s⁻¹

7



200 shots at 200 m s⁻¹

8



200 shots at 200 m s⁻¹

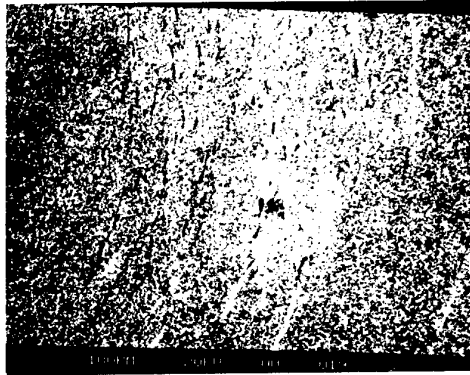
Plate 9.11.3 ZnS-20D (0 - 1 μm)

1



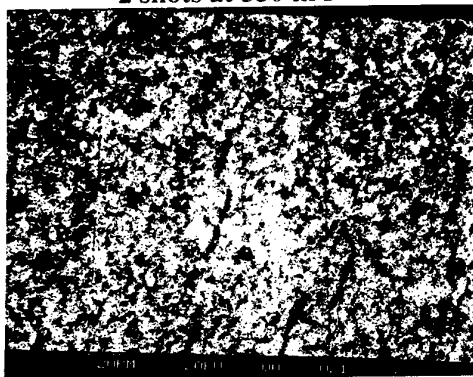
2 shots at 350 m s^{-1}

2



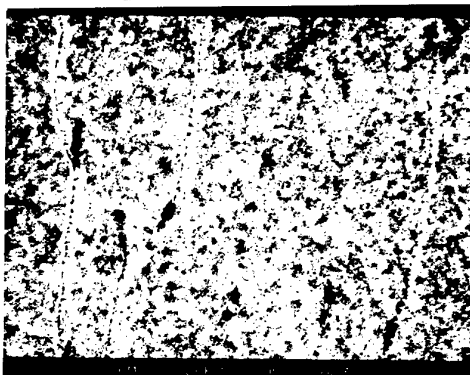
2 shots at 350 m s^{-1}

3



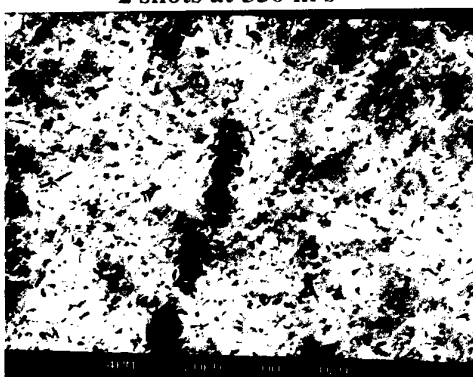
2 shots at 350 m s^{-1}

4



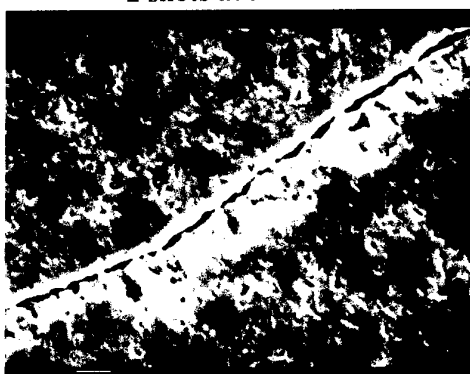
2 shots at 350 m s^{-1}

5



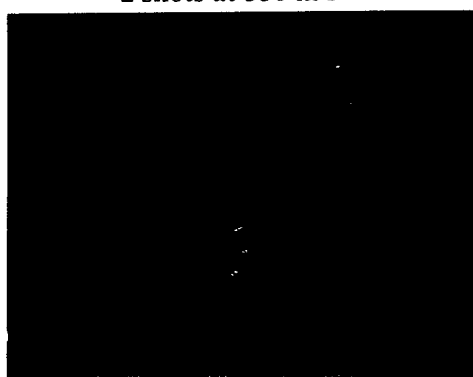
2 shots at 350 m s^{-1}

6



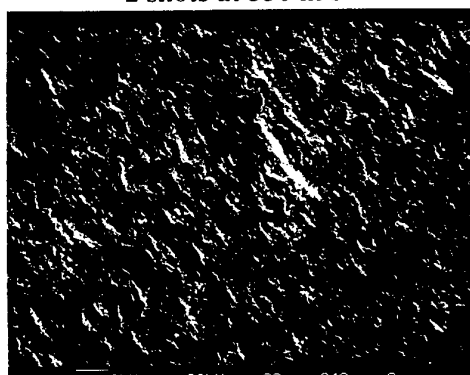
2 shots at 350 m s^{-1}

7



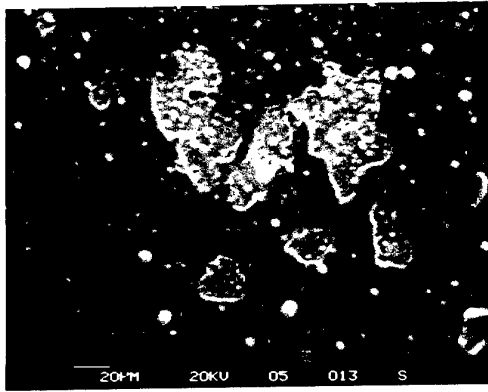
300 shots at 170 m s^{-1}

8

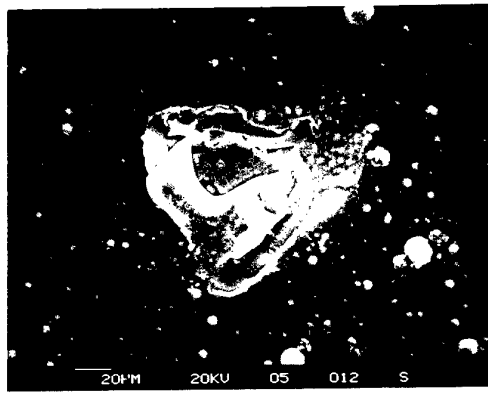


300 shots at 170 m s^{-1}

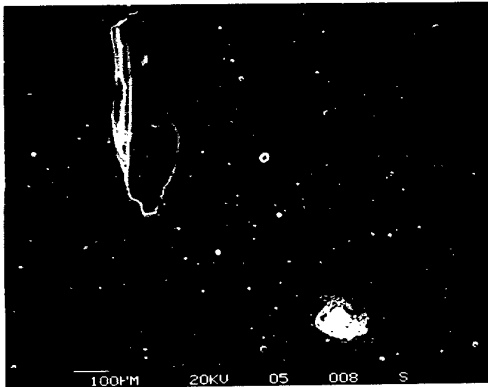
Plate 9.11.4 ZnS-20D (0 - 1 μm)



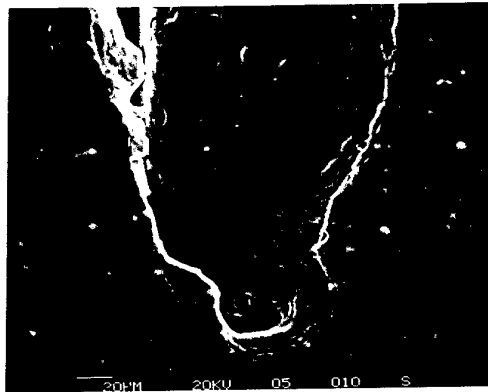
1. Central damage - 300 impacts at 190 m s^{-1}



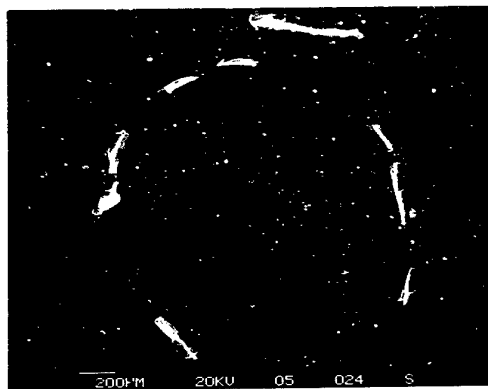
2. Chipping after 300 impacts at 200 m s^{-1}



3. Damage after 70 impacts at 220 m s^{-1}



4. Enlargement of 'A' in plate 3.28



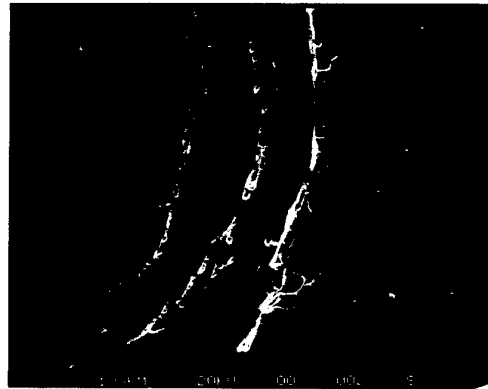
5. Damage after 2 impacts at 300 m s^{-1}



6. Damage after 264 impacts at 185 m s^{-1}

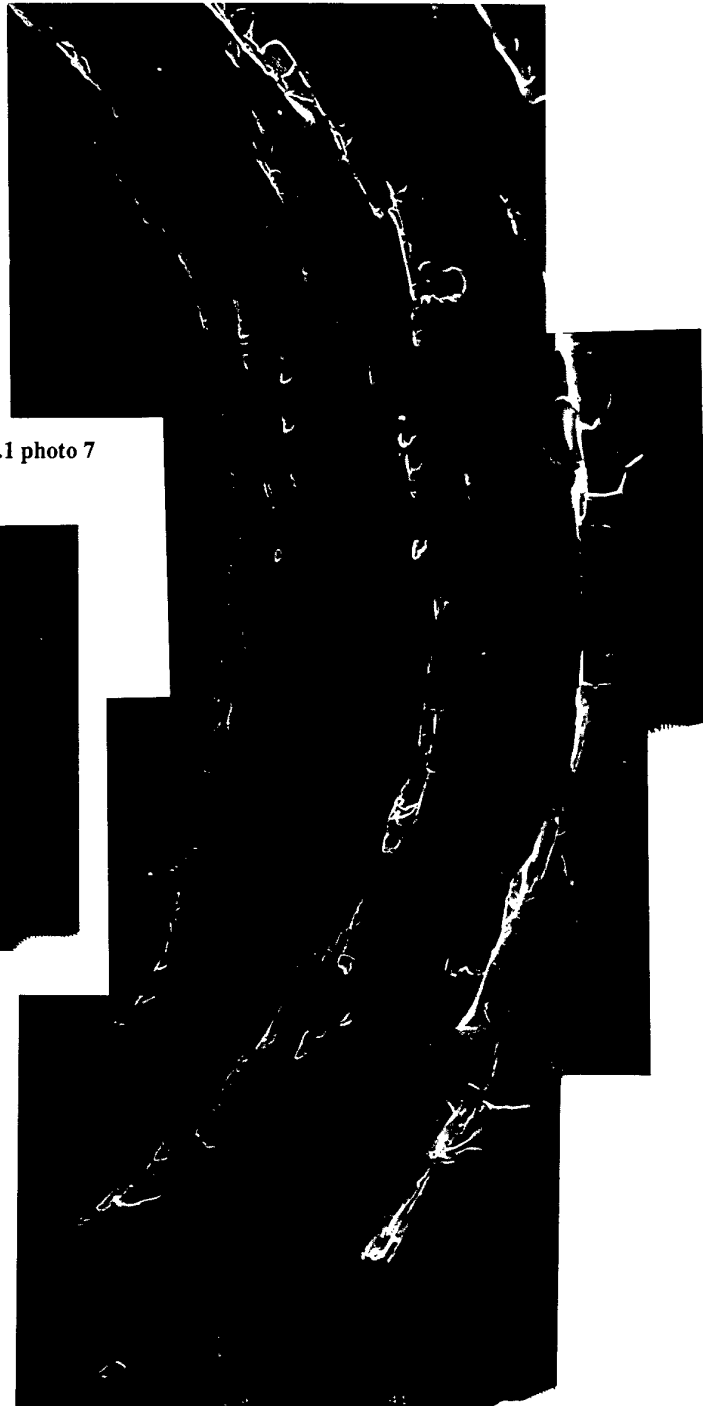


7. Damage after 1 impact at 410 m s^{-1}

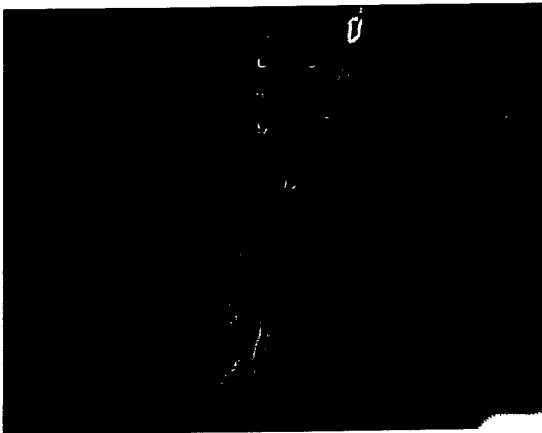


8. Enlargement of cracking in photo 7

Plate 9.14.1 Boron Phosphide Coating on ZnS

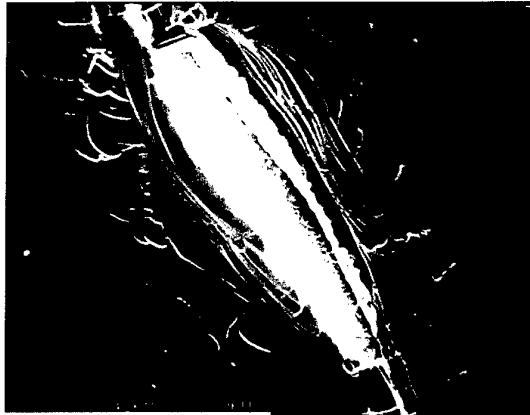


1. Montage of damage pattern in plate 9.14.1 photo 7

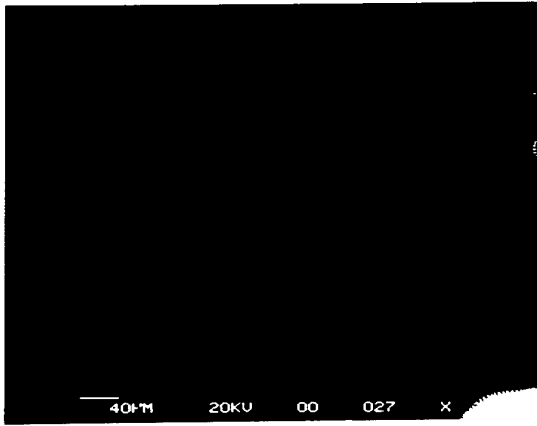


2. Close-up of cracks at 'A' in photo 1

Plate 9.14.2 Boron Phosphide Coating on ZnS



1. Enlargement of crack after 216 impacts at 185 m s^{-1}



2. X-ray dot mapping of zinc in top photo of montage



Plate 9.14.3 Boron Phosphide Coating on ZnS